

**3 DOF, LONG RANGE PLANAR LIFT AND SLIDE MICRO-CONVEYOR WITH  
VISION-BASED CONTROL SYSTEM**

by

Neil Ellerington

Submitted in partial fulfillment of the requirements  
for the degree of Doctor of Philosophy

at

Dalhousie University  
Halifax, Nova Scotia  
May 2012

© Copyright by Neil Ellerington, 2012

**DALHOUSIE UNIVERSITY**

**DEPARTMENT OF MECHANICAL ENGINEERING**

The undersigned hereby certify that they have read and recommend to the Faculty of Graduate Studies for acceptance a thesis entitled “3 DOF, LONG RANGE PLANAR LIFT AND SLIDE MICRO-CONVEYOR WITH VISION-BASED CONTROL SYSTEM” by Neil Ellerington in partial fulfillment of the requirements for the degree of Doctor of Philosophy.

Dated: May 22, 2012

External Examiner: \_\_\_\_\_

Research Supervisor: \_\_\_\_\_

Examining Committee: \_\_\_\_\_

\_\_\_\_\_

Departmental Representative: \_\_\_\_\_

# DALHOUSIE UNIVERSITY

Date: May 22, 2012

AUTHOR: Neil Ellerington

TITLE: 3 DOF, LONG RANGE PLANAR LIFT AND SLIDE MICRO-  
CONVEYOR WITH VISION-BASED CONTROL SYSTEM

DEPARTMENT: Department of Mechanical Engineering

DEGREE: PhD CONVOCATION: October YEAR: 2012

Permission is herewith granted to Dalhousie University to circulate and to have copied for non-commercial purposes, at its discretion, the above title upon the request of individuals or institutions. I understand that my thesis will be electronically available to the public.

The author reserves other publication rights, and neither the thesis nor extensive extracts from it may be printed or otherwise reproduced without the author's written permission.

The author attests that permission has been obtained for the use of any copyrighted material appearing in the thesis (other than the brief excerpts requiring only proper acknowledgement in scholarly writing), and that all such use is clearly acknowledged.

---

Signature of Author

# Table of Contents

List of Tables .....	ix
List of Figures .....	x
Abstract .....	xvi
List of Abbreviations and Symbols Used .....	xvii
Acknowledgements .....	xix
Chapter 1.0 Introduction .....	1
1.1 Background and Literature Review .....	1
1.2 Lift and Slide Conveyor System .....	5
1.3 Applications .....	5
1.4 Objectives and Scope .....	6
1.5 Multi-User MEMS Process .....	7
1.5.1 Design Rules .....	11
1.5.2 Availability of Other MEMS Processes .....	11
1.6 Micro Friction and Stiction .....	12
1.6.1 Stiction .....	13
1.6.2 Relative Contribution of Stiction Forces .....	15
1.6.3 Micro Friction .....	16
1.6.4 Friction and Stiction Comparison .....	17
Chapter 2.0 Background Lift and Slide Theory .....	19
2.1 Lift and Slide Conveyor Motion .....	19
Chapter 3.0 Control System .....	26
3.1 Overview .....	26
3.2 Hardware .....	26
3.2.1 DAQ Card .....	28
3.2.2 Amplifiers .....	28
3.2.3 Camera .....	29
3.2.4 Microscope Setup .....	29
3.3 LabView Vision Acquisition Program .....	30
3.3.1 Program Initialization .....	31

3.3.2 ROI Acquisition.....	32
3.3.3 Pattern Matching.....	33
3.3.4 Circle Detection.....	34
3.3.5 Waypoint Array.....	37
3.3.6 Position Deltas.....	40
3.3.7 Angle Range.....	40
3.3.8 Step Transition.....	41
3.3.9 Position Determination.....	42
3.3.10 Motion.....	42
3.3.11 Position Output to File.....	46
3.4 Control Lines.....	47
Chapter 4.0 Macro Proof of Concept Tests.....	49
4.1 Overview.....	49
4.2 Hardware Configuration.....	51
4.3 Servo Operation.....	52
4.4 NAND Gate Board.....	53
4.5 Functional Results of Macroscale Model.....	56
4.6 Lessons Learned from Macro Scale Model.....	59
Chapter 5.0 MEMS Lift and Slide Design Methodology.....	60
5.1 Arrays.....	60
5.2 XY polyMUMPs Pads.....	61
5.2.1 Pads.....	61
5.2.2 Chevrons.....	62
5.2.3 Springs.....	63
5.3 Vertical Thermal Actuator.....	65
5.4 Lifter Grids.....	67
5.5 Platforms (plates).....	68
5.6 Full Lift and Slide Assembly.....	69
5.7 Estimation of Maximum Conveyor Force.....	72
Chapter 6.0 XY Pad Micro Kinematic and Dynamic Model.....	73
6.1 Overview.....	73

6.2 Kinematic Model .....	73
6.3 Dynamic Model .....	77
6.3.1 From Kinematic model to Dynamic Model.....	77
6.3.2 Mass.....	78
6.3.3 Axial, Rotational and Lateral Stiffness.....	80
6.3.4 Equations of Motion .....	82
6.3.5 Matrix Equations .....	84
6.3.6 Natural Frequencies .....	85
6.3.7 Finite Element Analysis.....	86
Chapter 7.0 Chip Designs .....	92
7.1 Overview.....	92
7.1.1 IMUDTCV1.....	93
7.1.2 IMUDTCV2.....	94
7.1.3 IMUDTPH1 .....	95
7.1.5 IMUDTCV3.....	97
7.1.6 IMUDTCV4 & IMUDTCV5 .....	98
7.1.7 IMUDTCV6.....	100
7.1.8 IMUDTCV7 & IMUDTCV8.....	102
7.1.9 IMUDTCVX.....	110
7.1.10 IMUDTFR1 .....	112
7.2 Comparison of Chip Designs.....	114
7.3 Final Design.....	115
7.3.1 Grid Lifter and Pads.....	115
7.3.2 Wiring Resistance Considerations .....	115
7.3.3 Substrate grounding .....	116
Chapter 8.0 In-Plane Dynamic Measurements .....	117
8.1 Introduction.....	117
8.2 Derivation of blurred image Fourier Transform.....	119
8.2.1 1D Sidewall Profiles .....	119
8.2.2 Mathematical derivation .....	120
8.3 XY Actuator Pad.....	125

8.3.1 XY Pad Components .....	125
8.3.2 Thermal and Mechanical Response .....	126
8.3.3 FEM of XY Pad Resonant Modes .....	128
8.4 Experimental Results .....	130
8.4.1 Experimental Setup & Methods.....	130
8.4.2 Measurements .....	131
8.4.3 Out-of-plane and Rotational Resonances .....	141
8.5 Non-linear Motion and Duffing Equation. ....	143
8.6 Summary of Fourier Analysis of Blurred Images.....	146
Chapter 9.0 Open and Closed Loop Results .....	148
9.1 Testing .....	148
9.2 XY Pad Displacement.....	151
9.3 Open Loop .....	156
9.4 Closed Loop.....	164
9.5 Rotation.....	173
9.6 Following a Path .....	174
Chapter 10.0 Conclusion.....	181
10.1 Overview.....	181
10.2 Future Work.....	182
References.....	185
Appendix A – LabView Control System .....	191
A.1 Main VI.....	191
A.2 Sub VIs.....	196
Appendix B – Macro Friction, Micro Friction and Stiction .....	200
B.1 Introduction .....	200
B.1.1 What is the Difference Between Friction and Stiction?.....	200
B.1.2 Contributions.....	201
B.2 Macro Friction.....	203
B.2.1 Classical Models .....	203
B.3 Stiction .....	208
B.3.1 Capillary Forces .....	210

B.3.2 van der Waals Forces .....	217
B.3.3 Electrostatic Forces .....	218
B.3.4 Hydrogen Bridging (H-Bond) Forces .....	219
B.3.5 Relative Contribution of Stiction Forces .....	219
B.4 Micro Friction .....	221
B.4.1 Deformation .....	222
B.4.2 Stick-Slip.....	223
B.4.3 Friction and Stiction Comparison .....	224
B.5 Summary .....	225
Appendix C – Assignment of Copyright .....	226



## List of Tables

Table 1. Comparison of common MEMS actuators .....	4
Table 2. Field of view for various lens and zoom combinations .....	29
Table 3. Circle processing C code .....	37
Table 4. Number of control lines versus array size .....	48
Table 5. NAND gate logic table .....	54
Table 6. NAND circuit output .....	55
Table 7. S-Spring stiffness equations.....	64
Table 8. Paperclip spring stiffness equations.....	64
Table 9. Typical comparative spring stiffness values.....	65
Table 10. Parameters used for mass calculations.....	79
Table 11. Basic spring parameters.....	89
Table 12. Numerical comparison between FEM and analytical model.....	90
Table 13. Comparison of chip designs.....	114
Table 14. List of XY pad dimensions .....	129
Table 15. X & Y in-plane translational resonance data.....	141
Table 16. FEM predictions of in-plane rotational resonances .....	142
Table 17. Displacement and perpendicular disturbance .....	157
Table 18. Control parameters.....	172

## List of Figures

Figure 1. MUMPs layers and their respective thicknesses .....	8
Figure 2. Silicon substrate coated with nitride, polysilicon and photoresist layers.....	9
Figure 3. Photoresist exposed to UV light. ....	9
Figure 4. Unwanted polysilicon removed by etching .....	10
Figure 5. Photoresist stripped to complete layer.....	10
Figure 6. Complete structure consisting of all polysilicon and oxide layers .....	10
Figure 7. MUMPs structure after oxides are removed to release the structural layer .....	11
Figure 8. Two surfaces in contact only have a finite number of contact points .....	14
Figure 9. Relative contribution of various stiction forces.....	15
Figure 10. Dominant friction mechanisms with increasing velocity .....	17
Figure 11. A comparison of friction and stiction forces. ....	18
Figure 12. The three main components of the Lift and Slide conveyor system .....	19
Figure 13. The Floating Platform.....	20
Figure 14. Small delta ( $dX$ ) displacement with each cycle .....	21
Figure 15. Vertical (Y-axis) displacement of the platform.....	22
Figure 16. Horizontal (X-axis) displacement of the platform.....	22
Figure 17. Angular displacement of platform from opposed pad motion.....	23
Figure 18. Initial and final pad positions .....	25
Figure 19. Flowchart depicting the flow of data from computer station to the array .....	27
Figure 20. Photo view of the components .....	27
Figure 21. LabView Front Panel.....	31
Figure 22. Program Initialization.....	31
Figure 23. ROI Acquisition Sub-vi.....	32
Figure 24. Pattern Matching Sub-vi.....	33
Figure 25. Initialization for circle detection .....	34
Figure 26. Circle detection sub-vi.....	35
Figure 27. Circle processing code.....	36
Figure 28. Waypoint Addition .....	37
Figure 29. Waypoint Array Indexing.....	38
Figure 30. Entering Waypoint from a File.....	39

Figure 31. Position to Target Delta.....	40
Figure 32. Ensuring a -180 to 180 Degree Angle Range.....	40
Figure 33. Step Transition.....	41
Figure 34. Evaluates if the Object is at Target Position .....	42
Figure 35. Final link to the DAQ card is through a sub vi.....	43
Figure 36. Sub vi processes position and orientation of plate .....	43
Figure 37. Four analog signals are created .....	44
Figure 38. Four analog channels output to the DAQ card .....	45
Figure 39. Writing Positions to a File.....	46
Figure 40. Outputted Positional Data Format.....	47
Figure 41. Control line groupings.....	48
Figure 42. Macroscale model of a single cell .....	50
Figure 43. Macroscale model of a 4 cell array (2 x 2) lift and slide conveyor .....	50
Figure 44. Lifter servos raise the lifter grid slightly above the height of the pads .....	51
Figure 45. PWM pulses for different servo positions .....	52
Figure 46. 555 based servo controller.....	53
Figure 47. NAND Gate circuit used to control each channel .....	55
Figure 48. A 2x2 macro array with a single platform.....	56
Figure 49. A simple cross path to show basic functionality of the macro model .....	57
Figure 50. A more complex path .....	57
Figure 51. Multiple platforms occupying a 2x2 array .....	58
Figure 52. Two platforms following box paths over a 2x2 array .....	58
Figure 53. 3 x 3 polyMUMPs array.....	60
Figure 54. LEdit representation of the polyMUMPs pad, chevron and springs .....	61
Figure 55. 3D LEdit view of the pad assembly .....	62
Figure 56. Standard 200 $\mu\text{m}$ , 6° chevron.....	62
Figure 57. Paperclip Spring .....	63
Figure 58. S-Spring.....	63
Figure 59. Length, width and thickness of a standard polysilicon spring beam .....	65
Figure 60. LEdit representation of the chevron vertical thermal actuator (VTA) .....	66
Figure 61. 3D LEdit view of the chevron vertical thermal actuator (VTA) .....	66

Figure 62. Set of VTAs Connected to Lifter Grid .....	68
Figure 63. Larger 4x4 array .....	70
Figure 64. 50x zoom and 25x zoom respectively .....	71
Figure 65. 16x zoom and 8x zoom respectively .....	71
Figure 66. 4.5x zoom and 2.25x zoom respectively .....	71
Figure 67. Kinematic model of XY pad.....	74
Figure 68. The combination of Prismatic and Revolute joints .....	75
Figure 69. Kinematic model showing numbers of links and 1 DOF joints .....	76
Figure 70. Dynamic model .....	78
Figure 71. Typical center pad dimensions .....	79
Figure 72. Key dimensions of an S-spring.....	81
Figure 73. Key dimensions of a paperclip spring .....	82
Figure 74. Stretch of lateral and axial springs as a result of plate rotation.....	83
Figure 75. XY pad out of plane modes using FEM.....	87
Figure 76. XY pad in-plane modes using FEM .....	88
Figure 77. Comparison of lateral motion between FEM and analytical model.....	91
Figure 78. Comparison of rotational motion between FEM and analytical model.....	91
Figure 79. IMUDTCV1 .....	93
Figure 80. IMUDTCV2 .....	94
Figure 81. IMUDTPH1 .....	95
Figure 82. IMUDTEW1.....	96
Figure 83. IMUDTCV3 .....	97
Figure 84. IMUDTCV4 .....	98
Figure 85. IMUDTCV5 .....	99
Figure 86. IMUDTCV6 .....	100
Figure 87. Micro-profiler image of single XY pad on IMUDTCV6. 0 V .....	101
Figure 88. Micro-profiler image of single XY pad on IMUDTCV6. 12 V .....	101
Figure 89. IMUDTCV7 .....	102
Figure 90. IMUDTCV8 .....	103
Figure 91. Portion of 4x4 array on IMUDTCV7 profiled .....	105
Figure 92. Profile views of SOI plate sitting on 4x4 array on IMUDTCV7 (9 V).....	106

Figure 93. 3d view of SOI plate sitting on 4x4 array on IMUDTCV7 (9 V) .....	107
Figure 94. Profile views of SOI plate sitting on 4x4 array on IMUDTCV7 (0 V).....	108
Figure 95. 3d view of SOI plate sitting on 4x4 array on IMUDTCV7 (0 V). .....	109
Figure 96. IMUDTCVX.....	110
Figure 97. IMUDTCV7 .....	112
Figure 98. Plot of $ \text{Bessel } J_0 $ vs. blur in radians .....	124
Figure 99. Schematic of PolyMUMPs MEMS XY pad.....	125
Figure 100. FEM simulation.....	129
Figure 101. Two sample camera images of device driven at 3.5 Volts .....	132
Figure 102. Sampled 1D profiles of the two images .....	133
Figure 103. FFT of the two image .....	134
Figure 104. Graph of raw FFT magnitude of 9, 10, 13 and 14th harmonics .....	134
Figure 105. Graph of normalized magnitudes of harmonics .....	135
Figure 106. Experimentally measured attenuation .....	136
Figure 107. Long range scan of displacement vs. frequency.....	137
Figure 108. Fine scan at resonanc.....	138
Figure 109. Effect of averaging on noise.....	139
Figure 110. Comparison for three long range scans .....	140
Figure 111. Plot of non-linear response of a mechanical system .....	144
Figure 112. Experimental Duffing response.....	145
Figure 113. Experimental values of jump down frequency.....	146
Figure 114. Corner of polyMUMPs lift and slide array.....	148
Figure 115. Two frames demonstrating motion of an SOI platform .....	149
Figure 116. Composite image showing motion of SOI platform along the array.....	149
Figure 117. Motion of platform shown in four frames.....	150
Figure 118. XY pad displacement; 7 V, 10 V and 12 V at 4 Hz .....	152
Figure 119. XY pad displacement; 7 V, 10 V and 12 V at 8 Hz .....	153
Figure 120. XY pad displacement; 7 V, 10 V and 12 V at 16 Hz .....	153
Figure 121. XY pad displacement; 7 V, 10 V and 12 V at 24 Hz .....	154
Figure 122. XY pad displacement; 7 V, 10 V and 12 V at 50 Hz .....	154
Figure 123. XY pad displacement; 7 V, 10 V and 12 V at 100 Hz .....	155

Figure 124. average XY pad displacement; 7 V, 10 V and 12 V at 4-100 Hz.....	155
Figure 125. Plate travelling in a series of horizontal and vertical linear paths .....	156
Figure 126. Zoomed in view of the horizontal paths of three lines .....	157
Figure 127. Zoomed in view of the vertical paths of three lines .....	158
Figure 128. Speed of the plate .....	159
Figure 129. Speed of plate in direction perpendicular to intended path .....	160
Figure 130. Plate perpendicular disturbance relative to the plate speed.....	160
Figure 131. Frames showing the start and finish position of a platform .....	161
Figure 132. Displacement of each step vs frequency .....	162
Figure 133. Average perpendicular disturbance per step vs frequency.....	163
Figure 134. Plate displacement vs pad displacement (traction).....	163
Figure 135. Speed of plate at various voltages and frequencies .....	164
Figure 136. Speed of plate perpendicular disturbance.....	165
Figure 137. Plate perpendicular disturbance relative to the plate speed.....	166
Figure 138. Average plate perpendicular disturbance .....	166
Figure 139. The effect of perpendicular disturbance .....	167
Figure 140. Closeup view of the effect of perpendicular disturbance .....	168
Figure 141. Closeup view of the net platform perpendicular disturbance.....	169
Figure 142. The effect of perpendicular disturbance on long range Y motion.....	169
Figure 143. Closeup view of the effect of perpendicular disturbanc .....	170
Figure 144. The standard "dogleg" path used for point to point motion .....	171
Figure 145. Standard "dogleg" path for point to point motion .....	172
Figure 146. 90° rotation of a platform .....	173
Figure 147. Circular pattern of a single plate on the macro Lift and Slide prototype ...	175
Figure 148. Circular path of a single plate on the MEMS Lift and Slide platform .....	175
Figure 149. Box pattern of a single plate on the macro Lift and Slide prototype.....	176
Figure 150. Box pattern of a single plate on the MEMS Lift and Slide platform .....	176
Figure 151. Cross pattern of a single plate on the macro Lift and Slide prototype .....	177
Figure 152. Cross pattern of a single plate on the MEMS Lift and Slide platform.....	177
Figure 153. Three frames showing closed loop motion.....	178
Figure 154. Motion of a salt crystal travelling approximately 400 $\mu\text{m}$ .....	180

Figure 155. Main Labview control system VI.....	195
Figure 156. Region of Interest Capture Sub VI.....	196
Figure 157. Pattern Recognition Sub VI.....	197
Figure 158. DAQ Output Sub VI.....	199
Figure 159. Simple relay model (Coulomb Friction).....	204
Figure 160. Combination of Coulomb and viscous friction .....	205
Figure 161. Model combining Coulomb and viscous friction .....	206
Figure 162. Stribeck curve to remove discontinuity .....	207
Figure 163. Friction hysteresis loop from increasing and decreasing velocity.....	208
Figure 164. Two surfaces in contact.....	210
Figure 165. Droplet between two smooth surfaces.....	211
Figure 166. Droplet on a surface.....	212
Figure 167. Non-spreading liquid droplet between two surfaces .....	213
Figure 168. Spreading liquid droplet between two surfaces.....	213
Figure 169. Liquid condensate creates bridges between close asperities .....	215
Figure 170. Characteristic distance of capillary condensation .....	216
Figure 171. Capillary stiction as a function of temperature and relative humidity .....	216
Figure 172. Typical van der Waals surface interaction energy vs roughness.....	218
Figure 173. Relative contribution of various stiction forces.....	220
Figure 174. Dominant friction mechanisms with increasing velocity .....	221
Figure 175. Deformation zone of asperity .....	222
Figure 176. Stick-slip motion .....	223
Figure 177. A comparison of friction and stiction forces.....	225

## **Abstract**

The purpose of this thesis is to introduce a novel method of dry micro-object manipulation and to demonstrate predictable vision-based control. The Lift and slide conveyors presented utilize three main components: pads, lifters and a floating platform. The pads have a small planar displacement in the XY axis and lifters have a small Z axis displacement. Together they can be used to create minute displacements per cycle while carrying a floating platform that can hold the desired objects to be moved. These platforms can be handed off to other pad-lifter groups to create an unlimited planar envelope. The lift and slide conveyor theory was first demonstrated through the use of macroscale models that simulated the various required micro-scale components. Two degree of freedom control was established using LabView with open and closed loop routines. The open loop control allows basic directional control through pushbuttons, while closed loop control allows motion through preset paths using a vision recognition routine. A model is presented that predicts the resonance frequencies with different loading and geometric characteristics to aid in design optimization for various applications. This model is compared to FEM and experimental results based on Fourier analysis of blurred images that are captured using a standard video camera. Parameters such as velocity, drift and traction are well characterized for different operating conditions. Several paths were tested using the closed loop control system and compared with the equivalent paths followed by the macro Lift and Slide prototype. It was concluded that the presented macromodel successfully proved the concept of the lift and slide conveyor and worked well as a test bed for designing the Labview open loop and closed loop control systems. The proposed MEMS design has the potential to meet the needs of many applications where long range untethered control of micro-objects with multiple degrees of freedom is required.



## List of Abbreviations and Symbols Used

1D	One Dimensional
2D	Two Dimensional
3D	Three Dimensional
A	Hamaker constant
CAD	Computer Aided Design
cm	Centimeter
d	Displacement
DAQ	Data Acquisition
DC	Direct Current
$d_{cap}$	Capillary condensation
$d_o$	Universal Cutoff Distance
dX	X-Axis Displacement
dY	Y-Axis Displacement
d $\theta$	Angular Displacement
E	Dielectric permittivity <i>or</i> Young's Modulus
f	Frequency
F	Force Matrix
$F_f$	Force of Friction
$F_N$	Normal Force
$F_v$	Friction due to viscosity
FEM	Finite Element Modeling
FFT	Fast Fourier Transform
fps	Frames per Second
Hz	Hertz
I	Inertia
IC	Integrated Circuit
I/O	Input/Output
K	Stiffness Matrix
$K_{axial}$	Axial Stiffness
$K_{lateral}$	Lateral Stiffness
$K_{rot}$	Rotational stiffness
$\tilde{K}$	Mass Normalized Stiffness Matrix
kg	Kilogram
KHz	Kilo-hertz
kS	Kilo-samples
L	Length <i>or</i> applied load
M	Mass Matrix
mA	Milli-Amp
MEMS	Micro Electro Mechanical Systems
MHz	Mega-hertz
ms	Milli-second
MUMPs	Multi-User MEMS Process
nm	Nano-meter

P	Vapour pressure
$p_s$	Saturated vapour pressure
PWM	Pulse Width Modulation
r	Radius of curvature of meniscus
R	Gas constant
RF	Radio Frequency
ROI	Region of Interest
SDA	Scratch Drive Actuator
SOI	Silicon on Insulator
t	Thickness
T	Absolute temperature <i>or</i> Period
UV	Ultraviolet
V	Volts <i>or</i> Molar volume
VTA	Vertical Thermal Actuator
w	Width
Z	Distance between surfaces
$\beta$	Blur (radians)
$\gamma_{la}$	Surface tension
$\gamma_{sa}$	Surface tension of solid-air interface
$\gamma_{sl}$	Surface tension of solid-liquid interface
$\zeta$	Damping Ratio
$\Theta$	Angle
$\theta_c$	Contact angle
$\lambda$	Eigenvalue, Fundamental Wavelength
$\mu$	Coefficient of friction
$\mu\text{g}$	Micro-gram
$\mu\text{m}$	Micro-meter
$\mu\text{N}$	Micro-Newton
$\mu\text{S}$	Micro-second
$\rho$	Density
$\tau$	Thermal Time Constant
$\nu$	Poisson's Ratio <i>or</i> velocity
$\varphi$	Phase
$\omega$	Natural Frequency

## **Acknowledgements**

My appreciation goes out to the many people who helped me with this Thesis. I want to thank my supervisor Dr. Ted Hubbard for inviting me into the MEMS research group. Through his guidance and support, he helped to make my graduate studies a rewarding experience. Thanks go to my committee members Dr. Marek Kujath and Dr. Jason Gu, whom kept me on track with their timely advice and suggestions, and my colleagues Byron Shay, Mathew Bligh, Craig Arthur, Rene D'Entremont, Ben Bschaden, Rachael Schwartz, Merhdad Mottaghi and Ben Turnbull for all their inspiration, ideas and help.

I would also like to extend my gratitude to Mr. Stephen Rigden at the Canadian Forces Naval Engineering School, whom graciously gave me the time and support to further my education.

Thank you to my wonderful wife, Kim, for all of her support, encouragement and praise, and to my children, Michelle-Ashley and Scott for putting up with the many long days of my absence.

# Chapter 1.0 Introduction

## 1.1 Background and Literature Review

A number of applications require the manipulation of micro-objects with two or more planar degrees of freedom. Applications include movement of micro-stages, assembly of micro components and biomaterial (cell) control for analysis. Wet chip applications, where the movement equipment is submersed in a fluid, often use electrokinetics for control of particles. Particles can be manipulated over electrode arrays that are only limited in size by the chip dimensions. In a dry environment this is no longer practical, and a dynamic structure must be used to create the forces and displacements required. With existing MEMS (Micro-Electro-Mechanical Systems) thermal structures, this is usually limited to a small planar envelope, with each degree of freedom often having a range of less than 10 microns. Range amplification typically comes at the cost of a reduction in usable force.

Motion of particles can be divided into three ranges, short, medium and long range. Short range would be considered motion of less than 10 microns, the typical limit of a standard thermal actuator. Medium range would extend up to approximately 100 microns, which would be the limit of a typical amplified actuator. Long range motion would extend beyond 100 microns.

A number of designs have been developed to address the issue of small planar envelope actuators, and create a large range of motion in a dry environment. An inchworm mechanism presented by de Boer *et al* [1] moves a plate through a series of steps. Each step starts with a clamp holding one end of the plate. The center of the plate is then deflected causing a small displacement of the unclamped end of the plate. A second clamp holds the deflected end of the plate in position and the first clamp is released. The center plate deflection is released allowing the plate to return to its original shape, which results in a deflection of the unclamped end. The direction of motion is dependent on the phase of the clamping. This method results in a large potential displacement, with

relatively high forces. However, this device has a number of disadvantages. Firstly, it is constrained to linear motion and would be difficult to adapt to planar motion due to the requirement for clamps. Secondly, the plate does not remain flat due to the center deflection. This center deflection makes it difficult to carry particles and be used as a stage or conveyor. Lastly, the design cannot easily be chained together to create a potentially infinite range of travel. Similar designs have been published by Sarajlic *et al* [2] and Tas *et al* [3].

Planar frictional conveyors created by Shay *et al* [4] create full planar motion through a series of inverted feet. The design uses frictional forces to hold a free moving plate in place with respect to the feet. A series of three feet, two movable and one stationary is sufficient for a single degree of freedom. If one foot moves, the friction between the plate and the two stationary feet is enough to hold the plate stationary. If two feet move, then the friction of the single stationary foot is insufficient to hold the plate and it will move. Four movable feet and a single stationary foot can be configured to give either two or three degrees of freedom. However, there is a key disadvantage of this design. The design is completely dependent on differential friction, which means each foot must contribute the correct amount of friction for the device to operate correctly. Testing has shown that height variations in the feet results in feet often not making contact with the plate. Grease is required to create a bridge between the feet and the plate. The process of adding grease is difficult and time consuming.

Meller *et al* [5], Suh *et al* [6] and Ebefors *et al* [7] have all demonstrated a cilia biomimicry process. Inverted cilia, or feet, are used to create minute displacements per cycle while carrying a platform holding the desired objects to be moved. As the cilia feet curl up, they have a small horizontal tip deflection. Once deflected, a second set of cilia oriented in the opposite direction will rise and hold the platform in position while the first set returns to their seated position. As the second set of cilia now lower, the platform deflects further. This cycle is then repeated with cumulative steps. The platforms can be handed off to other cilia to create an unlimited planar envelope. By changing the operational phase of the cilia, bidirectional control can be achieved. Planar control is

created with additional feet aligned with the other axis. With an array of cilia in both axes, three planar degrees of freedom for a platform are possible. The disadvantage of this method is that current designs are quite large, with cilia feet typically at least 1mm across resulting in a minimum 3mm x 3mm platform size. Current standard MEMS processes provided by foundry don't allow for the necessary curling motion of the actuator tip that is required to give an adequate planar deflection that would be required for smaller devices.

There are a number of actuator designs commonly used in MEMS fabricated structures. The four most common categories of actuators are: electrostatic, thermal, piezoelectric and magnetic.

Electrostatic actuators function as a result of attraction between oppositely charged conductors [8]. As a capacitive device, they require higher voltages and relatively high surface areas, but benefit from low currents and power consumption [9]. They are simple to fabricate using standard MEMS fabrication techniques. Larger areas are achieved through interlaced fingers, creating a comb drive. Since force is relative to the surface area, generally they are low force devices. They have a small travel distance, but do have the advantage of fast switching speeds [10].

Thermal actuators use the principle of thermal expansion. When a current is passed across a semiconductor, typically polysilicon for MEMS structures, the material expands a small amount as it heats. This expansion can be used in several ways to create an actuator. In the first method, the difference between two expansions can be coupled to create a displacement [11]. By adjusting the geometries, variations in heating across the structure result in amplified differential expansion. The second method relies on thermal expansion of opposed anchored beams [12]. In this case, the two beams buckle as they expand towards each other. The displacement of the buckle can be harnessed as a usable force. There are a number of advantages of thermal actuators; they generate high force with low voltage, they have a small footprint with a relatively large travel, they are simple to fabricate and robust [13]. Their disadvantage comes from their relatively high

power consumption, as a thermal device, and their slow speed as a result of their thermal time constant [14].

Piezoelectric actuators generate a displacement through an electric field induced strain of a thin-film PZT material [15-19]. These actuators offer a relatively high force and fast response using a low voltage, but have extremely small strain limits, typically in the range of ~0.1-0.2% [20]. This minimal strain often requires amplification, at the cost of force, to create usable displacement.

Electromagnetic actuators are less common in MEMS applications due to the difficulty implementing them with conventional processing techniques [21]. Displacement is due to the interaction among various magnetic elements. The actuators require deposition of magnetic materials and often utilize a permanent magnet. While manufacturing techniques result in thick conductors and magnetic features to create coil structures, the result is a high force actuator with a large travel [22-26]. As a current driven actuator, it has a high power dissipation.

Table 1 shows a comparison of the main characteristics of electrostatic, thermal, piezoelectric and magnetic actuators used with MEMS structures.

	<b>Electrostatic</b>	<b>Thermal</b>	<b>Piezoelectric</b>	<b>Magnetic</b>
<b>Low Power</b>	Yes	No	Yes	No
<b>Fast Switch</b>	Yes	Somewhat	Yes	Somewhat
<b>High Force</b>	No	Yes	Yes	Yes
<b>Large Travel</b>	No	Yes	Somewhat	Yes
<b>Small Footprint</b>	No	Yes	Somewhat	No
<b>Simple Fab</b>	Yes	Yes	No	No
<b>Low Voltage</b>	No	Yes	Somewhat	Yes
<b>Robustness</b>	Somewhat	Yes	Yes	Yes

**Table 1. Comparison of common MEMS actuators. Adapted from [27]**

Based on the characteristics of the actuators presented in Table 1, this thesis has concentrated on thermal actuators for both in-plane and out-of-plane displacement.

## **1.2 Lift and Slide Conveyor System**

A proposed solution for long range manipulation of micro-objects in a dry environment is the Lift and Slide Conveyor system. This novel system utilizes a platform to carry micro-objects. The platform itself is manipulated by a series of pads that move back and forth a few microns in both planar directions. A lifter grid is used to decouple the pad movement from the platform as it moves back and forth ensuring that the resultant motion is a series of cumulative steps in the desired direction. Multiple pads can be placed next to each other, expanding the range of motion to the size of the chip. If pads are controlled independently then multiple platforms can be manipulated simultaneously. Opposed motion of adjacent pads can also be used to impart a torque on the platforms, resulting in 3 degrees of freedom of manipulation. If the particles or micro-objects being manipulated have a flat surface and are large enough to be fully supported by the grid, then the platform is not required and the objects can ride directly over the conveyor.

## **1.3 Applications**

The Lift and Slide conveyor system lends itself well to many micro-object manipulation applications.

Micro devices continue to become more complex and often cannot be constructed using a single MEMS process. Incompatibility of manufacturing methods of various components would lead to the requirement of a post-processing assembly. Human intervention may work for some assembly functions, but where environmental considerations, fatigue and human error become a concern then a mechanism for micro-assembly becomes more important. The Lift and Slide conveyor system allows for accurate alignment and orientation for micro-objects as part of the assembly process.

As fiber optics becomes more common as a means of data transfer, there is an ever increasing requirement for more complex switching mechanisms used for redirecting the



optical network. The use of Lift and Slide conveyors systems would allow for floating mirrors in complex networks to be reconfigured, without the requirement to have the network switch mechanism predesigned to allow for all conceivable layouts. This would be especially useful for remote applications where network reconfiguration would not otherwise be possible unless anticipated in the original design.

Stages are often used for manipulation of dry biomaterial for bio-medical research. This is normally a slow process where heavy human intervention is required one particle at a time. The Lift and Slide conveyor could be adapted for rapid biomaterial sorting and delivery to downstream test devices. This would allow for quick automation when testing large quantities of biomaterial, while directing sorted streams to appropriate testing apparatus.

#### **1.4 Objectives and Scope**

The purpose of this thesis is to introduce a novel method of dry micro-object manipulation and to demonstrate predictable vision-based control. Previous work has covered microfluidics and manipulation of objects in an aqueous environment. It is not the intention of this thesis to revisit these concepts.

This thesis investigates a long range conveyor system that allows accurate motion with 3 degrees of freedom and is not dependent on post processing for correct operation. A number of different size arrays have been fabricated to show the ability to expand an array of individual elements. Control is established with two and three degrees of freedom, using open and closed loop routines. Models will be presented that predict the resonance frequencies with different loading and geometric characteristics to aid in design optimization for various applications. Velocity will be shown to be dependent on pad chevron voltages and frequency.

New work presented by the author includes a novel micro-conveyor design that allows long range motion of micro-objects, a Labview based vision-based control routine and a model for resonance frequency prediction and design optimization.

### **1.5 Multi-User MEMS Process**

MEMS designs presented in this thesis are manufactured using the Multi-User MEMS Process (MUMPs) through CMC Microsystems. MUMPs is a low-cost fabrication technique that is suitable to many MEMS applications, without being optimized to any single application. MUMPs structures are constructed in a series of layers utilizing photolithography. This process is taken from well established procedures used in the construction of integrated circuits (IC's).

A finished MEMS structure consists of several polysilicon structural layers and silicon dioxide sacrificial layers bonded to an insulating nitride layer over a silicon wafer. The silicon dioxide layers are also insulators and can be left behind to create electrically insulating structural layers. A final gold metal layer is also available.

The layers available in MUMPs and their respective thicknesses are shown in Figure 1.

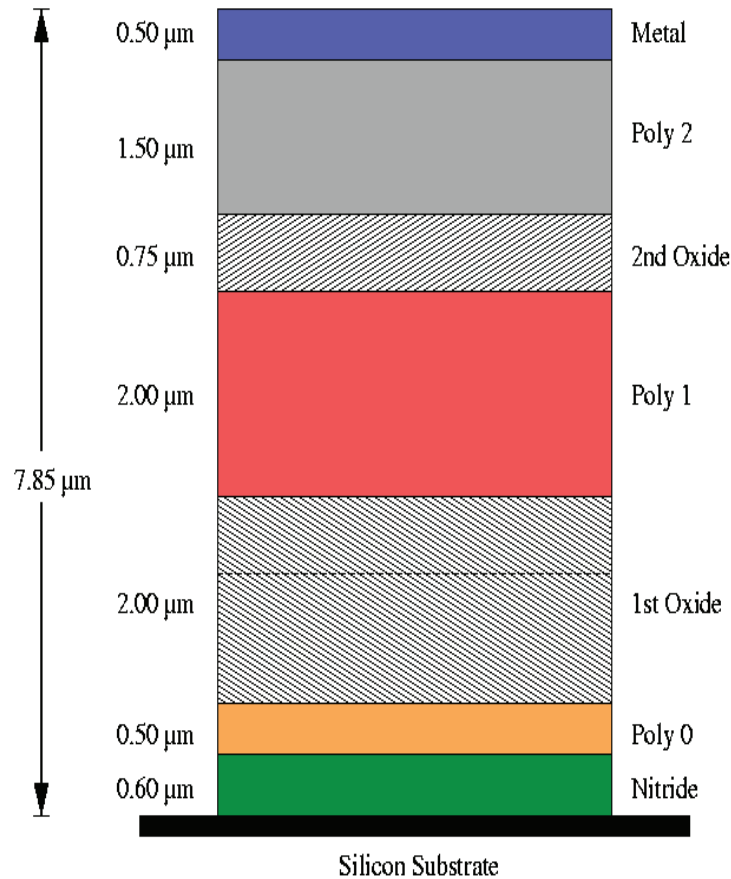


**Figure 1. MUMPs layers and their respective thicknesses. Adapted from polyMUMPs Design Handbook [28].**

The process begins with the design being separated into the various layers. Each layer is used to generate either a positive or negative mask. A mask is simply a two dimensional view of the layer imprinted on either a clear plastic or glass film. A positive mask allows light to pass through where no structure exists, and blocks light where the structure does exist. A negative mask is the reverse of this; light can pass through where the structure is and is blocked elsewhere. The use of a positive or negative mask varies both with the chemicals used and whether or not the structure is an object or a hole.

An even layer of nitride is deposited over the entire silicon wafer, followed by the first layer of polysilicon.

A chemical known as photoresist is evenly sprayed over the polysilicon (See Figure 2). Photoresist changes properties when subjected to UV light. Light is then shone through the first mask. A chemical is then used to remove all photoresist that was exposed (See Figure 3). Another chemical etchant is then used to remove the unwanted polysilicon, the photoresist layer that remains acts as an etch mask protecting the polysilicon structure (See Figure 4). Finally, the remaining photoresist is stripped chemically, leaving the desired polysilicon structure (See Figure 5).

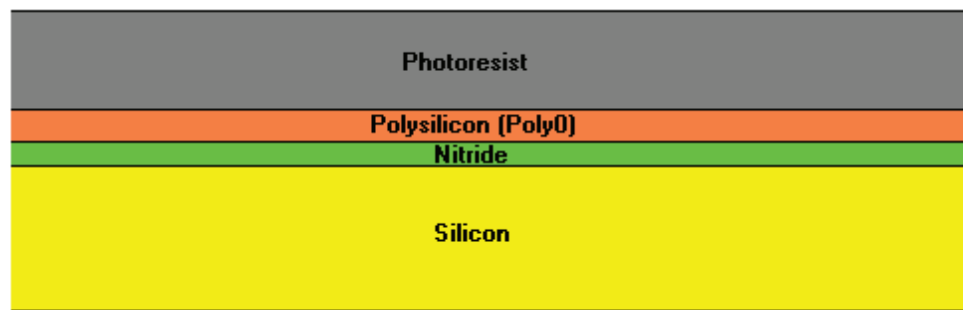


Figure 2. Silicon substrate coated with nitride, polysilicon (Poly0) and photoresist layers. Adapted from polyMUMPs Design Handbook [28].

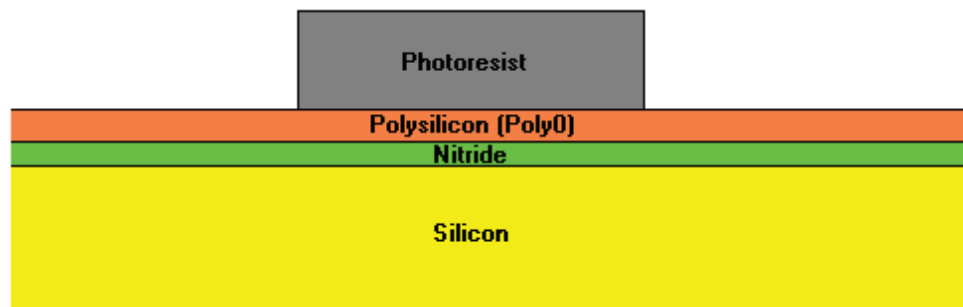


Figure 3. Photoresist exposed to UV light is removed leaving patterned photoresist mask. Adapted from polyMUMPs Design Handbook [28].

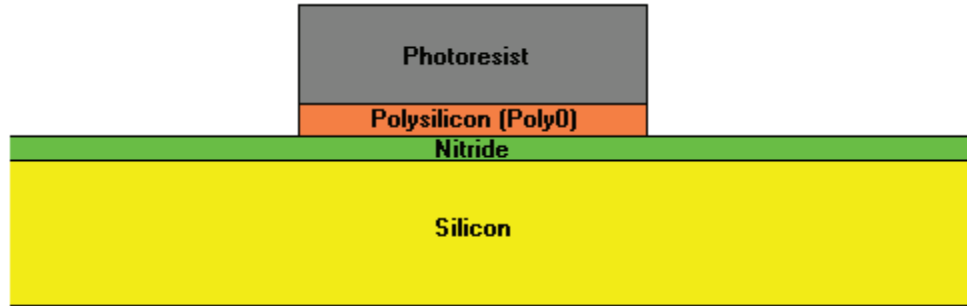


Figure 4. Unwanted polysilicon removed by etching. Adapted from polyMUMPs Design Handbook [28].

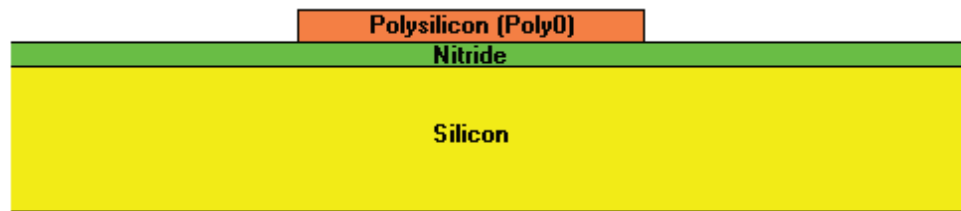


Figure 5. Photoresist stripped to complete layer. Adapted from polyMUMPs Design Handbook [28].

This procedure with photoresist, etching and stripping is repeated for each layer; the polysilicon, the silicon dioxide and the gold, until all layers are complete (See Figure 6).

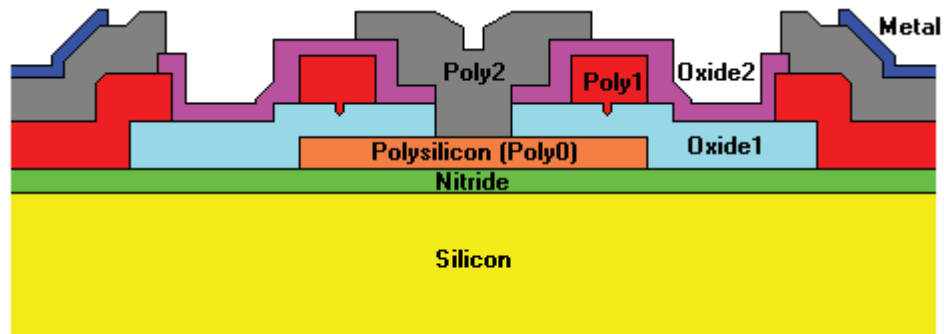
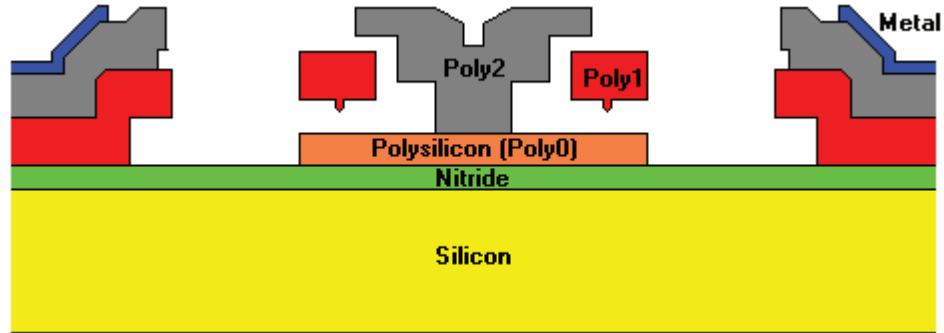


Figure 6. Complete structure consisting of all polysilicon and oxide layers. Adapted from polyMUMPs Design Handbook [28].

The final process involves the release of all structural components. A chemical is used to etch away all of the silicon dioxide layers, allowing for the polysilicon layers to be freed from one another (See Figure 7).



**Figure 7. MUMPs structure after oxides are removed to release the structural layer. The structure shown is a cross section through an electrostatic motor. Adapted from polyMUMPs Design Handbook [28].**

After releasing the MEMS structure on the wafer, the wafer is cut into separate dies (chips). Each chip is then bonded to the appropriate package housing.

### **1.5.1 Design Rules**

Design rules are required to ensure consistent results, and reduce to risk of damaged devices during the manufacturing process. The rules fall into two categories; rules that when broken may cause failure of the device, and those that when broken may cause damage to other devices on the wafer. The former may be broken, provided that justification is given. The latter is compulsory, and construction of the design will not begin until they are corrected. For example, the minimum polysilicon feature size is 2  $\mu\text{m}$  and the minimum spacing is 2  $\mu\text{m}$ .

### **1.5.2 Availability of Other MEMS Processes**

PolyMUMPs is not the only process available for use. There are many other MEMS processes, such as SOI (Silicon on Insulator), SOI MUMPs, and Metal MUMPs to name a few. Many others exist, however availability and suitability of each has to be assessed. Each process has a specific “recipe” of layer geometries and materials. Currently,

polyMUMPs has proven to be the optimum process for chevron design and its ease for constructing out of plane structures such as VTAs. However, polyMUMPs has also proven to have a shortcoming with regards to platform design. The extremely thin nature of the polysilicon layers results in platforms that are either too flexible and succumb to a “blanket effect” or platforms that are not flat due to residual stresses. In both cases, the lack of a flat surface results in incomplete contact with either the lifters or the pads. A rigid surface is required to ensure proper pad contact and subsequent decoupling. A number of layer materials and designs were tested. The optimum platform material proved to be constructed of SOI, with a thickness of 10  $\mu\text{m}$ .

## 1.6 Micro Friction and Stiction

Micro friction and stiction are two phenomena that have a great impact to the functionality of moving MEMS structures. The aim of this section is to give a general understanding of what elements contribute to micro friction and stiction, and outline the differences.

The terms are used frequently in literature, often incorrectly. Friction has been defined as a resistance to relative motion of in contact surfaces. This can be broken down into two basic types; static and dynamic. Static friction is the initial level of resistance to motion, before the two surfaces have a relative motion. Dynamic friction is resistance to motion while the two surfaces have a relative motion. Many publications, such as van Spengen *et al* [29] refer to stiction as a short term for static friction. It is, however, now widely accepted that the correct definition of stiction is actually an adhesion between two surfaces, as seen in papers by Olsson *et al* [30] and Hariri *et al* [31,32]. This adhesion is not only a force that resists relative motion in addition to friction, but also can be cause an increase in actual friction forces by increasing the normal force between surfaces.

### 1.6.1 Stiction

As previously defined, stiction is a phenomena that causes adhesion between two surfaces. It is a relatively minor force at the macro scale, and is usually ignored. However, at the micro scale it can play a significant role (for reasons that will be discussed shortly) and is often responsible for the failure of MEMS devices. Devices designed to function correctly at the macro scale can unexpectedly fail at the micro scale. Having said that, as with friction, when properly understood it can be used to the advantage of a device. For example, stiction can be used for self assembly of 3-D microstructures (van Spengen *et al* [29]), or to aid in transferring displacement forces from actuators such as with platforms resting on moving pads, or with linear impact drives. A solid knowledge of the underlying physics involved is required to make stiction forces controllable and predictable.

There are two types of stiction; fabrication stiction and in-use stiction. Fabrication stiction is major failure mode as a result of the use of wet etchants. The evaporation of the wet etchant between two surfaces can draw the surfaces together causing them to permanently adhere. Since this is a function of the manufacturing process, it will not be addressed in this Appendix. However, an understanding of in-use stiction will allow the reader to grasp the concept of fabrication stiction, since ultimately the failure is related.

van Spengen *et al* [29] and Tas *et al* [33] suggest that there are four major adhesion mechanisms that result in stiction; capillary forces, van der Waals forces, hydrogen bridging and electrostatic forces. These are analyzed in detail in Appendix B.

Despite knowledge of the adhesion mechanisms, stiction effects are actually not very predictable quantitatively. They are highly dependent on both the surfaces and the environment. Minor changes to either can have enormous effect on stiction. It can also be extremely complicated to get a true picture of surface geometry. Most models rely on either surface sampling or Gaussian predictions to approximate surface roughness



distributions. Surface sampling creates an extreme amount of data requiring large amount of computational power to analyze with the trade off being surface distribution predictions that are not very accurate.

In order to understand why stiction is a major factor at the micro scale, one must have a basic understanding of scaling laws. Stiction is a direct result of the dominance of surface forces over body forces (Hariri *et al* [32]). Surface forces become more pronounced over the body forces due to large surface over volume ratio (van Spengen *et al* [29]). As devices are scaled down, the volume of the device scales down with third power of dimension ( $L^3$ ), while surface area only scales down as square ( $L^2$ ) (Hariri *et al* [32]). Therefore as the size of the device decreases, the ratio of the surface area to the volume increases with a factor of the scaling ratio. The consequence of this is that body forces such as weight and inertial forces that are proportional to volume lose their significance against surface forces (Hariri *et al* [32]).

The surfaces themselves must first be defined to account for the surface roughness. Where in the macro scale surfaces have an apparent area of contact, for example length x width of a rectangular surface, when looking at the micro scale it becomes clear that two rough surfaces in contact only have a certain number of contact points. When investigating stiction, Hariri *et al* show that it is advantageous to map the contact between two rough surfaces as a smooth rigid surface and a single equivalent rough surface (Figure 164). The use of a single equivalent surface aids in stiction analysis and is used in most models including those developed by Hariri *et al* [31,32], van Spengen *et al* [29] and Tas *et al* [33].

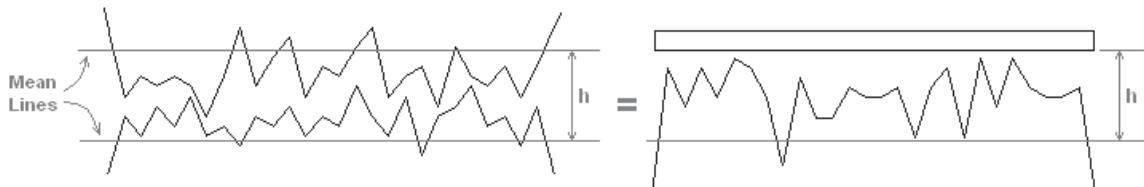


**Figure 8. Two surfaces in contact only have a finite number of contact points. An equivalent rough surface can be defined against a perfectly flat surface to aid in analysis. Adapted from Hariri *et al* [32]**

One thing not yet mentioned is plastic and elastic deformation. The real contact area will actual depend on the amount and type of deformation experienced by the surface contact points, known as asperities.

### 1.6.2 Relative Contribution of Stiction Forces

The four factors that result in stiction all have various significance (Figure 173). All reviewed papers concerned with stiction, Hariri *et al* [31,32], van Spengen *et al* [29] and Tas *et al* [33], are in agreement with the relative contribution of the forces. Capillary forces are usually the major dominant force, and often the only force that need be considered. However, in low pressure environments, or when relative humidity is significantly low, then van der Waals forces would be the next significant force. Electrostatic forces usually disappear with contact, and so are unlikely to be of any concern, though a high contact resistance could lead to forces in the order of magnitude of the capillary forces, leading to them being a significant stiction force contributor. Normally electrostatic forces are much lower than the van der Waals forces and unlikely to be considered. Hydrogen bridging implies hydrophilic surfaces that would be prone to capillary bridges, making hydrogen bridging forces negligible. Even in a completely dry environment (zero relative humidity) the van der Waals forces would dwarf the hydrogen bridging forces. Electrostatic forces are marginally larger than the hydrogen bridging forces.

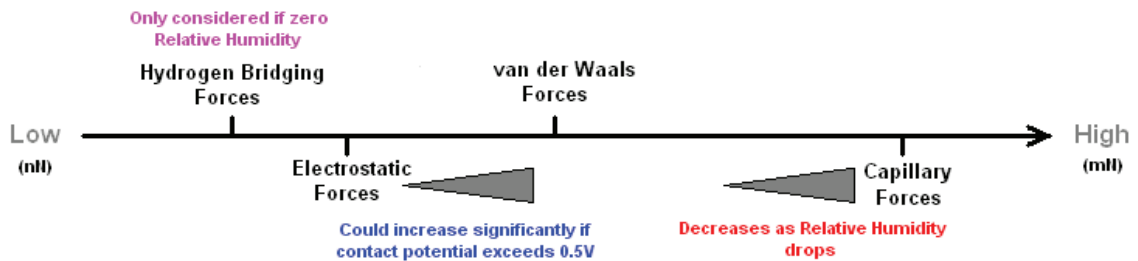


Figure 9. Relative contribution of various stiction forces

Relative motion of surfaces has a significant effect on stiction forces. Tambe *et al* [34] have shown that the number of capillary bridges formed increases with rest time (or

residence time of an asperity tip during sliding). The meniscus bridges will not form if the spacing is greater than a critical distance that can be calculated. As the velocity increases, the time for stable meniscus formation reduces resulting in a decrease in the number of bridges. The maximum height of the bridges also decreases logarithmically. The contribution of viscous shearing of the water film, at the contacting and near-contacting asperities where menisci are formed, to the adhesive stiction force is very small and can usually be neglected, according to Tambe *et al* [34]. The research of Tambe *et al* [34] shows that there is a critical sliding velocity that is too high for stable menisci to form, causing the adhesive force to drop off. At this point the adhesive force contribution to the overall friction force diminishes and friction is now dominated only by deformation-related friction force and stick-slip.

### **1.6.3 Micro Friction**

In traditional macroscale friction theories, the friction force is related to the normal load through a proportionality constant, the coefficient of friction. This force is considered independent of the apparent area of contact. However, as noted by Lumbantobing *et al* [35] this doesn't hold at the microscale.

Most static friction models are based on simple surface topography representation. Tas *et al* [36] have shown that MEMS surfaces can have a wide range of surface roughness, from atomically smooth, as with chemical-mechanical polished silicon, to rough surfaces of deposited polysilicon. It was noted in the previous section that greater roughness generally results in reduced adhesion forces. This contrasts micro friction forces that have increased forces when roughness increases.

Bowden and Tabor [37] indentified two basic micro friction mechanisms. These included the ploughing of asperities of a harder material through a softer material and the shearing of junctions formed in the region of contact of two surfaces. In MEMS, materials are usually of similar hardness and asperities are mostly blunt, although contaminations between surfaces can lead to friction variations (Olsson *et al* [30]).

Tambe *et al* [34] further defined an additional mechanism for micro friction, stick-slip, that represents the primary mechanism of static friction of an interface.

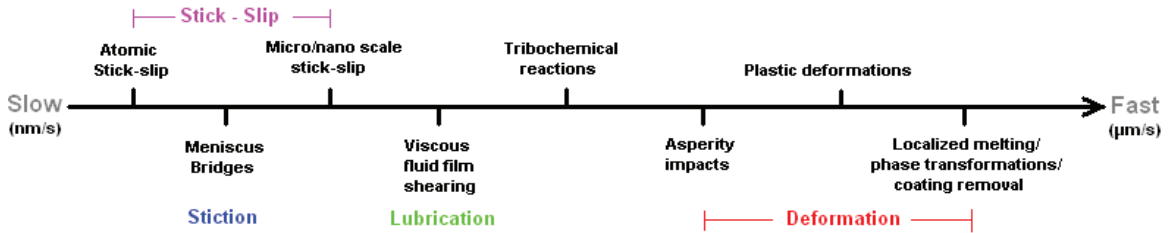


Figure 10. Dominant friction mechanisms with increasing velocity. Adapted from Tas *et al* [36]

Figure 174 outlines a more complete list of the dominant friction mechanisms as a function of velocity, as adapted from Tas *et al* [36]. For hydrophilic interfaces, meniscus (capillary) forces dominate at low velocities and hence the contributions of atomic stick-slip can be neglected.

Timpe *et al* [38] have shown that at the MEMS scale, adhesion forces also represent an additional normal force that can significantly raise the frictional forces when the external load is on the same order of magnitude as the adhesion forces. As the loads increase, such as in macro loads, the relevance of the adhesion forces to the friction forces becomes negligible. Stiction forces also tend to disappear as relative motion between surfaces increases.

#### 1.6.4 Friction and Stiction Comparison

Figure 177 shows a comparison of friction and stiction forces and their relative strengths. As can be seen, the actual magnitude of individual contributing mechanisms is dependent on the conditions. Generally, the micro/nano scale stick-slip mechanism of the static surfaces will have the highest values, unless there is higher humidity or pressure. In the static state, or at low velocities, the capillary forces not only contribute greatly, but also create an additional normal force that adds to the friction effect of the stick-slip

mechanism. As velocity increases from the static state, capillary forces drop off and kinetic energy reduces the stick-slip mechanism, leaving the deformation as the dominant friction force.

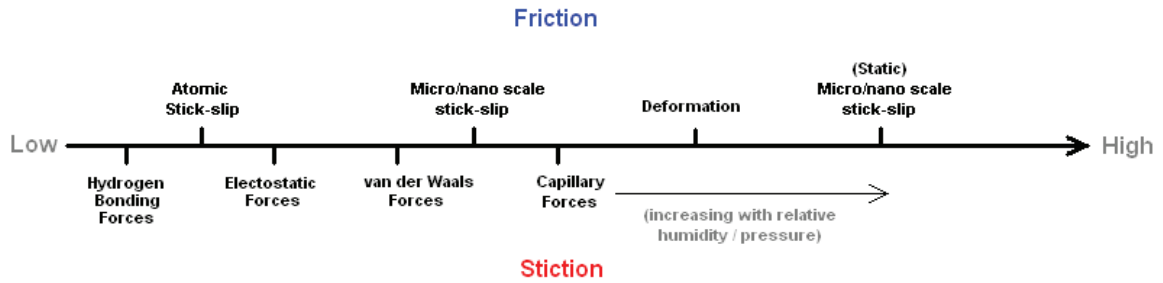


Figure 11. A comparison of friction and stiction forces.

## Chapter 2.0 Background Lift and Slide Theory

### 2.1 Lift and Slide Conveyor Motion

Lift and slide conveyors utilize three main components: pads, lifters and a floating platform (Figure 1). The pads have a small planar linear displacement in the XY axis and lifters have a small Z axis (out of plane) displacement. Together they can be used to create minute displacements per cycle while carrying a floating platform that can hold the desired objects to be moved. These platforms can be handed off to other pad-lifter groups to create an unlimited planar work envelope. By changing the operational phase of the pads and lifters, bidirectional control can be achieved. Planar control is created with pad displacement in the X direction, the Y direction or a combination of XY. With an array of pads, three planar degrees of freedom for a platform are possible (X, Y and rotation  $\theta$ ).

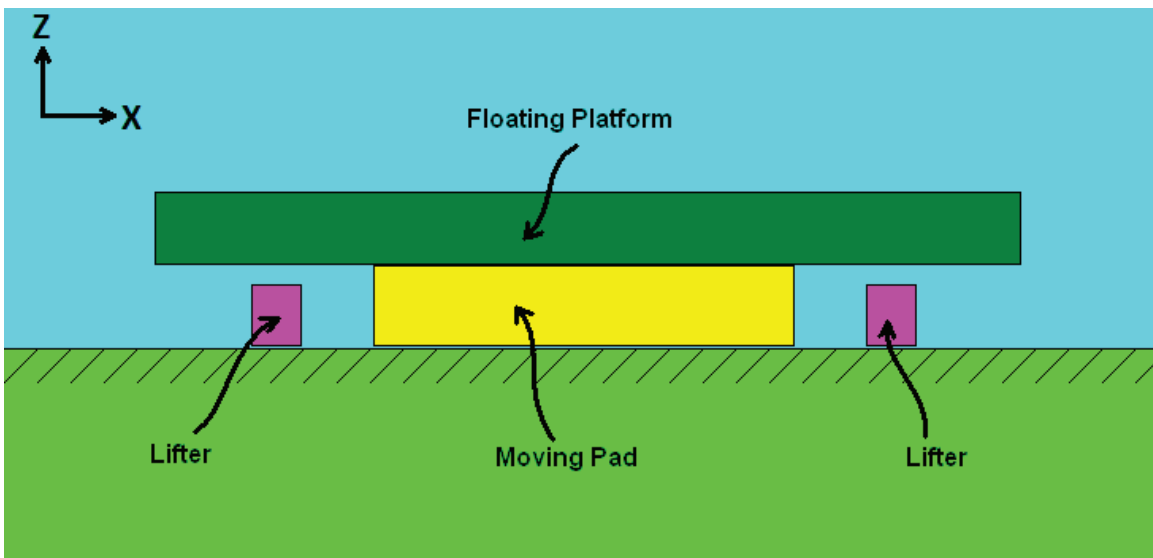


Figure 12. The three main components of the Lift and Slide conveyor system include the Lifters, the XY Moving Pad and the Floating Platform

A floating platform is used as a steady surface used to carry particles or components. With the lifter in the lowered state, the platform is coupled to the XY pad or pads through a frictional interface (Figure 2). Movement of the pad results directly in movement of the

platform. However, since the pads are constrained by the limitations of existing actuators (typically limited to 2-3 $\mu$ m for the high force of a non-amplified-motion actuator), extended range requires decoupling of the platform from the pad. When the pad has reached its range of motion, the lifter raises the platform and allows the decoupled pad to be free to return to its original position while leaving the platform with its previous delta increment  $dX$  displacement (Figure 3). The lifter can then be lowered, returning the platform to frictional contact with the XY pad and ready for the next cycle. Though each individual step of the cycle can be quite small, the small steps are cumulative allowing motion to continue as long as the pad to platform contact is maintained.



**Figure 13. The Floating Platform can be either coupled or decoupled from the XY Pad with the Lifter**

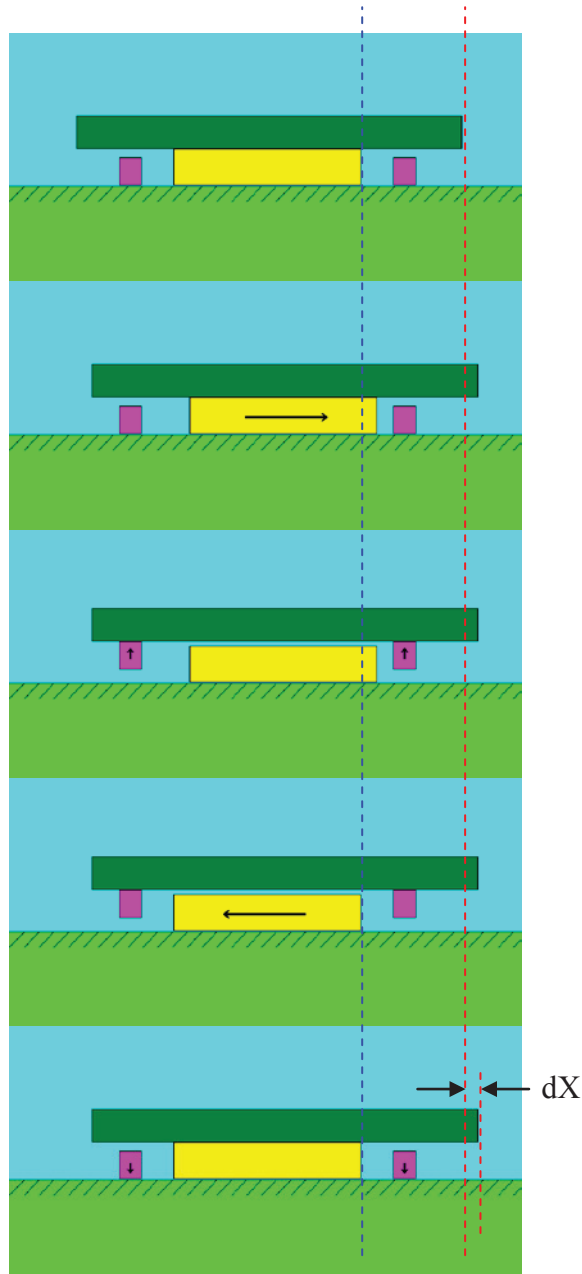


Figure 14. Small delta ( $dX$ ) displacement with each cycle

Additional pads can be positioned along the axis of motion. As the platform moves, it will land on the pads and their motion will impart a force on the platform, contributing to its motion. Pad motion along the same axis will result in platform motion in the given direction (Figure 15 and Figure 16). Opposite non-coincident motion of adjacent pads will result in a moment on the platform and subsequent rotation  $\theta$  (Figure 17). Therefore,



if the platform is in contact with a single pad, it will have two degrees of freedom (X, Y).  
If it is in contact with two or more pads, it will have three degrees of freedom (X, Y and rotation  $\theta$ ).

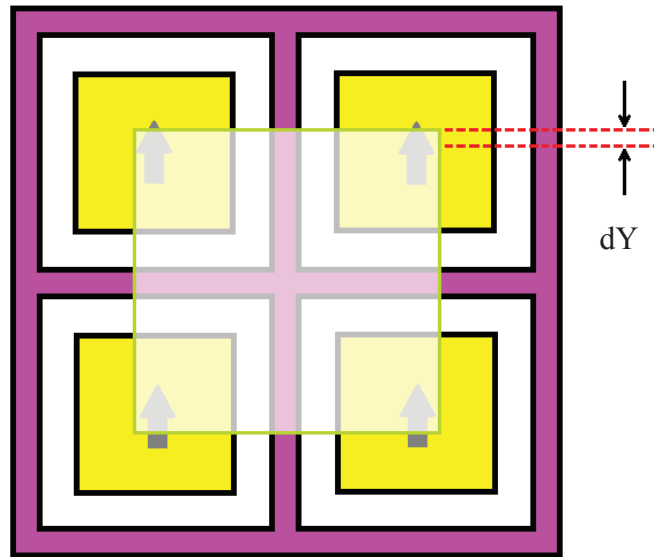


Figure 15. Vertical (Y-axis) displacement of the platform

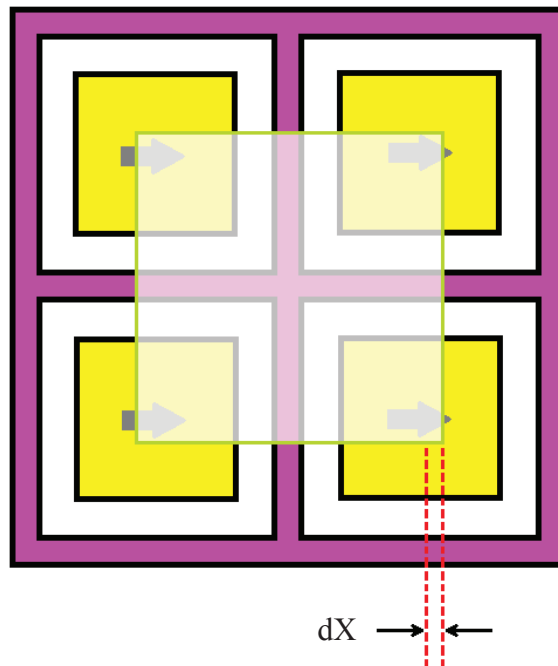
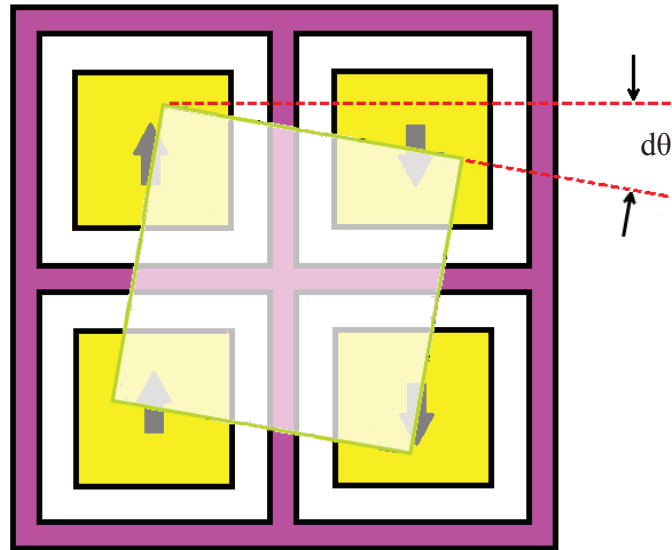


Figure 16. Horizontal (X-axis) displacement of the platform

X and Y axis displacement is straight forward. If the lifter grid is in the lowered position and all pads in contact with the platform move, then the platform moves in the same direction as the pads. To achieve motion in the opposite direction, the grid is raised before the pads are moved. Once the platform is decoupled from the pads, the pads are moved. Once the pads have been moved, the grid is lowered and the pads are returned to their initial rest position. This results in the platform motion in the opposite direction.



**Figure 17. Angular displacement of platform from opposed pad motion**

Angular motion is very similar, though there are some more considerations to determine the net combination of angular and axial displacement. Firstly, the platform is decoupled from the pads by lifting the grid. Non-coincident pads (i.e adjacent pads whose motion is parallel and offset) are then set into their “initial” position. This may require the pad to move to the shifted position (chevron “on”) or remain in its normal position (chevron “off”). Once the pads have been set in opposite “initial” positions, the grid is lowered and the pads move to their next position imparting a torque to the platform. If the pads are reversed in their “initial” position, then the direction of rotation will be reversed. Only two non-coincident pads are required to impart a torque on the platform, though all pads under the platform should move to provide the maximum rotation.

Several factors determine if the motion is pure rotation or a combination of rotation and translation; the positioning of the platform over the pads and the axial displacement of each pad. Full rotation is achieved when the platform sits evenly over the non-coincident pad pairs and the two non-coincident pairs move an equal distance. If the platform positioning is shifted or pads don't move evenly, then there will be a reduction in rotation and an increase in translation of the platform.

This can be seen if one considers the Y-axis of non-coincident pairs in Figure 18. In the first pair, Figure 18(i), the grid is lifted and the right pad shifts up for the "initial" position. When the lifter grid is lowered, the left pad shifts up and the right pad returns to its normal position. The net result is a translation transferred up to the left side of the platform from the left pad and an equal translation transferred down to the right side of the platform from the right pad. This coupled moment is evenly centered on the platform and it experiences pure rotation. If the "initial" position has neither pad shifting (Figure 18(ii)) and only the left pad moves up with the grid in the lowered position, then the platform will experience a translation transferred up from the left pad and no translation from the right pad. This results in a translation of the platform up equal to half the translation of the left pad, and a rotational deflection about half that of the pure rotation (Figure 18(i)).

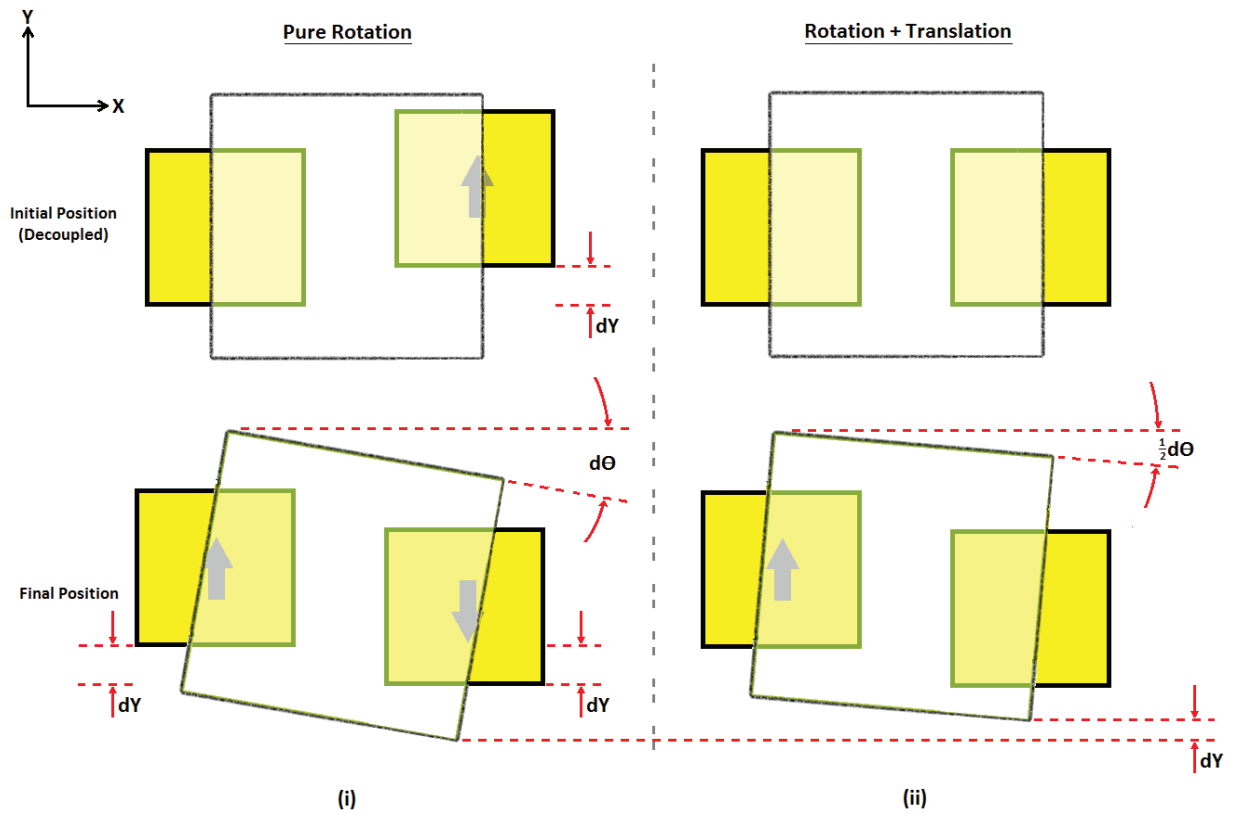


Figure 18. Initial and final pad positions to create either (i) pure rotation or (ii) rotation + translation

In this manner, a combination of displacement and rotation can be achieved simultaneously.

The second factor to be considered is the positioning of the platform over the pads. As friction is the key factor for transferring force from the pads to the platform, an uneven positioning of the platform over the pads will result in a reduction in the rotational displacement and an increase in the translation in favor of the pads with higher frictional contact. Micro-friction is a complex topic, and is further discussed in Appendix A.

## **Chapter 3.0 Control System**

### **3.1 Overview**

The control system is a closed loop program that is used to control the motion of either single or multiple platforms. The platforms can be programmed to either follow preset paths or move to specific locations and angles. The LabView (version 9.0) control system uses Vision Assistant scripts in order to process the real time image from the camera in order to detect location and orientation of the platform. Two vision processing techniques have been successfully tested; image recognition of specific features, and circle detection. The circle detection method uses two adjacent circles on each platform. One circle, which is the same size on every platform, marks the center of the platform. The second circle is a different size than the center circle, with the size being unique to each platform. The angle of each platform is easily calculated from the location of the second circle relative to the center circle. There are advantages of each method. The circle detection method is the quickest method; however this requires platforms with special markings and is difficult to implement with particles sitting on the platforms. The specific feature recognition routine works well for platforms with unique identifiable particles or markings, but is computationally expensive.

### **3.2 Hardware**

The complete setup starts with output from the LabView software passing to a DAQ card. The signals from the DAQ go to amplifiers and then to each channel of the chip to make a single step of the platform. An image is captured through the camera and passed back to the LabView software to complete the closed loop control circuit. The following sections describe each hardware subcomponent in more detail.

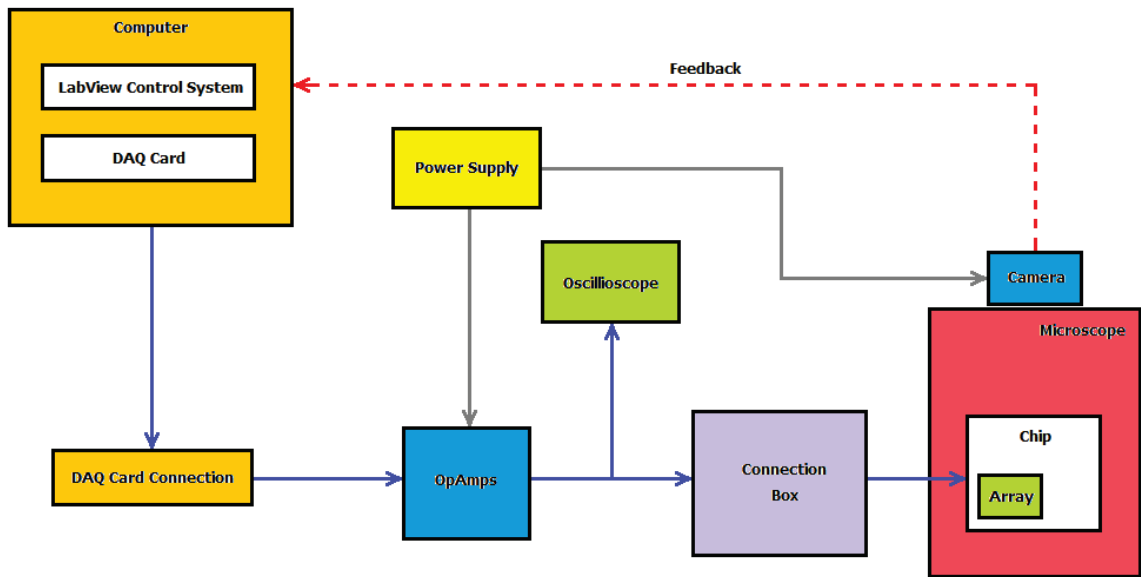


Figure 19. Flowchart depicting the flow of data from computer station to the array, with feedback

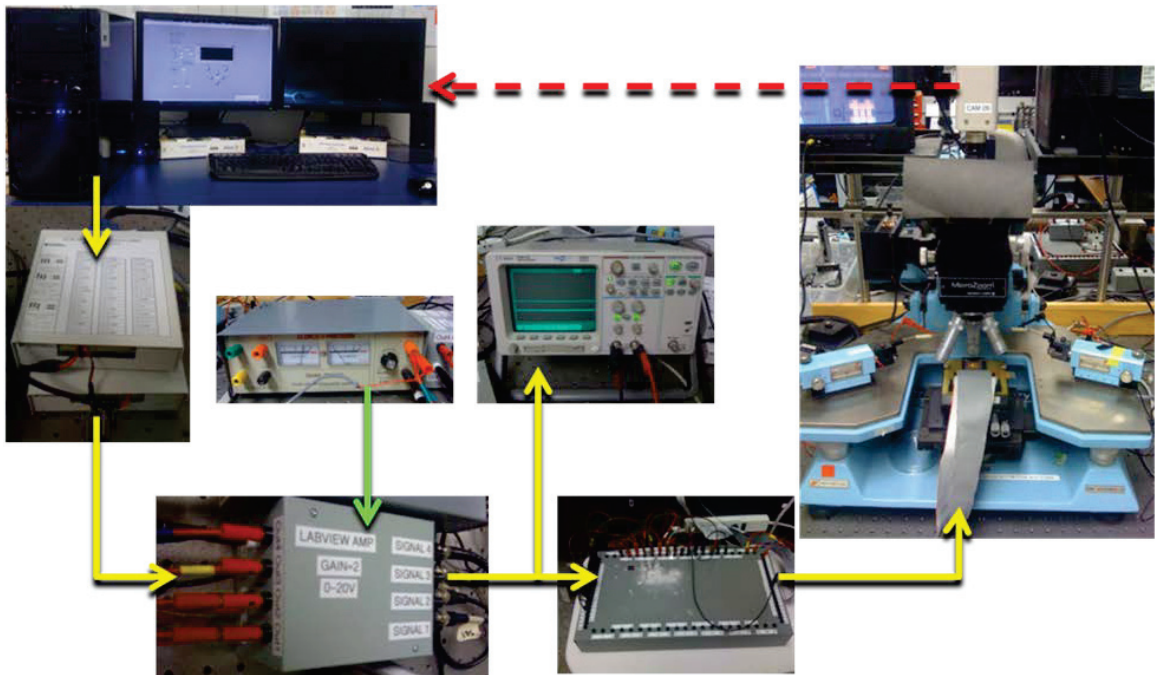


Figure 20. Photo view of the components from Figure 19

### **3.2.1 DAQ Card**

The LabView software is linked to the MEMS chips through a data acquisition card (DAQ card). The National Instruments PCI Express 6323 card has a number of features that make it useful for this application. Primarily it has 48 digital I/O (input/output) pins and four analog outputs. The pins are used slightly differently for the micro design and the macro model. The differences with the macro model connections are covered in Chapter 4. The maximum digital I/O rate for the card is 1 MHz, which far exceeds the processing power of the LabView image processing software, but does allow for expansion to a quicker computer at a later date, without having to upgrade the card. The maximum transfer rate is 900 kS/s (kilo-samples per second). This card also has 32 analog input connections, which at this time are not used but allow for the addition of sensor feedback in the future.

National Instruments SCB-68 68 pin shielded connector blocks are used to interface the DAQ card with the rest of the hardware. The blocks have screw connectors to allow for easy attachment of wiring to each output.

### **3.2.2 Amplifiers**

The analog and digital output channels from the PCI Express 6323 DAQ card cannot supply enough current to directly drive all the chevron actuators in the lift and slide array. To compensate, an OPA 551PA op amp is used to take an individual signal from the DAQ card as a reference, and increase the available current using power from a linear regulated power supply. Each control signal uses a separate current amplifier.

### 3.2.3 Camera

Images are captured using a Sanyo VCC 6674 1/3" super high-resolution color camera. It has 520 TVL of horizontal resolution with an effective picture element count of 768 (H) x 494 (V). The scanning system is standard NTSC at 30 frames/sec and 2:1 interlace. A Pinnacle DVC 100 Dazzle USB capture card is used to pass the video to the computer. Images are captured at a resolution of 640 x 480.

### 3.2.4 Microscope Setup

The microscope setup consists of a Wentworth probe station model MP0901 using a Baush & Lomb Microzoom microscope with three objective lenses; 2.25x, 8x and 25x. In conjunction with a zoom of 2x, the maximum field of view is 168  $\mu\text{m}$  x 126  $\mu\text{m}$  with a corresponding resolution of 0.263  $\mu\text{m}/\text{pixel}$ . Table 2 shows the field of view and corresponding resolution for various lens and combinations. For each objective lens, the zoom has an infinite adjustment between the range of 1 and 2.

The optimum magnification depends on the size of the array and the desired resolution. The highest magnification objective lens (25x) would only be used for fine adjustments of a single platform, and is not practical for most lift and slide control. A 2x2 array fits on 8x magnification with 1x zoom. For complete view of larger arrays, 2.25x magnification will be required.

<b>Lens</b>	<b>Zoom</b>	<b>X (<math>\mu\text{m}</math>)</b>	<b>Y (<math>\mu\text{m}</math>)</b>	<b>Resolution (<math>\mu\text{m}/\text{pixel}</math>)</b>
2.25	1	3500	2625	5.488
2.25	2	1800	1350	2.813
8	1	972	729	1.519
8	2	504	378	0.788
25	1	312	234	0.488
25	2	168	126	0.263

**Table 2. Field of view and corresponding resolution for various lens and zoom combinations**



### 3.3 LabView Vision Acquisition Program

A LabView vision tracking program has been developed to operate the MEMS Lift and Slide micro-conveyors through a closed loop control system. The program allows for accurate control of multiple objects with 3 degrees of freedom. It can consistently position objects to an accuracy of 1 pixel in both the X and Y planes, and within 3° of rotation. The program provides output to both the analog and digital channels of the DAQ card, representing the lifters and the XY pads.

Two versions of the program have been written; one designed to operate with specific object features captured with a user set Region of Interest (ROI) and the other designed for a circle detection mode that seeks out the various platforms automatically. Other than the initialization and image processing, the two versions are identical. Waypoints are used to control the position and angle of the objects. These can be set manually, or can be loaded from preset pattern files.

The user interface is the LabView front panel (Figure 21). The interface contains an image window that shows a realtime image of the pad array, and a smaller window that shows the ROI. Displayed data includes the current x, y and  $\Theta$  of the objects, target x, y and  $\Theta$ , position and angular deltas, waypoints and actual path points. A number of user controls are available, including axis enable/disable features, loop on/off and positional accuracy inputs.

LabView code, called a 'vi', is a graphical language that operates from left to right using symbolic boxes that represent each code step within the program. Boxes have inputs and outputs, with the output from one function connected to the input of the next function linking the next step in the code. Numerical or user inputs can feed into each function to provide the required parameters. Boxes may also represent a whole section of code, called a sub-vi, graphically simplifying the code representation. Outputs from the code can be linked to LabView front panel to give visual feedback to the user during program operation. Feedback loops allow continued operation of the code once it reaches an

endpoint. This allows points of code or the complete code to cycle, as with closed loop control.

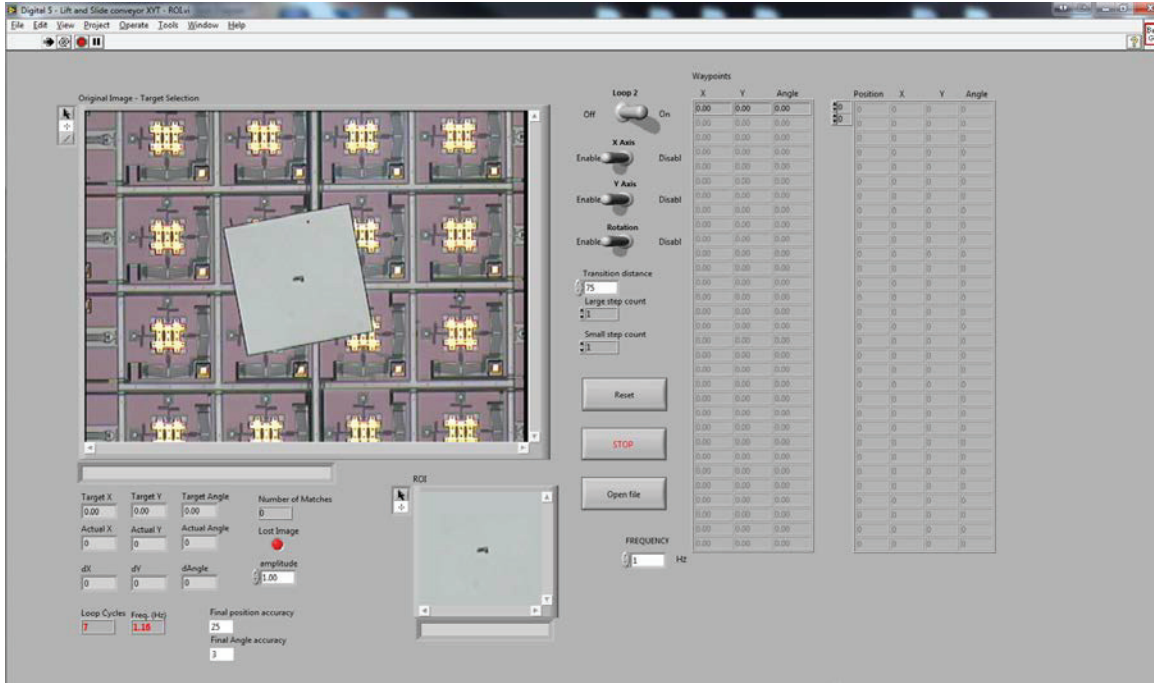


Figure 21. LabView Front Panel

### 3.3.1 Program Initialization

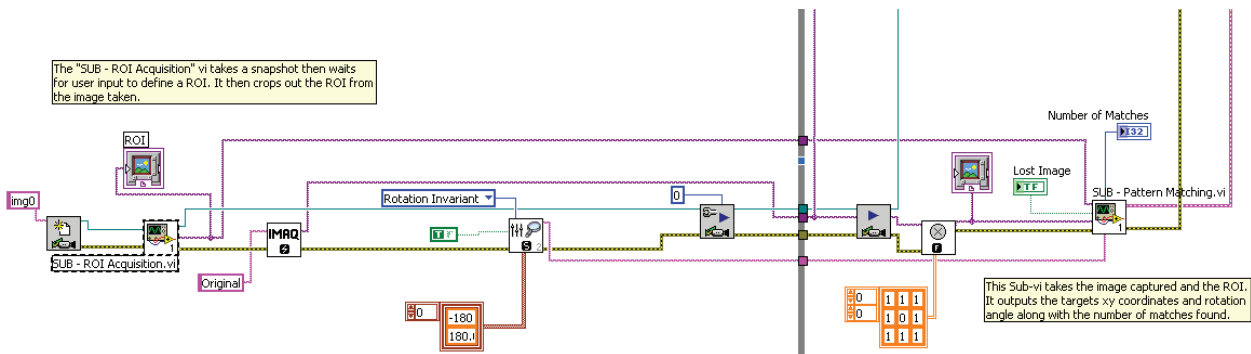


Figure 22. Program Initialization

The first step for the program is to initialize the camera feed (Figure 22). When using the feature tracking version of the program, the camera feed is used by a sub-vi that allows the user to select and capture the ROI image that will be tracked. This sub-vi is broken down further in the next Section. The ROI image is compared with each full frame that is captured inside a program loop using a pattern matching sub-vi. Defined parameters set the pattern matching sub-vi to search for the ROI image within the current frame at any angle (-180° to 180°), and defines a minimum matching score.

Inside the loop, the first step is to capture the image for processing. As the color camera has an interlaced color pixel image and the video acquisition card converts it to monochrome, the image is convoluted to slightly blur it and provide some consistency from frame to frame. The convoluted image runs through the pattern matching sub-vi, which returns the x & y coordinates, angle, and number of matches. A front panel display also indicates if the image is lost on any given frame.

### 3.3.2 ROI Acquisition

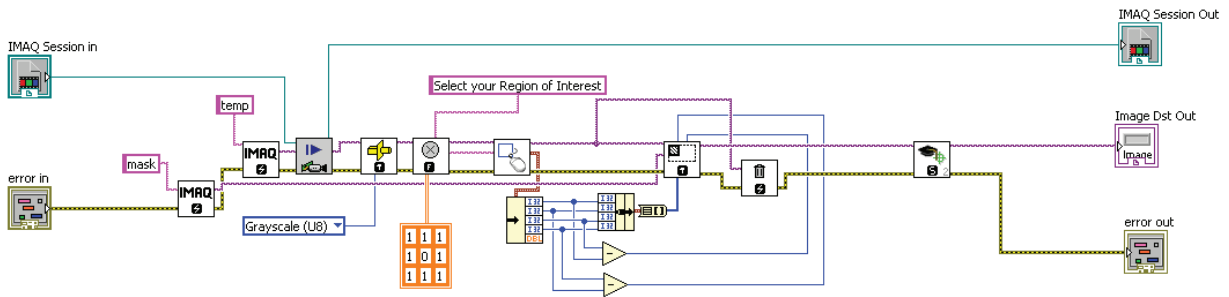


Figure 23. ROI Acquisition Sub-vi

The ROI Acquisition sub-vi (Figure 23) allows the user to pick specific features on an object to be tracked. The best features for tracking are those that are unique from the rest of the image. The sub-vi starts by creating a temporary image in memory of the current frame. This image is converted from the default 16-bit image to an 8-bit image that can be pattern matched, and then convoluted to blur the image for consistency. The next block takes a user defined rectangle on the displayed image and outputs the four corner

coordinates. The image contained within the rectangle coordinates is converted to the ROI, saved as an image template and output back to the main code.

The ‘error in’ and ‘error out’ blocks constitute an error buffer that collects error information from the vi and stores it for output for user debugging. All functions that can give an error code will be connected with this error line.

### 3.3.3 Pattern Matching

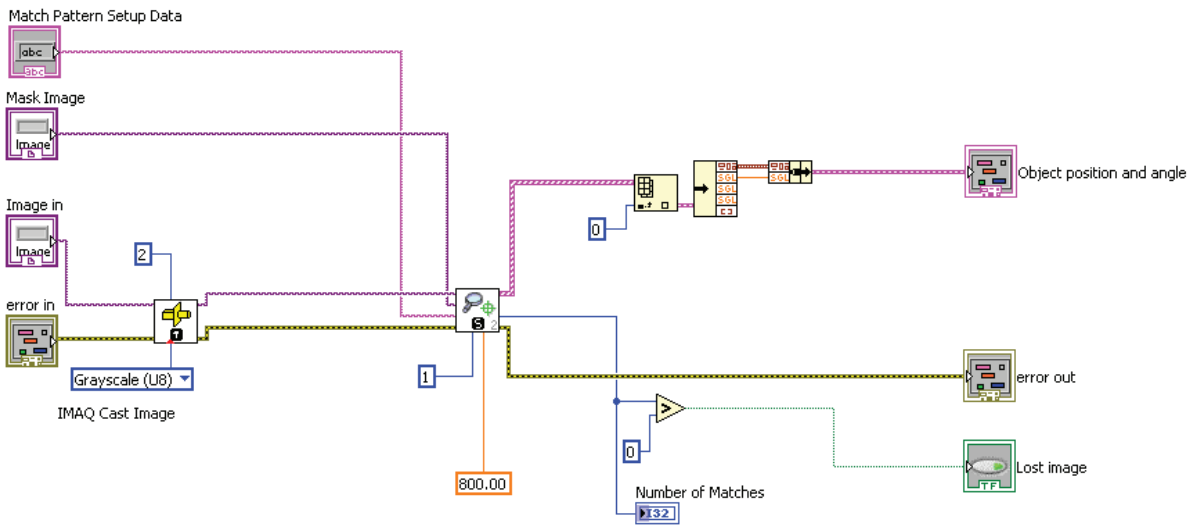


Figure 24. Pattern Matching Sub-vi

The pattern matching sub-vi (Figure 24) has three main inputs: Match Pattern Setup Data, Mask Image and Image In. The ‘Image In’ is the current video frame that has been captured. It is first converted to an 8-bit image to allow for comparison with the 8-bit ROI mask data template that has been stored in memory. The converted 8-bit image, the ROI mask data template and match pattern setup data is fed into the pattern matching routine, along with a minimum score required. The pattern matching routine outputs the ROI’s coordinates, angle and the number of matches. The coordinate and angle data are stored as an array, whereas the number of matches is directed to the front panel. A red indicator light lets the user know if there are no matches found.

### 3.3.4 Circle Detection

The function of the circle detection routine is ultimately the same as the feature recognition routine; locate the plate(s) and stack their coordinates and orientation into an array for processing. The circle detection routine is used to speed up processing, since the computational power required to locate a circle is insignificant compared to the power required to locate a complete object or feature, especially when object orientation is considered. As a ROI is no longer required, the initialization routine is simplified (Figure 25).

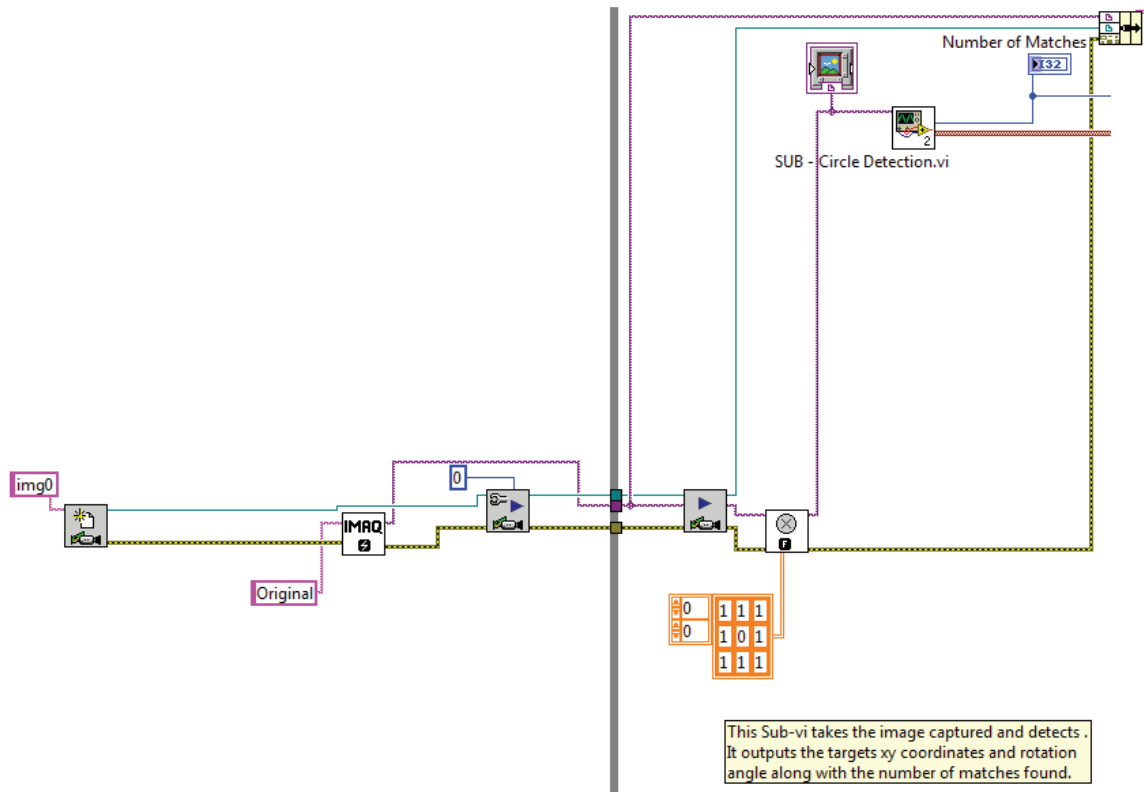


Figure 25. Initialization for circle detection

With circle detection, all circles on the image are located and their coordinates and sizes are stored in an array (Figure 26). Since circles are detected without concern for their orientation, the process is relatively quick. Minimum and maximum radius parameters

are used to eliminate minor objects that could be incorrectly reported as circles and skew the results.

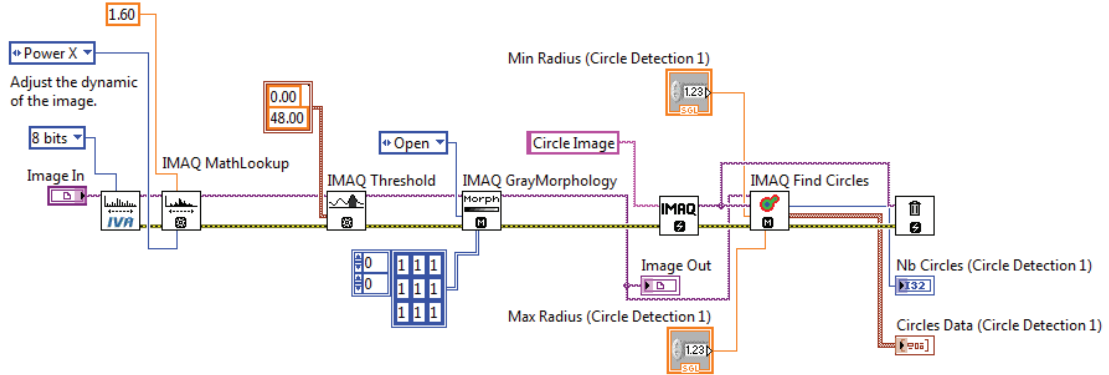
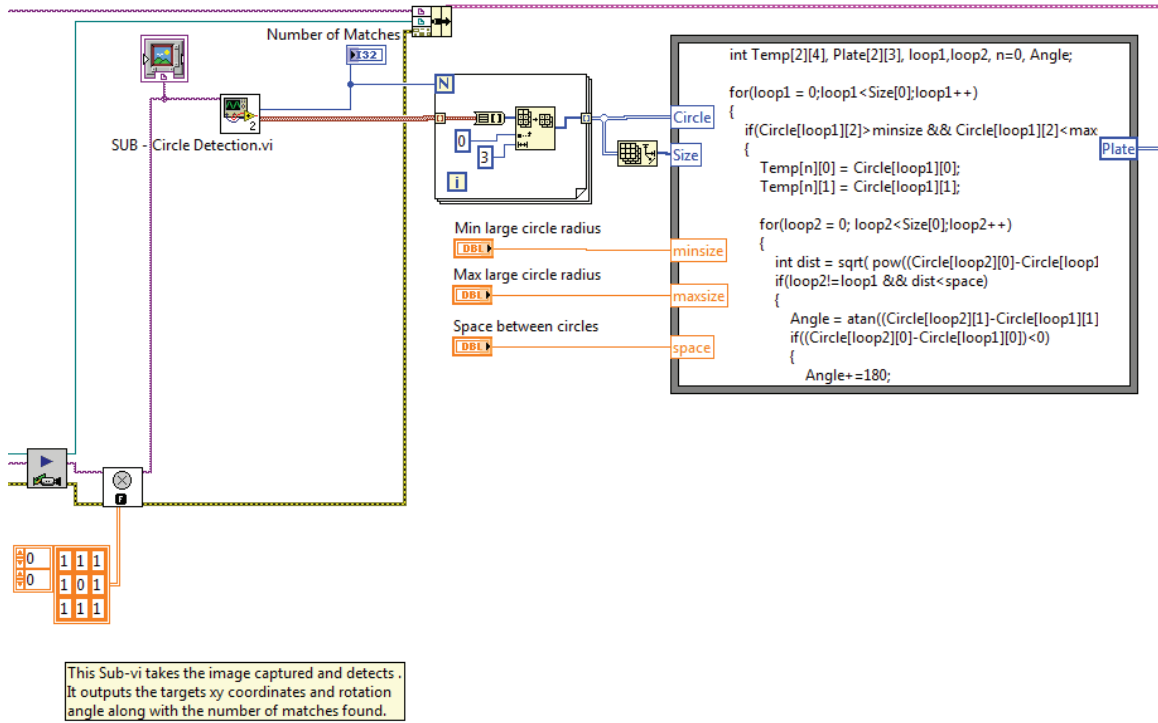


Figure 26. Circle detection sub-vi

The list of circles and their sizes is passed to a C code window (Figure 27). In addition, three parameters are passed to the code; the minimum and maximum size of the plate center circle, and the maximum distance between the center circle and its orientation reference circle. The code (Table 3) is used to find the large center circle for each plate, which determines the center coordinates of each plate, and then it pairs each circle with the closest orientation reference circle. The orientation of each plate is determined by calculating the angle between a line connecting both circles and a vertical line.

The center coordinates and orientation angle for each plate are put into an array. The plates are ordered by the size of the orientation reference circle, starting with the plate with the smallest reference circle. The code then outputs this array.



**Figure 27. Circle processing code takes an array of circles coordinates and their sizes and outputs the location and orientation of the plates**

```

int Temp[2][4], Plate[2][3], loop1,loop2, n=0, Angle;

for(loop1 = 0;loop1<Size[0];loop1++)
{
if(Circle[loop1][2]>minsize && Circle[loop1][2]<maxsize)
{
Temp[n][0] = Circle[loop1][0];
Temp[n][1] = Circle[loop1][1];

for(loop2 = 0; loop2<Size[0];loop2++)
{
int dist = sqrt( pow((Circle[loop2][0]-Circle[loop1][0]),2)+pow((Circle[loop1][1]-Circle[loop2][1]),2) );
if(loop2!=loop1 && dist<space)
{
Angle = atan((Circle[loop2][1]-Circle[loop1][1])/(Circle[loop1][0]-Circle[loop2][0]))/6.283*360;
if((Circle[loop2][0]-Circle[loop1][0])<0)
{
Angle+=180;
}
}
if((Circle[loop1][0]-Circle[loop2][0])>0 && (Circle[loop2][1]-Circle[loop1][1])<0)
{
Angle+=0;
}
Temp[n][2] = Angle;
Temp[n][3] = Circle[loop2][2];
}
}
}
n++;
}
}

```

```

for(loop1 = 0;loop1<int(Size[0]/2);loop1++)
{
  n = 0;
  int rad = 99;
  for(loop2 = 0;loop2<int(Size[0]/2);loop2++)
  {
    if(Temp[loop2][3]<rad && Temp[loop2][3]!=-1)
    {
      n = loop2;
      rad = Temp[loop2][3];
    }
  }
  Plate[loop1][0] = Temp[n][0];
  Plate[loop1][1] = Temp[n][1];
  Plate[loop1][2] = Temp[n][2];
  Temp[n][3] = -1;
}

```

Table 3. Circle processing C code

### 3.3.5 Waypoint Array

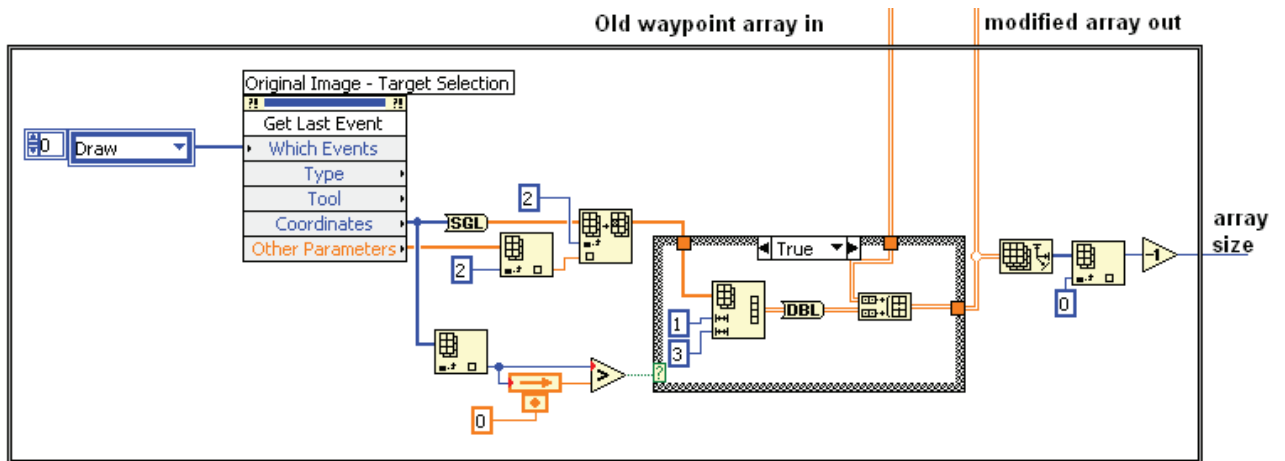


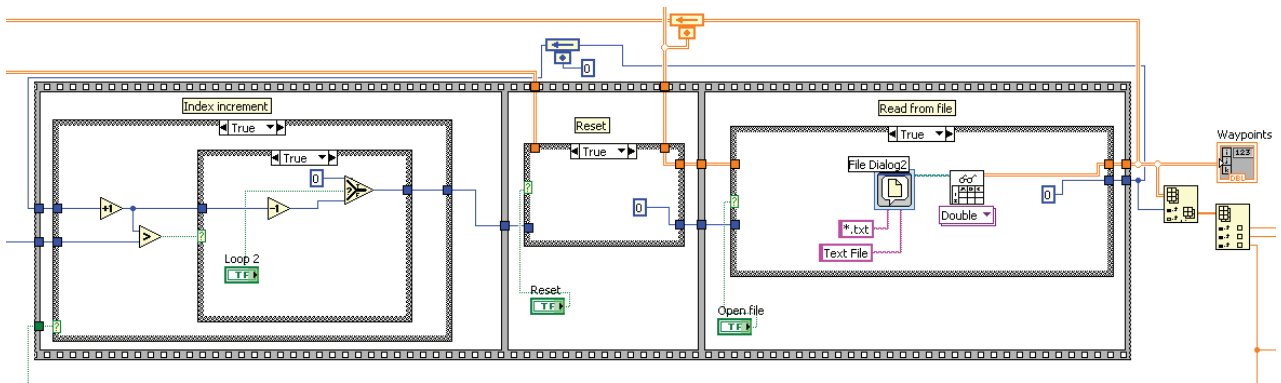
Figure 28. Waypoint Addition

Figure 28 shows the code for waypoint addition to the routine. Waypoints are used as a method to control the motion of the objects. Waypoints are a series of sequential target points that define the required location and angle of the object. The control system moves the object to a specific waypoint. Once this waypoint is reached then the object will carry on moving to the next waypoint. By spacing the waypoints close together, complex motion or patterns can be defined.



It should be noted that the motion of the object will not necessarily be in a straight line from its current location to the next waypoint. The program attempts to zero both planar axes and the angular orientation simultaneously. The plate will move in one step along the x-axis and one step in the y-axis, followed by one angular step until each delta is zeroed. This means the plate will move at a 45° angle along the planar surface until it is aligned, either along the x-axis or the y-axis, with the waypoint, at which time it then will move in a straight line directly to the waypoint.

When activity is detected on the front panel, in the form of the operator using the mouse to select two points, the program calculates the line angle between the two points in relation to the first point. After this line has been set by the user, the coordinates of the first point and its defined angle are added to the existing waypoint array. This operation will keep occurring every time the user creates a line on the display. If no “line draw” event is detected, then this function is ignored and the program continues until the next time that it is detected.



**Figure 29. Waypoint Array Indexing**

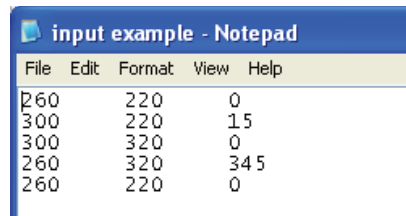
Figure 29 shows the code for the Waypoint Array Indexing. This is the routine that defines the next target coordinates. It is divided into three “frames” that vary the index; “Index Increment”, “Reset” or “Read From File”.

The first frame, “Index Increment” increases the waypoint array index if the waypoint has been reached. This frame next checks to see if the new waypoint is a valid point. If it is,

then the code continues to the next frame. If not, the waypoint array index is put back to the last waypoint if the loop function is turned off, or returned to the first waypoint of the array if the loop function is turned on.

The “Reset” frame links the user reset button to the program. When pressed, the index is simply set to zero returning the waypoint back to the first waypoint of the array. If it isn’t pushed then the frame is ignored.

The “Read From File” frame will allow the user to select a text file that contains waypoint data. Once selected at the prompt, the existing waypoint array will be overwritten with the waypoint array data from the file and the index will be reset to zero, to the start of the array. The file format follows the structure of  $x$ ,  $y$  and  $\theta$ , delimited with tabs and ending with a carriage return, as show in Figure 30.



File	Edit	Format	View	Help
260		220		0
300		220		15
300		320		0
260		320		34.5
260		220		0

**Figure 30. Entering Waypoint from a File**

### 3.3.6 Position Deltas

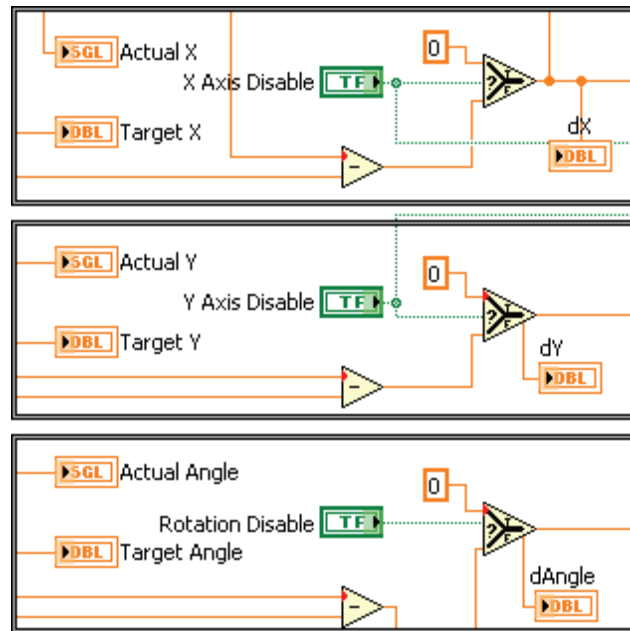


Figure 31. Position to Target Delta

Figure 31 shows the code to calculate the position and angular deltas. The actual position is subtracted from the target position, as defined by the waypoint array, to give a delta. The sign will be used to determine the direction of motion. Each degree of freedom can be turned off by sending a zero delta. This makes the code think that the subject axis or angle has reached its desired value and stops motion in that degree of freedom.

### 3.3.7 Angle Range

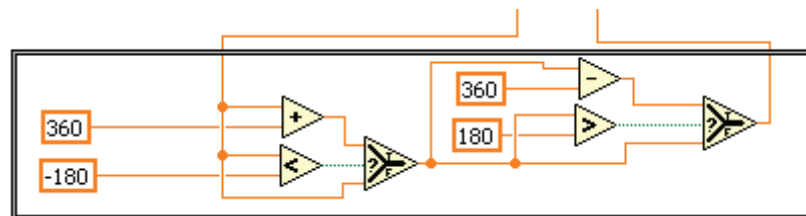


Figure 32. Ensuring a -180 to 180 Degree Angle Range

The delta angle range is adjusted to be between the range of  $-180^\circ$  and  $180^\circ$  (Figure 32). This is accomplished by adding  $360^\circ$  to the delta angle if it is below  $-180^\circ$  and subtracting  $360^\circ$  if it is above  $180^\circ$ . As the delta angle is a difference between the actual and target angles, the sign of the delta can be used to determine the required direction of rotation of the plate in order to rotate to the target angle. If the delta is negative, the plate rotates in a counter-clockwise direction. If the delta is positive then the plate rotates in a clockwise direction.

### 3.3.8 Step Transition

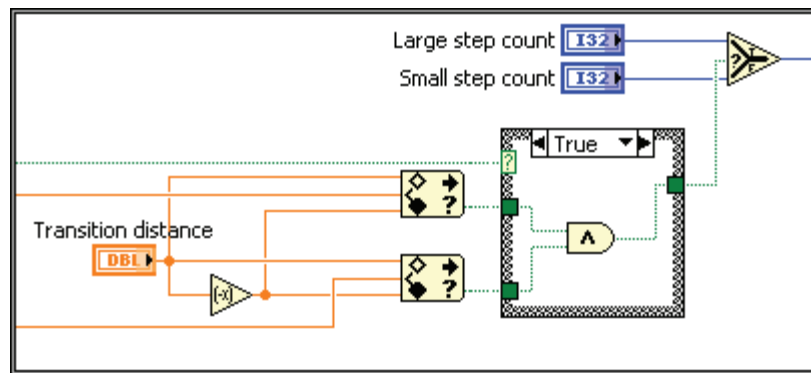


Figure 33. Step Transition

While normal expected operation would be for one video image to be captured and processed, and then one step for each degree of freedom, in reality the video processing capability and speed of the computer is not sufficient. MEMS chevrons are limited to about 1-2KHz, whereas the video processing capability of the code is approximately 30Hz. This is dealt with using the Step Transition code (Figure 33). This part of the code defines a large step count, a small step count and a transition distance. When the plate is outside the transition distance to the target, the code will move each degree of freedom of the plate a total number of unit steps as defined by the large step count before processing the next frame. Once the plate is inside the transition distance to the target, the small step count will define the number of steps between frames.

### 3.3.9 Position Determination

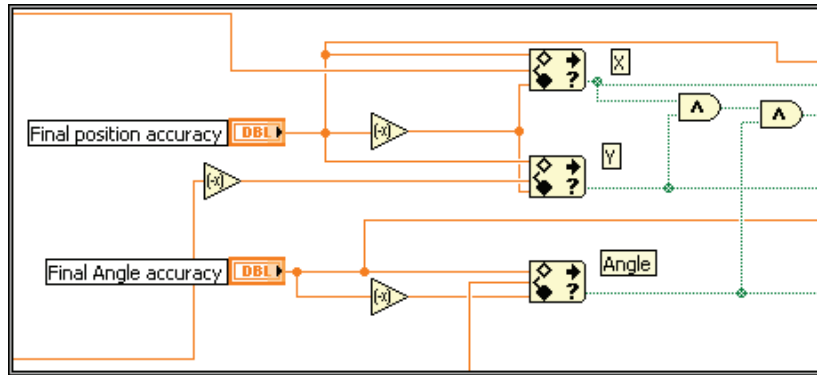


Figure 34. Evaluates if the Object is at Target Position

Figure 34 shows the code required to determine if the plate has reached the next waypoint target position. If a specific degree of freedom is within the user defined accuracy then a Boolean “True” value is returned to the specific “Position to Target Delta” routine, stopping further motion in that direction. If all three are “True” then the waypoint has been reached, then a “True” flag is sent to the “Waypoint Array Indexing” routine and the next array index will be selected.

### 3.3.10 Motion

The specific location and orientation of each plate for a given frame is passed to the final sub-vi for processing (Figure 35). The sub-vi routine (Figure 36, Figure 37 and Figure 38) is called individually for each plate. The output of the sub-vi is an analog signal through the DAQ card, one for each channel (X1, X2, Y1 and Lift). Since the current DAQ card was limited to four analog channels, the current sub-vi uses the two separate X channels so that rotational moments could be tested. Future versions of the sub-vi could easily incorporate an increase in analog channels (should a larger DAQ card be installed) to handle all available control lines on the MEMS chip. The concept of control lines is covered in Section 5.4.

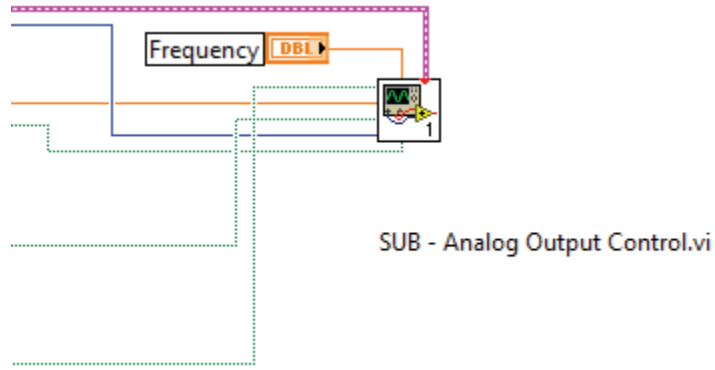


Figure 35. Final link to the DAQ card is through a sub vi

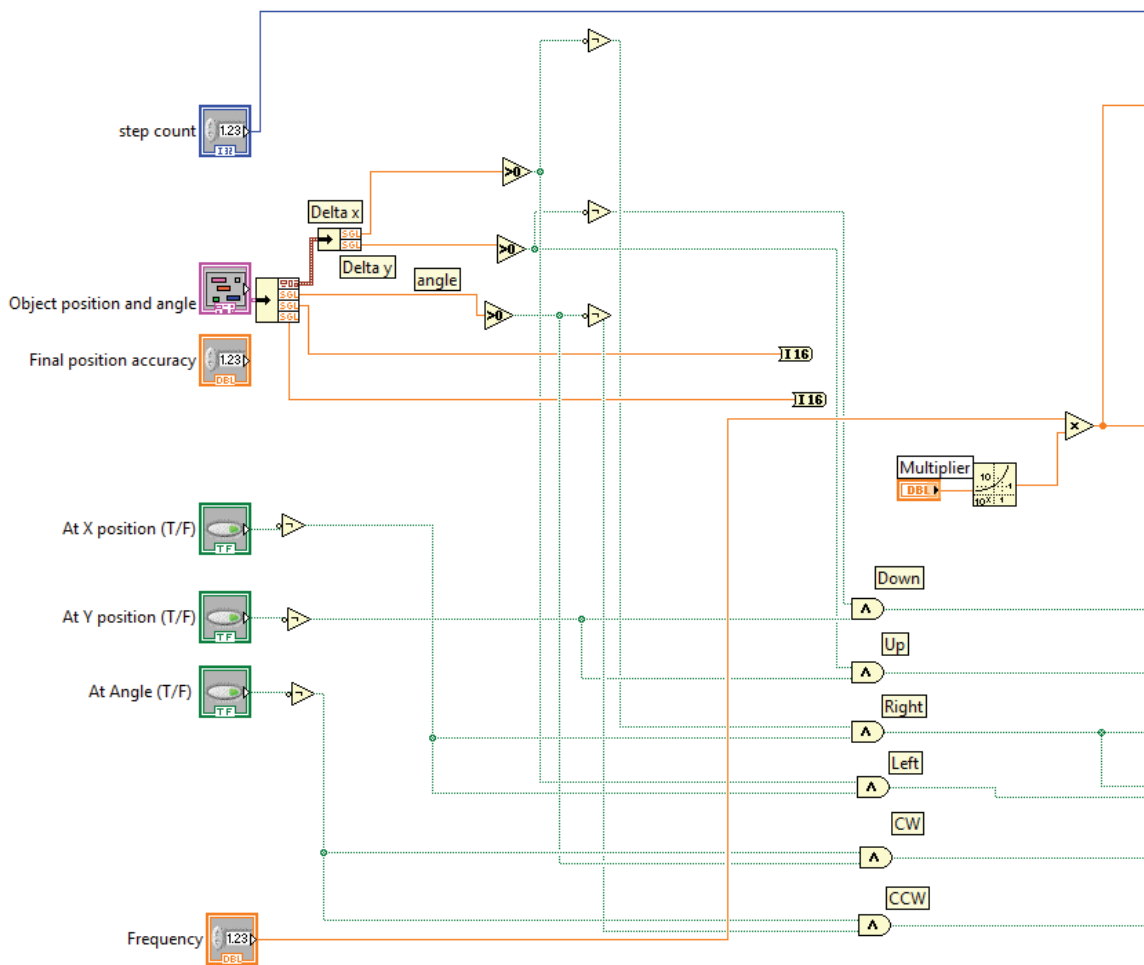
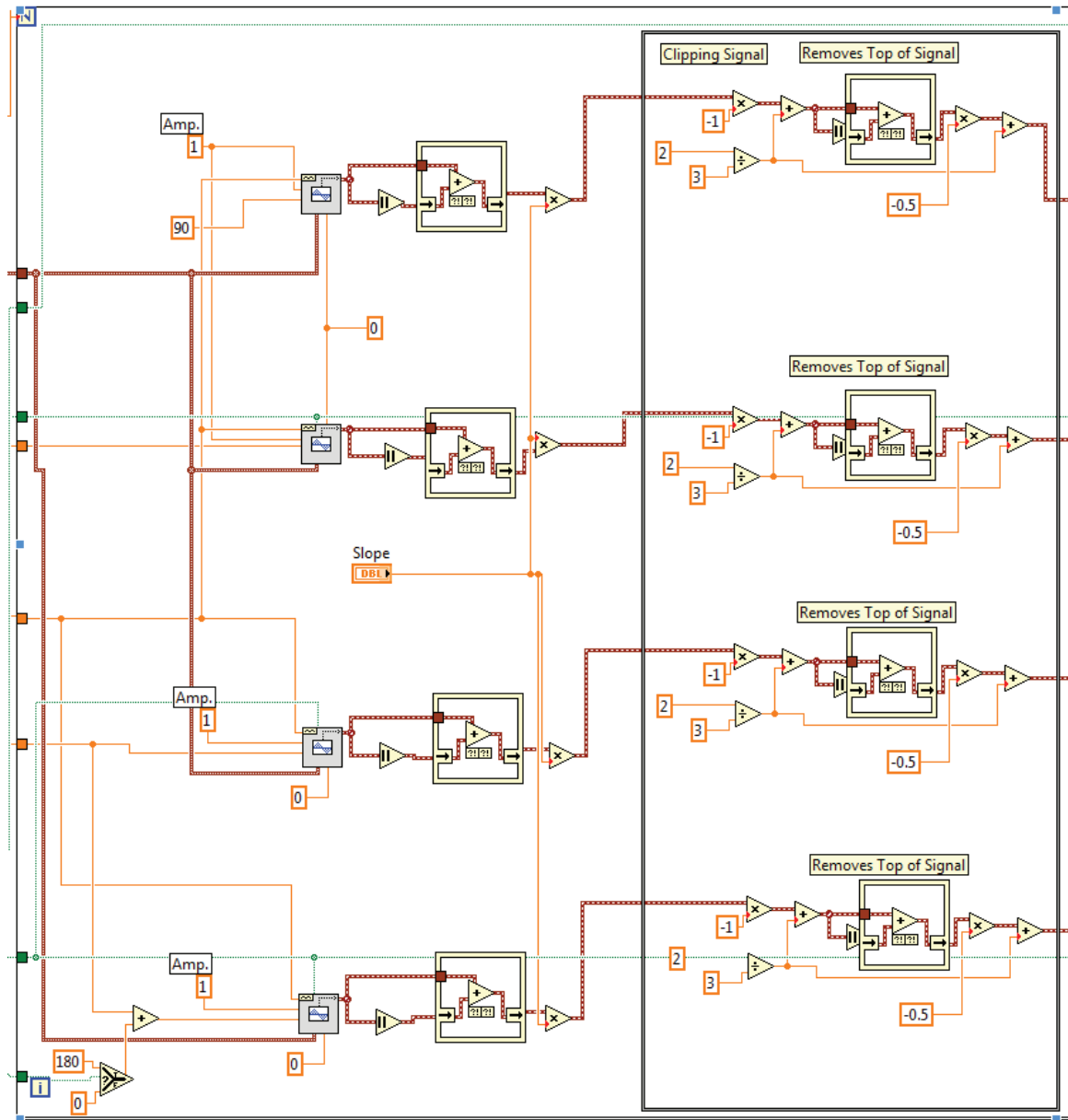


Figure 36. Sub vi processes position and orientation of plate and generates required lift and slide control responses

The position and angle deltas (difference between actual position or angle and the desired position or angle) are converted to a simple Boolean true/false signal for each direction (left, right, up, down, and rotation clockwise or counterclockwise) (Figure 36).



**Figure 37. Four analog signals are created with pre-determined amplitude, frequency and wave type. Phase angles are set relative to the constant lifter phase**

An analog signal is created using defined parameters of amplitude, frequency and wave type. The phase angle for each directional channel is a function using the previous determined Boolean logic. This allows combinations of direction and angle to be passed

simultaneously through the X1, X2 and Y channels. The phase for the lifter is kept as a constant, with the other phase angles relative to the lifter phase (Figure 37 and Figure 38).

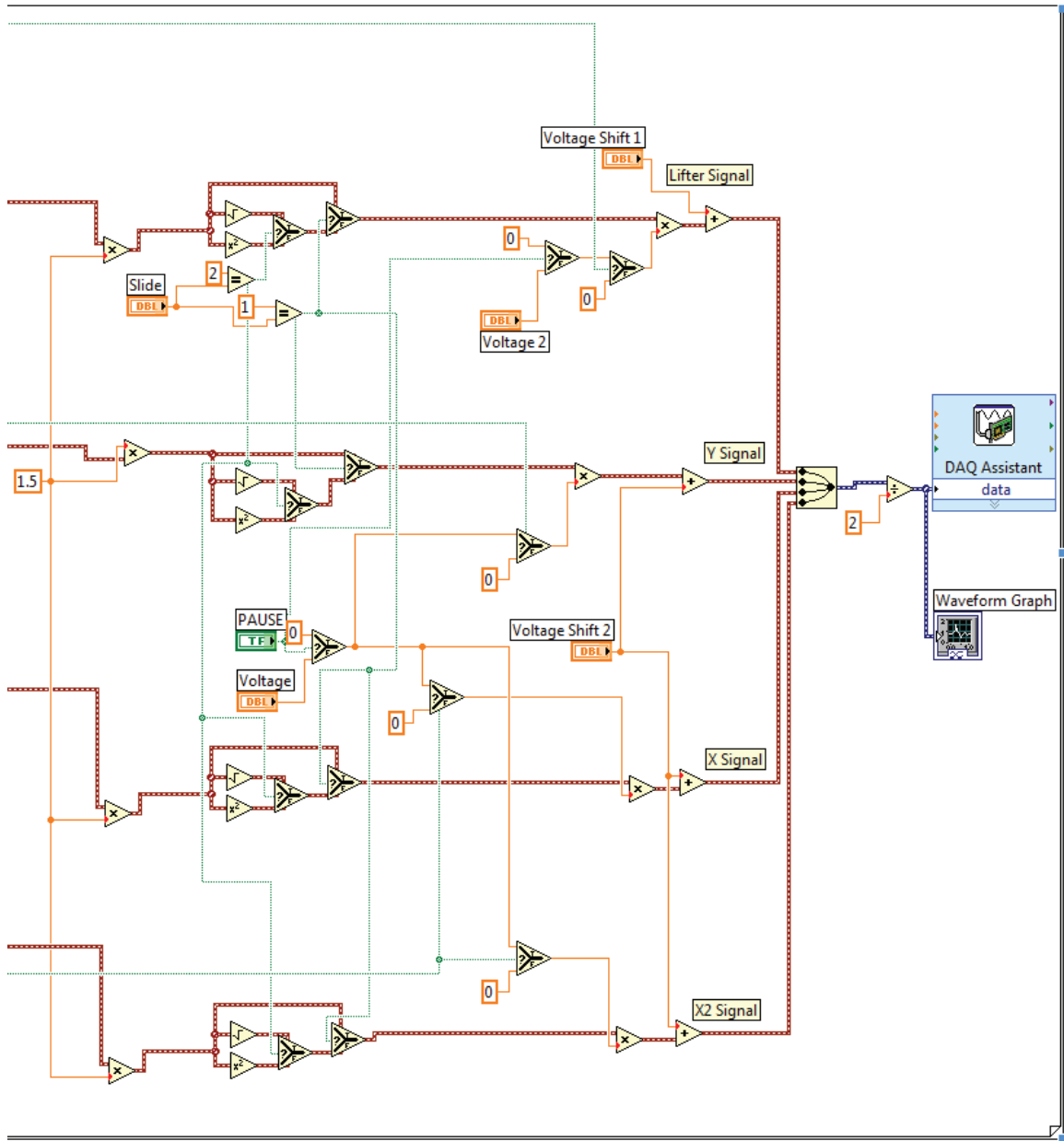


Figure 38. Four analog channels output to the DAQ card

Finally, the four individual analog signals are sent to the DAQ card. A step counter can be used (see Step Transition) to repeat multiple steps without the requirement of taking a



new image for processing. This can improve processing when working at frequencies above that of the camera rating.

### 3.3.11 Position Output to File

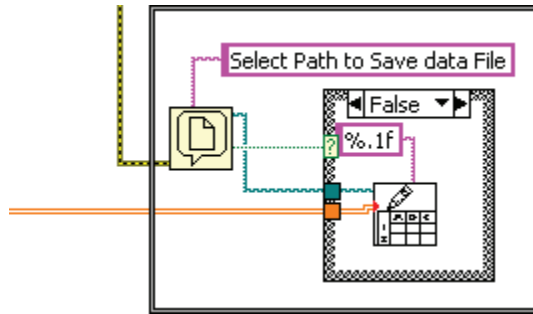


Figure 39. Writing Positions to a File

Positional data for each captured frame is stored in a buffer that can be saved once the program is exited. The vi, Figure 39, prompts for the name and location to store a text file containing all positional points and angles recorded. This follows the same format as the waypoint data files that can be loaded, with an additional index number at the beginning of each line (index number, the x position, the y position and the rotation angle), each delimited by a tab (Figure 40). This format can be opened directly by Microsoft Excel to allow plots of the exact path of an object. If there are multiple objects, the positional data for each additional object will be appended to the end of each index number line (i.e. Index number,  $x_1$ ,  $y_1$ ,  $\theta_1$ ,  $x_2$ ,  $y_2$ ,  $\theta_2$ , ...,  $x_n$ ,  $y_n$ ,  $\theta_n$ ) all delimited with tabs. Cancelling the file output prompt simply ends the program without saving any data.

File	Edit	Format	View	Help
0.0	403.5	209.0	0.0	
1.0	403.5	209.0	-0.0	
2.0	403.5	209.0	0.0	
3.0	403.5	209.0	0.0	
4.0	403.5	209.0	0.0	
5.0	403.5	209.0	0.0	
6.0	403.5	209.0	0.0	
7.0	403.5	209.0	0.0	
8.0	403.5	209.0	0.0	

Figure 40. Outputted Positional Data Format

### 3.4 Control Lines

The lifter actuators will always be connected in parallel and therefore only account for a single control line. However, as array sizes increase, so do the number of control signals required for complete independent XY pad actuator control. The number of control lines that can be processed depends on the number of analog/digital outputs of the control card, with more lines requiring a more expensive card. In order to reduce the number of control lines, multiplexed control can be used. Where independent control allows the system to control each actuator separately, multiplexed control groups actuators together to minimize the number of control lines while maintaining the maximum number of degrees of freedom. The X actuators along each X axis row are connected and the Y actuators along each Y axis column are connected. (Figure 41) This configuration slightly decreases the control of multiple platforms, but significantly reduces the control line requirements. Table 4 demonstrates examples of control lines versus array size with both independent control and multiplexed control.

Array Size	Control Lines	
	Independent Control	Multiplexed Control
1 x 1	3	3
2 x 2	9	5
3 x 3	19	7
4 x 4	33	9
5 x 5	51	11

⋮		
$n_x \times n_y$	$2(n_x)(n_y) + 1$	$n_x + n_y + 1$

Table 4. Number of control lines versus array size

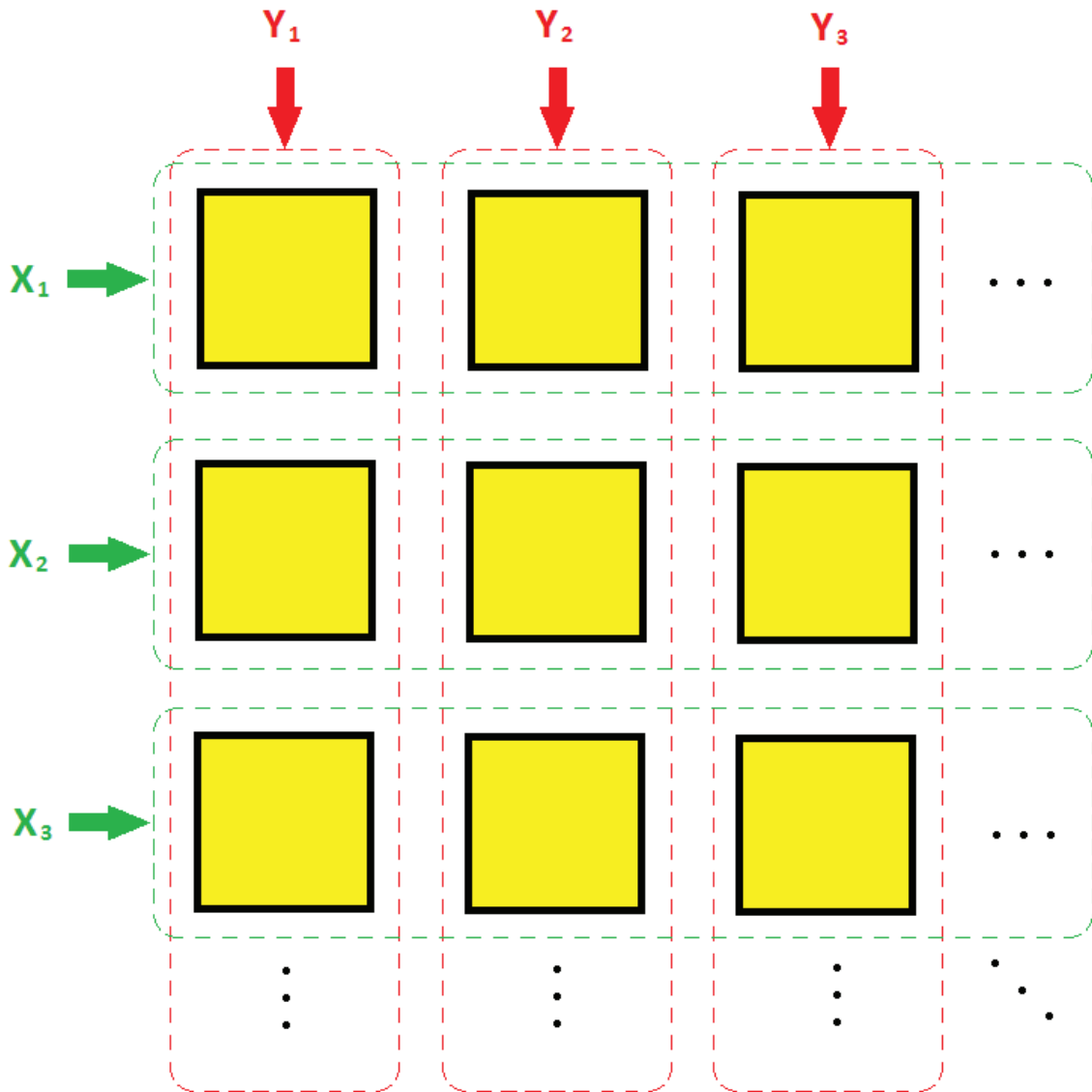


Figure 41. Control line groupings

## **Chapter 4.0 Macro Proof of Concept Tests**

### **4.1 Overview**

Before progressing with the manufacturing of microscale designs, the lift and slide conveyor theory was first demonstrated through the use of macroscale models that simulated the various required components. The macroscale model also allowed for ease of design and testing of the vision-based control software without using up the limited supply of chips available for each manufacturing run. Problems with control were easily identified as software problems instead of hardware design errors or stiction issues. By using a macroscale model, different platform designs could easily be tested prior to sending a chip for manufacture.

Servomotors are an effective substitute for micro actuators and are easily controlled through a LabView control system (Figure 42). Simple elastic bands were used to provide the pad return force that is inherent in the micro actuator. The structures were built using standard plastic beams with a focus on height variations between the pads and lifter.

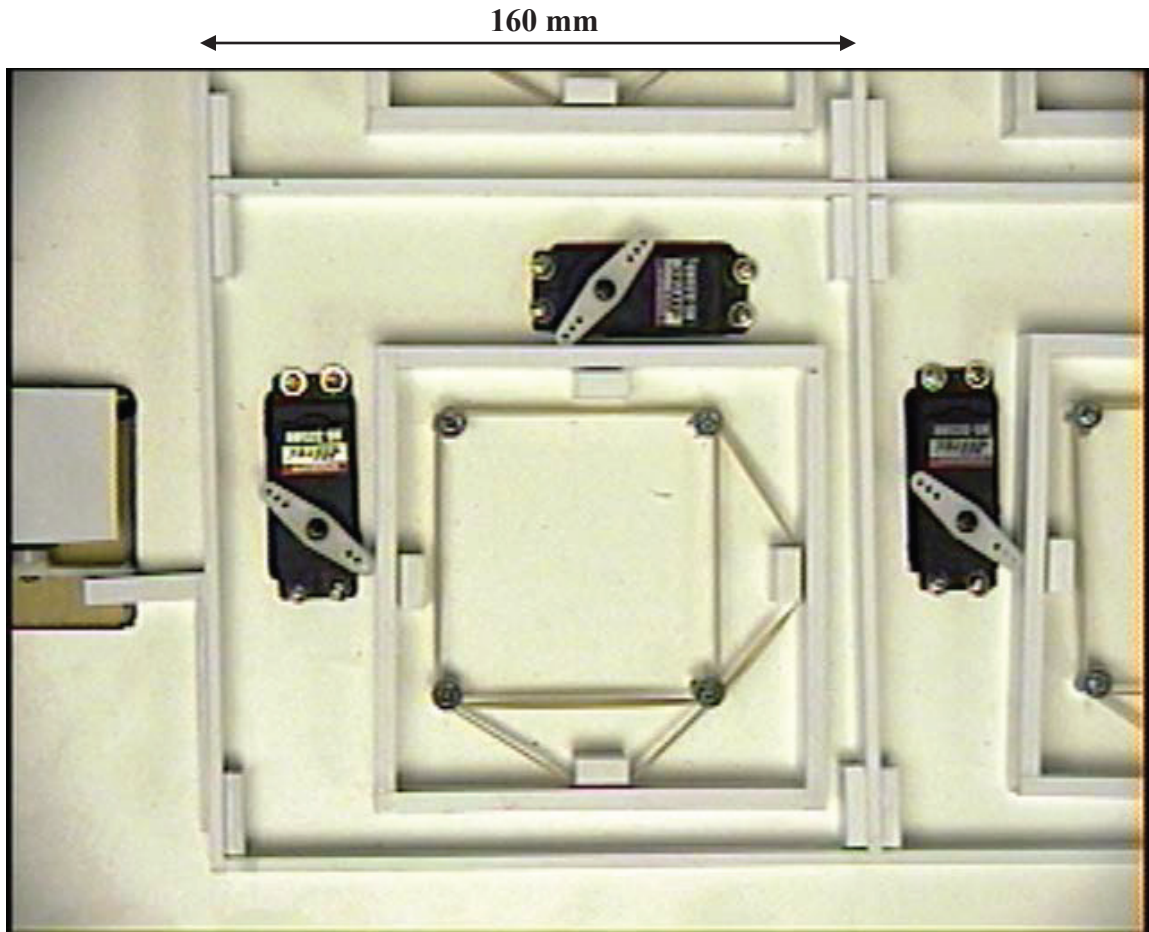


Figure 42. Macroscale model of a single cell used to simulate micro lift and slide conveyor. Key features are the servomotors, elastic return springs and plastic beams of various required heights

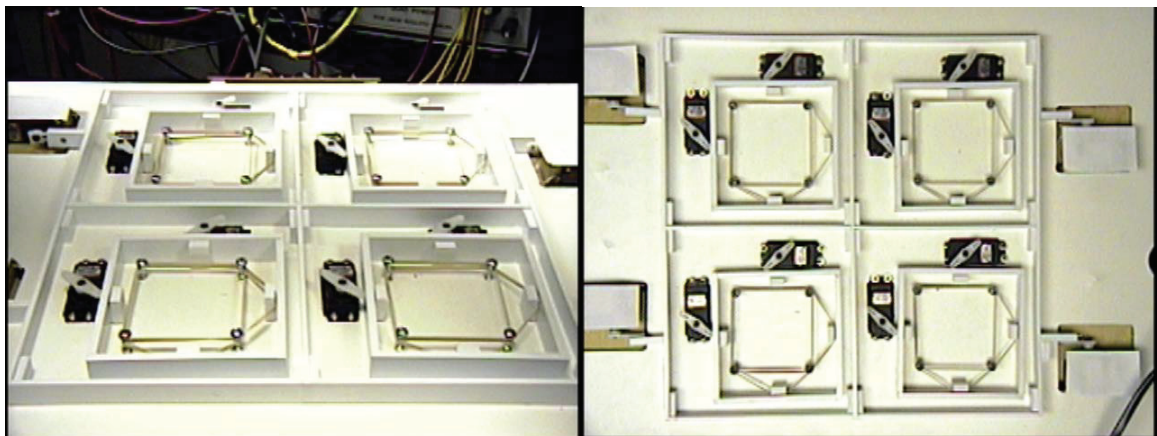
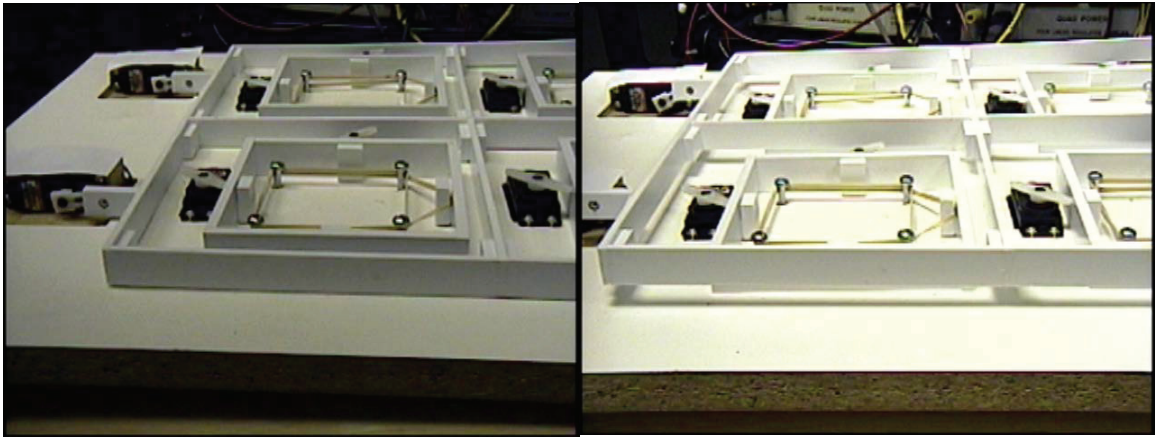


Figure 43. Macroscale model of a 4 cell array (2 x 2) lift and slide conveyor, angle view and top view

A single cell consists of an X servo and a Y servo. Multiple cells were arranged in an array with a single servo lifter mechanism (Figure 43). As the size of the lifter grid

increases, so must the number of servos used to raise and lower it. The lifter servos are wired in parallel to ensure consistent control. A pulse width modulation signal (PWM) is used as a control signal; this ensures all lifters rise to the same height. The lifter grid is required to rise slightly above the height of the pads (Figure 44) to ensure the platform is decoupled.



**Figure 44. Lifter servos raise the lifter grid slightly above the height of the pads. The left picture shows the lifter grid in the lower position. The right picture shows it fully raised**

## 4.2 Hardware Configuration

The design of the macroscale model hardware was done with the thought of easily transferring the system to the microscale chips. The LabView software was written to be almost universal for both and only minor hardware changes are required to switch between the macro and microscale components. The different LabView output sub-vi is used for the macroscale model, using two analog lines to set the “on” and “off” positions of the servos and incorporating digital outputs for each control line.

For the macroscale model, two analog signals are generated in LabView using two of the analog output lines of the DAQ card. These two analog signals are converted to two PWM signals that represent the two positions required for each servo; either an “on” signal or an “off” signal. The PWM signals feed a digital control board that uses the

digital output from DAQ and switches each associated channel to one of the two PWM signals, depending on whether that channel is on or off.

### 4.3 Servo Operation

As previously described, the servos utilize a PWM signal for control instead of a direct voltage control. The PWM signal allows for fine angular adjustment. The servos themselves are geared to provide about 3 kgcm of torque with a slew rate of 0.19 s/60° and an operating frequency of approximately 1 Hz.

The PWM signal operates at 50 Hz with each pulse ranging in duration from 500 to 2000  $\mu$ S. The servo pulses are varied to set the initial and final positions of the servo, requiring approximately 10  $\mu$ S/°. For example, a separation of 900  $\mu$ S between the two settings will move the servo arm 90° (Figure 45). This is useful for setting the amount of lift of the grid so that it just clears the height of the XY pads with minimal movement.

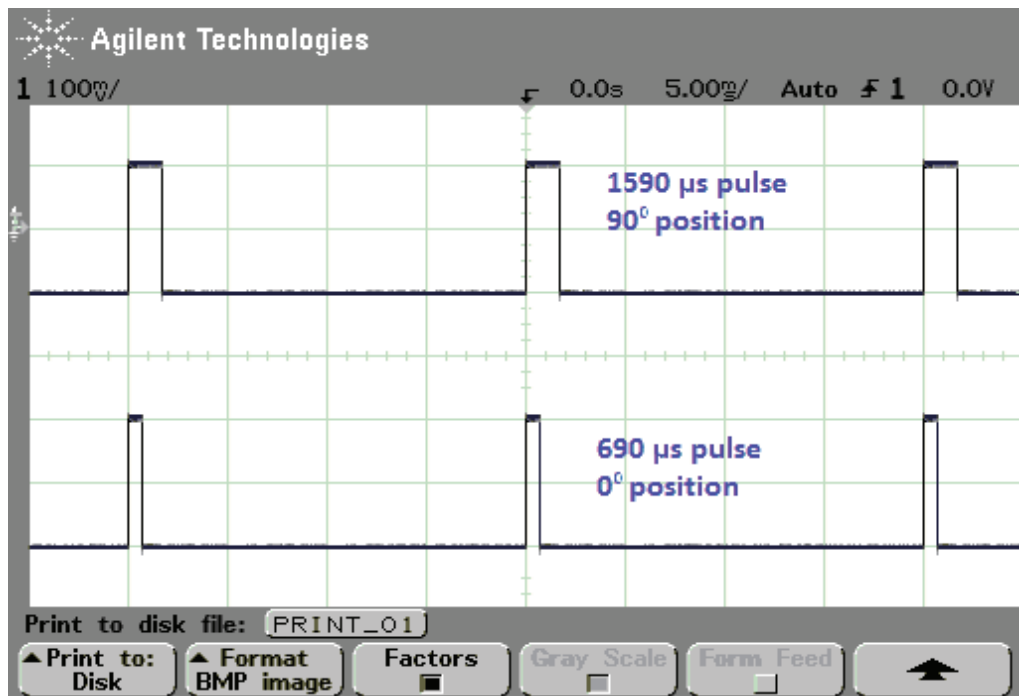


Figure 45. PWM pulses for different servo positions

A simple circuit (Figure 46) is used to convert the analog voltage from the DAQ card into a 50 Hz pulse train. A similar circuit is used for each analog channel.

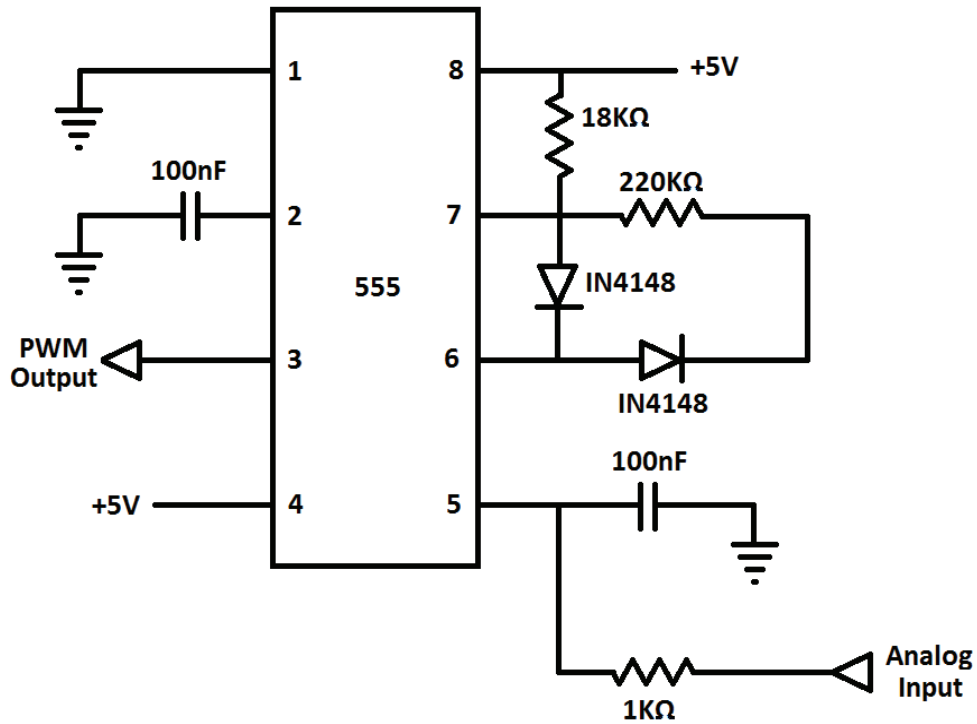


Figure 46. 555 based servo controller

#### 4.4 NAND Gate Board

A NAND Gate board is used to send a PWM signal to each of the servos being controlled. The 2x2 array used for the macroscale model has a total of 12 servos; eight for XY pads and four for lifters. As previously described for the microscale designs, a reduction in control channels is achieved by grouping the respective X rows and Y columns, and combining the lifters. This gives a total of five required channels (two X, two Y and one lift). Each of these five channels requires a separate PWM signal.

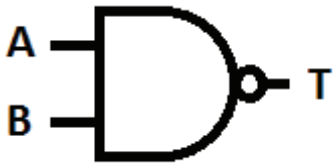
The analog signal inputs to the 555 based servo controllers are adjusted to give an optimized on and off position for all servos. With only two analog signals, hence only two PWM settings, this optimization is a compromise for the best XY pad settings and the best lifter settings since all servos use the same on and off position settings. If completely different on and off positions are required for the lift servos compared to the



XY pad servos, then a hardware voltage ladder can be used (instead of the analog output from the DAQ) in conjunction with additional 555 servo controllers to generate four PWM signals.

The digital signals, one per channel, feed into the NAND Gate board to control the PWM signals distributed to the channels. Each digital channel signal feeds into a circuit, as shown in Figure 47, along with both PWM signals that come from the 555 based servo controllers. The PWM output from that circuit depends on the digital input signal.

A NAND gate is a simple logic element that takes two digital inputs and provides a digital output based on the criteria in Table 5. A digital input of 0 is normally equal to a 0 V signal, and a digital input of 1 is normally equal to a 5 V signal. Therefore the digital signal can be passed from to the NAND gate from either the DAQ digital output or from a PWM signal that oscillates between 0 V and 5 V.

		
A	B	T
0	0	1
1	0	1
0	1	1
1	1	0

**Table 5. NAND gate logic table**

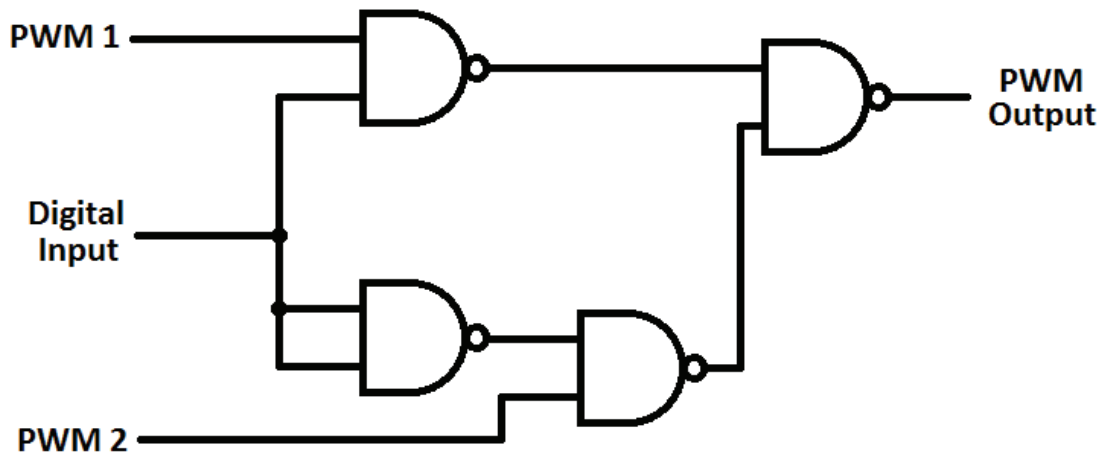


Figure 47. NAND Gate circuit used to control each channel

Table 6 demonstrates that if the digital input signal is 0, then the PWM output is simply the PWM 2 input signal. Likewise, if the digital input signal is 1, then the PWM output is the input signal from PWM 1. From this, each channel can be either set on or off with the digital output from the DAQ, and send the correct PWM to each respective servo. If PWM 1 represents the ‘on’ pulse train and PWM 2 represents the ‘off’ pulse train, then a digital input of 0 will move the servos on that channel to the ‘off’ position and a digital input of 1 will move the servos to the ‘on’ position.

PWM 1	PWM 2	Digital Input	PWM Output
0	0	0	0
1	0	0	0
0	1	0	1
1	1	0	1
0	0	1	0
1	0	1	1
0	1	1	0
1	1	1	1

Table 6. NAND circuit output

#### 4.5 Functional Results of Macroscale Model

Plots of the platform paths from the macroscale model for both single platform (Figure 48) and multiple platforms (Figure 51) show the ability of the vision-based control system to follow both simple (Figure 49 and Figure 52) and complex paths (Figure 50), even with the course steps associated with the macro model.

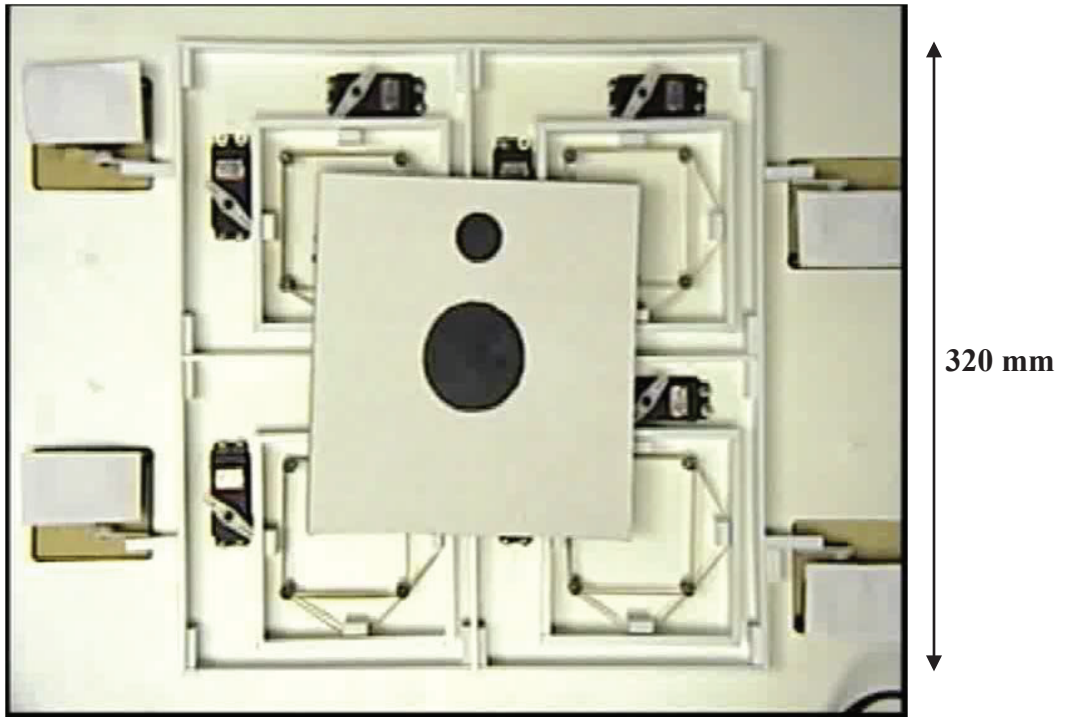


**Figure 48. A 2x2 macro array with a single platform. The larger black circle marks the center of the platform. The smaller black circle is used as a reference to calculate the platform angle**

Figure 49 shows the ability of the control system to move a platform back and forth in a simple horizontal line followed by a vertical line. There is some degree of slippage, but the path of the platform follows the expected path within 10 pixels. This was the limit of the plate resolution based on the large individual steps of the XY pads. This path was traced using only five waypoints.

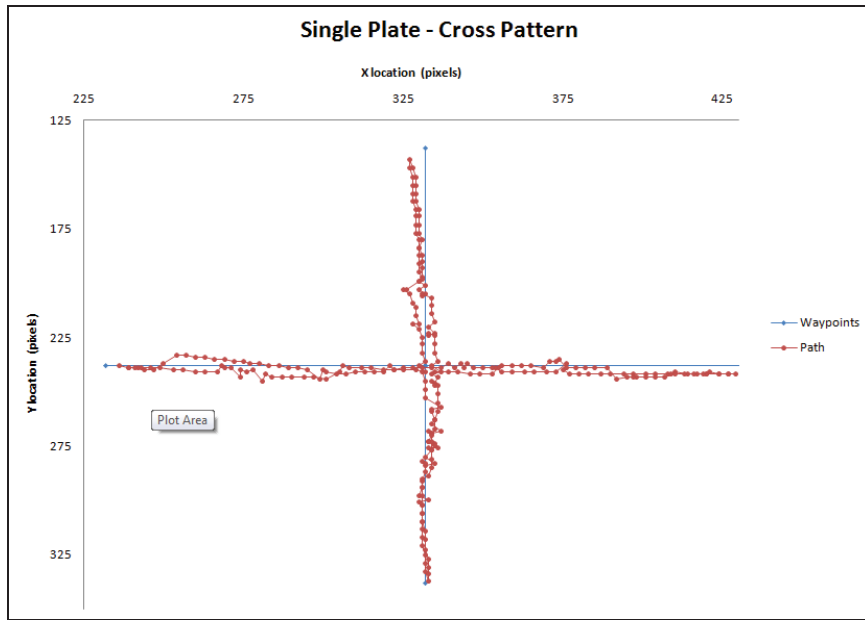


Figure 49. A simple cross path to show basic functionality of the macro model

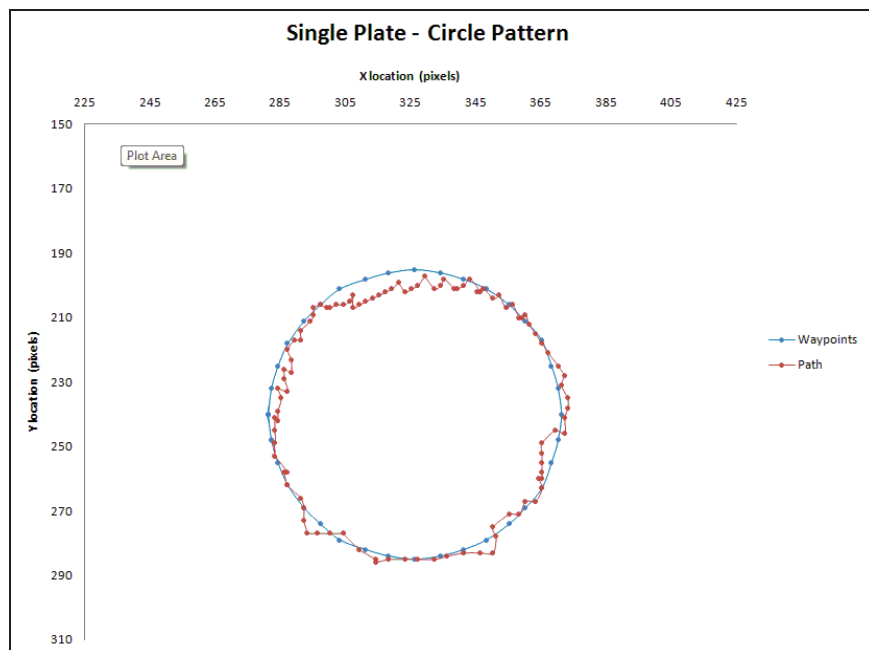
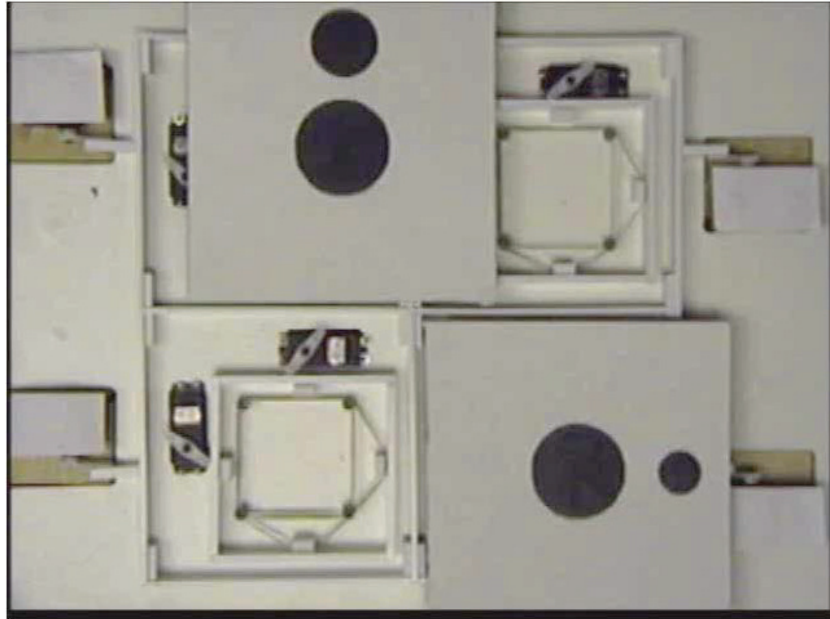
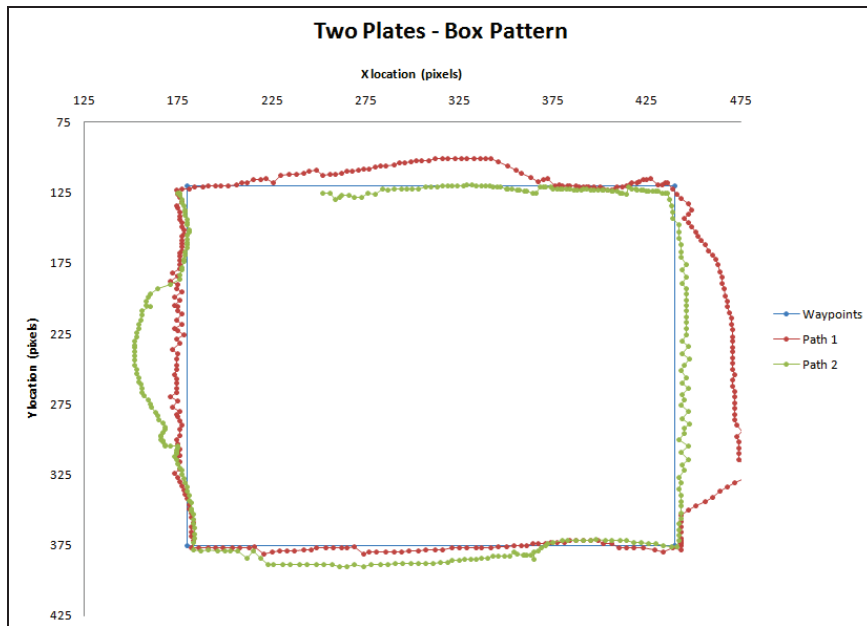


Figure 50. A more complex path demonstrating how sequential waypoints can be used to map out a detailed path

Figure 50 demonstrates that a complex waypoint path can be also be traced within about a 10 pixel resolution with the macrosteps used.



**Figure 51. Multiple platforms occupying a 2x2 array. Note the different sizes of the black circles to indicate the platform centers, platform orientation and differentiate the two plates**



**Figure 52. Two platforms following box paths over a 2x2 array. Despite the tight space, the control program can still successfully navigate the paths**

Figure 52 shows that path plots of two platforms over the 2x2 macro model array, as seen in Figure 51. As with the single platform path plots shown previously, it can be seen that the control system can drive two platforms. The limiting factor in this case is the lack of

area for the two platforms to navigate around each other. Each platform is moved independently ( i.e. first platform moves a step, then the second platform moves a step, then back to the first platform and so on), with the control system attempting to correct the positioning for each platform during each step. The error is greater than 10 pixels at one point, simply because there isn't enough room for the two platforms as they pass. As soon as the platforms pass each other, the control system is able to pull them back on to their waypoint defined path.

#### **4.6 Lessons Learned from Macro Scale Model**

The first function for the macro model was use as a platform for design of the LabView vision-based control system. The large model allowed the platforms to be manually manipulated while testing and retesting many different parts of the program. Microscale structures have a long life span when isolated from the environment, but tend to be prone to damage when physical interaction is required. This is especially noted when probes are required to slide platforms back and forth for repositioning. With macroscale models, it is easier to determine if problems are a function of the code or if there are hardware problems. Once the code was fully functional, less time was required for testing with the microscale structures, and issues could be quickly diagnosed.

In addition to being a proving ground for the control system, several issues were identified, which lead to improvements in the final microscale designs. Issues included the requirement for steady pad alignment, which led to improved spring design and the requirement for torsional links between the lifters and the grids. Friction and vibration were flagged as possible problematic areas and were monitored during microscale testing.

## Chapter 5.0 MEMS Lift and Slide Design Methodology

### 5.1 Arrays

Individual components were designed and fabricated using the polyMUMPs MEMS process. Various size arrays of actuated pads have been developed (Figure 53), from 2 X 2 up to 4 x 4. Later chips have concentrated on smaller arrays to maximize area available for design variations to determine optimum configurations. Larger pad arrays were created from the successful 2 x 2 arrays.

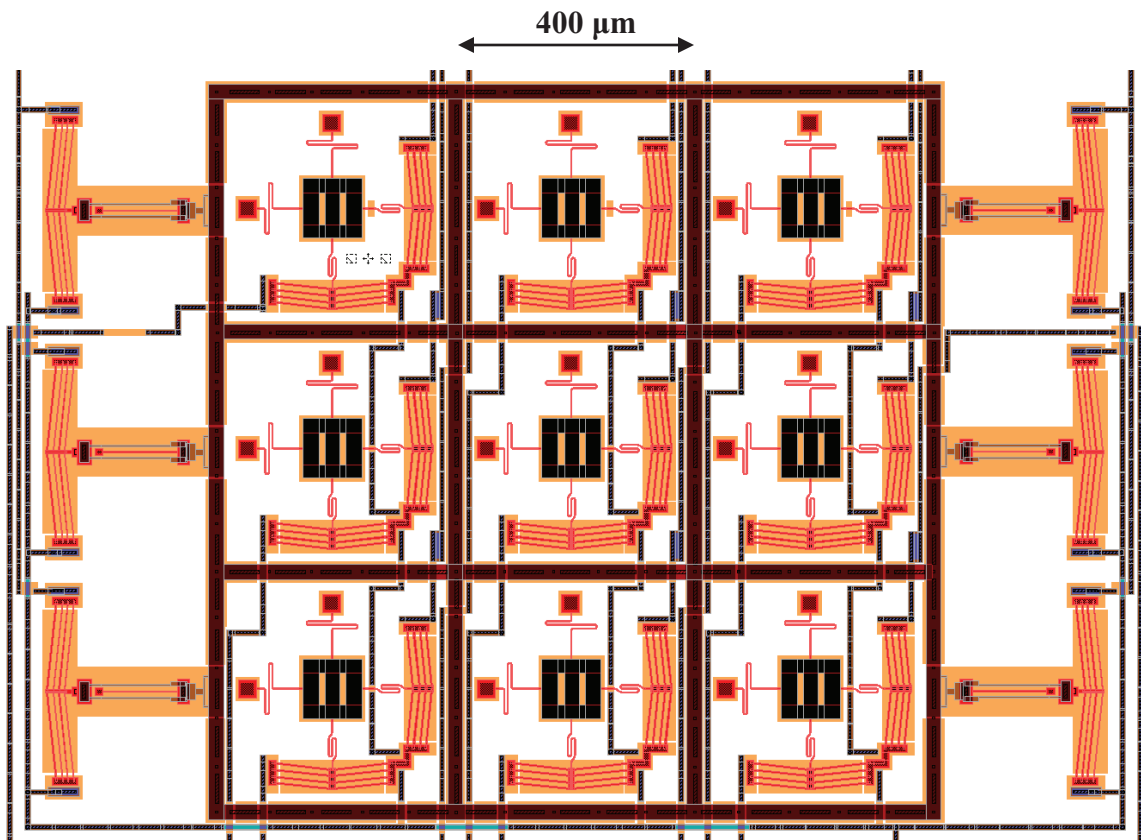


Figure 53. 3 x 3 polyMUMPs array

The key components of the polyMUMPs arrays are representative of the theoretical models.

## 5.2 XY polyMUMPs Pads

### 5.2.1 Pads

The XY polyMUMPs pads (Figure 54) are designed to be the highest structures in the Z direction with the lifter grid in the lower position. This is achieved through the use of all structural polyMUMPs layers (poly0, poly1, poly2 and metal). Poly1-poly2 vias are used to connect the two structural layers, but only as required since a complete poly1-poly2 via connection would result in a double height structure with lower than desired height. The structure is not anchored to the poly0 layer, but this layer is required to give an additional 0.5  $\mu\text{m}$  in height. The total thickness of the layers is 7.25  $\mu\text{m}$ .

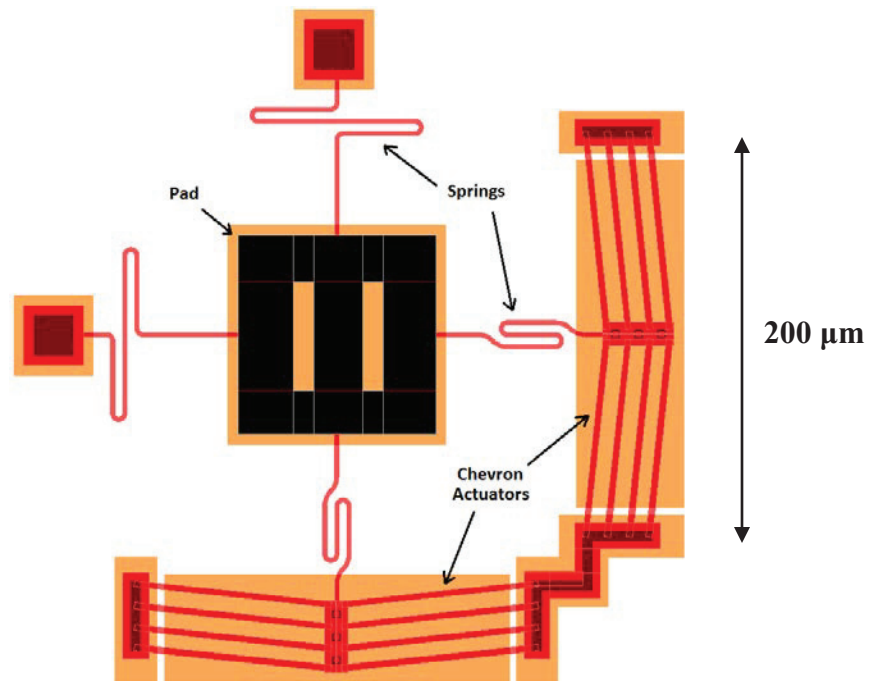


Figure 54. LEdit representation of the polyMUMPs pad, chevron and springs



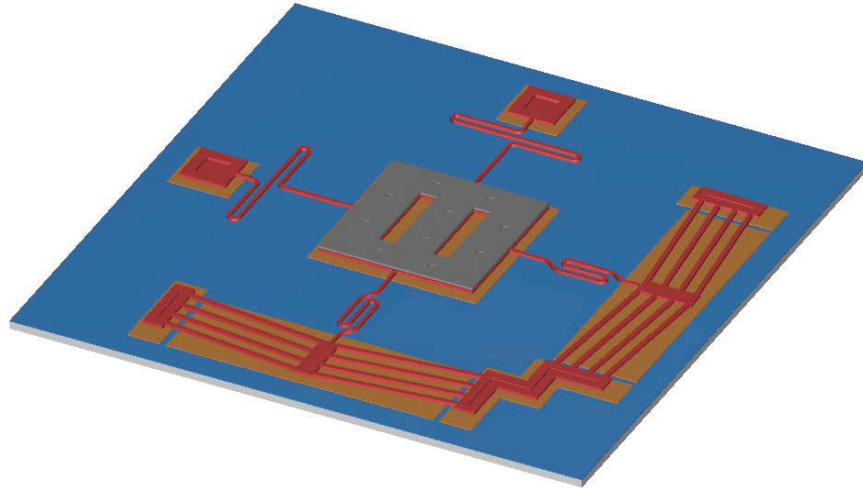


Figure 55. 3D LEedit view of the pad assembly

### 5.2.2 Chevrons

Four bar chevron actuators with a total length of  $200\ \mu\text{m}$  and a  $6^\circ$  angle have been used (Figure 56). These standard chevrons were selected as they fit within the available space and are known to have a good amount of force and displacement for most applications. Previously estimated force is approximately  $80\ \mu\text{N}$  with a  $3\ \mu\text{m}$  displacement [39]. The chevrons are constructed using the poly1 layer to ensure the height ( $4.5\ \mu\text{m}$  when over poly0,  $4.0\ \mu\text{m}$  when directly over the nitride) is well below the platform at all times. The gap between the chevron and the transported platform, when it is in the lowered position, should be sufficient to minimize possible heat sink effects between the chevron and the transported platform.

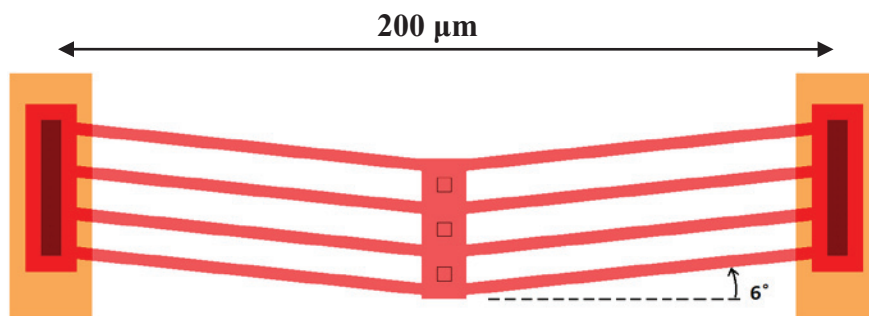


Figure 56. Standard  $200\ \mu\text{m}$ ,  $6^\circ$  chevron

### 5.2.3 Springs

The last key features of the pad assembly are the connection springs. Two types of springs are used, each offering different properties allowing for the desired results. The chevrons are connected directly to “paperclip” springs (Figure 57). Paperclip springs have a high stiffness in the axial direction (here X). This allows maximum force from the chevron to be transferred to the pad. The chevrons are oriented on a “pull” configuration to eliminate the possibility of buckling in the connection bars between the paperclip springs and the pad. The paperclip springs also allow rotation. This combination allows the pad to be pulled in either axis without interference from the opposing chevron. Opposing S-springs (Figure 58) are used in order to ensure the pad itself doesn’t rotate when moved in either direction. These have a rotational stiffness similar to the paperclip springs ensuring balanced forces on either side of the pad, but have very little stiffness in the axial direction so as not to offer a resistive axial force to the chevron (here Y).

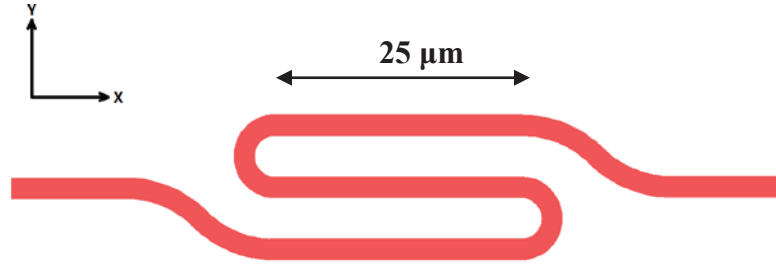


Figure 57. Paperclip Spring

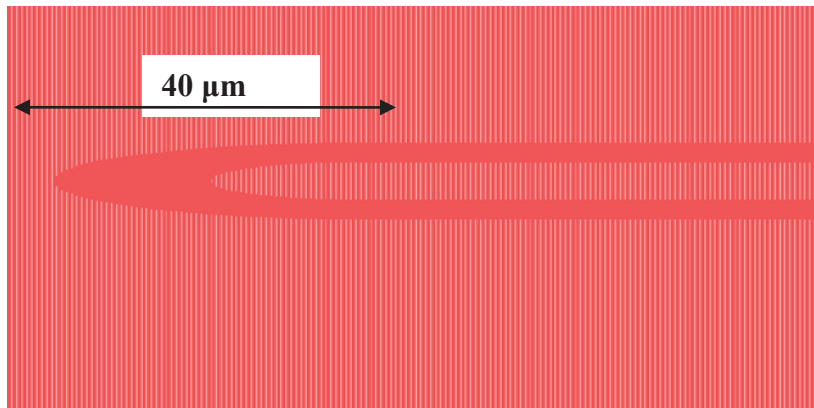


Figure 58. S-Spring

Both spring types are constructed using the poly1 layer to ensure the top of the spring, 4.0 $\mu\text{m}$  above the nitride, is well below the transported platform above at all times.

Fettig [40] determined the equations of spring stiffness based on standard polysilicon parameters and cross sectional dimensions. Table 7 and Table 8 show the axial, rotational and lateral stiffness equations for S-springs and paperclip springs, respectively. Note that rotational stiffness is the same for both springs.

	<b>Root Equation</b>	<b>Stiffness Equation</b>	<b>Units</b>
<b>Rotational</b>	$K_{\theta} = EI/L$	$K_{\text{rot}} = 900(250/L)$	$\mu\text{N}\mu\text{m}/\text{rad}$
<b>Axial</b>	$K \propto EI/L^3$	$K_{\text{axial}} = 0.83(250/L)^{3.19}$	$\mu\text{N}/\mu\text{m}$
<b>Lateral</b>	$K \propto EI/L$	$K_{\text{lateral}} = 35(250/L)^{0.72}$	$\mu\text{N}/\mu\text{m}$

**Table 7. S-Spring stiffness equations**

	<b>Root Equation</b>	<b>Stiffness Equation</b>	<b>Units</b>
<b>Rotational</b>	$K_{\theta} = EI/L$	$K_{\text{rot}} = 900(250/L)$	$\mu\text{N}\mu\text{m}/\text{rad}$
<b>Axial</b>	$K \propto EI/L^3$	$K_{\text{axial}} = 41(250/L)^{1.13}$	$\mu\text{N}/\mu\text{m}$
<b>Lateral</b>	$K \propto EI/L$	$K_{\text{lateral}} = 0.16(250/L)^{3.18}$	$\mu\text{N}/\mu\text{m}$

**Table 8. Paperclip spring stiffness equations**

The stiffness equations are based on based on the following poly1 parameters:

$$t = 2 \mu\text{m}$$

$$w = 2 \mu\text{m}$$

$$E = 169 \text{ GPa}$$

$$\nu = 0.22$$

$$\rho = 2330 \text{ kg}/\text{m}^3$$

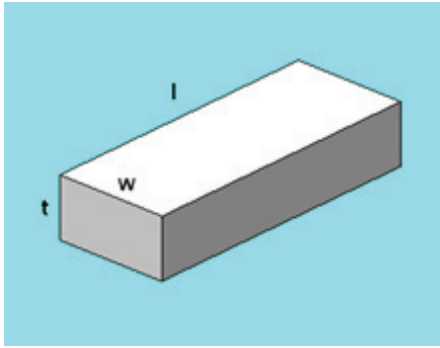


**Figure 59. Length (l), width (w) and thickness (t) of a standard polysilicon spring beam**

Table 9 shows typical values for axial, rotation and lateral stiffness based on equal length S-springs and paperclip springs, based on dimensions shown in Figure 59. Length (l), width (w) and thickness (t) of a standard polysilicon spring beam. These values represent the stiffness of the springs independent of additional structures [40].

	<b>Axial</b>	<b>Rotational</b>	<b>Lateral</b>
<b>S-Spring</b>	1.69 $\mu\text{N}/\mu\text{m}$	1125 $\mu\text{N}\mu\text{m}/\text{rad}$	41.1 $\mu\text{N}/\mu\text{m}$
<b>Paperclip Spring</b>	52.8 $\mu\text{N}/\mu\text{m}$	1125 $\mu\text{N}\mu\text{m}/\text{rad}$	0.33 $\mu\text{N}/\mu\text{m}$

**Table 9. Typical comparative spring stiffness values (based on  $t = 2 \mu\text{m}$ ,  $w = 2 \mu\text{m}$ ,  $E = 169 \text{ GPa}$ ,  $\nu = 0.22$ ,  $\rho = 2330 \text{ kg/m}^3$  and equal overall lengths of  $200 \mu\text{m}$ )**

### 5.3 Vertical Thermal Actuator

The chevron vertical thermal actuator (VTA) (Figure 60) is used to raise the lifter grid to a height above the pad's upper surface height above the substrate. The lifter grid is the portion of the lifter assembly that makes contact with the platform. Various lifter grids are being tested to find the optimum design. Currently lifter grids have been developed using poly1 and poly1-poly2 with various dimple and via configurations to vary the geometry and bar stiffness.

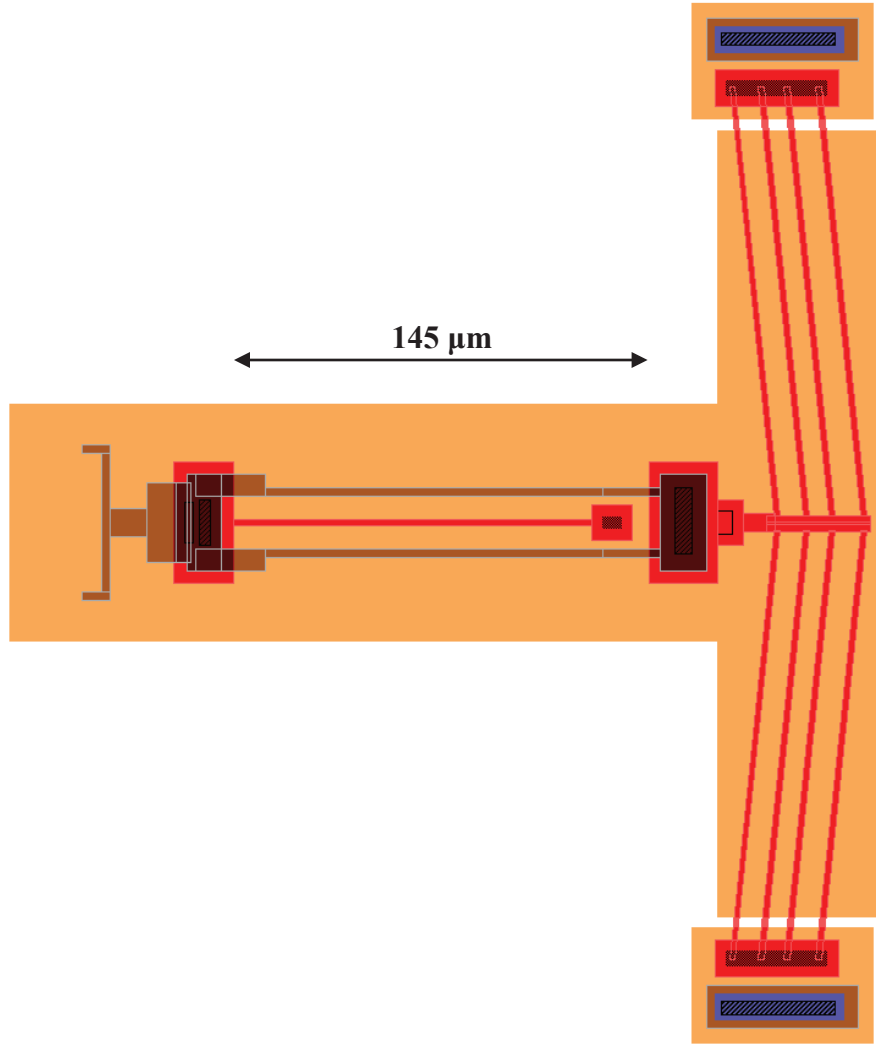


Figure 60. LEdit representation of the chevron vertical thermal actuator (VTA)

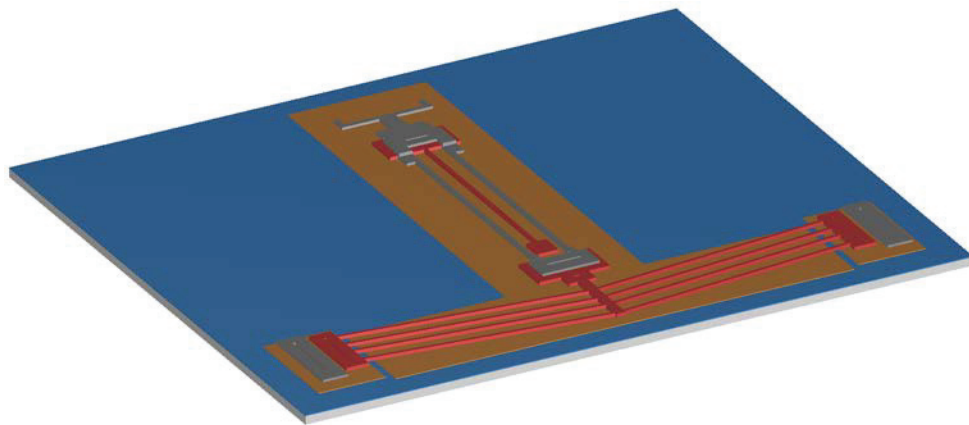


Figure 61. 3D LEdit view of the chevron vertical thermal actuator (VTA)

The chevron VTA works in a similar fashion to a standard MEMS hot/cold bar thermal actuator turned on its side. Poly2 bars are connected to the chevron, while a poly1 bar is anchored to the substrate. As the chevron moves, it pulls on the poly2 bars. The poly1 bar resists the chevron's motion. Since there is a height difference between the poly2 and poly1 bars, a moment is generated, resulting in an out of plane curl of the actuator tip. The total height of the structure is below that of the pads. The connection of the tip to the lifter grid is achieved through the use of a torque bar. The length and resulting stiffness of this structure is critical and is a compromise between desired height of the grid and potential lift capacity of the structure. A soft torque bar allows for greater lift height of the VTA tip, but results in sagging under a load. A stiffer bar resists load sagging, but reduces the VTA lift height. Future analysis will be done to optimize the components.

#### **5.4 Lifter Grids**

While the design of the pads are relatively straight forward, i.e. all layers used to raise the pad to be the highest structure, the design of the lifter grid (Figure 62) poses the largest challenge for the Lift and Slide design. Grids are a compromise between rigidity, and overall height. Multiple layers allow for more rigid structures, but bring the grid surface closer to the height of the pads. An object/platform resting on a pad may cause the pad height to drop until the pad is resting on the poly0/dimple interface. This could represent a drop in pad height of as much as 1.5  $\mu\text{m}$ , from 7.25  $\mu\text{m}$  down to 5.75  $\mu\text{m}$ . Further consideration includes a level and flat grid surface. There are numerous poly 0 control wires that run under the grid. Obviously the grid must be designed so that the control wires can never be shorted out. In order to ensure a level and flat grid surface free of small "bumps" resulting from the "noodle effect" of polysilicon layering, the grid must sit over a poly0 plate with gaps to allow spacing for the wires.

Two issues make the lifter grid design more problematic. Firstly, residual stress from the manufacturing process affects long structures with multi-layer anchor points, i.e. lifter

grids with opposed VTAs. The effect is a small increase in height over the predicted design height of the structure. This can be as much as 1-2  $\mu\text{m}$ . A stiction effect, fully discussed in a later Section, tends to draw flat surfaces together, in this case the lifter grid and the platform. If this is not controlled, then the lifter grid will never truly be decoupled from the platform, rendering the motion of the pads ineffective. Various designs of grids have been tried. Thus far the most successful grid is a simple poly1 grid with 25  $\mu\text{m}$  wide beams, over a poly0 plate.

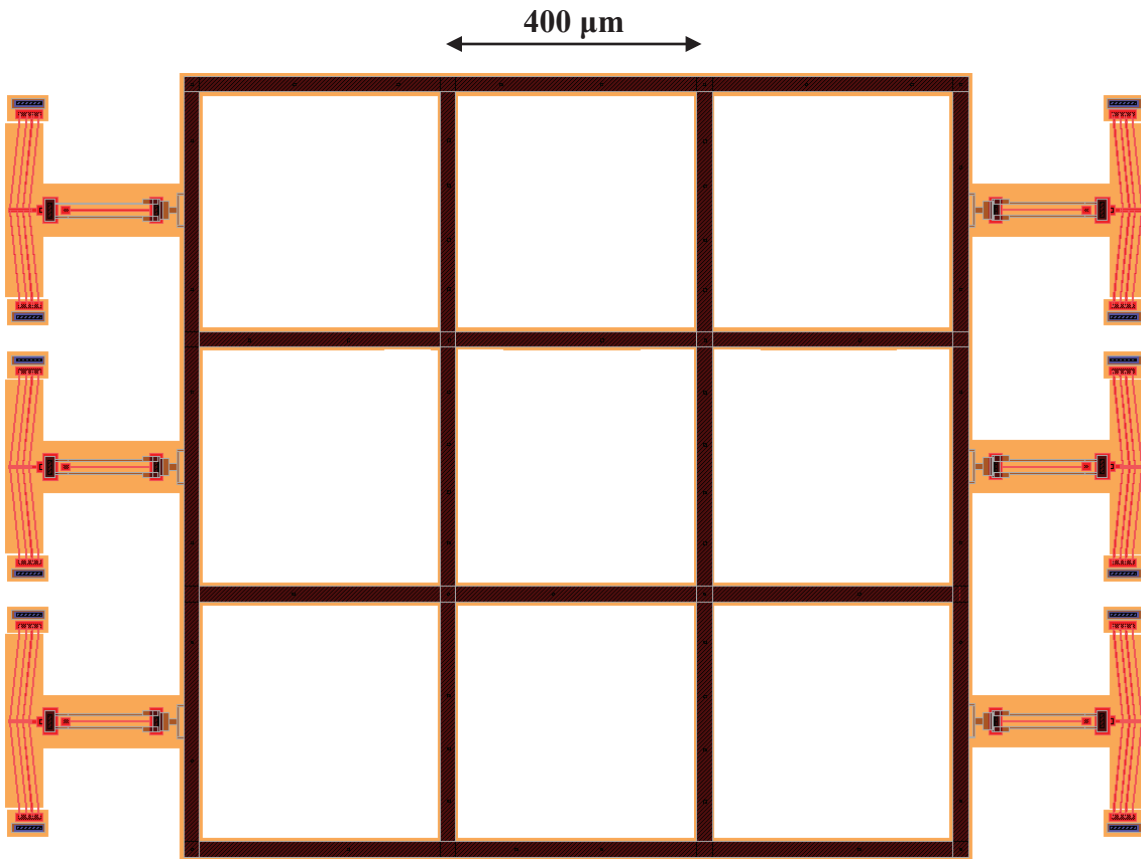


Figure 62. Set of VTAs Connected to Lifter Grid. Wire gaps in the poly0 layer are not shown.

## 5.5 Platforms (plates)

The platforms (plates) used to carry particles must also be optimized for proper operation. Two types of platforms have been tested with varying results. PolyMUMPs platforms would be preferable, since they could be constructed on the same chips as the conveyor

arrays. However, tests have shown several issues with the thin platforms. Firstly, they are difficult to lift off the substrate without breaking. Secondly, dimples are required to reduce possible stiction with the substrate. These dimples interfere with the movement of the platforms by catching on the pads and lifter grids. This problem can be solved by “flipping” a platform over, but this is a complex procedure that often results in damaged platforms. Also, if a plate is thought to be flipped, it must be verified with a height profiler since visually from above it is not clear if the dimples are on the top or bottom of the platform after an attempt to flip the platform. Lastly, they are not completely rigid, resulting in a flexible plate that can conform to the pad array. This results in contact with both the lifter grid and the pads, regardless of lifter height. The solution is either multi layer platforms that are more rigid, which are flipped over to stop dimples catching or the use of SOI platforms. SOI platforms are ideal due to their rigid and rugged nature. They are rugged enough to be easily moved and lifted with probes, and rigid enough to resist flexing and conforming to the array.

## **5.6 Full Lift and Slide Assembly**

Figure 63 demonstrates a full lift and slide assembly consisting of a 4x4 array with 16 lifters. Figure 64, Figure 65 and Figure 66 show the field of view over the MEMS fabricated 4x4 array using the various lens and zooms of 1x and 2x.



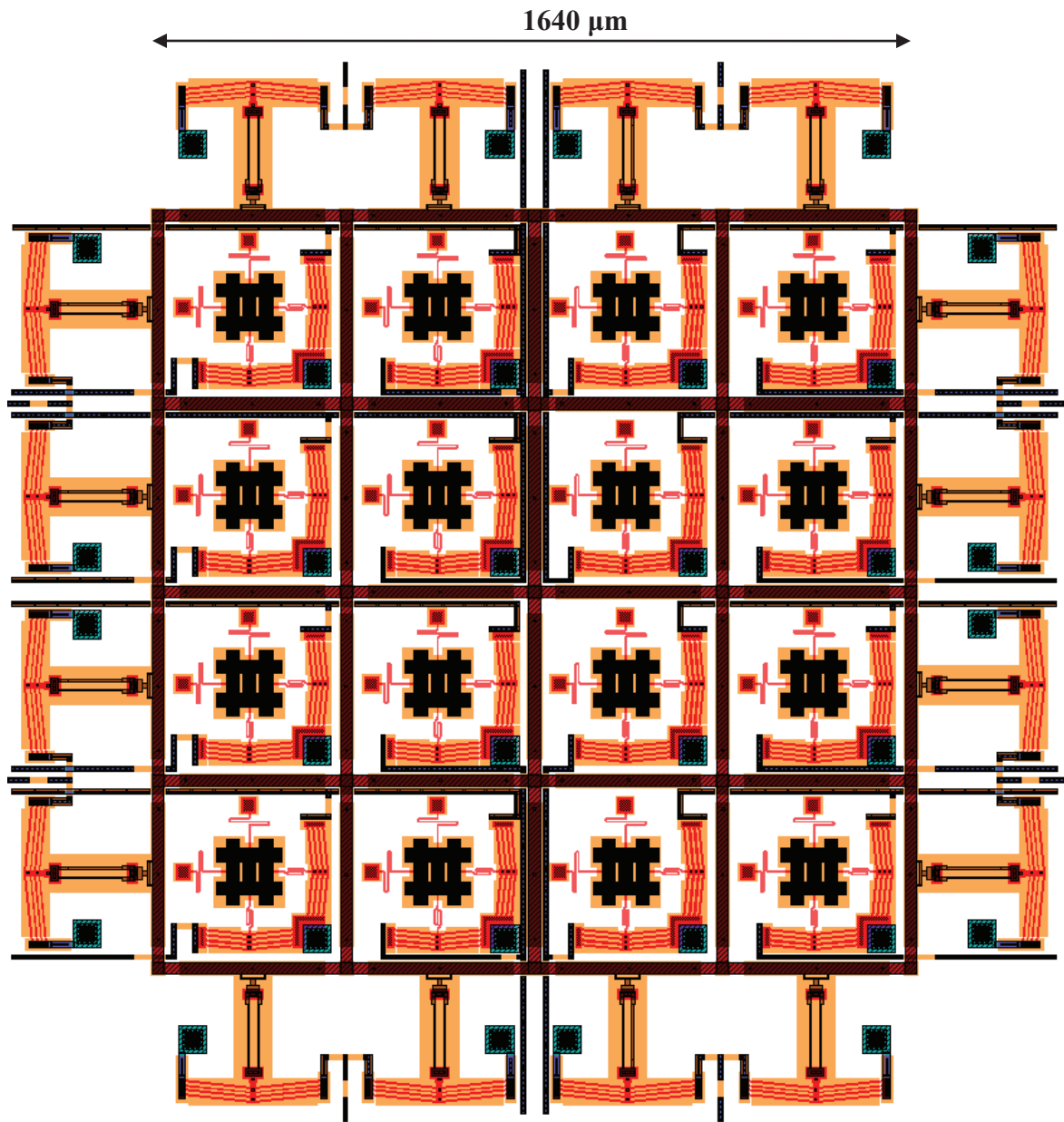


Figure 63. Larger 4x4 array

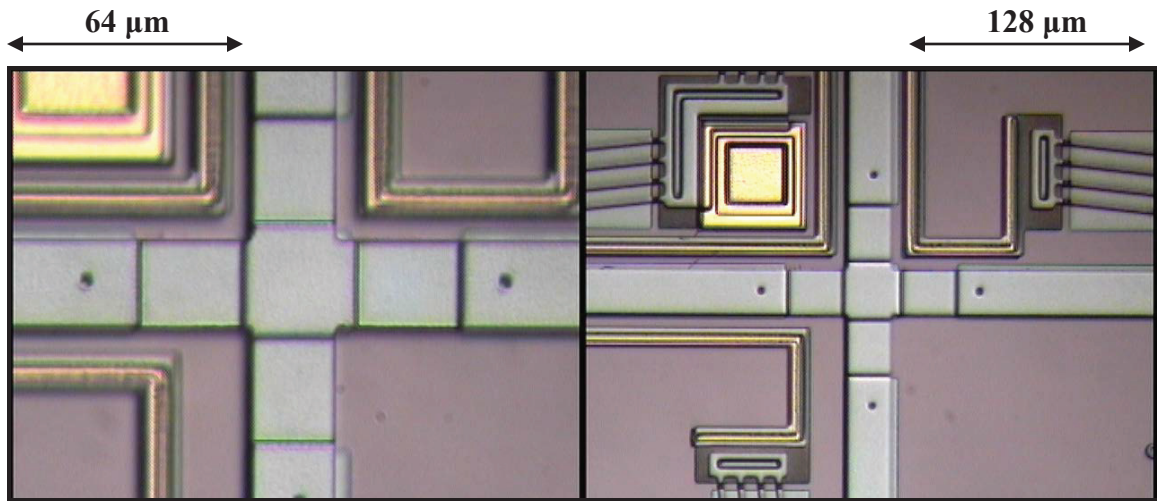


Figure 64. 50x zoom and 25x zoom respectively

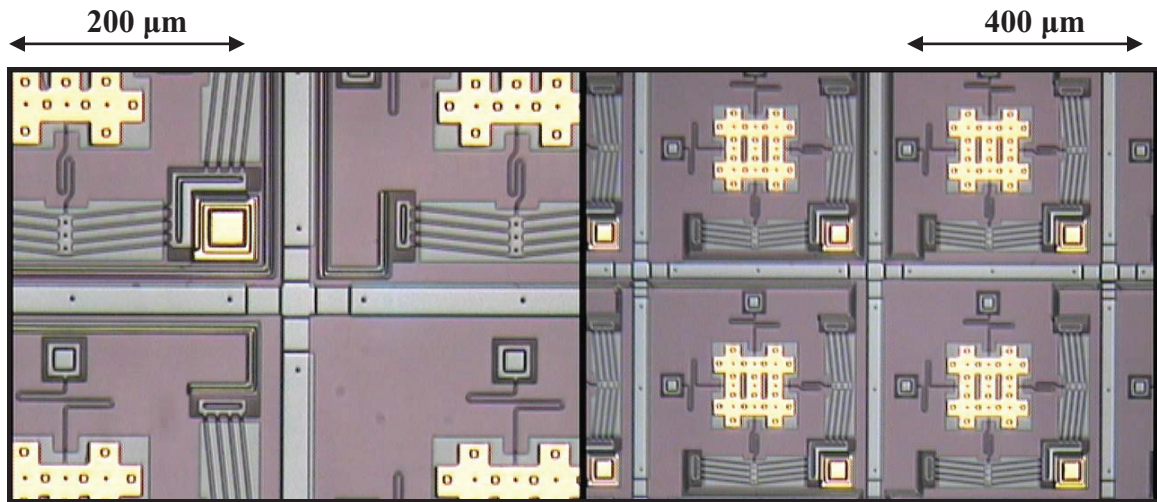


Figure 65. 16x zoom and 8x zoom respectively

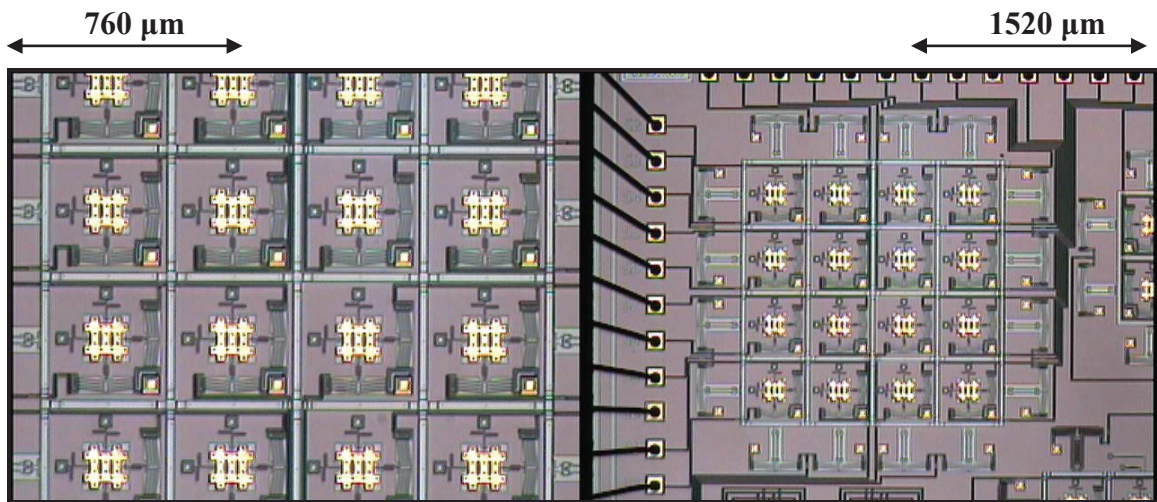


Figure 66. 4.5x zoom and 2.25x zoom respectively

## 5.7 Estimation of Maximum Conveyor Force

The maximum force available for transporting an object can be estimated based on the given geometries of the complete conveyor. The exact limits vary according the specific array dimensions and operating characteristics.

There are three main limiting factors that determine what the maximum usable force is for the conveyor. The force limit that the XY pads can generate is a function of the maximum chevron force, the stretch of the springs and the frictional contact between the pads and the substrate. The grid lifter limit is a function of the maximum chevron force and the required amplification to achieve the required lifter height. Lastly, the flexibility of the grid will limit the maximum mass that can be raised above the pads.

Given a standard 4x4 array operating at 12V for both the XY pads and 7V for the lifters, with a platform riding on four XY pads, a comparison of the first two factors can be done. The maximum planar force will be four times the maximum planar chevron force, or approximately  $4 \times 80\mu\text{N} = 320\mu\text{N}$  [39]. The typical geometry of the lifter is a length of approximately  $150\mu\text{m}$  and a layer separation of  $1.5\mu\text{m}$ . This gives a moment arm ratio of 100:1. As such, the maximum expected lifter force for a single lifter will be  $0.8\mu\text{N}$ . When multiplied by 16 lifters, a 4x4 array, we have a maximum lift force of  $16 \times 0.8\mu\text{N} = 12.8\mu\text{N}$ . Given that an average salt crystal has a mass of approximately  $80\mu\text{g}$ , this equates to approximately 16 salt crystals. From this is it clear that the maximum lifter force is significantly less than the maximum planar force.

## **Chapter 6.0 XY Pad Micro Kinematic and Dynamic Model**

### **6.1 Overview**

Two types of models are used to analyze the XY pads. Kinematic models are used to study the geometric relationships within the model, without considering the forces that affect the motion. This is useful to initially define the available degrees of freedom and the geometric envelop of motion. The dynamic model is used when considering forces that may act on the bodies and is especially useful when considering vibration within the system.

At the microscale, vibration can be of great concern. Dynamic modeling is used to better predict the response of the various components and create a quick way to see if various loading conditions will result in undesirable effects such as poor control or even component damage.

### **6.2 Kinematic Model**

Figure 67 shows the kinematic model of the XY pad. It is divided into a frame, a mass and a series of links connecting them. The links are either Revolute (rotational motion) or Prismatic (linear motion). All components of the XY pad are divided into these classifications (Figure 68). Both types of springs, or spring/chevron combination can be thought to have an axial, rotational and lateral component.

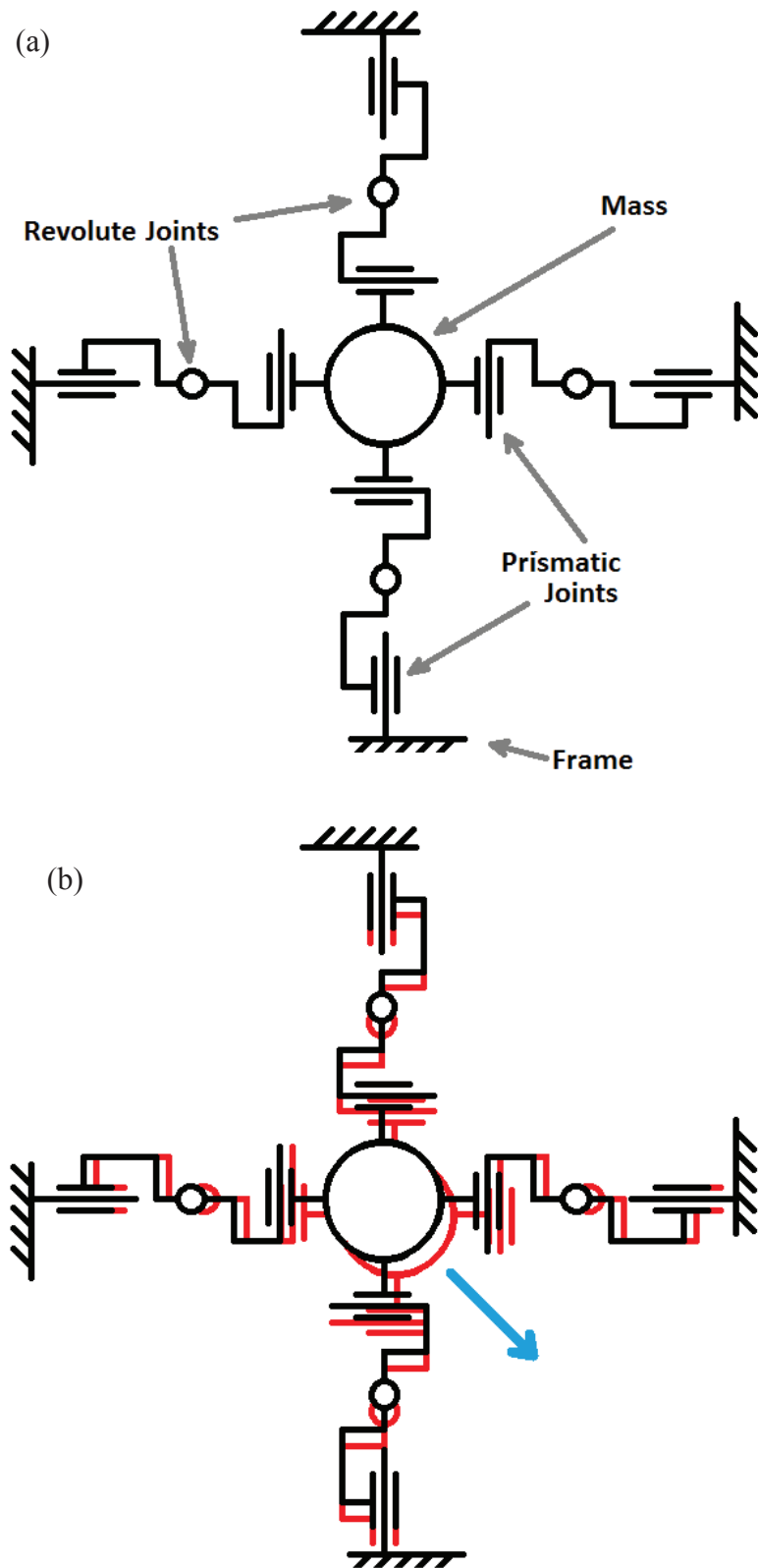


Figure 67. Kinematic model of XY pad: (a) components (b) effect of motion on components

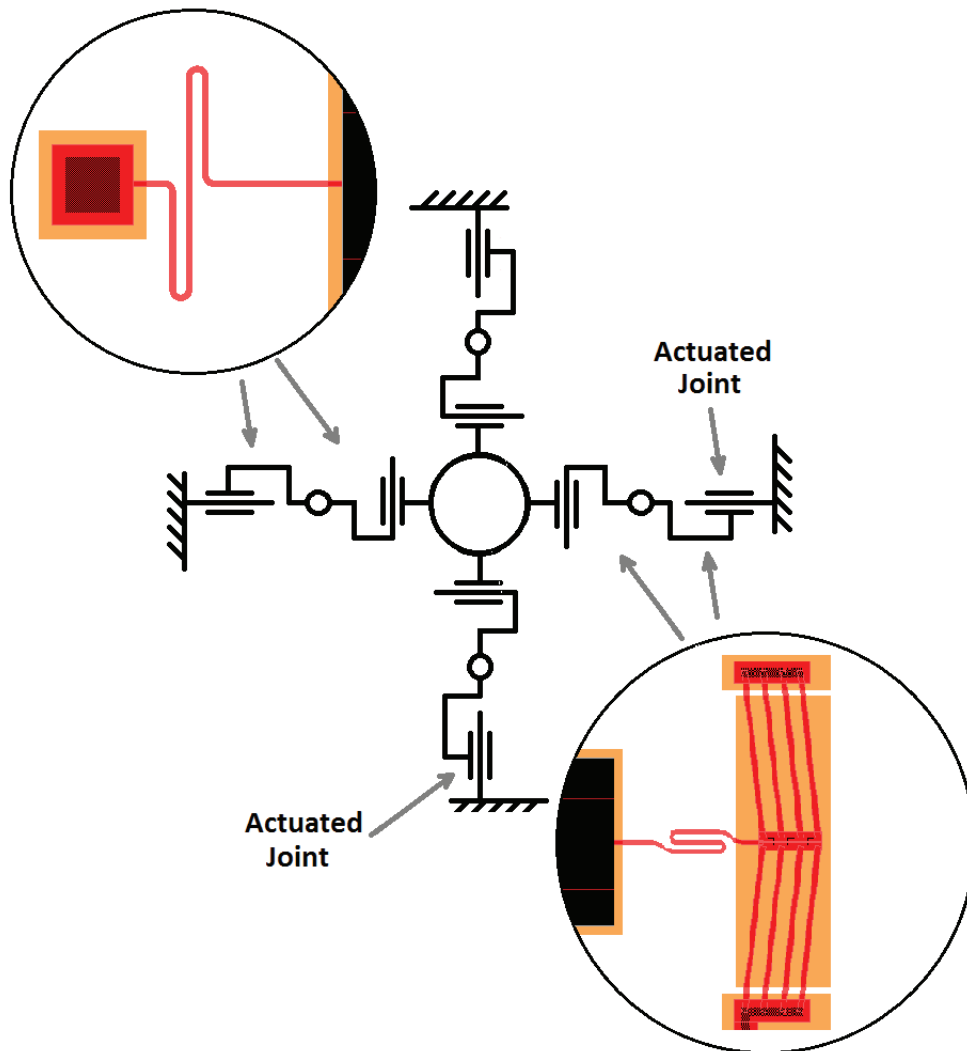


Figure 68. The combination of Prismatic and Revolute joints are equivalent to both the S-Spring and the Paperclip spring/Chevron combination, giving each a resultant axial, rotational and lateral motion

A simple formula is used to calculate the degrees of freedom of the kinematic model.

$$m = 3(L - 1) - 2J_1 - J_2 \quad (7.1)$$

Based on Figure 69, the total planar degrees of freedom of the XY pad can be calculated as follows:

$$m = 3(10 - 1) - 2(12) - 0$$

$$m = 3$$

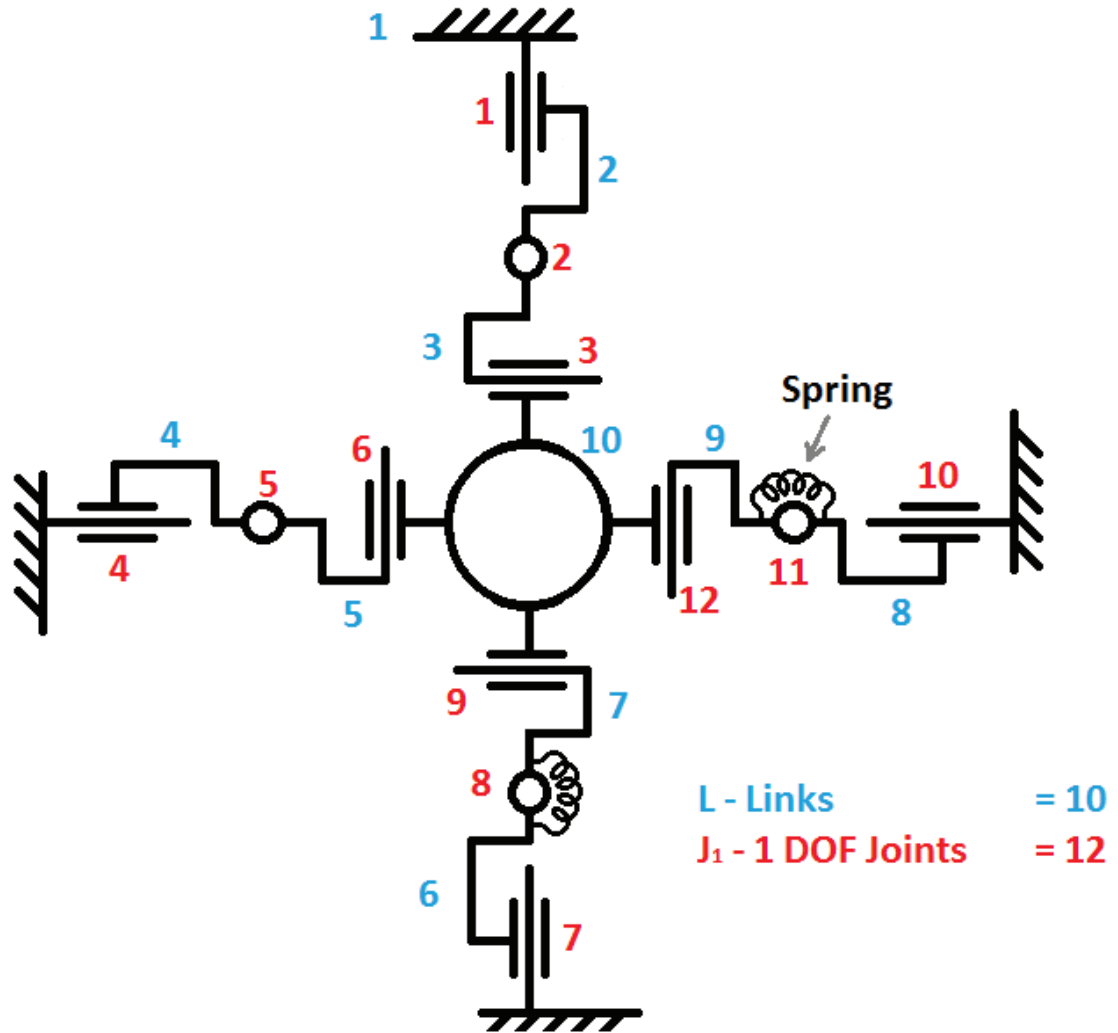


Figure 69. Kinematic model showing numbers of links and 1 DOF joints

Therefore, the basic kinematic analysis of the XY pad shows it to have three planar degrees of freedom: X, Y and  $\theta$ . Movement of the chevrons can actuate two degrees of freedom, X and Y, with the passive third rotational degree of freedom that can be actuated by vibration. This DOF is controlled by the stiffness, so springs can be added. Dynamic analysis is used to further investigate the vibrational response of the three degrees of freedom.

## **6.3 Dynamic Model**

In order to fully characterize the XY pads, a dynamic model is used. The dynamic model relates the motion observed with the kinematic model to the real world response as a function of the mass components.

The key parameters for the dynamic model include the mass, location of the mass center, the axial, rotational and transverse stiffness and the center of rotation. This information is used to generate the equations of motion. Matrix equations are then created that are used to calculate the resonant frequencies and the corresponding modes of vibration. The following sections break these parts down.

### **6.3.1 From Kinematic model to Dynamic Model**

When considering the model from a vibration point of view, the chevron now becomes axially stiffer than the paperclip spring since it is not activated. With the kinematic model, the chevron moves axially and the paperclip spring doesn't. With the dynamic model, the paperclip spring axial stiffness is significantly smaller than the chevron axial stiffness, and therefore paperclip spring axial motion will be considered. Figure 70 shows the resulting dynamic model. Note that the springs are shown next to each other for clarity, but they all share a single center point, defined as the center of rotation.



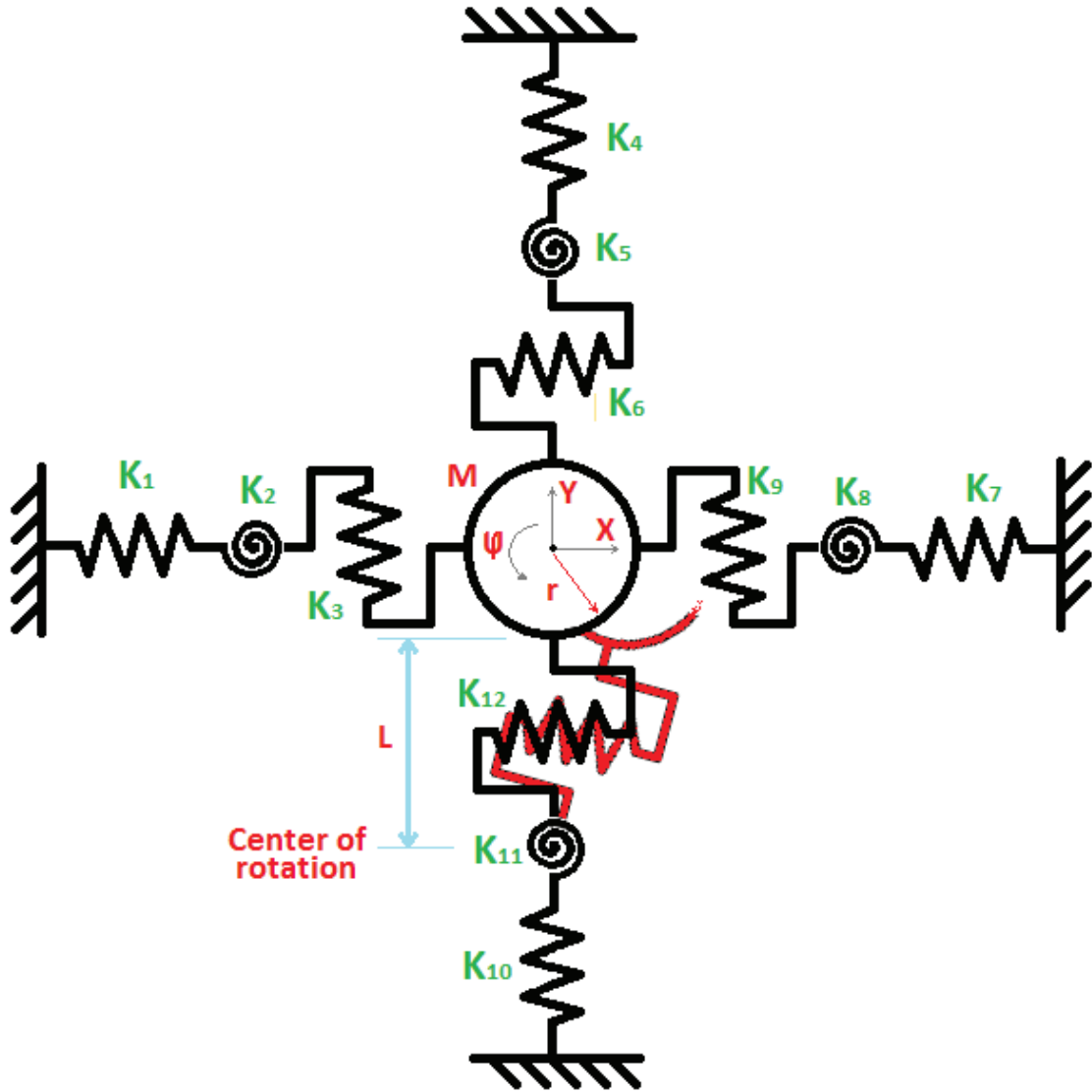


Figure 70. Dynamic model

### 6.3.2 Mass

The main structures of the XY pad are the center pad, the S-springs and the paperclip springs. The center pad is constructed using layers of poly1, poly2 and gold, whereas the springs are constructed using just poly1.

The parameters for the materials are shown in Table 10.

	Poly1	Poly2	Gold
Thickness ( $\mu\text{m}$ )	$2.00 \pm 0.15$	$1.50 \pm 0.10$	$0.52 \pm 0.06$
Density ( $\text{kg}/\text{m}^3$ )	2,330	2,330	19,300

Table 10. Parameters used for mass calculations [28]

Based on the dimensions of a standard XY pad (Figure 71) the mass of the pad can be easily calculated. Note that the effect of the vias and dimples is minimal on the mass and can be ignored.

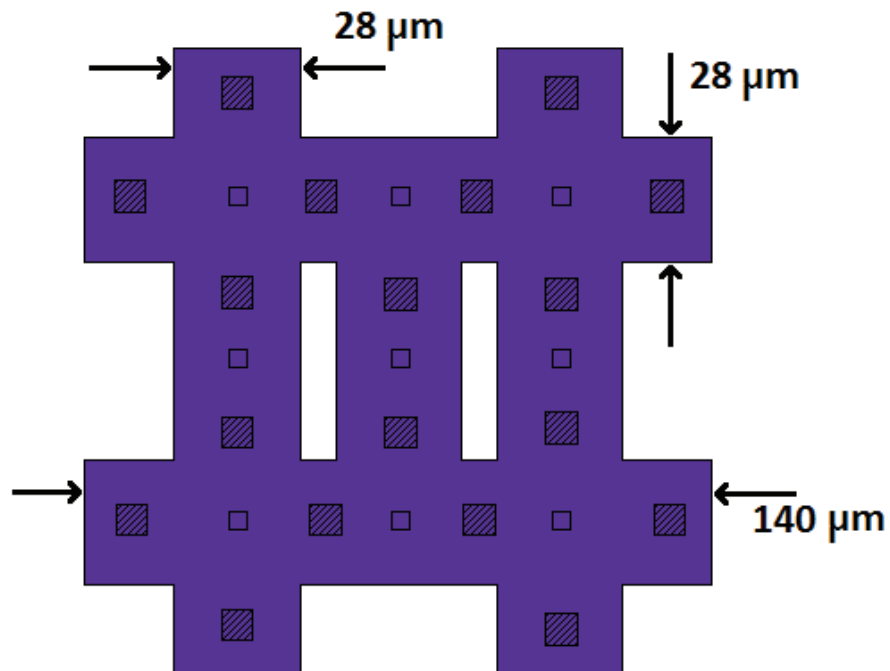


Figure 71. Typical center pad dimensions

This gives a mass range of  $0.219 \mu\text{g}$  to  $0.266 \mu\text{g}$  for a standard pad, and an average mass of  $0.242 \mu\text{g}$ .

Similar calculations can be done for the S-spring and the paperclip spring. When considering medium length springs, the average masses are found to be  $0.00024 \mu\text{g}$  and  $0.00014 \mu\text{g}$ , respectively. Since the center pad has a mass more than 1000 times greater than the springs, the mass of the springs are ignored for all spring-mass calculations.

### 6.3.3 Axial, Rotational and Lateral Stiffness

Calculations for axial, rotational and transverse stiffness for both S-springs and paperclip springs can be done using equations that were developed by Fettig [40] specifically for MEMS springs constructed using poly1.

Rotational stiffness does not vary with spring shape and can be written as:

$$K_{rot} = 900 \frac{\mu N \mu m}{rad} * \left( \frac{250 \mu m}{L} \right)^{1.00} \quad (7.2)$$

Where L is the overall length of the spring. Spring dimensions are shown in Figure 72 and Figure 73.

Axial stiffness is calculated for the S-spring as:

$$K_{axial} = 0.83 \frac{\mu N}{\mu m} \left( \frac{250 \mu m}{L} \right)^{3.19} \quad (7.3)$$

Axial stiffness is calculated for the paperclip spring as:

$$K_{axial} = 41 \frac{\mu N}{\mu m} \left( \frac{250 \mu m}{L} \right)^{1.13} \quad (7.4)$$

From this it is clear that the axial stiffness of the paperclip spring is much greater than the axial stiffness of the S-spring.

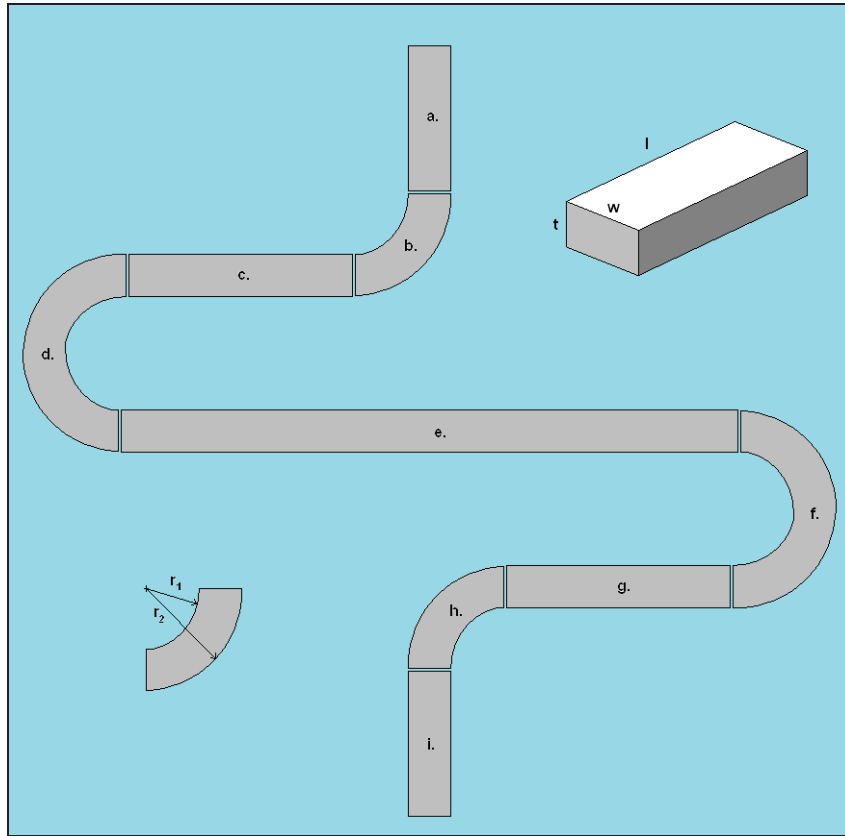


Figure 72. Key dimensions of an S-spring

Lateral stiffness is calculated for the S-spring as:

$$K_{lateral} = 35 \frac{\mu N}{\mu m} \left( \frac{250 \mu m}{L} \right)^{0.72} \quad (7.5)$$

Lateral stiffness is calculated for the paperclip spring as:

$$K_{lateral} = 0.16 \frac{\mu N}{\mu m} \left( \frac{250 \mu m}{L} \right)^{3.18} \quad (7.6)$$

From this it is clear that the lateral stiffness of the paperclip spring is much less than the lateral stiffness of the S-spring.

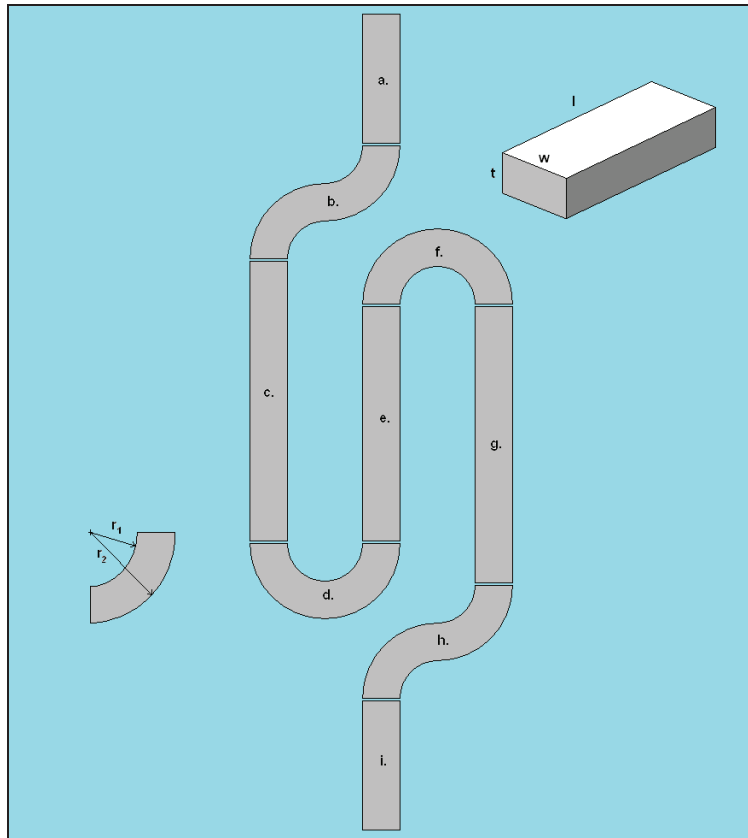


Figure 73. Key dimensions of a paperclip spring

### 6.3.4 Equations of Motion

Based on Figure 70, a series of equations of motion can be written to describe the motion of the center pad in each degree of freedom as a function of the attached springs.

As X and Y motion only involves axial and lateral springs, these two equations are quite simple.

$$m \ddot{x} + k_2 x + k_6 x + k_8 x + k_{12} x - f_x(t) = 0 \quad (7.7)$$

$$m \ddot{y} + k_3 y + k_5 y + k_9 y + k_{11} y - f_y(t) = 0 \quad (7.8)$$

Rotation is a bit more complex and must consider associated spring stretch as a function of the pad rotation.

Consider Figure 74. If  $r$  is the radius of the plate and is considered rigid, then for the pad to rotate about its center with only a single rotational spring between the center of the pad and the center of rotation of the spring combination there must be a lateral stretch ( $S_1$ ) and an axial stretch ( $S_2$ ). Note that as the pad rotates in one direction the spring rotation is in the opposite direction.

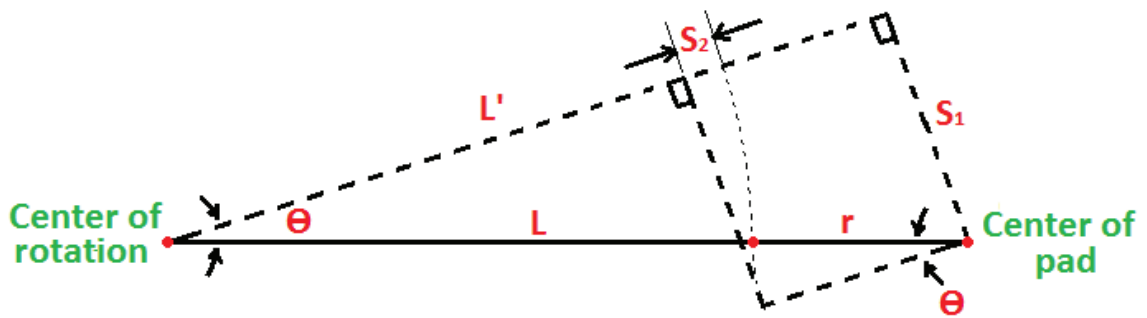


Figure 74. Stretch of lateral and axial springs as a result of plate rotation

Since this is a vibration problem, small angle approximations will be used.

$$\sin \theta \approx \theta \quad (7.9)$$

$$\cos \theta \approx 1 - \frac{\theta^2}{2} \approx 1 \quad (7.10)$$

From Figure 74:

$$\sin \theta = \frac{S_1}{L+r} \quad (7.11)$$

$$S_1 = (L+r)\sin \theta \quad (7.12)$$

Using the small angle approximation, and substituting equation 7.9 into 7.12:

$$S_1 = (L + r)\theta \quad (7.13)$$

Likewise we can solve for  $S_2$ :

$$\cos \theta = \frac{L' + r}{L + r} \quad (7.14)$$

$$S_2 = (L + r) - (L + r)\cos \theta \quad (7.15)$$

Substituting 7.10 into 7.14:

$$S_2 = 0 \quad (7.16)$$

From this, the equation of motion for rotation can be defined.

$$\begin{aligned} m\ddot{\theta} + k_1 \frac{1}{L_1 + r_1} \theta + k_3 \frac{L_1 + r_1}{L_1 + r_1} \theta + k_4 \frac{1}{L_2 + r_2} \theta + k_6 \frac{L_2 + r_2}{L_2 + r_2} \theta + k_7 \frac{1}{L_3 + r_3} \theta + \\ k_9 \frac{L_3 + r_3}{L_3 + r_3} \theta + k_{10} \frac{1}{L_4 + r_4} \theta + k_{12} \frac{L_4 + r_4}{L_4 + r_4} \theta - f_\theta(t) = 0 \end{aligned} \quad (7.17)$$

$$\begin{aligned} m\ddot{\theta} + k_1 \frac{1}{L_1 + r_1} \theta + k_4 \frac{1}{L_2 + r_2} \theta + k_7 \frac{1}{L_3 + r_3} \theta + k_{10} \frac{1}{L_4 + r_4} \theta + \\ k_3 \theta + k_6 \theta + k_9 \theta + k_{12} \theta - f_\theta(t) = 0 \end{aligned} \quad (7.18)$$

### 6.3.5 Matrix Equations

Assuming that the matrix form of equation of motion is  $M\ddot{Q} + KQ = F$ , and all forces  $F$  are zero when analyzing the free undamped vibration of the system, matrix equations can be written from equations 7.7, 7.8 and 7.18.

Mass matrix:

$$M = \begin{bmatrix} m & 0 & 0 \\ 0 & m & 0 \\ 0 & 0 & m \end{bmatrix} \begin{bmatrix} \ddot{x} \\ \ddot{y} \\ \ddot{\theta} \end{bmatrix} \quad (7.19)$$

Stiffness matrix:

$$K = \begin{bmatrix} k_2 + k_6 + k_8 + k_{12} & 0 & 0 \\ 0 & k_3 + k_5 + k_9 + k_{11} & 0 \\ 0 & 0 & \frac{k_1}{L_1 + r_1} + \frac{k_4}{L_2 + r_2} + \frac{k_7}{L_3 + r_3} \\ & & + \frac{k_{10}}{L_4 + r_4} + k_3 + k_6 + k_9 + k_{12} \end{bmatrix} \begin{bmatrix} x \\ y \\ \theta \end{bmatrix} \quad (7.20)$$

Force matrix:

$$F = \begin{bmatrix} 0 \\ 0 \\ 0 \end{bmatrix} \quad (7.21)$$

### 6.3.6 Natural Frequencies

In order to solve for the natural frequencies of the system, the mass normalized stiffness matrix ( $\tilde{K}$ ) is first calculated.



$$\tilde{K} = M^{-\frac{1}{2}} K M^{-\frac{1}{2}} \quad (7.22)$$

Software is now used to solve for the eigenvalues of the mass normalized stiffness matrix, which gives three values:  $\lambda_1$ ,  $\lambda_2$  and  $\lambda_3$ .

$$\lambda_i = \omega_i^2 \quad (7.23)$$

Where  $\omega_i$  is the natural frequency for each vibration mode.

The model was set up and run from a Microsoft Excel spreadsheet using a math package (MatrixL.xla v2.2 Light, written by Foxes Team, 2006, <http://digilander.libero.it/foxes> ) capable of solving eigenvalue problems.

Results of the model will be shown and compared to a FEM model in the next Section.

### 6.3.7 Finite Element Analysis

The Finite Element (FEM) package ANSYS™ V10.0 was used for comparison with the analytical model. A design was first created and exported from LEdit™ V15.02 to SolidWorks™ 2004 in DXF format, and then from SolidWorks to ANSYS in IGES format. Tetrahedral coupled-field SOLID98 elements are used for the mesh. The element supports six degrees of freedom: *UX*, *UY*, *UZ*, *Temp*, *Volt* and *Mag*. For modal analysis, the key material parameters used for polysilicon were Young's Modulus (E=158 GPa), Poisson Ratio ( $\nu=0.22$ ) and Density ( $\rho=2330 \text{ kg/m}^3$ ) (Sharpe [41]). Auto meshing was used. The Block Lanczos method is used for solving for all modes and natural frequencies up to 200 kHz.

Analysis of the XY pads revealed six significant modes of vibration; three out-of-plane (Figure 75) and three in-plane (Figure 76). Out-of-plane modes include a flat Z axis

mode and two diagonal tilting modes. In-plane modes include two translational and one rotational modes.

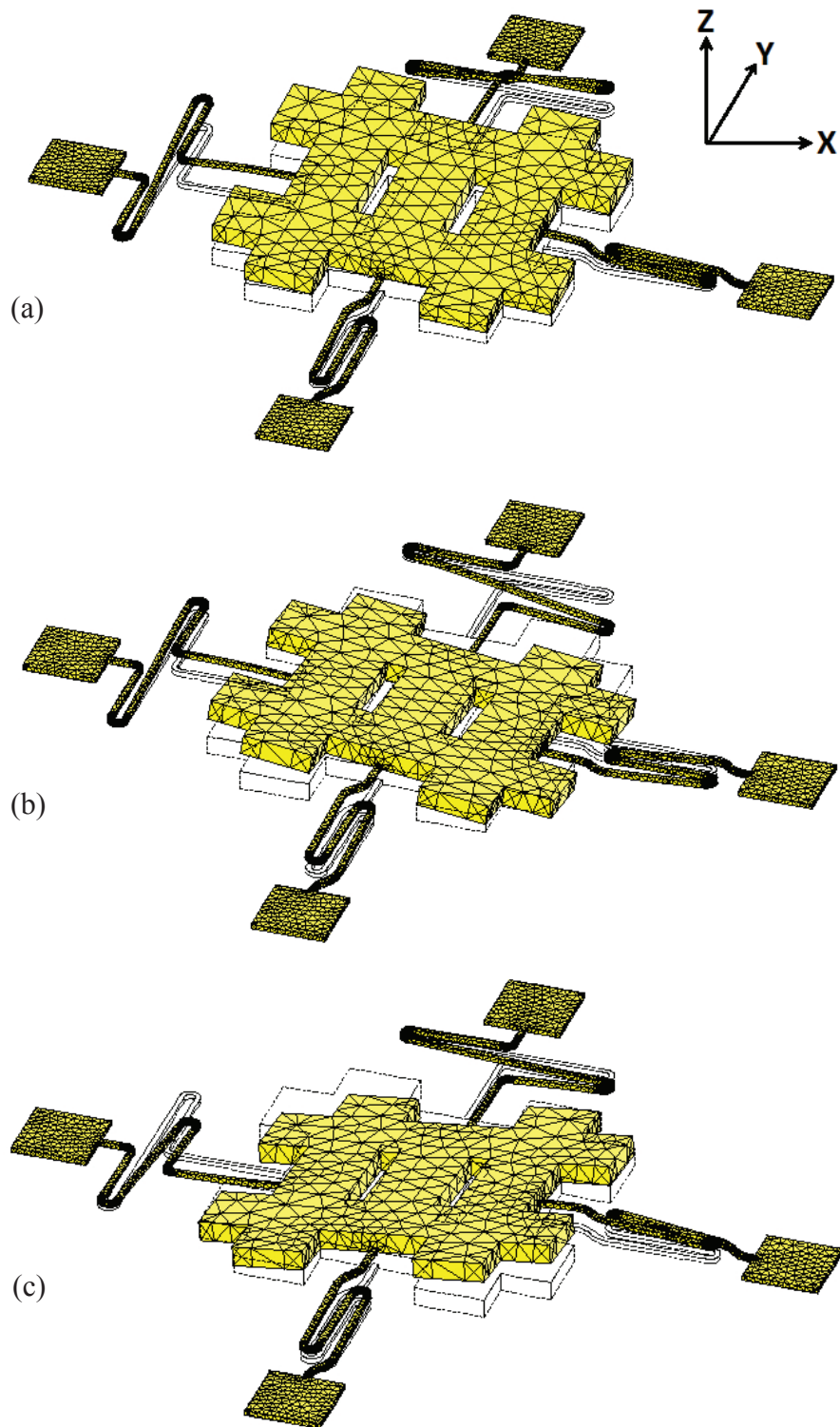


Figure 75. XY pad out of plane modes using FEM. (a) Z translational vibration mode (b) first diagonal tilting vibration mode (c) second tilting diagonal vibration mode

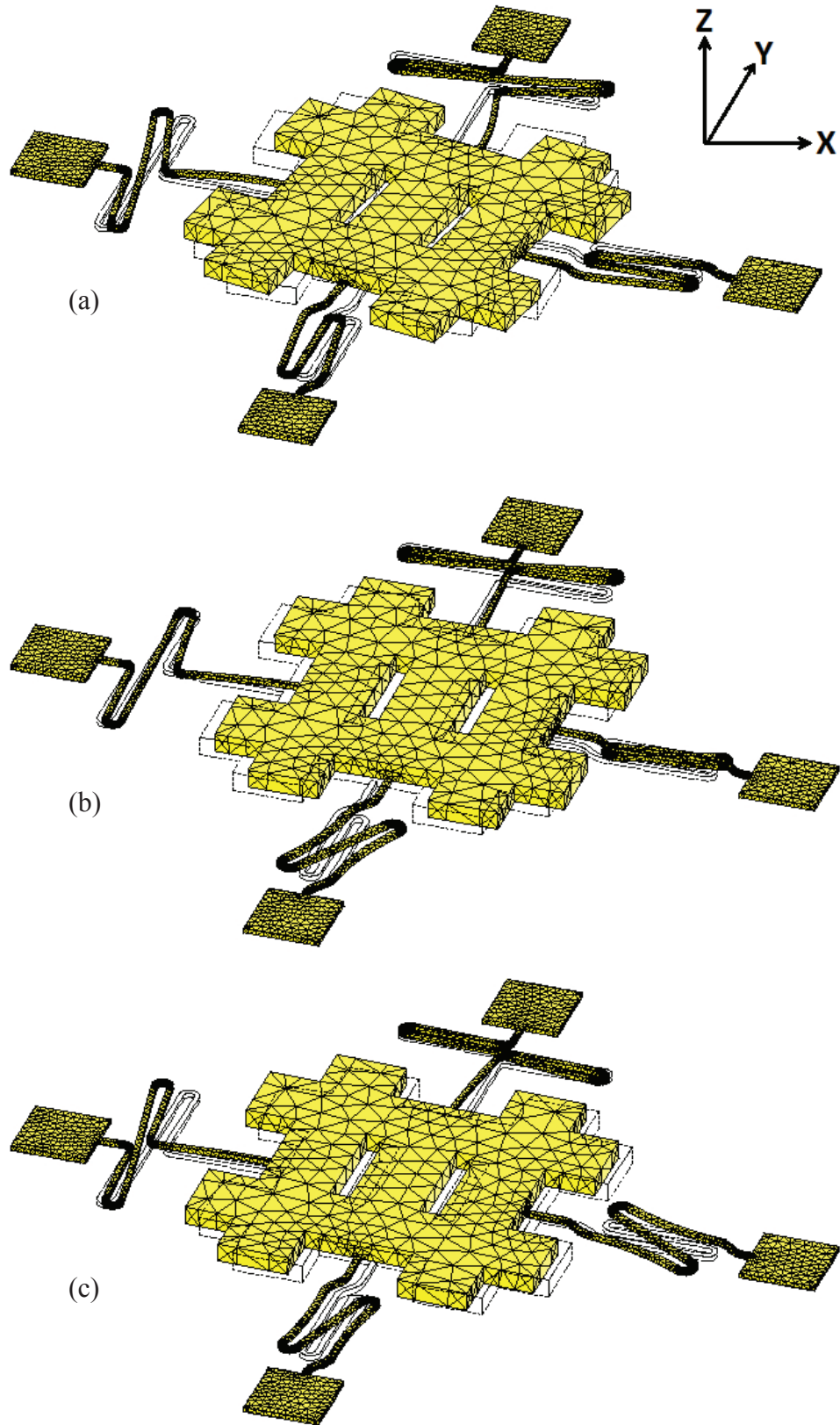
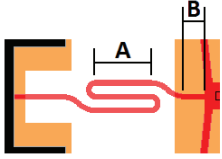
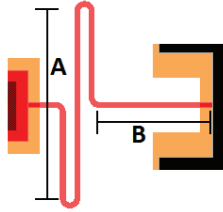






Figure 76. XY pad in-plane modes using FEM. (a) rotational vibration mode about Z axis (b) Y axis translational vibration mode (c) X axis translational vibration mode

The results of the previously described analytical model were compared to the FEM model. Table 11 shows the spring parameters used for three XY pad designs.

XY pad	Spring Lengths ( $\mu\text{m}$ )	PC Spring Image	Spring Lengths ( $\mu\text{m}$ )	S Spring Image
A: Low stiffness	Total: 174 A: 40 B: 14		Total: 242 A: 80 B: 48	
B: Medium stiffness	Total: 143 A: 25 B: 22		Total: 142 A: 30 B: 48	
C: High stiffness	Total: 114 A: 10 B: 38		Total: 142 A: 30 B: 48	

**Table 11. Basic spring parameters used for example comparison between FEM and analytical model**

These designs are compared in Table 12 showing the difference between the models for natural frequencies in two translational and one rotational mode. Note that the analytical model predicts frequencies slightly lower than the FEM model. The analytical model also assumes that the pad is symmetrical and therefore gives two lateral frequencies that are equal. The FEM uses the original L-Edit CAD files that were used when designing the MEMS components. Minute asymmetry results in a slight difference in the lateral natural frequencies for the FEM model.

The models are very symmetric and the direction of vibration in the translational modes are very close to the assigned axis of coordinates, therefore these axes are used to describe the different modes in Table 12.

XY pad	Axis	FEM (kHz)	Analytical Model (kHz)	% difference (Model – FEM) /FEM
A: Low Stiffness	X	89.6	75.2	16.1%
	Y	88.7	75.2	15.2%
	Θ	74.0	64.1	13.4%
B:Medium Stiffness	X	121.1	117.8	2.7%
	Y	120.2	117.8	2.0%
	Θ	84.4	74.8	11.4%
C: High Stiffness	X	145.1	136.1	6.2%
	Y	144.7	136.1	5.9%
	Θ	85.9	75.5	12.1%

**Table 12. Numerical comparison between FEM and analytical model based on Table 11**

Figure 77 shows a comparison of lateral motion between the FEM model and the analytical model while changing the various spring parameters. Similarly, Figure 78 shows a comparison of rotational motion between the FEM model and the analytical model while changing the various spring parameters. 45 different spring combination were compared between the two models to demonstrate a large sample range.

Chapter 8 presents experimental results for validation of the two models.

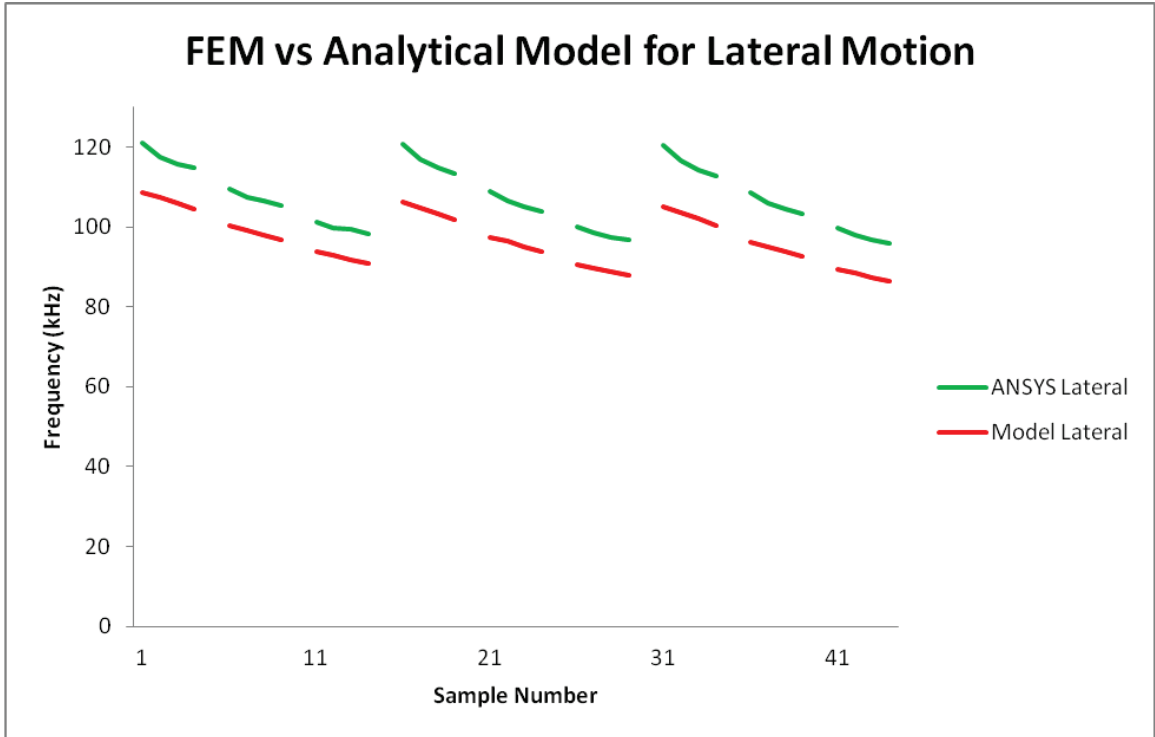


Figure 77. Comparison of lateral motion between FEM model and analytical model

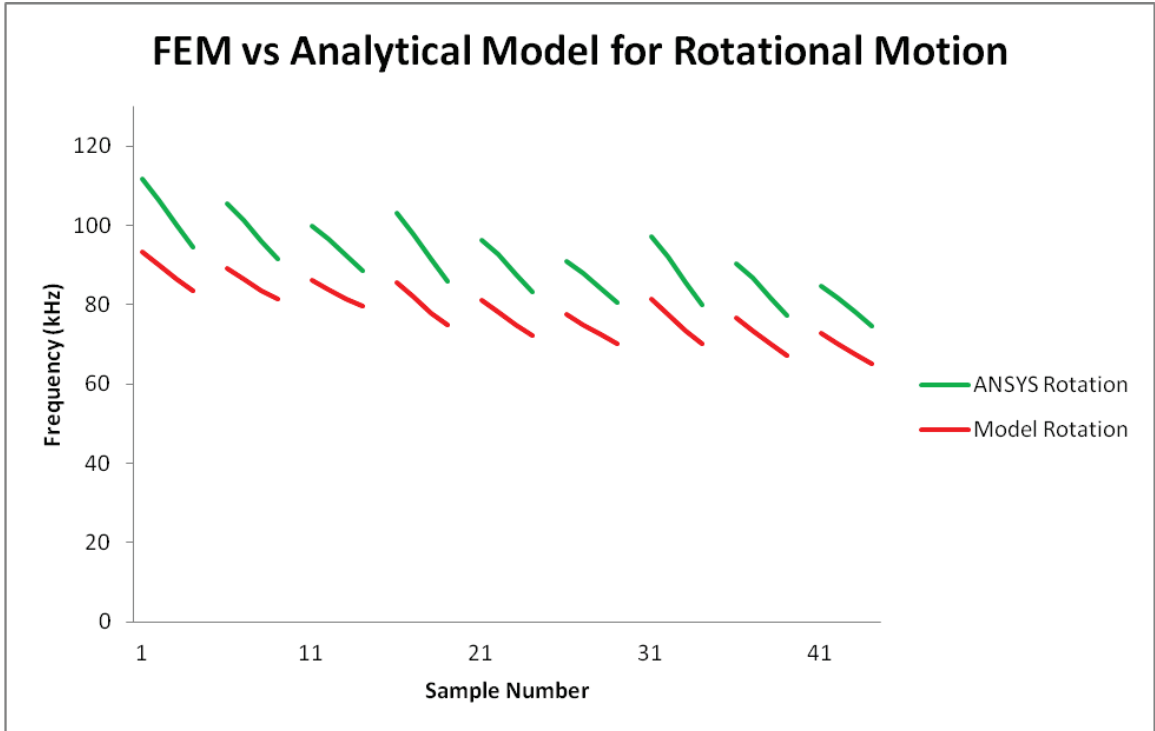


Figure 78. Comparison of rotational motion between FEM model and analytical model

## **Chapter 7.0 Chip Designs**

### **7.1 Overview**

A number of MEMS designs have been successfully manufactured using the polyMUMPs process, on a total of 12 chips (IMUDTCV1-IMUDTCV8, IMUDTPH1, IMUDTEW1, IMUDTCVX and IMUDTFR1). The design methodology ensured that each chip built on the strengths of previous chips where possible. This wasn't always possible due to the chip manufacturing schedule, where occasionally the next chip in the sequence had to be submitted for manufacture prior to receiving the last submitted chip for testing.

This Section outlines each chip, including the main focus and the lessons learned.

### 7.1.1 IMUDTCV1

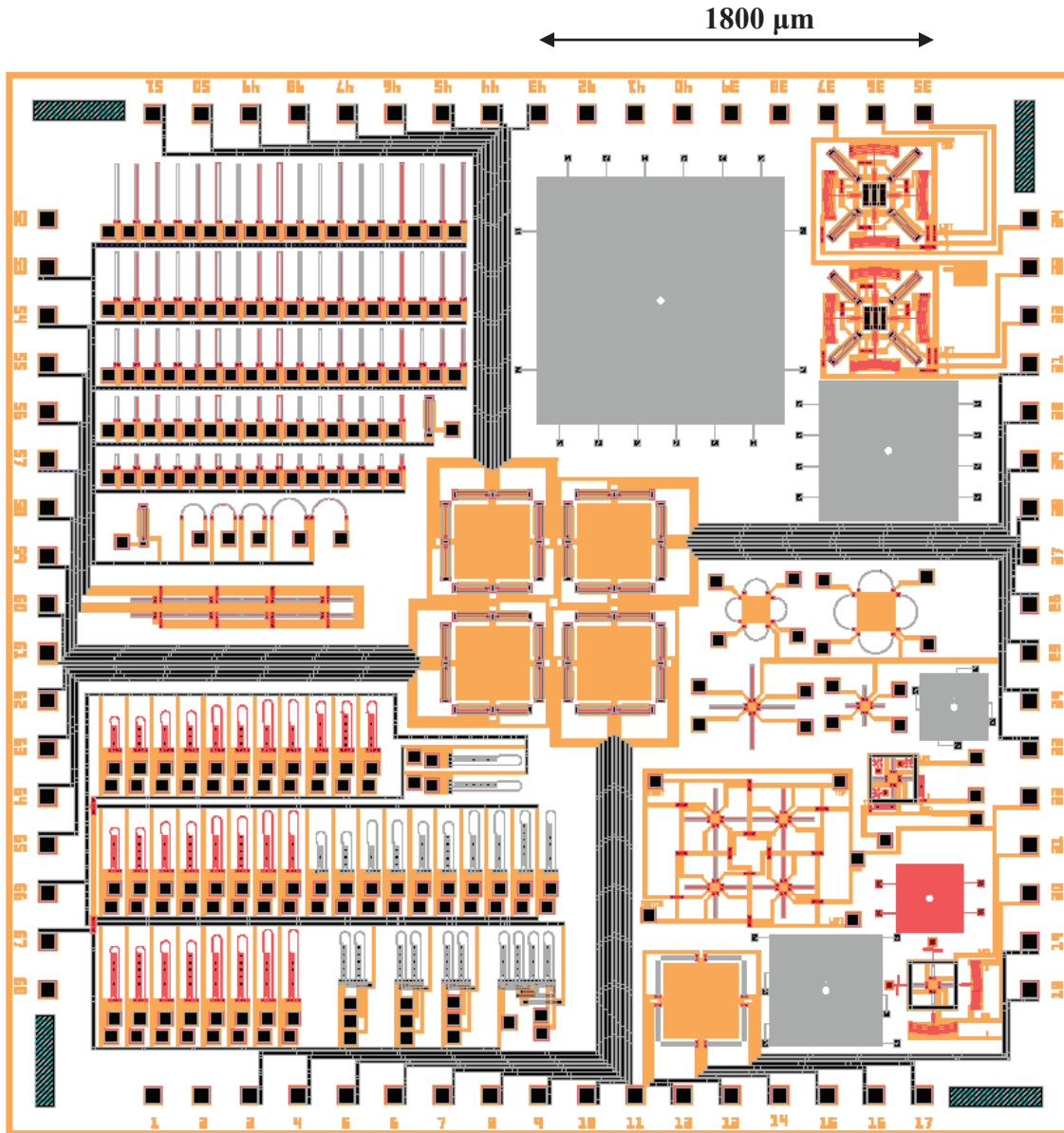


Figure 79. IMUDTCV1

The primary focus on IMUDTCV1 was the concept of Cilia and a new form of “curl” lifter. Initial designs proved incapable of generating the required vertical lift that was required for a functional cilia conveyor. However, two items showed promise, an XY sliding pad and a standard vertical lifter. From these, the focus was shifted to the lift and slide concept used on subsequent chips.



## 7.1.2 IMUDTCV2

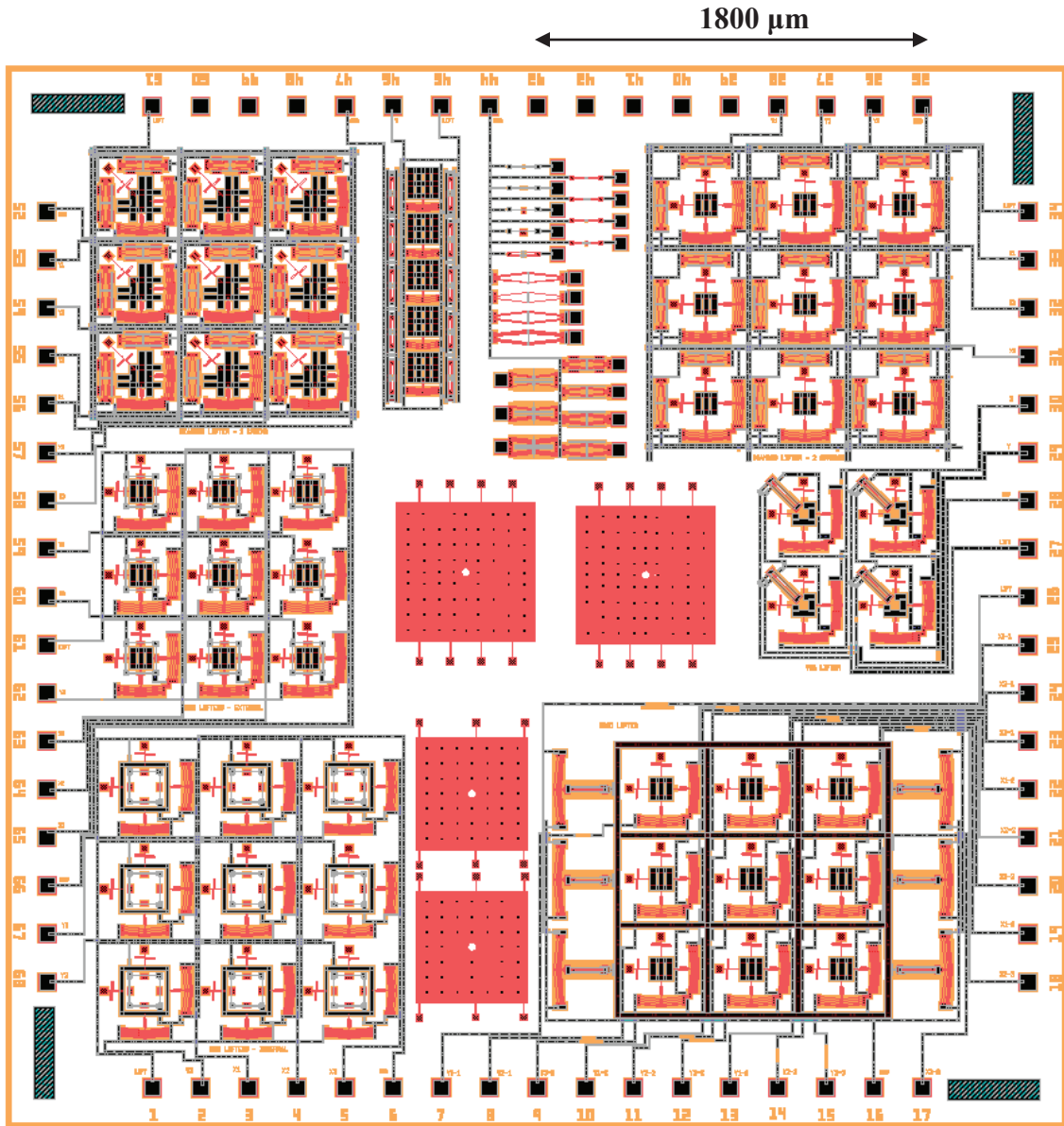


Figure 80. IMUDTCV2

IMUDTCV2 expanded on a number of lifter methods. The standard VTA had proven to have a good amount of force, but other lifters with smaller footprints and potentially greater forces were investigated. The grid lifter with opposed VTAs was introduced. More variations of the XY pads were used to refine the concept. Opposed chevron lifters and vertical bar lifters were introduced. Though both worked, they did not produce the vertical height that was desired.

### 7.1.3 IMUDTPH1

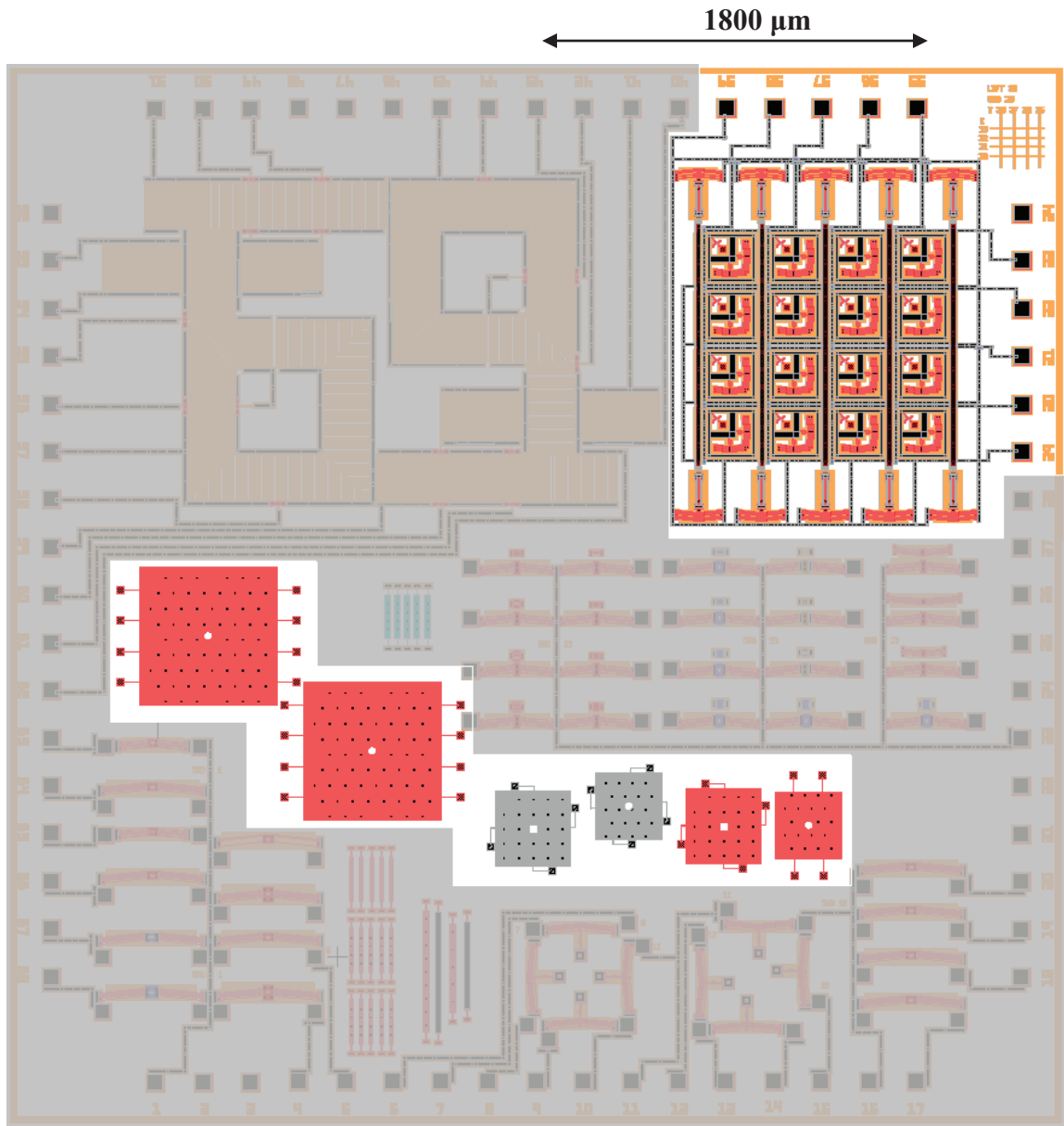


Figure 81. IMUDTPH1

A small portion of IMUDTPH1 was devoted to Lift and Slide design work. An attempt was made to minimize the size requirements of a 4x4 array by compressing the components and using singular bars instead of grids for lifting. However a wiring design flaw rendered this design non-functional due to excessive resistance. While the singular bars allowed for more straight gold wire runs through the center section of the array, this

was completely negated by a large number of the ground wires running through a set of poly0 jumpers in series.

### 7.1.4 IMUDEW1

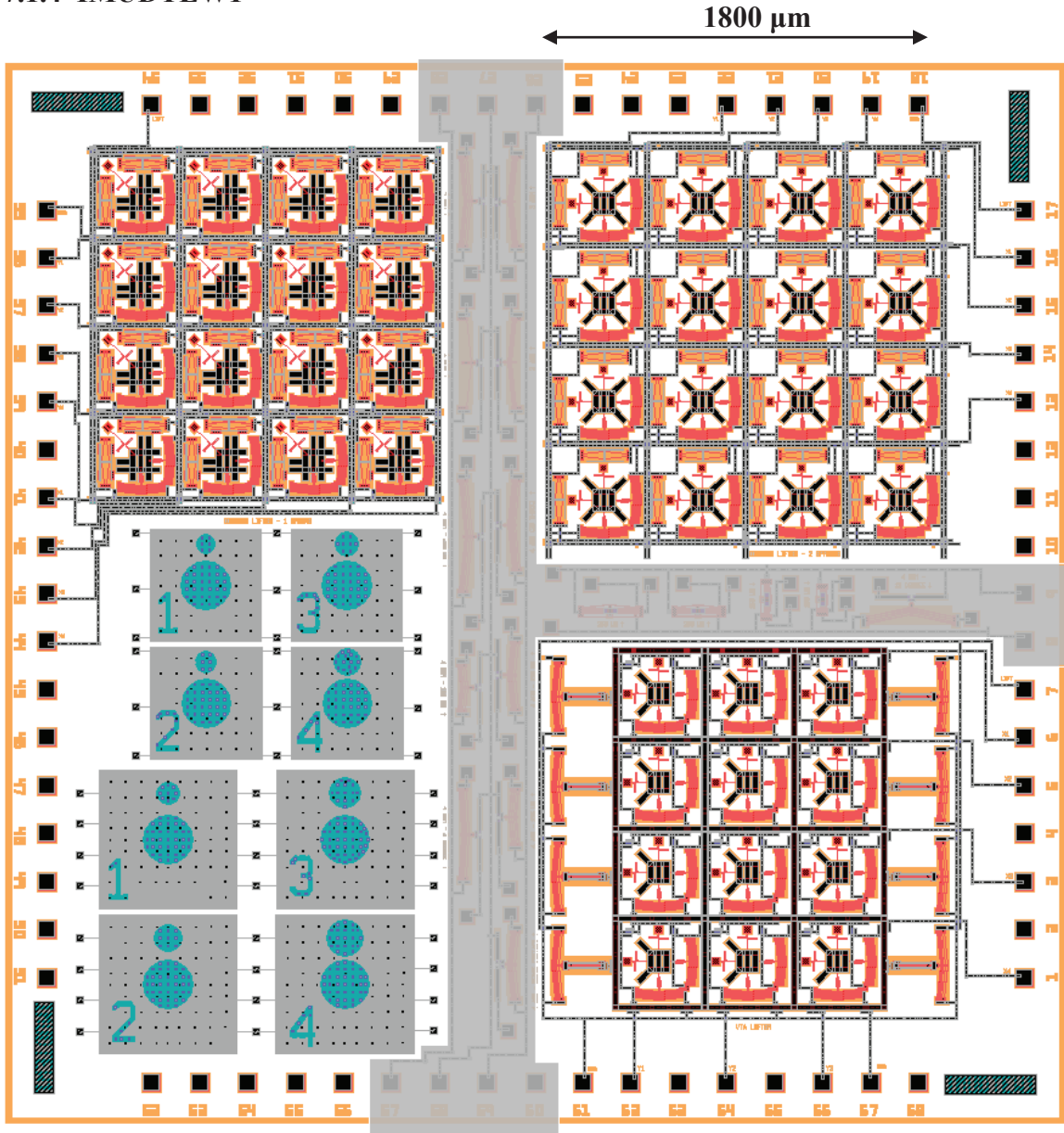


Figure 82. IMUDEW1

IMUDEW1 had been sent for manufacture prior to receiving IMUDTCV2. Opposed chevron VTAs had been primarily used based on FEM analysis. As with IMUDTCV2, testing proved that the vertical lift was not adequate to be used for this design. The grid lifter was refined slightly and proved to have sufficient force to lift polyMUMPs plates.

The XY Pads were not correctly electrically balanced and were mostly non-functional. Plates were constructed using poly2, however residual stresses resulted in curled edges and an uneven plate. The plates were also too flexible for practical usage.

### 7.1.5 IMUDTCV3

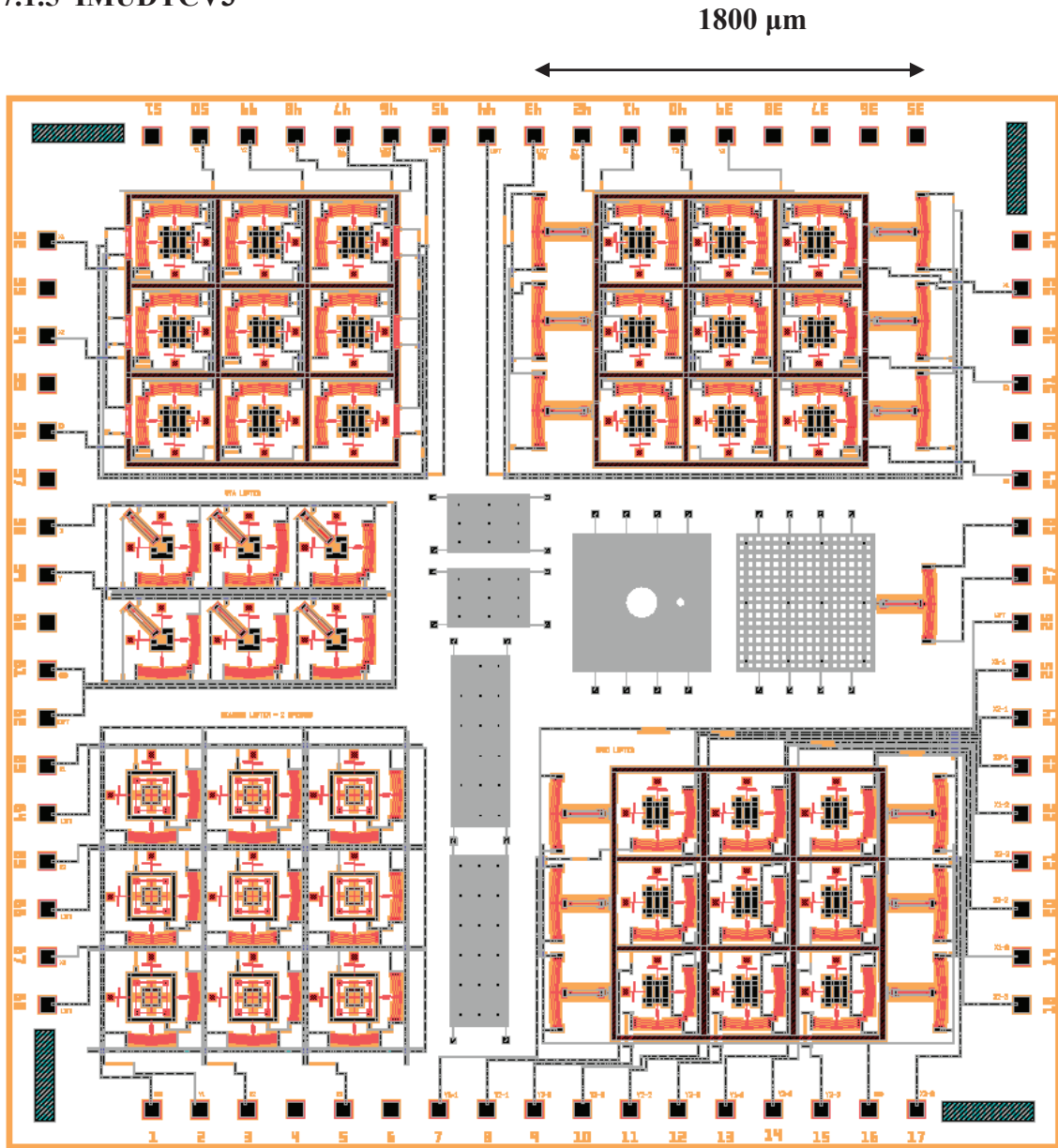


Figure 83. IMUDTCV3

A further attempt was made to manufacture operational vertical bar lifters, and also incorporate them directly into a grid. These were not successful. A grid lifter with refined XY pads did prove to be fully operational for a short time. The next two chips

were designed with variations on this particular design. However, at the time it was not clear why the design was not fully successful. This would not become clear until later testing using a micro-profiler.

### 7.1.6 IMUDTCV4 & IMUDTCV5

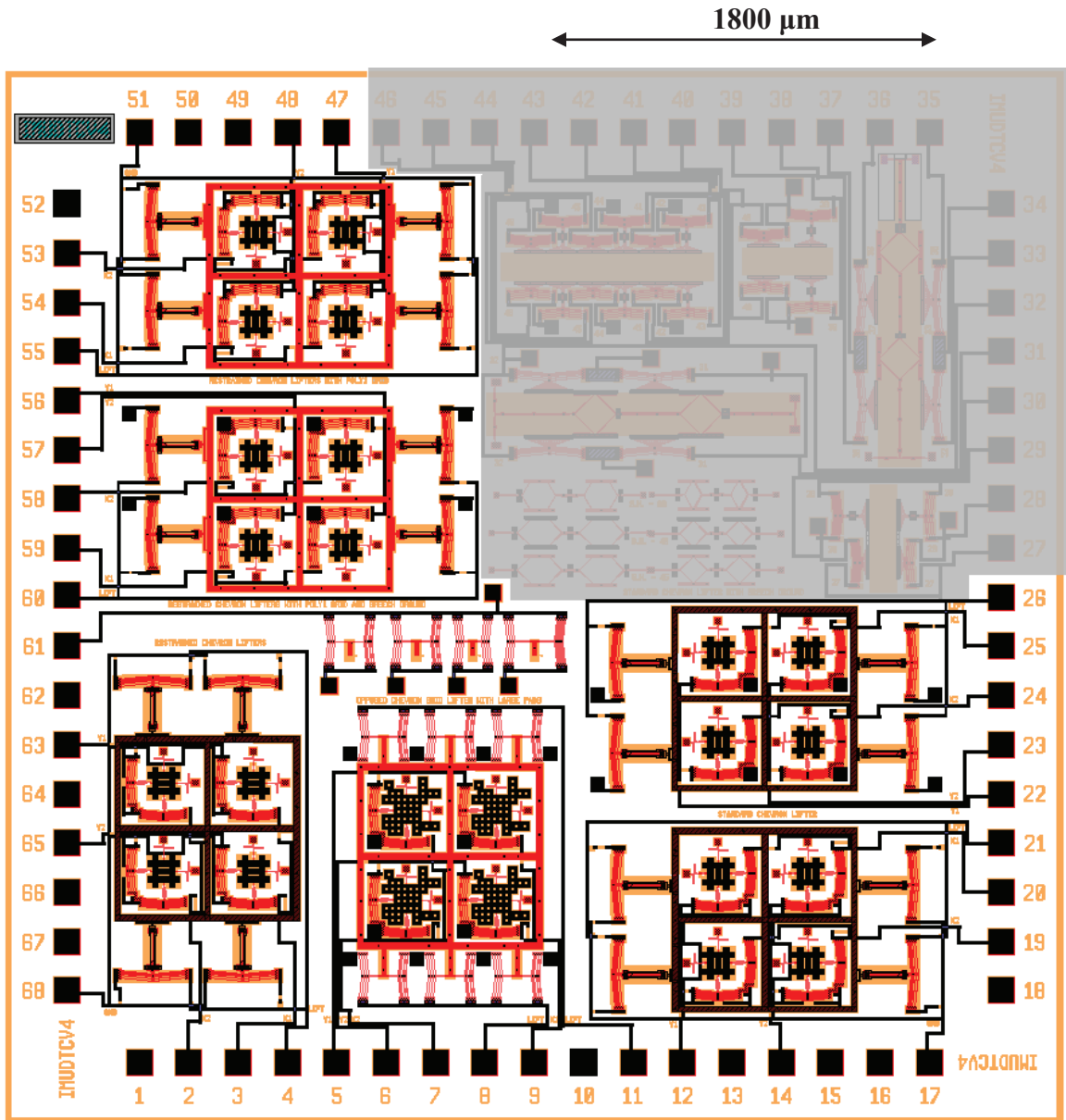


Figure 84. IMUDTCV4

IMUDTCV4 and IMUDTCV5 were both designed at the same time providing variations on pad size, grid height and introducing two new concepts. Firstly a “restrained” lifter was trialed after it was noted that the lifter chevron itself was moving out of plane. It was believed that by restraining the lift of the chevron, more grid lift would result. Unfortunately, these completely failed to operate. Secondly, breach pads were used to eliminate ground wires. These proved highly successful and significantly reduced wire resistance. Based on these characteristics, multiple combinations were trialed on the two chips.

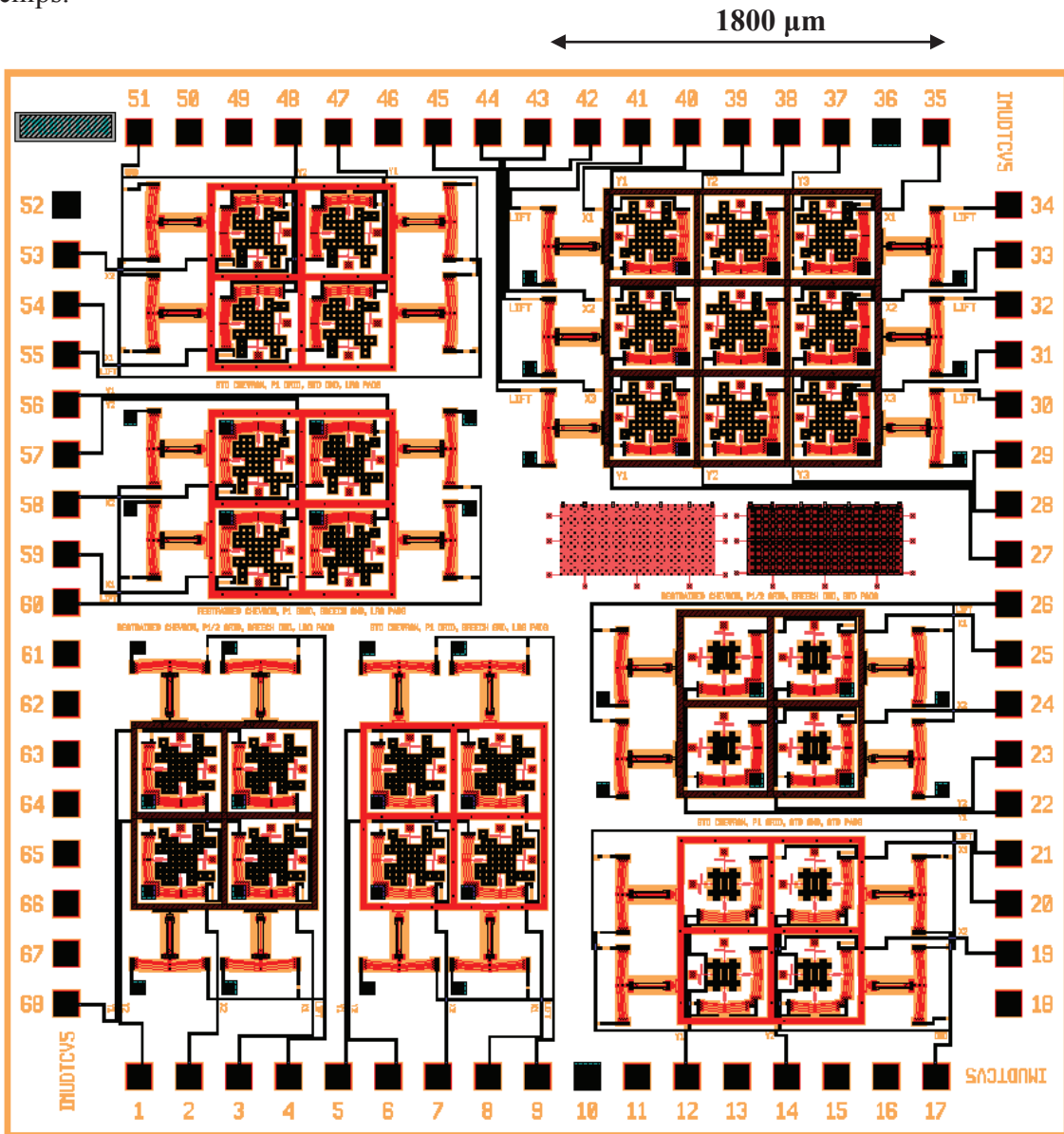
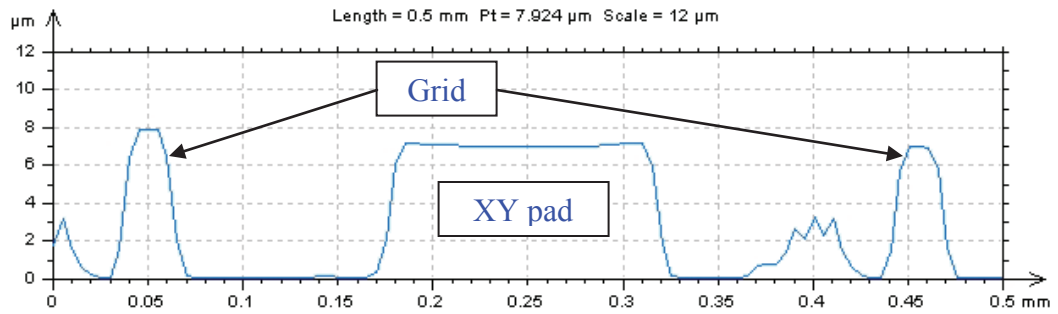


Figure 85. IMUDTCV5



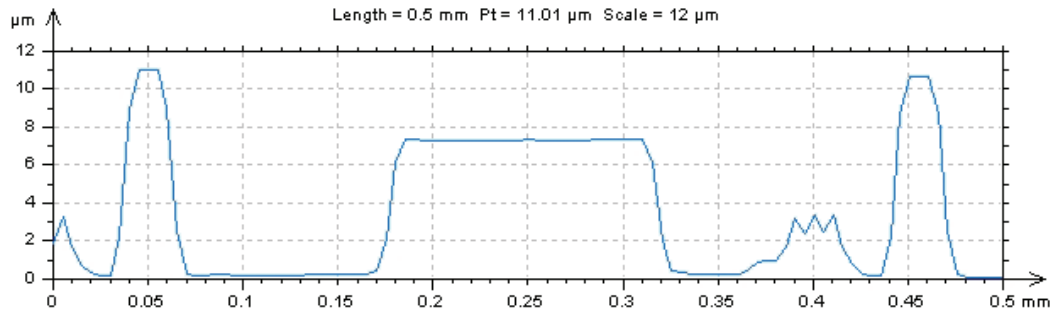
therefore the conveyor could never operate as designed. This was determined to be the reason for failure of many of the previous designs.

Figure 87 shows the relative heights of a pad and two arms of a grid lifter at 0 V. The arms should be about 1  $\mu\text{m}$  below the top surface of the pad, and yet are almost 1  $\mu\text{m}$  above the pad. This means that the platform will never be in contact with the XY pad.



**Figure 87. Micro-profiler image of single XY pad on IMUDTCV6. Grid lifter height at 0 V is already above the pad height. Scale = 12  $\mu\text{m}$**

Figure 88 shows that when the grid lifter is activated, the grid is well clear of the top surface of the pad.



**Figure 88. Micro-profiler image of single XY pad on IMUDTCV6. The grid lifter is well above the pad height at 12 V, as would be expected. Scale = 12  $\mu\text{m}$**

The 4x4 grid with 16 lifters was shown to generate more than adequate force to overcome any stiction and was capable of lifting larger objects such as salt crystals. Single element



XY pads with lifters were added to this chip for use in testing and comparing the model to actual resonance results.

### 7.1.8 IMUDTCV7 & IMUDTCV8

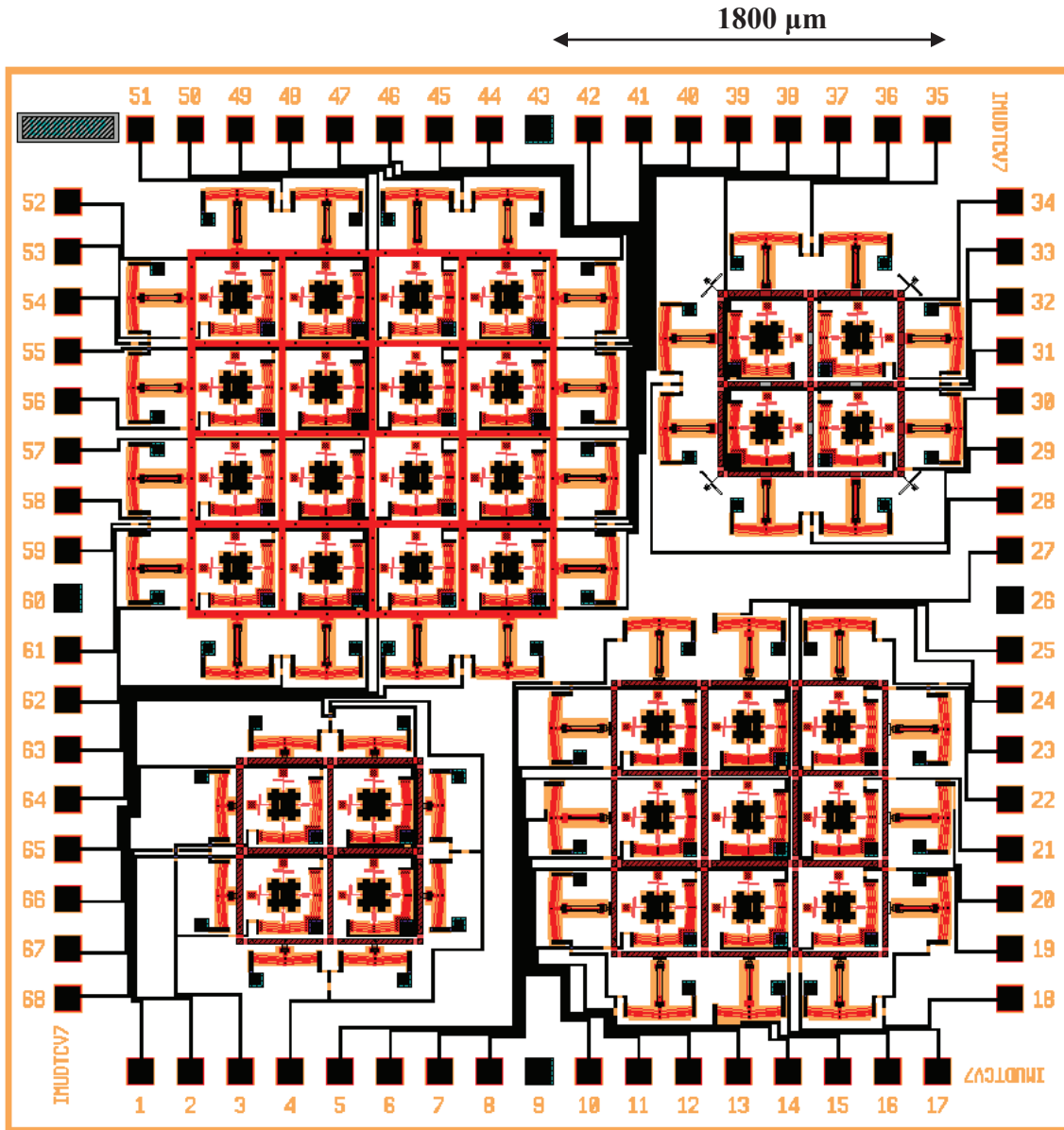


Figure 89. IMUDTCV7

IMUDTCV7 and IMUDTCV8 were designed together providing multiple methods to overcome the grid height issues discovered with the micro-profiler. Variations include use of a poly1 grid and modified lifters that reduce or counter the residual stress. Additionally, one design was included with reversed lifters that could be used to actively

push the grid down to the substrate. 2x2, 3x3 and 4x4 arrays were designed due to space constraints. A design flaw affected a number of double height structures resulting in grids being etched completely through the joints. These grids were non-functional as they literally fell into pieces.

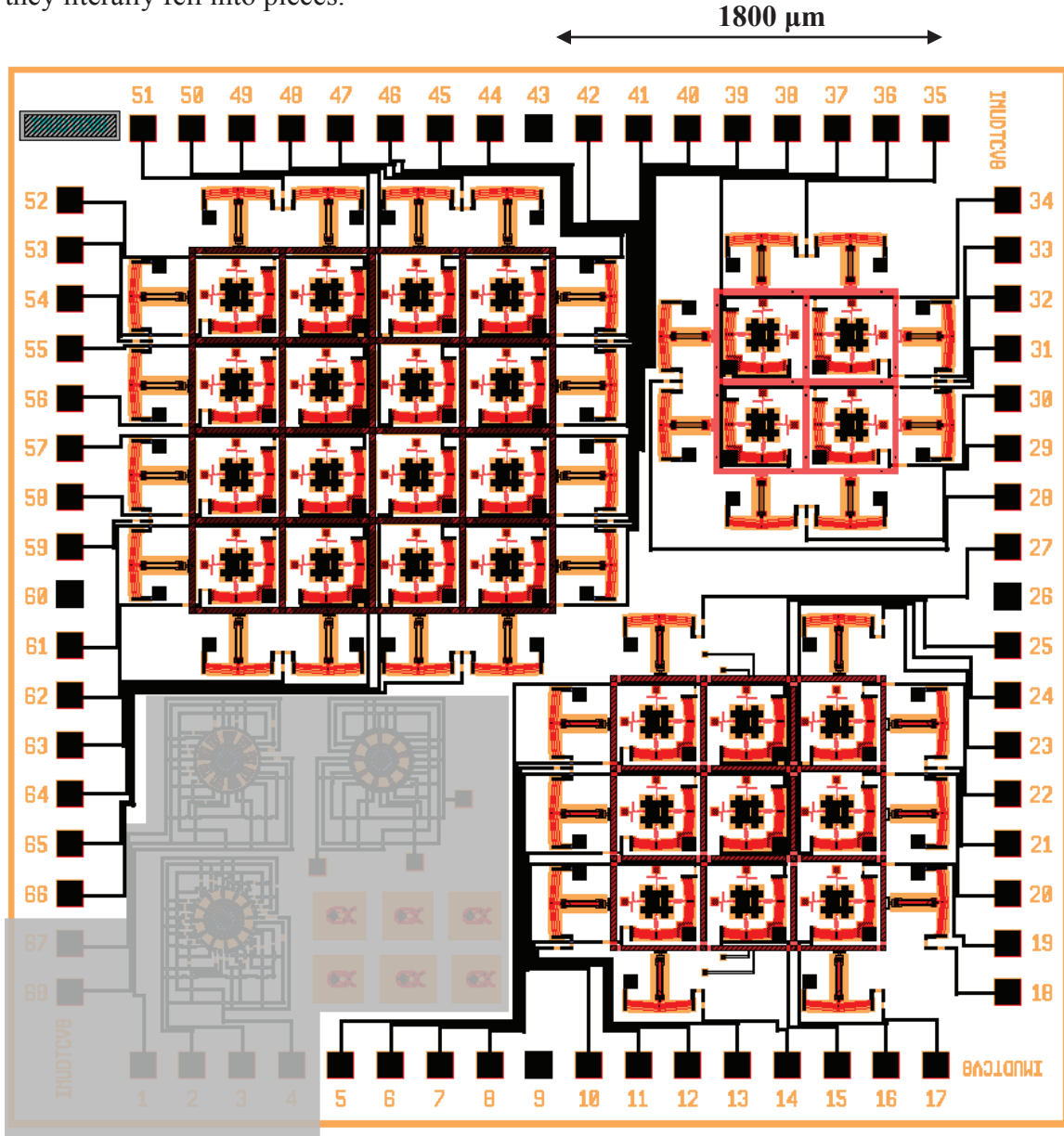


Figure 90. IMUDTCV8

A number of manufacturing flaws with these two chips resulted in almost no functional arrays. The exact nature of the flaws were never fully identified, however many features that had been manufactured successfully on previous chips did not respond as expected on these chips. Some of the sample chips experienced some sort of galvanic corrosion,

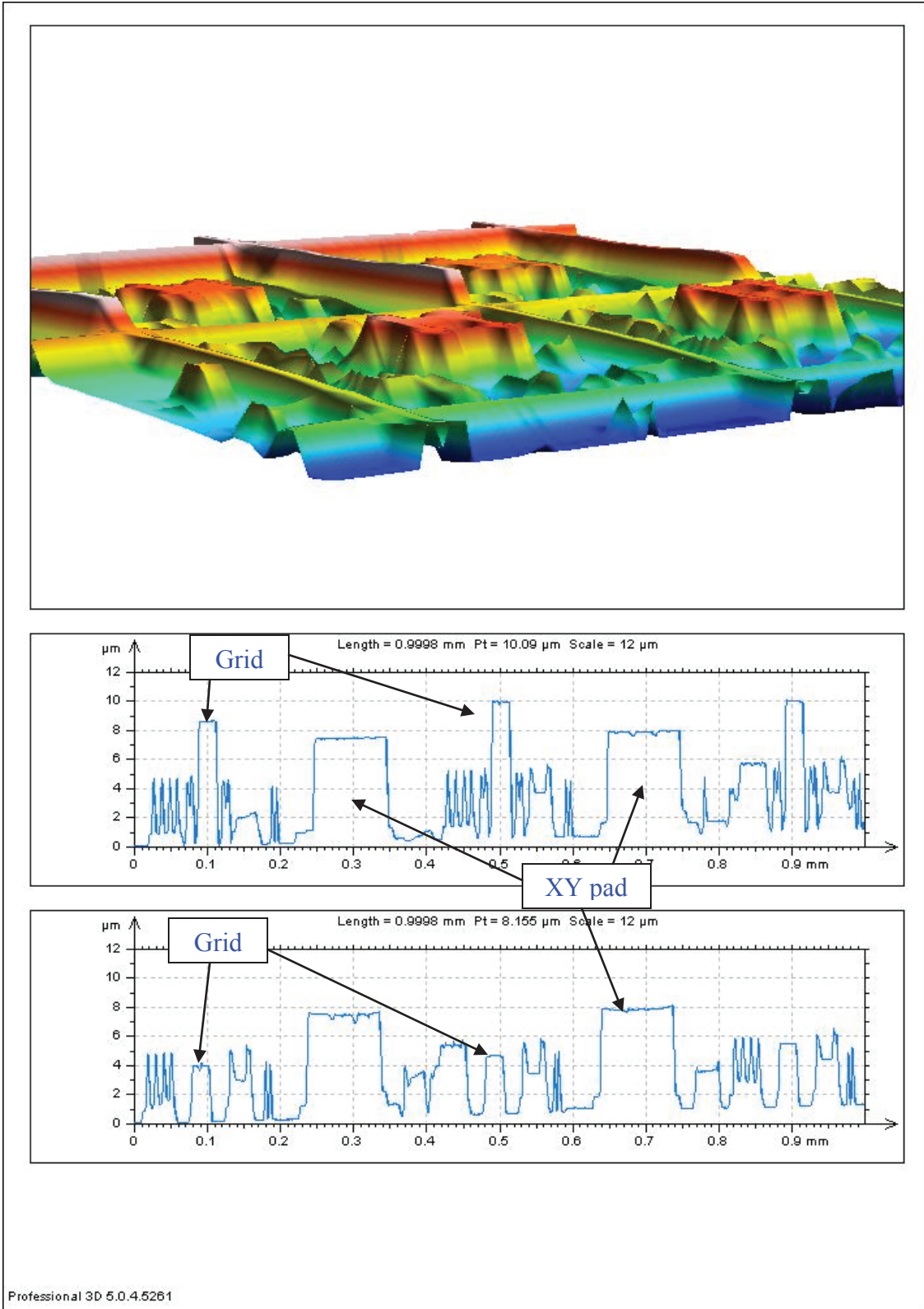
others had multiple broken structures and occasionally the poly0 seemed to have different electrical properties. The differing properties of the poly0 also resulted in a different visual appearance, the poly0 being darker than normal and having an infinite resistance. Despite the flaws in manufacturing, several 4x4 arrays on IMUDTCV7 were functional and tested. The testing again had negative results and revealed another interesting phenomenon when profiled.

Figure 91 shows a composite 3d image of a portion of the 4x4 array on IMUDTCV7 consisting of both the off (0 V) position and the on (9 V) position. Profile lines taken across the grid and pads in each position clearly show that the grid is well below the pad in the off position (2.5-3.5  $\mu\text{m}$ ) and well above the pad in the on position (1.5-2.5  $\mu\text{m}$ ). This would indicate that the conveyor should function correctly.

Figure 92 and Figure 93 show a profile and a 3d view, respectively, of a 10  $\mu\text{m}$  thick SOI plate on the 4x4 array. The grid is in the on (9 V) position and the SOI plate has been raised approximately 2.5-3.0  $\mu\text{m}$  above the pads, which is consistent with Figure 91 and again indicates that the conveyor should work properly.

The reason for the failure of the conveyor is evident in Figure 94 and Figure 95, the profile and 3d view, respectively, of the grid in the off (0 V) position. Figure 91 had indicated that with no plate, the grid should drop back down to a height well below the pads. However, with a plate in place, the grid drops down to a height in line with the pads. This is indicative of stiction between the plate and the grid. Since the grid and pad both are in contact with the platform, the resulting motion is unpredictable or non-existent.

The concept of both friction and stiction at the microscale is quite complex and is discussed in detail in Appendix A.



**Figure 91. Portion of 4x4 array on IMUDTCV7 profiled. The 3d image is a composite image showing both the off (0 V) position and the on (9 V) position. Scale = 12  $\mu\text{m}$**

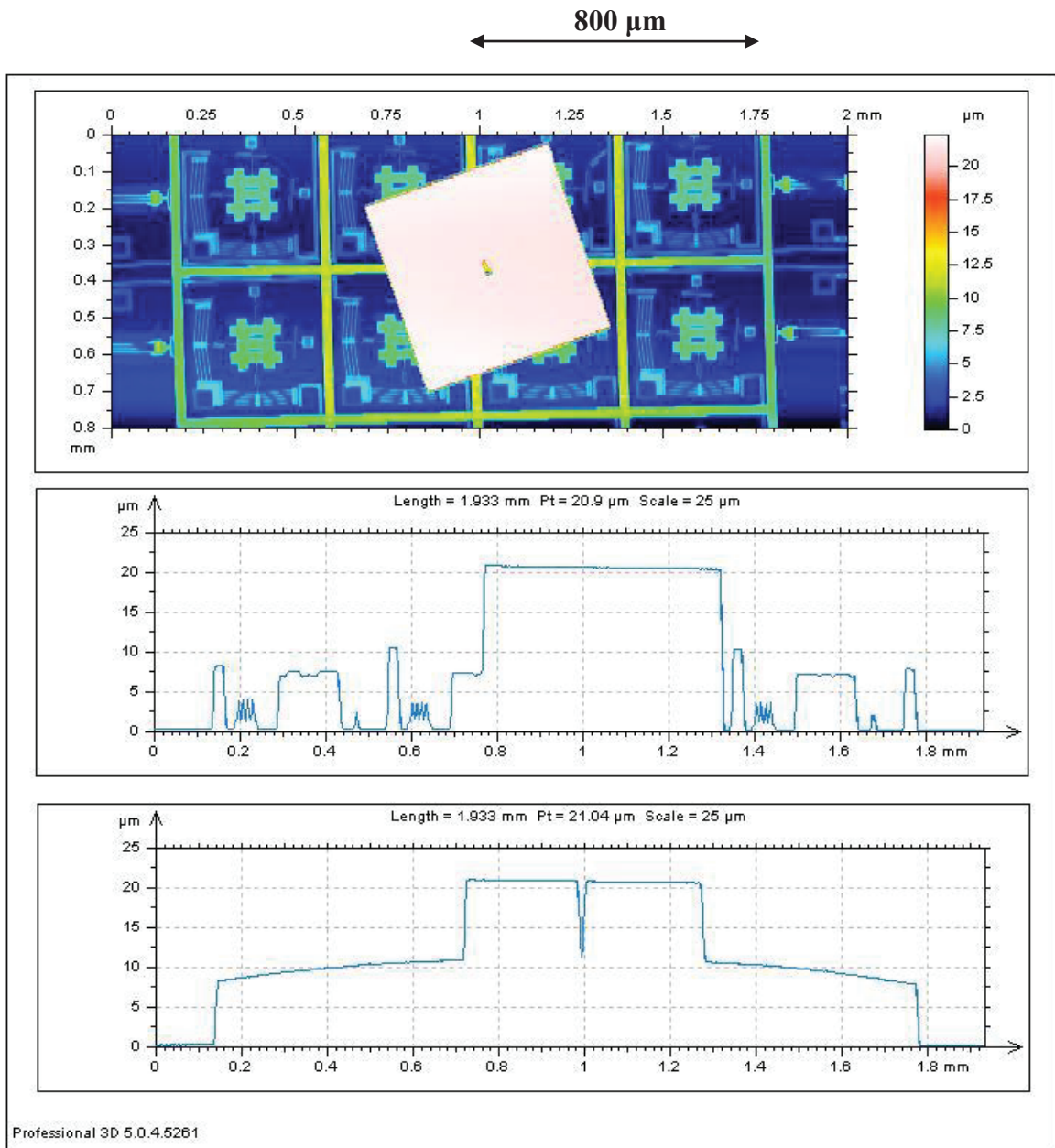


**Figure 92. Profile views of SOI plate sitting on 4x4 array on IMUDTCV7 in the on (9 V) position. Scale = 25  $\mu\text{m}$**

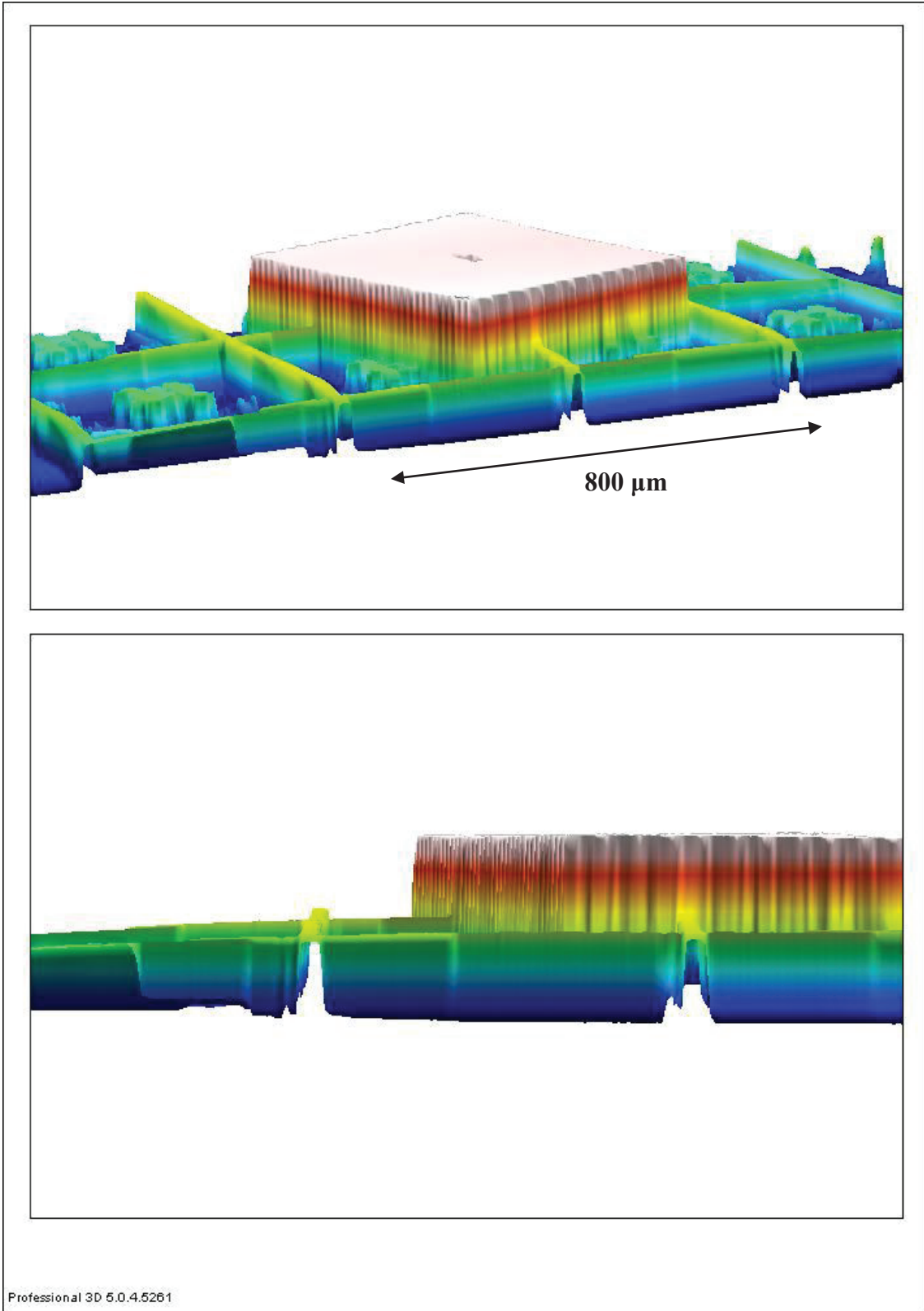
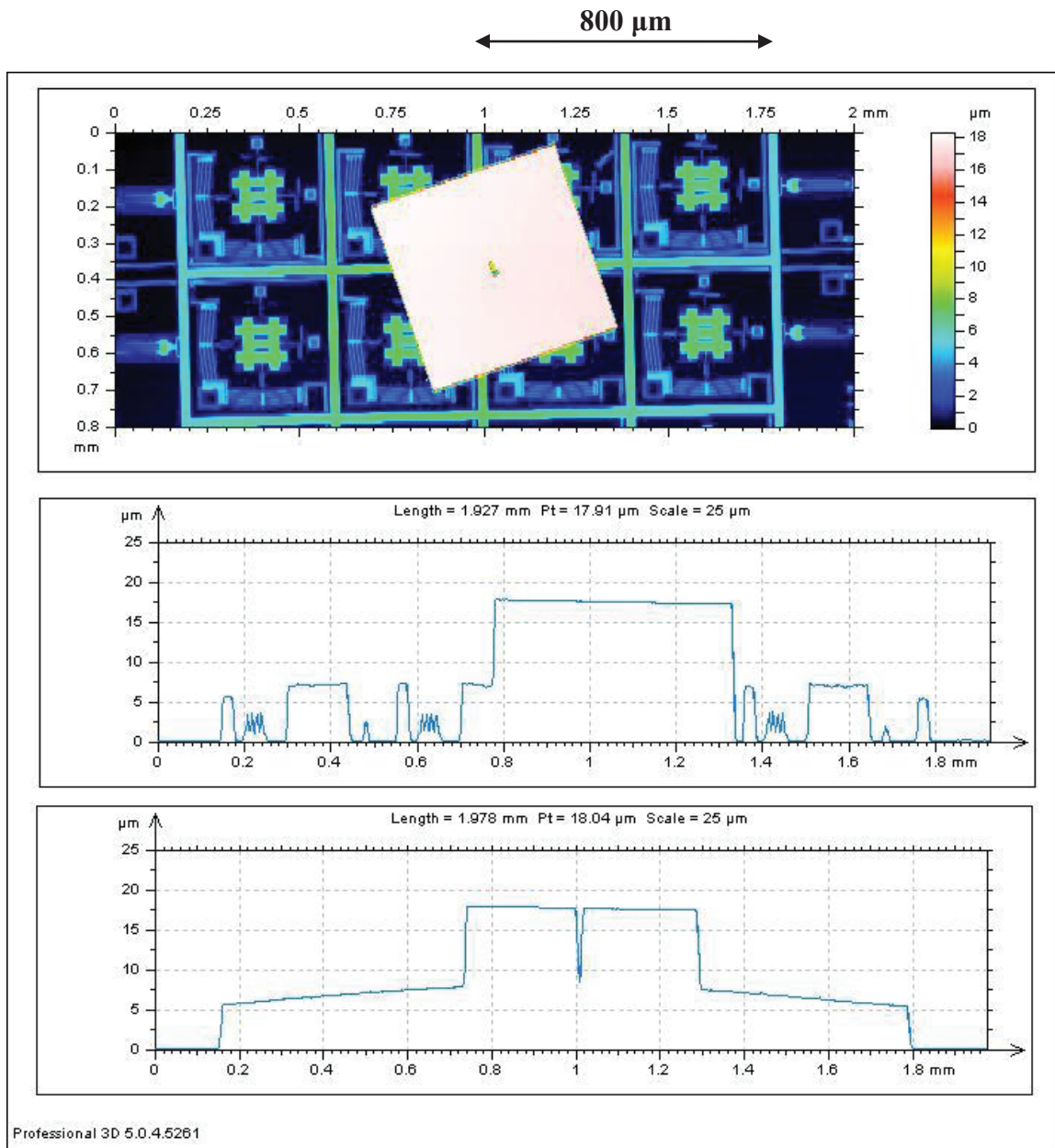


Figure 93. 3d view of SOI plate sitting on 4x4 array on IMUDTCV7 in the on (9 V) position



**Figure 94. Profile views of SOI plate sitting on 4x4 array on IMUDTCV7 in the off (0 V) position.  
Scale = 25  $\mu\text{m}$**

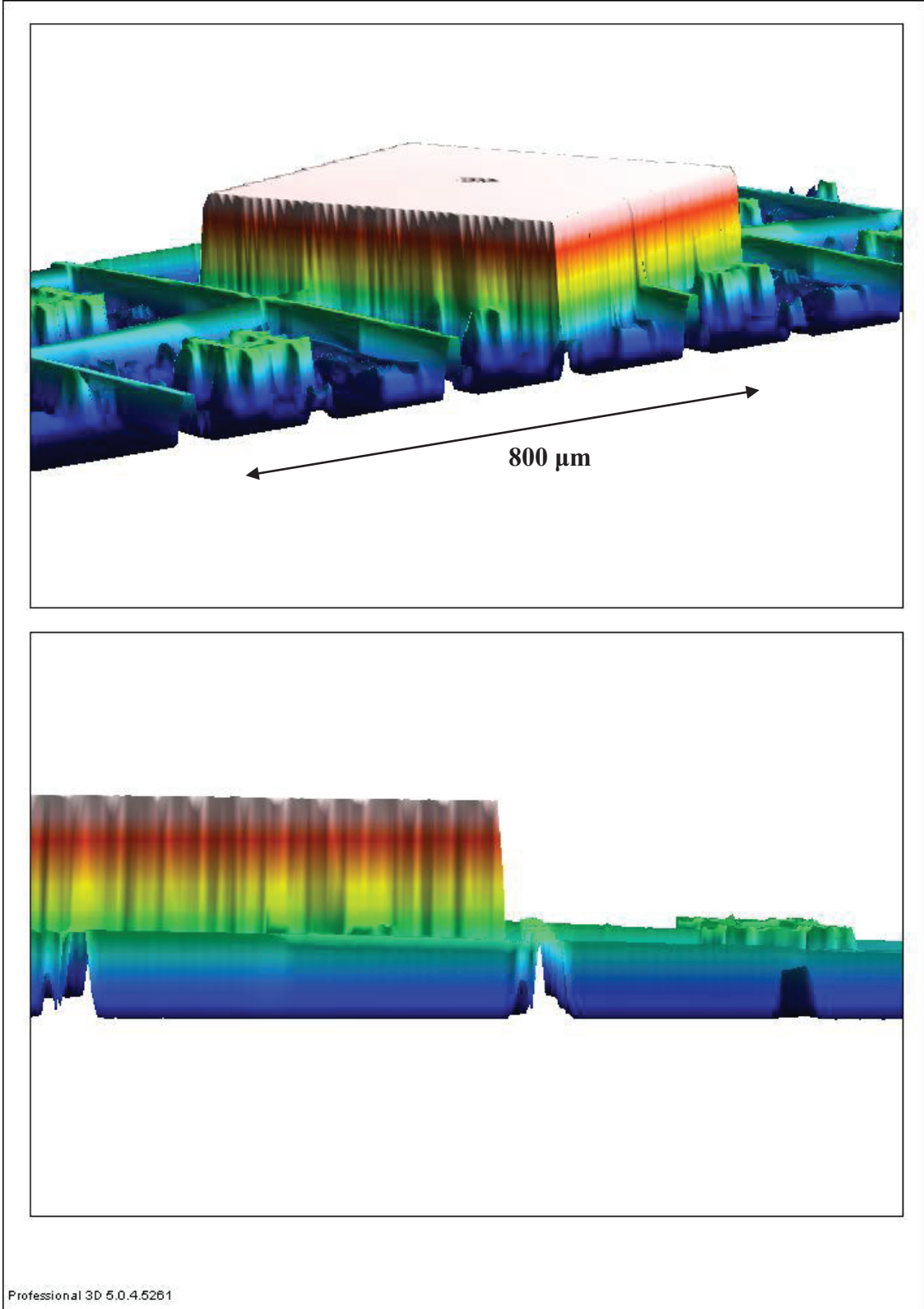


Figure 95. 3d view of SOI plate sitting on 4x4 array on IMUDTCV7 in the off (0 V) position.



### 7.1.9 IMUDTCVX

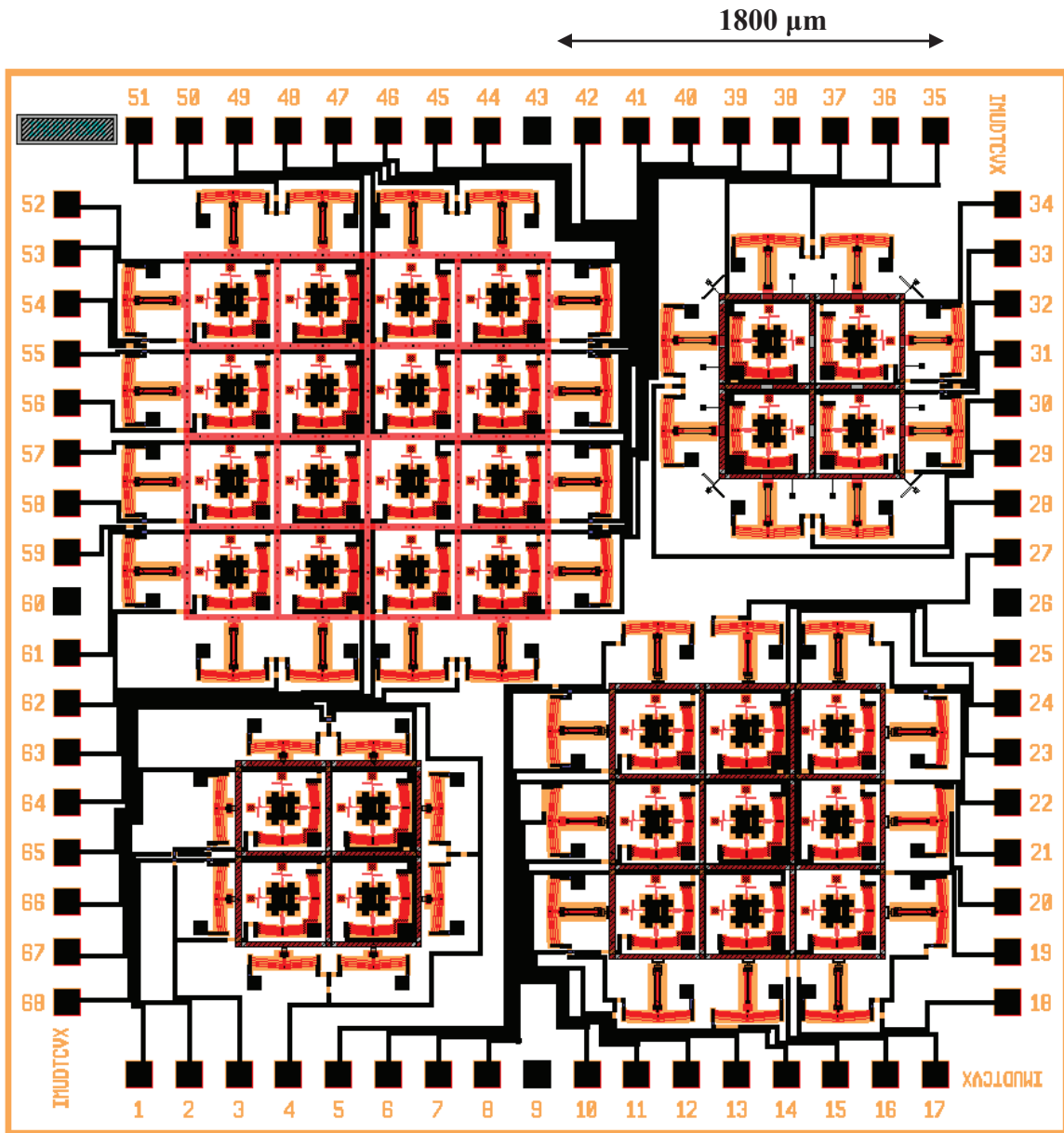


Figure 96. IMUDTCVX

IMUDTCVX is a rebuild of IMUDTCV7 as a result of the major manufacturing flaws from the previous chip run. Standard wires were replaced with a wire 4 μm wider. This was as a result of failed wire runs on the previous chip. These previously used narrow wires had never been a problem, but as IMUDTCVX was a rebuild, it was felt that all efforts should be used to eliminate the same problems that had plagued the last chips. The opportunity was also taken to modify the designs slightly to compensate for design

issues without changing the spirit of the original IMUDTCV7 design. Double height structures were modified to account for the etching effects that result from poly1-poly2-via extending right to the edge of poly2. Reverse dimples were created on the 4x4 array in an effort to eliminate stiction between the grid and the platforms. These bumps were created by removing the full poly0 plates under the grids and using small squares of poly instead. The effect of multiple poly0 squares is a 0.5  $\mu\text{m}$  high bump, which is just enough to separate the flat plates in a similar fashion to the regular dimples reducing stiction between the poly1 and the substrate. The modifications proved to be effective during testing. The reverse dimples eliminated, or at least reduced, the problematic stiction effects.

The 2x2 array proved to be the most successful design on IMUDTCVX. This was largely a result of the shortened lifters that stiffened the grid significantly. The 4x4 array also proved to be somewhat successful though was not as reliable as the 2x2 due to the highly flexible grid.

### 7.1.10 IMUDTFR1

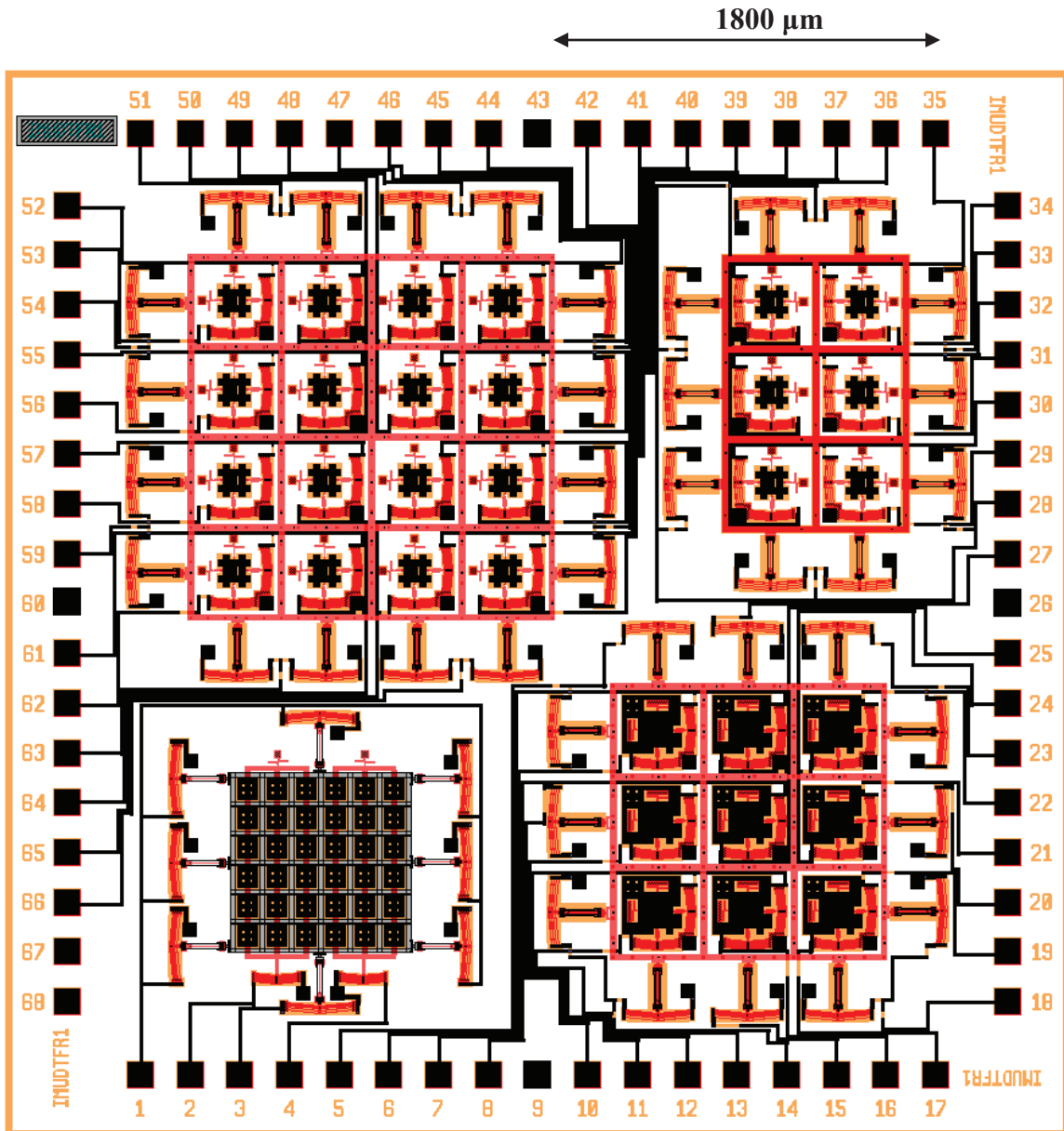


Figure 97. IMUDTCV7

IMUDTFR1 was submitted at the same time as IMUDTCVX. The chip design returned to the previously used small wires. This was a risky move, but as the smaller wires had always been successful up until IMUDTCV7, it was believed that they should work on normal runs. The smaller wires were necessary to minimize the space requirements of components. There were four designs on the IMUDTFR1. The 4x4 array was identical to the 4x4 on IMUDTCVX, using a poly1 grid with poly0 squares to generate small

bumps to eliminate stiction. This grid configuration was used on all other arrays on the chip. The 2x3 array included stiff lifter to grid connection points, in an effort to compensate for residual stress curvature of the grid. The 3x3 array used extremely large pads to try to improve the frictional contact between the pads and the platform.

The final design for the chip moved away from the standard arrays that had been tested so far. It consisted of multiple tiny pads joined in two groups that could move with one DOF. The grid lifter was constructed using poly2 draped over the poly1 pad connections. The chevrons for the pad motion were kept external to the pad array. As each pad grouping only has one DOF, the resultant platform motion is restricted to two DOF, parallel with the chevron motion and rotation when the pad groups move out of phase.

All designs on IMUDTFR1 proved to be functional, with the 3x3 yielding the best, and most consistent results. The 3x3 benefited from the large frictional area of the enlarged XY pads, though some rotation of the pads was noted from the dimple to substrate contact.

## 7.2 Comparison of Chip Designs

A number of chip generations have been presented. Table 13 summarizes the evolution of designs to illustrate the improvements realized from one generation to the next.

Chip Name	Description of improvement	Reason for improvement
IMUDTCV1	<ul style="list-style-type: none"> <li>• Initial XY pad design</li> <li>• Standard vertical lifter</li> </ul>	
IMUDTCV2	<ul style="list-style-type: none"> <li>• Switched to chevron lifter</li> <li>• Created first 3x3 grid</li> </ul>	<ul style="list-style-type: none"> <li>• Improve lift height and force</li> <li>• Maximize concentration of XY pads</li> </ul>
IMUDTPH1	<ul style="list-style-type: none"> <li>• Compressed XY pads</li> <li>• Lift bars instead of grid</li> </ul>	<ul style="list-style-type: none"> <li>• Minimize space requirements</li> <li>• Allow for wiring without jumpers</li> </ul>
IMUDTEW1	<ul style="list-style-type: none"> <li>• XY pad variations</li> </ul>	<ul style="list-style-type: none"> <li>• Improve frictional contact</li> </ul>
IMUDTCV3	<ul style="list-style-type: none"> <li>• Improved wiring</li> </ul>	<ul style="list-style-type: none"> <li>• Balanced resistance</li> </ul>
IMUDTCV4	<ul style="list-style-type: none"> <li>• Breech pads for ground</li> <li>• Restrained lifters</li> </ul>	<ul style="list-style-type: none"> <li>• Reduce resistance and chevron crosstalk</li> <li>• Improve lift height and force</li> </ul>
IMUDTCV5	<ul style="list-style-type: none"> <li>• Poly1 grids</li> <li>• Enlarged XY pads</li> </ul>	<ul style="list-style-type: none"> <li>• Improve clearance to platform</li> <li>• Maximize frictional contact</li> </ul>
IMUDTCV6	<ul style="list-style-type: none"> <li>• 4x4 grid</li> <li>• Fully balanced components</li> </ul>	<ul style="list-style-type: none"> <li>• Maximize area</li> <li>• Consistent voltages</li> </ul>
IMUDTCV7	<ul style="list-style-type: none"> <li>• Height reduction for grid</li> </ul>	<ul style="list-style-type: none"> <li>• Stiction reduction</li> </ul>
IMUDTCV8	<ul style="list-style-type: none"> <li>• Stiffer lifter connections</li> </ul>	<ul style="list-style-type: none"> <li>• Improve grid lift, counter stiction</li> </ul>
IMUDTCVX	<ul style="list-style-type: none"> <li>• Height reduction for grid</li> </ul>	<ul style="list-style-type: none"> <li>• Stiction reduction</li> </ul>
IMUDTFR1	<ul style="list-style-type: none"> <li>• Reverse dimples on grid</li> </ul>	<ul style="list-style-type: none"> <li>• Stiction reduction</li> </ul>

Table 13. Comparison of chip designs

## **7.3 Final Design**

The lessons learned from each chip were used to move towards the optimum conveyor design. The key issues (stiction, grid stiffness, height differential and wire resistance) were addressed resulting in a design that lends itself to well to expansion and larger arrays.

### **7.3.1 Grid Lifter and Pads**

The final design was realized as a combination of features on both IMUDTCVX and IMUDTFR1. The essential elements of the final design include a grid constructed using poly1, with poly0 bumps spaced around the grid. The pads are constructed using all available structural layers to maximize the height. The surface area of the pads needs to be substantial enough to create a good frictional surface, but too large a pad tends to rotate as dimples drag on the substrate. A compromise is required for optimum results. It is important that lifters are located all around the grid to ensure sufficient force is available to lift the grid and platform. Consideration must also be given to the mass of the objects being carried. The short lifters on the 2x2 array of IMUDTCVX proved to offer the best results.

### **7.3.2 Wiring Resistance Considerations**

Wiring resistance was consistently an issue that, if not properly considered, resulted in failed designs. During early chips, no calculations were done to ensure balanced resistance. This frequently ended with XY pads that responded quite differently dependent on their position within the array. Careful analysis of the individual current requirements in lines to each chevron allowed the arrays to be properly balanced. The greatest issue was the use of poly0 under the grid. Resistance of wiring runs was generally negligible, except when these “jumpers” were required. In order to balance wires, the highest resistance run would be taken as the reference, and all other runs would then be given “poly0 balance resistors” to compensate; the larger the array, the greater

the resistance requirements. Complete balancing between lifters and XY pads was not as big a concern, since there was no requirement for the XY pad chevrons to have an identical displacement as the lifters, just as long as all lifters were balanced to each other and all XY pads were balanced to each other. Care was still observed to try to ensure that maximum chevron displacements could be reached with minimum voltages.

### **7.3.3 Substrate grounding**

Substrate grounding was introduced during IMUDTCV4. This proved to be highly successful for reducing the overall resistance of wiring runs and balancing all components. The substrate grounding utilizes all available etching processes and layers to breach the 0.6  $\mu\text{m}$  thick insulating nitride to access the resistance substrate before building up a conductive pad. By using the highly conductive silicon substrate, a large reduction in the number of wires is achieved, contributing to the ease of balancing the components and a reduction in the overall space requirements and in some cases reducing the number of bonding pads required.

## Chapter 8.0 In-Plane Dynamic Measurements

This Chapter contains a reproduction of the paper “Fourier analysis of blurred images for the measurement of the in-plane dynamics of MEMS”, published in the Journal of Micromechanics and Microengineering [42]. [http://m.iopscience.iop.org/0960-1317/22/3/035019?v\\_showaffiliations=yes](http://m.iopscience.iop.org/0960-1317/22/3/035019?v_showaffiliations=yes) The Assignment of Copyright is located in Appendix C.

### 8.1 Introduction

This chapter investigates the dynamic response of the XY pads and compares the theoretical results of both FEM and the analytical model to experimental results. The dynamic response of the XY pads is very fast with the mechanical resonant frequencies occurring at high frequency (10's to 100's of kHz). Because of the size and frequency constraints, non-contact measurement techniques must be used to measure the dynamics. A number of different optical non-contact experimental techniques exist to measure dynamic response of MEMS structures. Bosseboeuf [43] reviewed a wide range of different techniques for the characterization of dynamic behaviour of micro devices. Some examples of dynamic measurement systems include interferometric systems, laser Doppler vibrometry and laser deflection systems. Such systems are commonly used to measure out-of-plane motion as they have very high out-of-plane resolution (~nm). Such specialized equipment can be expensive and is not necessarily found in all laboratories. As noted in [43] there exist a number of options for measuring out-of-plane motion, but relatively fewer options exist for in-plane motion measurement. While optical profilometers may be common in labs, the in-plane scanning frequencies are still too low (low kHz range) to give a direct reading of dynamic response.

This chapter concentrates on the measurement of in-plane XY pad motion using optical microphotographs. Three methods are usually used for MEMS in-plane motion: high speed photography, stroboscopic methods, and blur methods; Wang [44] provides a good overview. In microphotographs of moving objects, high speed in-plane motion of an object leads to blurring of the images. High speed cameras and stroboscopic techniques



seek to remove the blur effects. High speed cameras have a short shutter speed that takes a snap shot of the unblurred motion; however such cameras are expensive, especially at the higher frequency ranges attained by MEMS devices. Stroboscopic techniques use short illumination pulses to freeze the motion, however as the frequency increases, the illumination time decreases and the image intensity decreases, limiting the maximum speeds.

Blur methods treat blurring not as a degradation of the image but as a source of motion information. These methods measure the blur and analytically model the blur effects to deduce the dynamic motion. Blur methods have the advantage that they require no specialized or expensive equipment and can be carried out using commonly available and inexpensive optical cameras. Sinusoidal in-plane motion widens the image in the direction of motion, with the width varying as the frequency changes. However these widths / changes in width can be quite small and challenging to measure. A number of researchers have used the blur width to measure the frequency response of MEMS actuators. Le [45] used the PSF (point spread function) of microphotographs to measure the motion of an electrostatic combdrive. Krylov [46] measured the blur width of microphotographs of an electrostatic oscillator. Burns and Helbig [47] synthesized blurred images from a static image and matched the synthesized image to measured blurred images to determine dynamic motion amplitudes. A related blur technique measures the blur-induced reduction of the slope of the sidewall profile of MEMS devices: Bscheiden [48] measured sidewall profile slopes and matched them to synthesized blurred slopes to determine the time constants of MEMS thermal actuators. Blur methods can also be applied to SEM photographs: Gilles [49] and Sehr [50] measured the dynamic blur width of MEMS actuators in SEM images.

The above mentioned MEMS work was primarily but not universally done in the temporal domain. There also exists a body of work in the non-MEMS field of image processing and computer science related to the restoration of macro scale blurred images (see for example Ben-Ezra [51] and Shuan [52]). Two common applications are the improvement of astronomical images and blur reduction for cameras. In these research

fields the analysis is sometimes done in the spatial frequency domain and the image is analyzed using Fourier transforms, see for example Yitzhaki [53] and Tanaka [54]. In the MEMS research field FFT (Fast Fourier Transform) analysis was used by Yamahata [55] to measure sub-nanometer in-plane static displacements of MEMS structures. Optical microphotographs of periodic combs were analyzed using FFT and the phase information was used to retrieve the static translation.

This chapter presents a method to combine MEMS based blur width techniques with image processing based FFT methods for the measurement of the in-plane high frequency dynamics of MEMS devices. This method is then used to detect and measure in-plane resonances of the XY pads from blurred microphotographs where the blur of resonance motion is not visually discernible.

## **8.2 Derivation of blurred image Fourier Transform**

### **8.2.1 1D Sidewall Profiles**

Consider a surface micromachined MEMS device with feature sizes on the order of a few microns and suspended above the substrate. Further consider a two dimensional image of the device taken using an optical camera. The different layers of surface micromachined devices have different optical properties such as roughness and reflectance and under illumination result in separate regions of different reflected light intensity. If we choose from within the image a 2D rectangular crop box and average the box columns, we can extract a 1D grayscale side wall profile  $p(x)$  where  $p(x)$  is a vector. While surface micromachined devices are composed of clearly defined layers of known thickness and elevation (a few microns typically) with well defined planar boundaries, the observed side wall profiles of the edges will not be simple sharp square steps up or down, instead, there will be observed sloping profiles with significant irregularities and short wavelength features. It is these short wavelength / high spatial frequency components that permit detection and measurement of submicron scale resonant motions.

### 8.2.2 Mathematical derivation

In this study we make use of the periodic structures that are inherent with the XY pads. Not all MEMS devices will have periodic structures, but many devices commonly have many pre-existing regularly spaced etch holes, dimples and vias etc. that can serve this purpose. Assuming some pre-existing repeating structures as outlined above, the spatial model of the static non-blurred sidewall profile  $p(x)$  can be expressed as a series of Fourier sine wave components:

$$p(x) = \sum_{i=1}^N p_i \sin(v_i x + \phi_i) \quad (9.1)$$

where  $p_i$  is the magnitude of the  $i^{\text{th}}$  Fourier component,  $v$  is the *spatial* frequency of the  $i^{\text{th}}$  component and  $\phi_i$  is the phase of the  $i^{\text{th}}$  component. The spatial frequency is of major importance in this study. The fundamental spatial frequency is found from the fundamental wavelength  $\lambda_1$  of repeating pattern  $v = 2\pi/\lambda_1$ . The  $i^{\text{th}}$  spatial frequency is  $v_i = 2\pi/\lambda_i$  where  $\lambda_i$  is the spatial wavelength of the  $i^{\text{th}}$  component.

The response to temporal blurring can be modeled as follows: let the spatial blur amplitude in microns as a function of time  $t$  be given by a periodic sinusoidal function with period  $T$ :

$$blur(t) = b_0 + b * \sin\left(2\pi * \frac{t}{T}\right) \quad (9.2)$$

where  $b_0$  is the DC or static value of the blur in microns (if present this is a static lateral shift in the space domain),  $b$  is the oscillatory component in microns and  $T$  is the temporal period of the oscillations:  $T = \frac{2\pi}{\omega}$  where  $\omega$  is the temporal frequency. Note that the spatial frequency  $v_i$  is not to be confused with the temporal frequency  $\omega$ .

We will now consider the response to spatial blurring of a single sine component:  $\sin(v_i x + \phi_i)$ . Because camera images (15-30 fps, 67-33 ms shutter speed) of MEMS device are obtained over an exposure time  $T_e$  that is much larger than the oscillation period  $T$  ( $<50 \mu\text{sec}$ ), the resultant blurred image is the temporal average of the profile. Let the resultant blurred image of a single sine wave component of  $p(x)$  as a function of position be given by  $\sin_{blur}(v_i x + \phi_i)$ :

$$\sin_{blur}(v_i x + \phi_i) = \frac{1}{T} \int_{-\frac{T}{2}}^{\frac{T}{2}} \sin[v_i x + \phi_i + v_i blur(t)] dt \quad (9.3)$$

where  $T$  is the temporal period of the oscillations and the term  $blur(t)$  is defined above. Note that the whole image is not blurred, only the moving part. The periodic features are on the moving part and therefore the sin wave components of the blurred image can be expressed as in Equation (9.3).

The integration can be simplified using the trigonometric identity:

$$\sin(A + B) = \sin(A) \cos(B) + \cos(A) \sin(B) \quad (9.4)$$

where  $A$  represents the components that do not vary with time:  $A = v_i x + \phi_i + v_i b_0$   
and  $B$  represents the components that do vary with time:  $B = v_i b * \sin\left(2\pi * \frac{t}{T}\right)$

The  $A$  components can be moved outside of the integral. Next, the  $\cos(A) * \sin(B)$  term vanishes as the  $\sin(B)$  term is an odd function and thus the integral over the period is zero. The resultant expression is:

$$\sin_{blur}(v_i x + \phi_i) = \sin[v_i x + \phi_i + v_i b_0] \left[ \frac{1}{T} \int_{-\frac{T}{2}}^{\frac{T}{2}} \cos \left[ v_i * b * \sin \left( 2\pi * \frac{t}{T} \right) \right] dt \right] \quad (9.5)$$

The first term on the right is the original sine wave component of  $p(x)$  phase shifted by an amount  $v_i b_0$ , the second term (the integral) is an attenuation factor. Because  $\cos$  is an even function, the integral from  $-T/2$  to  $T/2$  is also equal to double the integral from  $0$  to  $T/2$ .

Finally, making a substitution for the time variable  $\gamma = \left( 2\pi * \frac{t}{T} \right)$  and defining the attenuation as the ratio of the blurred and unblurred magnitudes, we find that the attenuation factor is a Bessel function of the first kind order 0  $J_0$  (see Yitzhaki [53]):

$$Attenuation_i = \frac{1}{\pi} \int_0^{\pi} \cos[v_i * b * \sin(\gamma)] d\gamma = J_0(v_i b) = J_0 \left( 2\pi \frac{b}{\lambda_i} \right) \quad (9.6)$$

Note that if the sinusoidal blur is replaced by linear blur:  $blur(t) = b_0 + b * \frac{t}{T}$ , the attenuation is modeled by a *sinc* function ( $sinc = \sin(a)/a$ ) instead of a Bessel function (Tanaka [54]). Note that the *sinc* function is the zero<sup>th</sup> order Spherical Bessel function:  $j_0$ .

Of more interest is the absolute value of the Bessel function as FFT algorithms display the magnitude of the Fourier components. Figure 1 shows a plot of  $|Bessel J_0|$  vs. blur amplitude. For the same spatial blur amplitude  $b$  (measured in microns) the higher order harmonics (shorter wavelengths) correspond to higher values of  $b/\lambda_i$  (dimensionless ratio). Let the blur in radians be defined as  $\beta_i = 2\pi * (b/\lambda_i)$ . Since the wavelength of the  $i^{\text{th}}$  component is  $i$  times shorter than the fundamental's wavelength ( $\lambda_i = \lambda_1/i$ ),  $\beta_i$  is proportional to the harmonic number  $i$ :  $\beta_i = 2\pi b/\lambda_1 * i$ . The blurring acts as a low pass

filter; attenuating all frequency components, but preferentially attenuating the higher order harmonics more effectively.

To confirm the derivation of the Bessel curve attenuation, a simplified side wall profile was numerically blurred. Real MEMS side wall profiles can have a wide range of features, but the XY pads considered in this study are generally repeated patterns of light and dark bands with a gradual transition from light to dark. To model this, an idealized trapezoidal side wall profile constructed from the 1<sup>st</sup> to 13<sup>th</sup> Fourier components (trapezoidal waveforms contain only odd harmonics) was chosen:

$$trap(x) = \sum_{n=1,3,5}^{13} \frac{a_n}{n^2} \sin(n, x) \quad (9.7)$$

where  $a_n$  is the alternating sequence 1, 1, -1, -1, 1, 1, -1, -1 etc. for  $n = 1, 3, 5 \dots$

The waveform was numerically blurred by shifting symmetrically about the x axis,  $-\lambda/20$  to the left and  $+\lambda/20$  to the right in 50 intermediary steps and the 51 shifted waveforms averaged. The interpolation spacings were not uniform, but rather were spaced sinusoidally to simulate sinusoidal blurring, with more curves near the extremas and fewer curves near the origin:

$$trap_{blur}(x) = \frac{1}{51} \sum_{t=-25}^{25} \sum_{n=1,3,5}^{13} \frac{a_n}{n^2} \sin \left[ n \left( x + \frac{2\pi}{20} * \sin \left( \pi * \frac{t}{25} \right) \right) \right] \quad (9.8)$$

A FFT with a 256 point sample was performed on the original waveform and on the blurred average waveform. The attenuation for each harmonic is the ratio of the two Fourier transforms (blurred harmonic/ unblurred harmonic): the resultant ratio of the FFT components is plotted vs. blur in radians  $\beta$  and superimposed on the |Bessel| function. The results are shown in Figure 98. The numerically simulated results match the |Bessel| function.

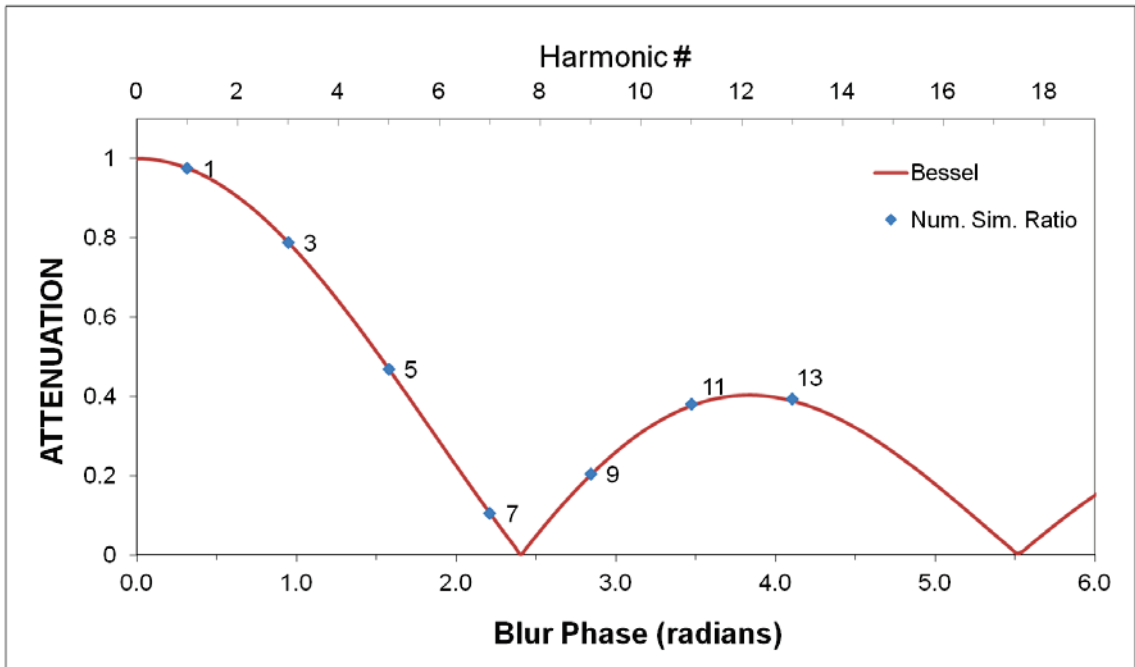


Figure 98. Plot of  $|Bessel J_0|$  vs. blur in radians. Superimposed dots show numerically simulated attenuation (ratio of blurred to unblurred magnitudes) for 1<sup>st</sup>, 3<sup>rd</sup>, 5<sup>th</sup> etc. harmonics of an idealized trapezoidal sidewall profile. Data labels show the harmonic number

## 8.3 XY Actuator Pad

### 8.3.1 XY Pad Components

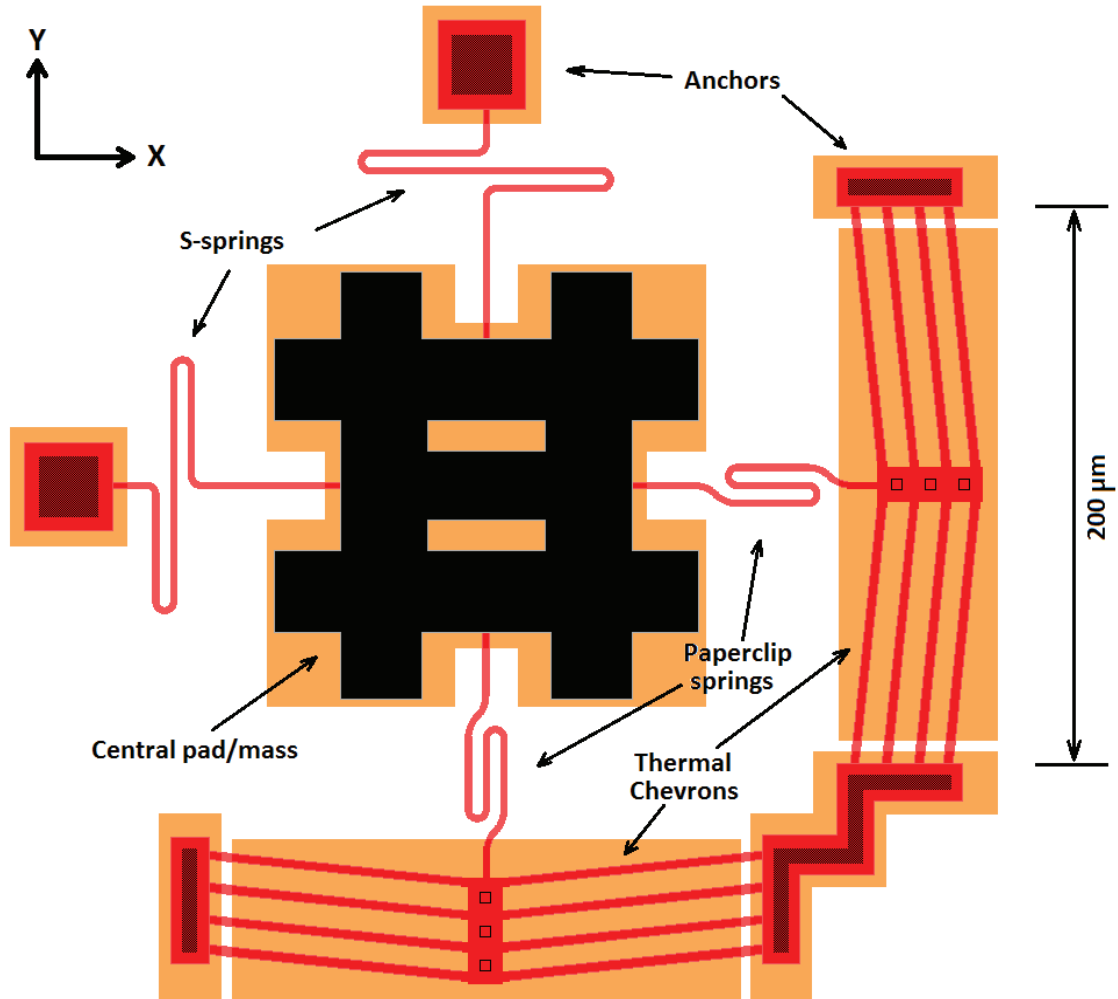


Figure 99. Schematic of PolyMUMPs MEMS XY pad showing: Central pad/mass, two chevron thermal actuators, two ‘S-springs’, and two ‘Paperclip’ springs

In order to experimentally verify the technique outlined above, XY pads fabricated using the PolyMUMPs process [28] were tested. The XY pad used (see Figure 99) is typical of many thermally driven MEMS devices in terms of range of motion ( $\sim\mu\text{m}$ ), thermal response ( $\sim\text{kHz}$ ) and resonances ( $\sim 50\text{-}200\text{ kHz}$ ). As well described in Section 4.2, the XY pad is thermally actuated with two degrees of actuation X & Y, and has three planar degrees of freedom; X and Y and in-plane rotation  $\theta$ . The pad has three main components: a) a central mass, b) a pair of chevron type thermal actuators, c) two pairs of



springs. The actuators are typically driven with 3-10 Volts and 10-30 mA and produce a maximum movement envelope of the central mass of about 2-3  $\mu\text{m}$  in each axis. The springs and the chevrons are constructed using the Poly1 layer. The center pad has Poly1, Poly2 and Metal layers for added mass. The thermal actuators are four bar chevrons (see Lai [39]) with a total length of 200  $\mu\text{m}$  and a 6° angle. Passing a current across the chevron causes a thermal expansion of the chevron arms. Since they are anchored at the ends and angled to each other, the expansion of the angled arms results in a deflection of the center connection point. Estimated force is approximately 80  $\mu\text{N}$  with a 3  $\mu\text{m}$  displacement (Lai [39]).

The X and Y motions were decoupled through the selection and placement of different spring types. Two types of selectively compliant springs are used, each offering different directional properties. The chevrons are connected directly to paperclip (PC) springs that maintain a high stiffness in the axial direction but are relatively soft in the transverse direction. This allows maximum force from the chevron to be transferred to the pad and allows the pad to be pulled in either axis without interference from the opposing chevron. The opposing S-springs have little stiffness in the axial direction but have a high stiffness in the transverse direction. The chevrons are oriented in a “pull” configuration to eliminate the possibility of buckling in the springs.

### **8.3.2 Thermal and Mechanical Response**

Thermal actuators respond to the input electrical power or Voltage<sup>2</sup> (Hickey [56]). From the trigonometric identity:  $\sin^2(\theta) = \frac{1}{2}(1 - \cos(2\theta))$ , the response has two parts: 1) a DC or static response equal to the RMS value of the input, and 2) a sinusoidal component that exhibits frequency doubling: an input signal of frequency  $f$  produces a response at frequency  $2f$ . The amplitude of the sinusoidal component decreases with increasing frequency characterized by the thermal time constant  $\tau$  (Hickey [57]). The thermal response is given by:

$$\text{Thermal Response}(\omega) \propto \left[ \frac{1}{\sqrt{1 + (2\omega\tau)^2}} \right] \quad (9.9)$$

where  $\omega = 2\pi f$  in rads/s is the temporal frequency. Typical  $\tau$  values for thermal actuators are in the 50-200  $\mu\text{s}$  range with cut off frequencies in the few kHz range. At high frequencies ( $f > 10$  kHz)  $\omega \gg 1/\tau$  and the 1 in the denominator in the above equation can be neglected and thermal response is approximately reciprocal with frequency.

The mechanical sinusoidal response is characterized by the resonant frequency  $f_o$  and the damping ratio  $\zeta$ :

$$\text{Mechanical Response}(\omega) \propto \left[ \frac{1}{\sqrt{\left(1 + \frac{\omega^2}{\omega_0^2}\right)^2 + \left(\frac{2\zeta\omega}{\omega_0}\right)^2}} \right] \quad (9.10)$$

where  $\omega_0 = 2\pi f_o = \sqrt{K/M}$  is the undamped resonant frequency, determined by the mass  $m$  and the stiffness  $k$ . The damping ratio is defined as  $\zeta = c/2m\omega_0$  where  $c$  is the viscous damping coefficient. At the low values of damping ratio found in MEMS devices ( $\zeta \ll 1$ ) (Hickey [57]) the resonant frequency is very close to  $\omega_0$ . Typical resonant frequencies for MEMS devices vary widely in the 10's to 100's of kHz range. The net sinusoidal response of a thermal excited resonant structure is the product of the 1<sup>st</sup> order thermal response multiplied by the 2<sup>nd</sup> order mechanical amplification (Hickey [57]). Because the resonance frequencies are typically so much larger than the thermal cutoff frequencies, the thermal response is relatively small and relatively flat at resonances and does not significantly alter the shape of the resonant peaks, only their amplitude: at high frequencies, the thermal response gradually decreases.

### 8.3.3 FEM of XY Pad Resonant Modes

The Finite Element (FEM) package ANSYS<sup>TM</sup> V10.0 was used for comparison with the analytical model. A design was first created and exported from LEdit<sup>TM</sup> V15.02 to SolidWorks<sup>TM</sup> 2004 in DXF format, and then from SolidWorks to ANSYS in IGES format. Tetrahedral coupled-field SOLID98 elements are used for the mesh. The element supports six degrees of freedom: *UX*, *UY*, *UZ*, *Temp*, *Volt* and *Mag*. For modal analysis, the key material parameters used for polysilicon were Young's Modulus ( $E=158$  GPa), Poisson Ratio ( $\nu=0.22$ ) and Density ( $\rho=2330$  kg/m<sup>3</sup>) (Sharpe [41]). Auto meshing was used. The Block Lanczos method is used for solving for all modes and natural frequencies up to 200 kHz.

Three different device variations (A, B, C) were simulated, each with different spring stiffnesses (see Table 14). Different lengths of S-springs and paperclip (PC) springs were tested: Device A: Low Stiffness with longer springs, Device B: Medium Stiffness with middle length springs, Device C: High Stiffness with short springs. Spring dimensions are provided in Table 14. All central pads had the same mass of 0.25  $\mu\text{g}$ . FEM analysis revealed six modes below 200 kHz. The first three modes were out-of-plane. The next three modes were of greatest interest as they were all planar modes: translational Y motion, translational X motion, and rotational motion. Note that due to symmetry ideally the X and Y modes should be identical. The out-of-plane and rotational modes will be discussed in a later section; the following sections will concentrate on the planar X & Y translational modes. Figure 100. FEM simulation of Device A: Low Stiffness, showing exaggerated X translation mode shows the simulated exaggerated X in-plane translation mode for Device A: Low Stiffness. The Figure shows an exaggerated X motion of approximately 8 microns, actual motions observed were less than a micron. The last column of Table 14 lists the predicted FEM X in-plane translational resonant frequencies from ~90 to 145 kHz.

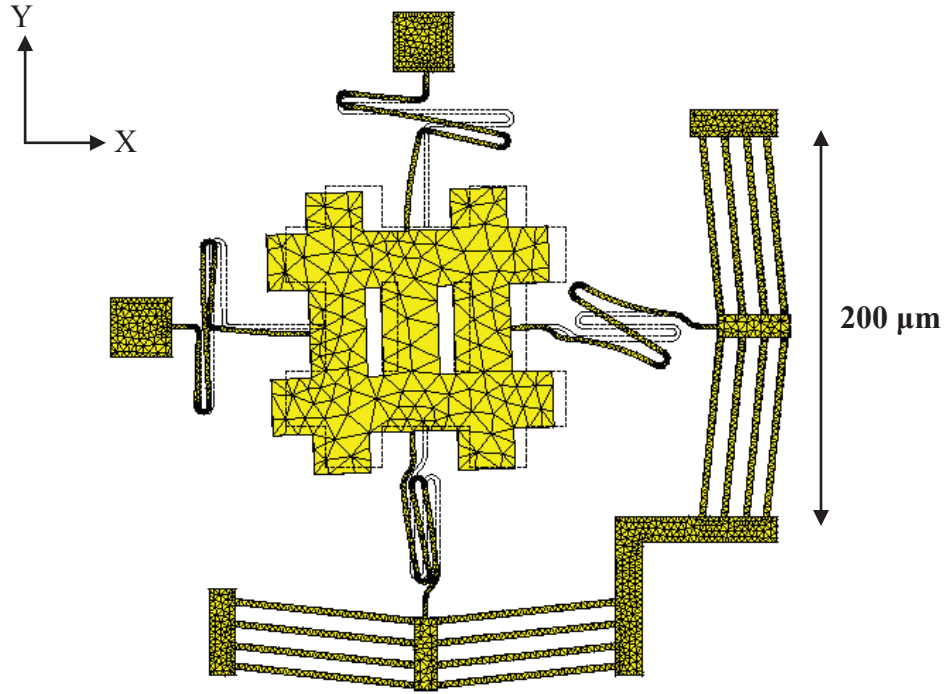


Figure 100. FEM simulation of Device A: Low Stiffness, showing exaggerated X translation mode

Device	Spring Lengths (μm)	PC Spring Image	Spring Lengths (μm)	S Spring Image	FEM X Resonance (kHz)
A: Low stiffness	Total: 174 A: 40 B: 14		Total: 242 A: 80 B: 48		89.6
B: Medium stiffness	Total: 143 A: 25 B: 22		Total: 142 A: 30 B: 48		121.2
C: High stiffness	Total: 114 A: 10 B: 38		Total: 142 A: 30 B: 48		145.2

Table 14. List of XY pad dimensions and FEM simulated X in-plane translational resonant frequencies

## 8.4 Experimental Results

### 8.4.1 Experimental Setup & Methods

To measure the frequency response of a device the frequency is scanned and at each sampling frequency the following steps are performed (details on the each step are outlined below):

- 1) Acquire the Image
- 2) Crop the Image around a periodic pattern on the device
- 3) Average the cropped image to get a 1D Profile
- 4) Truncate the 1D Profile to an integer number of wavelengths of the periodic pattern
- 5) FFT the 1D profile to get Harmonics
- 6) Normalize the FFT results to get attenuations of the individual harmonics
- 7) Fit the attenuations to a Bessel curve to get displacement

In Step 1) images were obtained using a Point Grey<sup>TM</sup> camera model GRAS-14S3M-C: a 1.4MP B&W 1394b Firewire CCD Camera with a maximum resolution of 1280x960 pixels, 16 bit grayscale. The camera was mounted on a Wentworth Probestation model MP0901 with a maximum magnification of 50x. In this configuration the camera provided a field of view of  $\sim 200 \times 150 \mu\text{m}$  and a resolution of  $0.163 \mu\text{m}/\text{pixel}$ . The images were sent to a computer via a Firewire cable and the shutter triggered via a Labview VI. Images were stored as a sequence of numbered files. The actuators were powered using an Agilent Model 33210A function generator, controlled by a Labview VI via a RS232 cable.

A Matlab program performed the following steps on each image: Step 2) Crop the image to a user defined Region of Interest (ROI), Step 3) Average the columns in the 2D image to produce a 1D sidewall profile, Step 4) Truncate the side wall profile sample to an integer number of fundamental spatial wavelengths, Step 5) Calculate the FFT for the

sidewall profile. The user selection of crop box was only performed on the first image; the same crop sizes and locations used on all subsequent images.

Sidewall profile sample truncation to an integer number of fundamental wavelengths is necessary because edge effects such as a fractional wavelength can alter the FFT results. FFT algorithms use a discrete set of frequency bins: if the sample includes an integer number of wavelengths, then the sample wavelength will lie exactly in one of those bins, if not then the algorithm will calculate components in the nearest bins. If many wavelengths are used, truncation is less important, but as the samples here typically included only a few wavelengths truncation was needed. The truncation was performed by calculating the sidewall profile mean value and detecting how many times the profile crosses the mean: 1 full wavelength = 3 crossings,  $n$  full wavelengths =  $2n+1$  crossings. The data was then cropped from the first crossing to the last full fundamental wavelength crossing. Typical cropped sample sizes would be: 650 x250 pixel user defined crop box, 650 pixel long profile, truncated to a 460 pixel long profile.

#### **8.4.2 Measurements**

First a manual frequency scan of Device A (see Table 14) at high voltage (7 Volts) was conducted and a slight resonance visually observed at ~75 kHz. No resonance blurring was visually discernable below this voltage. To test the FFT method, the voltage was reduced by a factor of two to 3.5 Volts, this results in a quarter the amplitude. Figure 101 shows two 3.5 Volt sample camera images of the central mass of Device A. A: off resonance at 70 kHz, B: translational resonance at 75.2 kHz, C & D: 4x zoom on center of images A & B. Note that at this voltage resonance is not apparent from visual inspection. The dashed boxes indicate user selected ROI from which sidewall profiles were averaged.

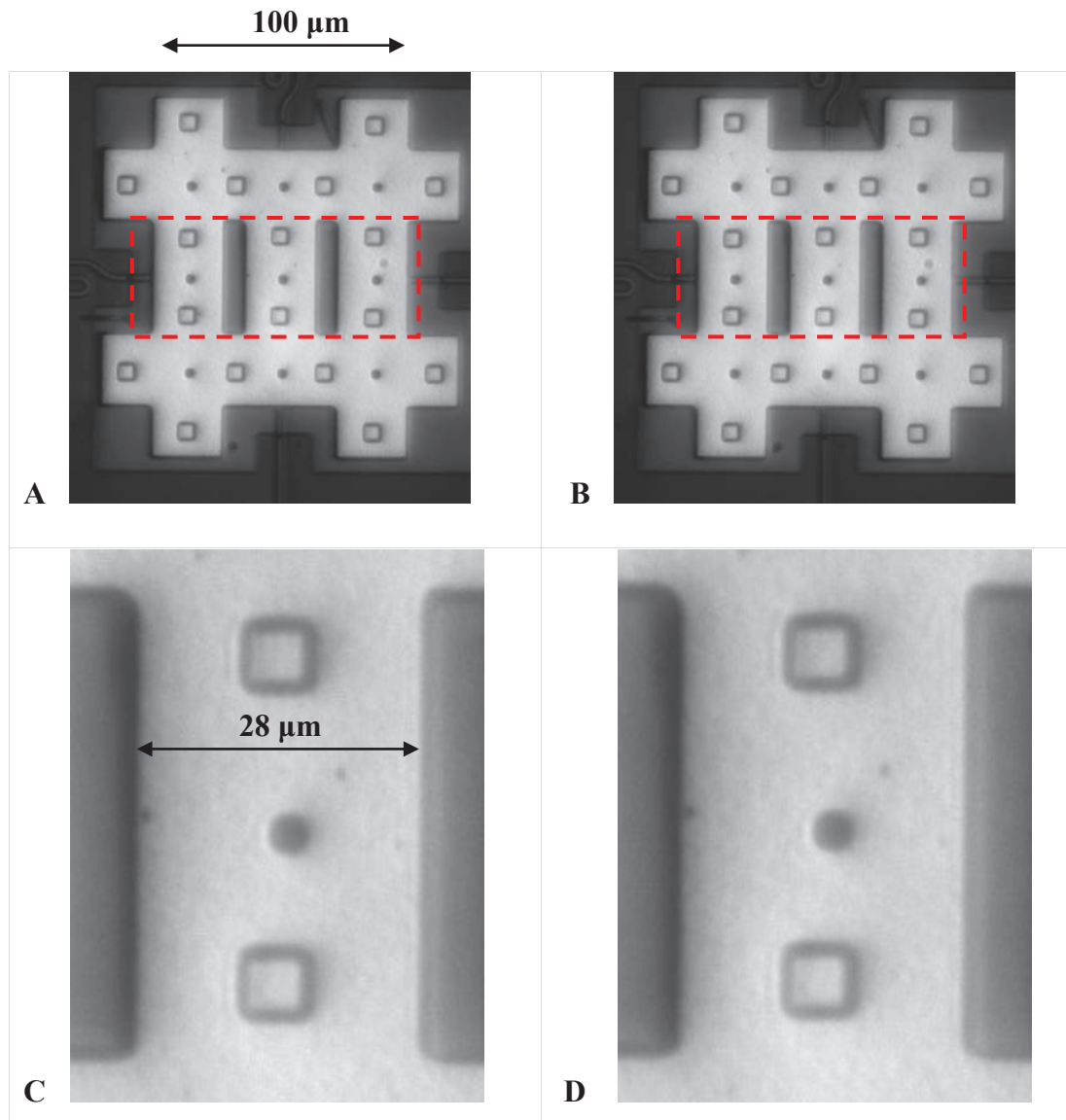


**Figure 101. A & B: Two sample camera images of Device A (Low Stiffness) driven at 3.5 Volts. A: off resonance at 70 kHz, B: resonance at 75.2 kHz. 1D profiles were column averaged from dashed ROI box. C & D: 4x zoom on center of images A & B. Note that resonance is not apparent from visual inspection. Scale: the square Vias are 7 x 7 microns, the circular dimples are 3 microns**

Figure 102 shows Step 3) the unblurred and blurred 1D profiles. Figure 103 shows Step 4) the Fourier components of the profiles in Figure 102. The first and second harmonics are much larger than the higher harmonics and have been cropped in the Figure so that the detail in the higher and smaller harmonics may be more clearly seen.

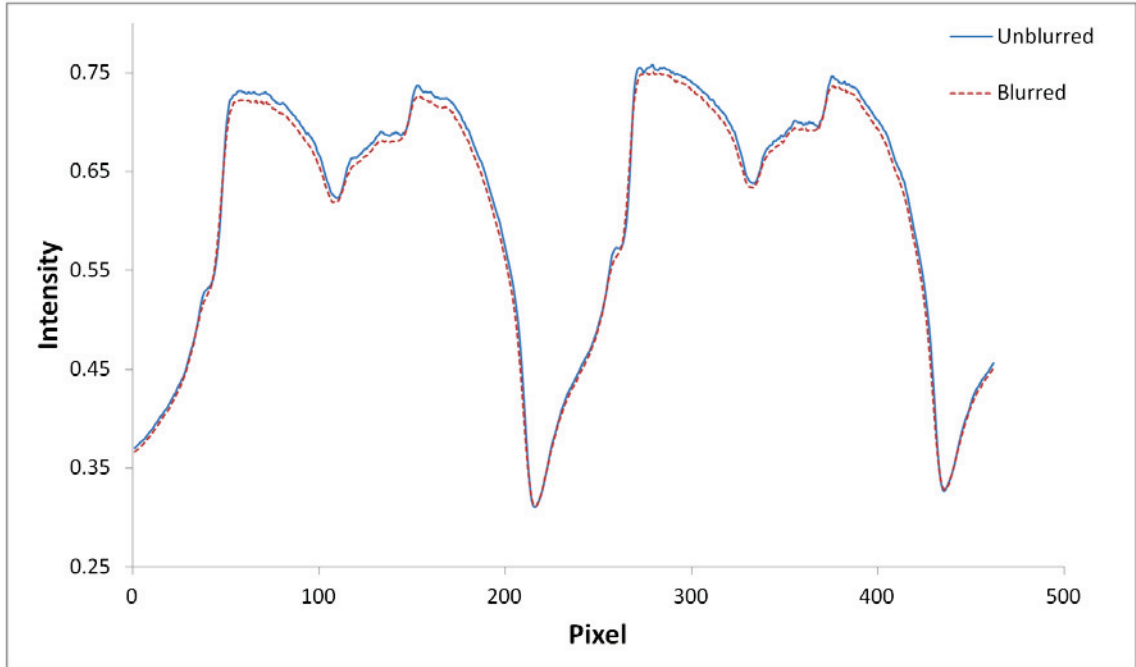


**Figure 102. Sampled 1D profiles of the two images from Figure 101. Solid line is off resonance (non-blurred) at 70 kHz, dashed line is on resonance at 75.2 kHz (blurred)**

Figure 104 shows the result of a frequency scan of Device A at 3.5 Volts from 20 to 140 kHz in 0.2 kHz steps. Each image required approximately one second to acquire. Five scans were taken and the results averaged. The Y axis has arbitrary units produced by the Matlab FFT algorithm. The Matlab algorithm required approximately 60 seconds to calculate the FFT components for 600 points. There were 15 harmonics calculated by the FFT algorithm; but for clarity only four harmonics are displayed here: 9, 10, 13 and 14<sup>th</sup> harmonics. All four harmonics show a clear dip at 75.2 kHz indicating increased blur due to resonance. The slight upward drift as frequency increases is due to the thermal response gradually decreasing (reduced attenuation) at high frequency as outlined in Section 9.3.2.



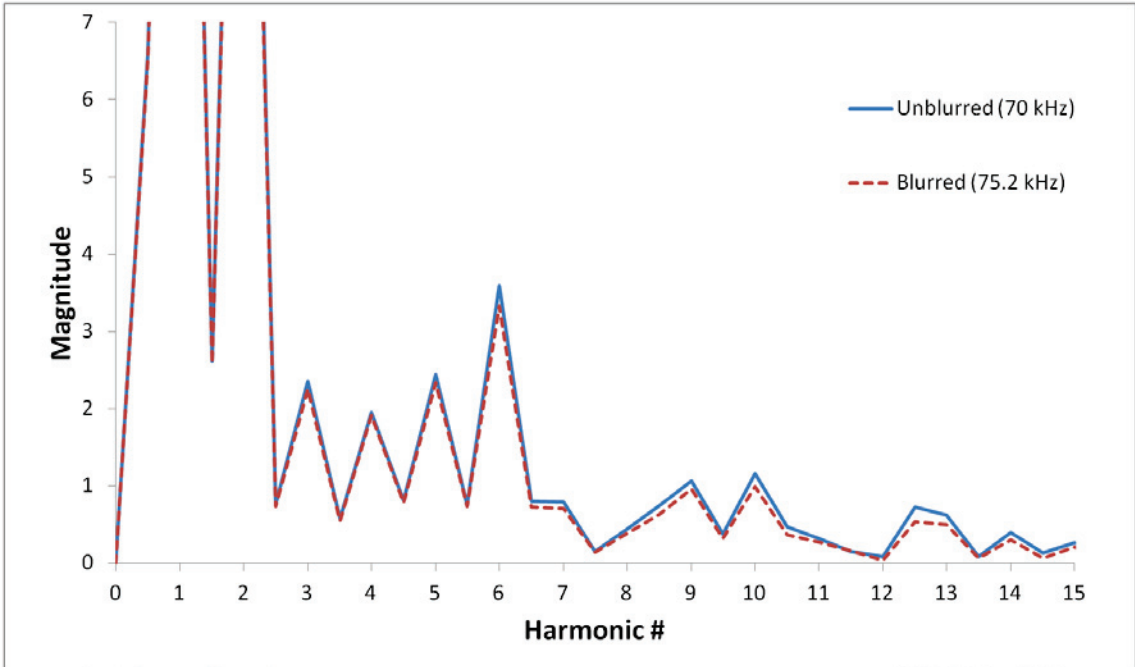


Figure 103. FFT of the two images from Figure 101 driven at 3.5 Volts. Solid line is off resonance (non-blurred) at 70 kHz, dashed line is on resonance at 75.2 kHz (blurred)

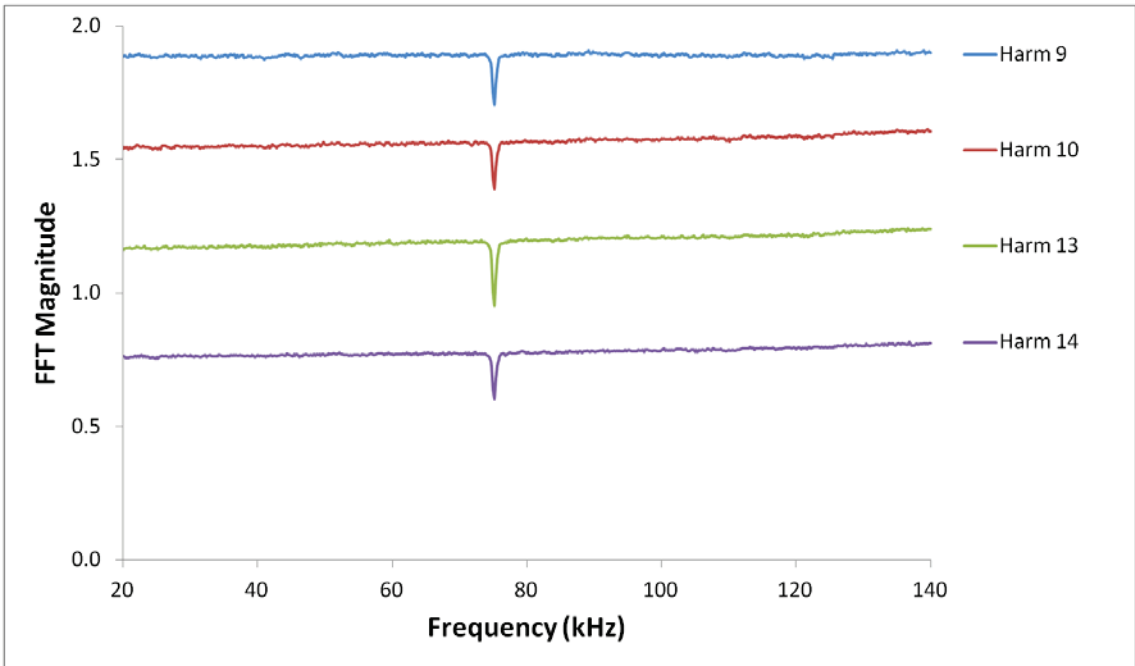
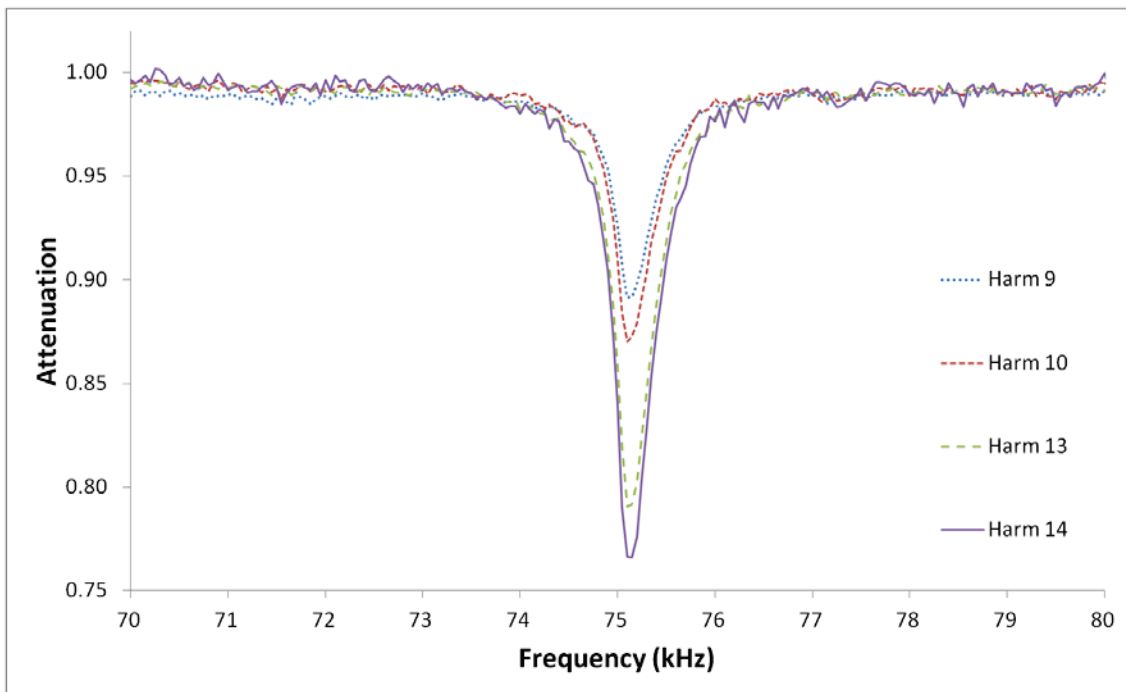


Figure 104. Graph of raw FFT magnitude of 9, 10, 13 and 14th harmonics of Device A (Low Stiffness) at 3.5 Volts showing a clear resonance attenuation of higher harmonics at 75.2 kHz due to blurring

In Step 5) to convert the raw FFT magnitudes into attenuation factors, each frequency data point for the  $i^{\text{th}}$  harmonic must be divided by the unblurred amplitude for  $i^{\text{th}}$  harmonic. The unblurred amplitudes could be obtained from the FFT of an off (stationary) image or from the FFT of a high frequency image. The disadvantage of the off image is that it has no offset. From Section 9.3.2 and from Hickey [57], any blurred image will have a DC offset equal to the RMS value of the input sine wave. By going to higher frequency, the sinusoidal response is removed and a quasi static image obtained, but the DC offset is retained (see Bscheiden [48]). High frequency scans for each harmonic were averaged from 85-90 kHz and then all data points for that harmonic divided by the calculated average to obtain each harmonic's attenuation. Figure 105 shows a zoom into the resonance region of Figure 104 from 70 to 80 kHz in 0.05 kHz steps and showing 9, 10, 13 and 14<sup>th</sup> normalized harmonics. Five scans were taken and the results averaged.



**Figure 105. Graph of normalized magnitudes of harmonics of Device A at 3.5 Volts near resonance showing 9, 10, 13 and 14<sup>th</sup> harmonics. Each harmonic has been normalized by its high frequency value**

In order to confirm the theoretically derived blur induced Bessel attenuation from Section 9.2, Figure 106 plots the experimental attenuations vs. harmonic number for three

different frequencies. Any frequency can be used, on or off resonance, in this specific case, resonance was at 75.2 kHz and measurements were done at 74.2, 75.0 and 75.2 kHz. Five measurements were done at each frequency and the points show the average attenuation value of each harmonic. The error bars in Figure 106 are calculated from the uncertainty in the high frequency normalization value. This uncertainty is used as the noise level when calculating  $\pm$  error bars in the attenuation ratio. Note that some of the harmonic amplitudes were low prior to normalization and show more variation. At each voltage the best fit |Bessel| curves were calculated and are shown as solid lines. The experimental data fits the predicted curves well, with more attenuation with increasing blur amplitude as resonance is approached. Note that at 3.5 Volts, the attenuation is relatively small ( $>0.7$ ), the |Bessel| fit was also valid at higher voltages and much larger attenuations ( $<0.1$ ).

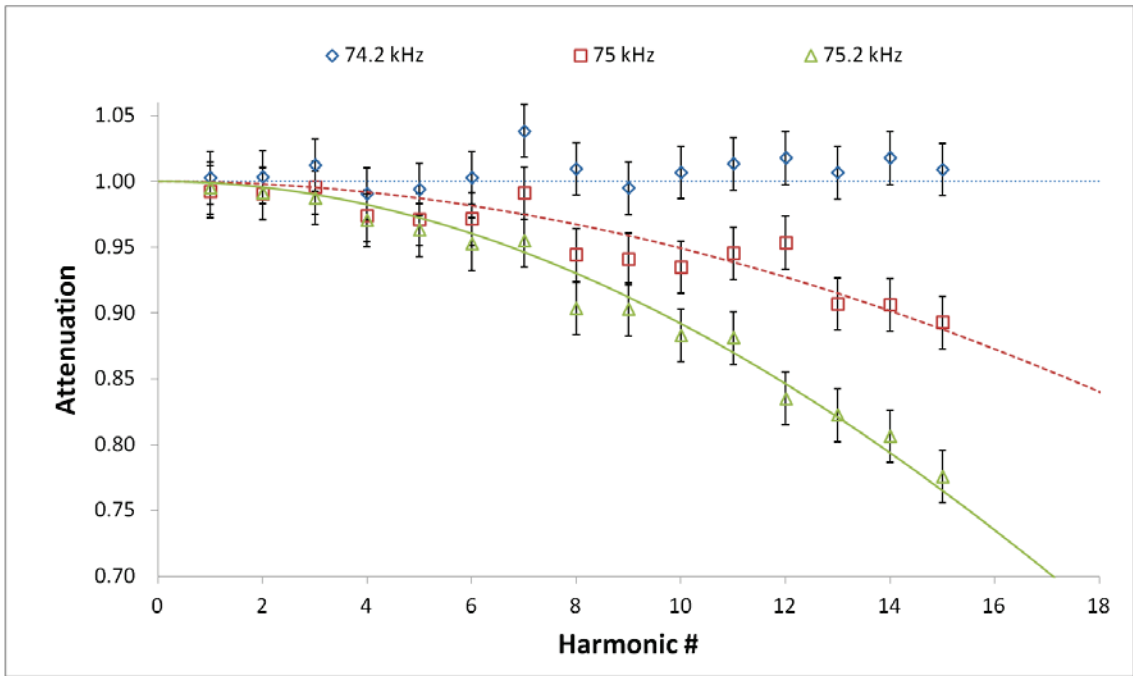


**Figure 106. Experimentally measured attenuation for Device A vs. Harmonic # at 3.5 Volts and three frequencies 74.2, 75 and 75.2 kHz. Points are experimental data, solid lines are best fit |Bessel| curves**

In Step 6) the |Bessel| curves can now be used to convert attenuation to displacement amplitude. At each frequency the attenuation is calculated for each harmonic. At each frequency an Excel program finds the least squares fit |Bessel| function to the harmonic

attenuations. The blur phase  $\beta$  is varied until the best fit is achieved for that frequency. The blur phase is converted from radians to a multiple of the primary spatial wavelength  $\lambda_1$  in microns. This is repeated for each frequency; the Bessel fitting takes less than a second for 600 points. Figure 107 shows a long range scan (20 to 140 kHz in 0.2 kHz steps) of displacement vs. frequency for Device A. Five scans were taken and the results averaged.

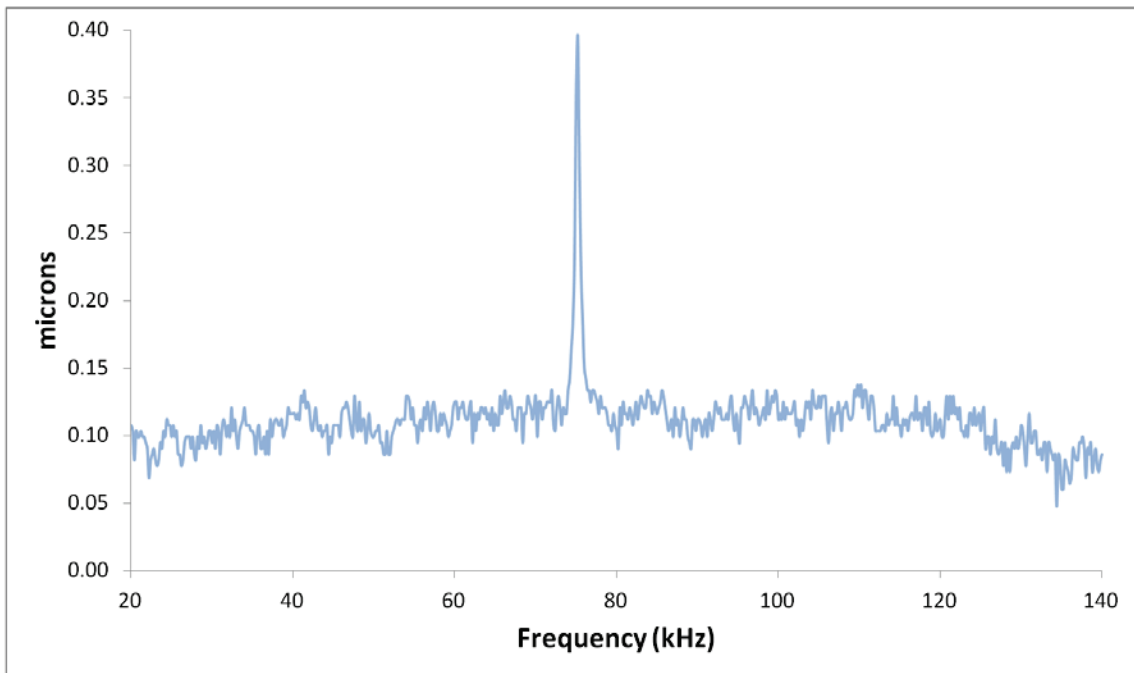


**Figure 107. Long range scan of displacement vs. frequency for Device A at 3.5 Volts. Resonance is at 75.2 kHz**

Figure 108 shows a finer scan of Device A at 3.5 Volts in the region between 70 and 80 kHz in 0.05 kHz steps showing a resonance at  $\sim 75.2$  kHz. Superimposed are the results for lower voltages: 2.5 and 2 Volts. Note that the resonance peak is shifted slightly to the right as the voltage is decreased, this will be discussed in Section 9.6. A resonance peak was still detectable at 2 Volts compared to the visual detection limit of 7 Volts. Since the response amplitude goes as  $V^2$ , this corresponds to an amplitude of  $(2/7)^2 = 0.08 = 1/12$  times the amplitude that is visually detectable.

The results can be significantly improved by taking multiple images at each frequency or averaging multiple scans. A signal to noise ratio can be defined as the height of the

resonance peak above the higher frequency average divided by twice the standard deviation or noise in the higher frequency range. In this case the higher frequency range 85-90 kHz was chosen. Figure 109 shows the results near resonance for Device A at 3.5 Volts using the average of N = 1, 5 and 10 runs. Curves for 1 and 5 runs have been shifted up for clarity; Y axis is 0.1 microns/division. The noise levels for N = 1, 5, 10 were  $\pm 0.027$ , 0.016 and 0.011 microns respectively. The signal to noise ratios for N = 1, 5, 10 were 9.9, 16.1, and 24.1 respectively. The noise levels for N = 5 runs were then compared at 3 different voltages: 1.75 V, 3.5 V and 7 V and were found to be approximately the same to within  $\pm 10\%$ , but the resonance amplitude and thus the signal to noise ratio increases as voltage increases, rising to above 50 for 7 V.

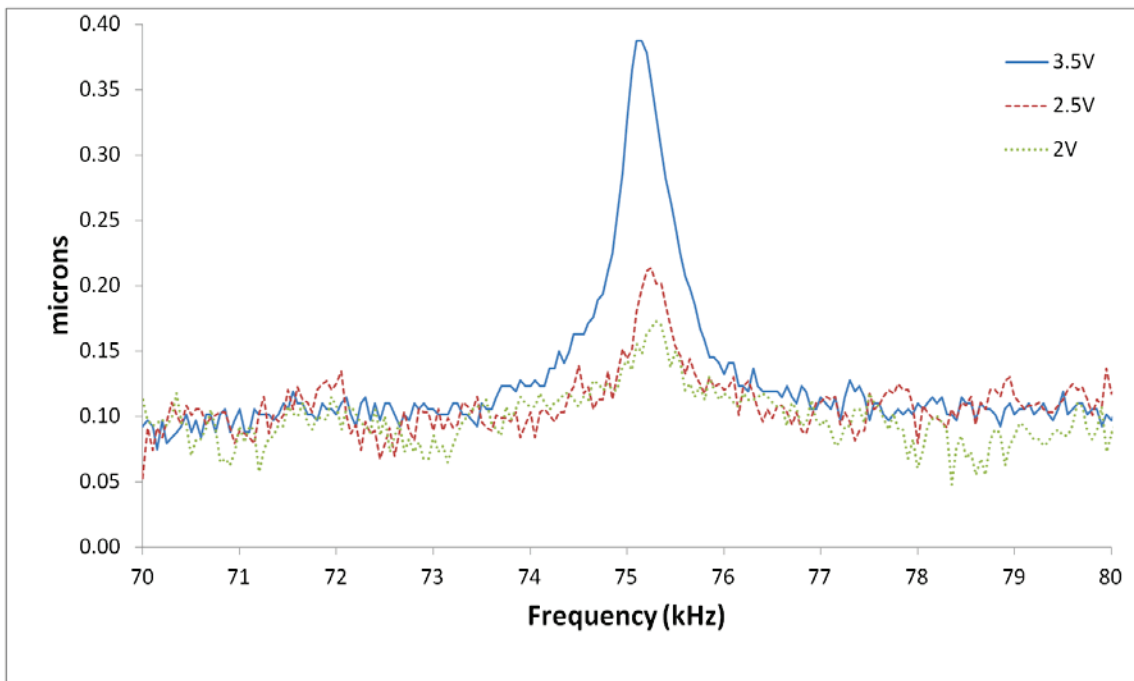
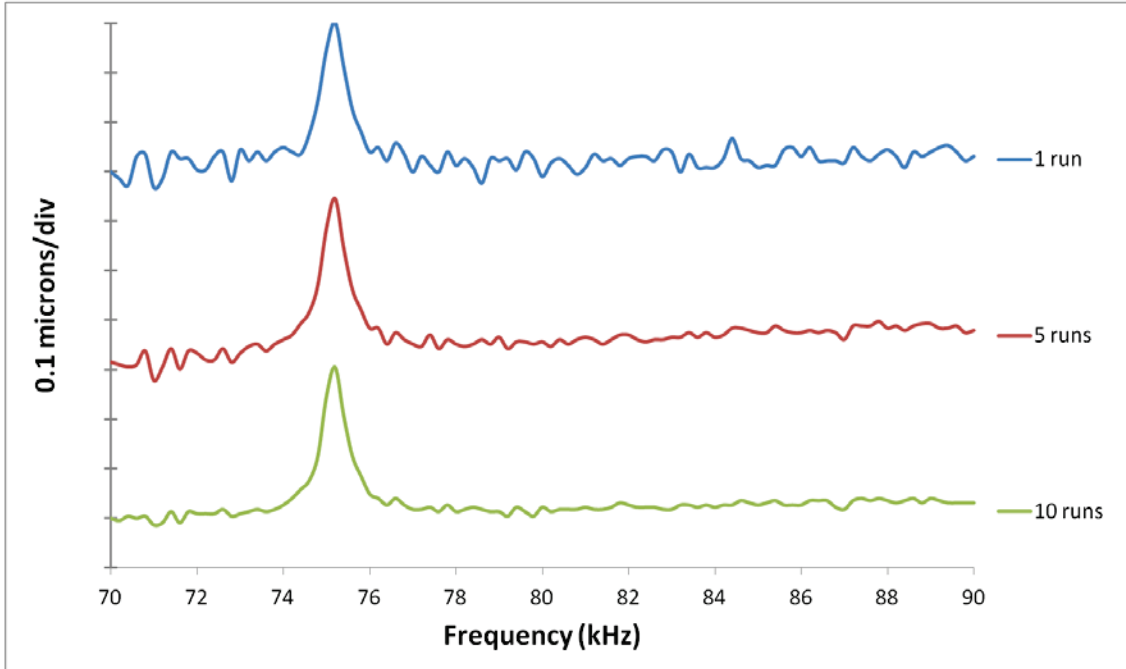
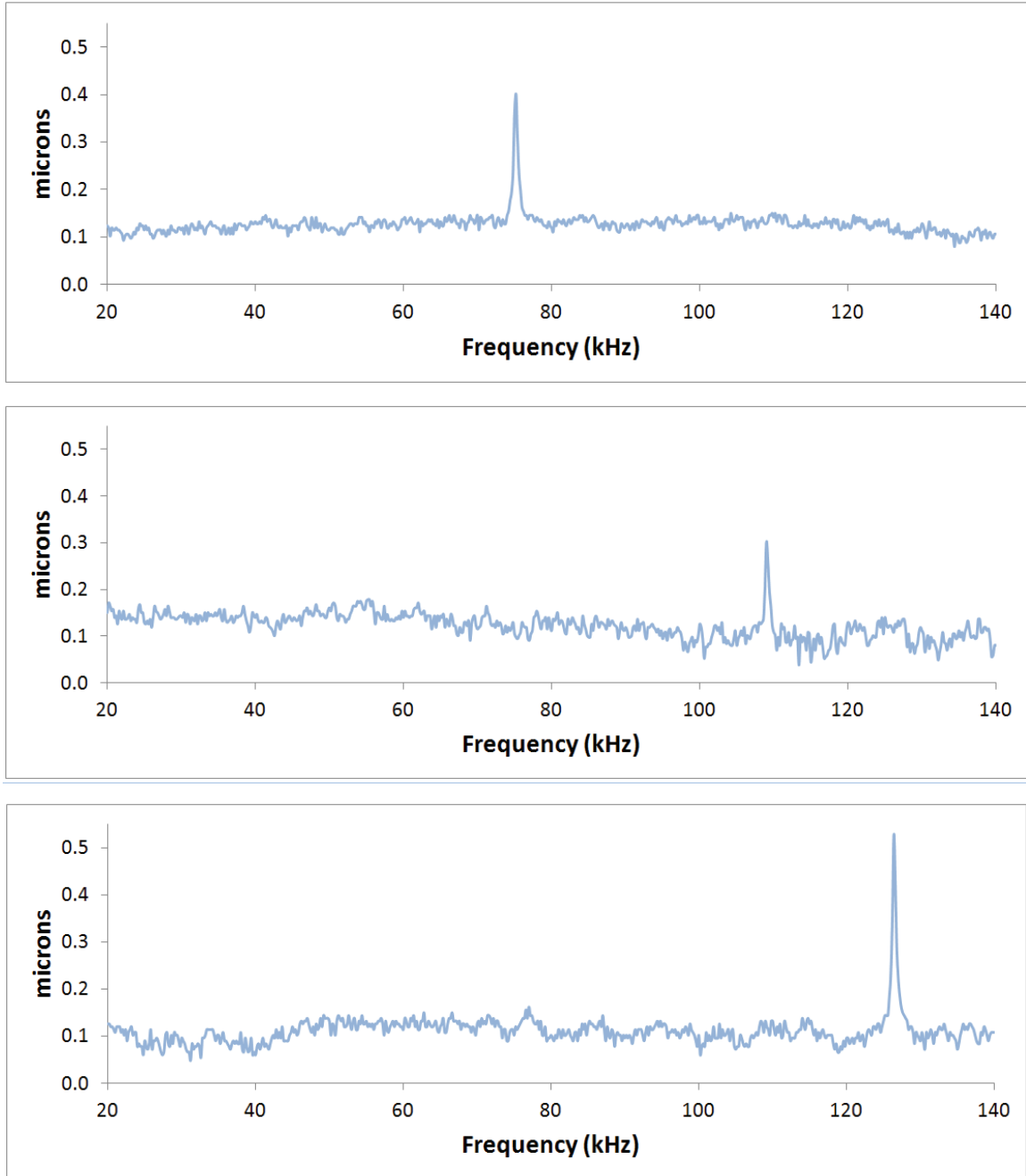


Figure 108. Fine scan at resonance for Device A at 3.5, 2.5 and 2 Volts. Resonance is at  $\sim 75.2$  kHz



**Figure 109. Effect of averaging on noise for Device A at 3.5 V. Top: 1 run, Middle: average of 5 runs, Bottom: average of 10 runs. Y axis is 0.1 microns/division**

Resonance tests were carried out on three different XY pads (Devices A, B, C). Figure 110 shows a comparison of three long range scans for Devices A, B, C (Low, Medium and High Stiffnesses respectively) at 3.5 Volts, showing X resonances at 75.2, 109.2 and 126.6 kHz respectively. The signal to noise ratio varied with different XY pads, ranging from 4.7 to 15.1.



**Figure 110. Comparison for three long range scans for Devices A, B, C (Low, Medium and High Stiffnesses respectively) at 3.5 Volts, showing X resonances at 75.2, 109.2 and 126.6 kHz respectively**

Table 15 shows experimentally measured resonant frequencies for different translational modes, along with predicted frequencies and % difference. Note that ideally the X and Y modes should be identical, but the XY pad is not perfectly diagonally symmetrical, resulting in small differences (<1%) between the natural frequencies in the X and Y

planes. Experimentally, the Y modes were found by simply rotating the image prior to cropping and column averaging. The FEM results consistently overestimated the experimental values by ~10-20%, modeling the device stiffer than it actually was, while the analytical model overestimated stiffness by approximately 8%. Note that the analytical model assumes a symmetric XY pad resulting in identical values for both axes, while the FEM accounted for minute differences while using the exact L-Edit component designs that were used for experimentation.

XY pad	Axis	FEM (kHz)	Analytical Model (kHz)	Exp (kHz)	% difference (FEM – Exp) /Exp	% difference (A.M. – Exp) /Exp
A: Low Stiffness	X	89.6	75.2	75.2	19.1%	0.0%
	Y	88.7	75.2	74.4	19.2%	1.1%
B:Medium Stiffness	X	121.1	117.8	109.2	10.9%	8.6%
	Y	120.2	117.8	105.2	14.3%	12.0%
C: High Stiffness	X	145.1	136.1	126.6	14.6%	7.8%
	Y	144.7	136.1	125.6	15.2%	8.4%

**Table 15. Table comparing experimental X & Y in-plane translational resonance data with FEM and analytical model**

### 8.4.3 Out-of-plane and Rotational Resonances

FEM simulations also revealed out-of-plane and rotational modes. The three devices A, B, & C each had three predicted out-of-plane modes. The nine predicted out of plane modes ranged from 17 to 69 kHz. No out-of-plane modes were detected experimentally. Note that the system was only excited in-plane. While moving up and down out-of-plane does alter the focus and thus blur the image, the focus blurring is only a weak function of displacement and for small displacements of less than a few microns, little to no blurring would be observed.



The three devices A, B & C each had one predicted in-plane rotational mode. The three predicted rotational modes ranged from 74 to 86 kHz. The FFT method was able to detect in-plane rotational resonances that were not visually discernable with some caveats: 1) The voltage required to detect the resonance was higher (~2-3x higher than for the translational modes). 2) The rotational motion is not uniform. There is little motion close to the center of rotation, and large motion at the periphery. 3) For translational modes, the selection crop box has little effect. For rotational modes, central crop boxes did not detect resonance, and peripheral crop boxes did. 4) The calibration from attenuation to microns is not consistent, different crop boxes produced different amplitudes of motion. Thus the FFT method is suitable for detecting larger in-plane rotational resonances, for characterizing the rotational frequencies, but not accurate for determining the rotational amplitudes. Table 16 shows the FEM predicted and experimentally measured rotational frequencies with good agreement (15-20%) between predicted frequencies and detected frequencies. The analytical model proved to be even closer, with predictions within 6% of the experimental results.

XY pad	Axis	FEM (kHz)	Model (kHz)	Exp (kHz)	% difference (FEM – Exp) /Exp	% difference (Mod – Exp) /Exp
A: Low Stiffness	$\Theta$	74.0	64.1	64.2	15.3%	0.2%
B: Medium Stiffness	$\Theta$	84.4	74.8	71.9	17.4%	4.0%
C: High Stiffness	$\Theta$	85.9	75.5	71.6	19.9%	5.4%

**Table 16. Table comparing FEM predictions of in-plane rotational resonances with experimental data**

## 8.5 Non-linear Motion and Duffing Equation.

The experiments in the previous sections were carried out at 3.5 Volts. As the displacement varies as the voltage squared, the amplitude produced was a factor of  $\sim 4x$  smaller than the visually detectable amplitude level. This was done for two reasons: 1) to demonstrate the FFT method's ability to measure small signals and 2) to minimize the non-linear effects. Non-linear resonance in MEMS devices has been reported previously, for example Krylov [46] measured it in the few kHz range and Reichenbach [58] measured it in RF resonators in the MHz range. To test the validity of the FFT method for non-linear motion, the voltage was doubled from 3.5 Volts to 7 Volts, quadrupling the thermal actuator amplitude.

From Brennan [59] the Duffing equation can be used to model systems by adding a cubic term to the stiffness:  $kx \rightarrow k_1 x + k_3 x^3$ :

$$\ddot{y} + 2\zeta\omega_0 \dot{y} + \omega_0^2 (y + \alpha y^3) = \omega_0^2 \cos(\omega t) \quad (9.11)$$

where  $y$  is the normalized displacement  $= x/x_o$  and  $x_o$  is the static amplitude  $= F/k_1$ ,  $F$  is the applied force,  $\omega_0$  is the undamped resonant frequency, and  $\omega$  is the driving frequency.  $\alpha$  is the non-linear coefficient:

$$\alpha = \frac{k_3}{k_1} x_o^2 \quad (9.12)$$

Positive and negative  $\alpha$  correspond to softening and hardening springs respectively. In the case of the XY pad studied here, at larger amplitudes the springs open up and deform and sections that were loaded in stiff axial modes are now offset and loaded in softer bending modes, thus  $\alpha$  is negative. Figure 111 shows a plot of Brennan's [59] solution for  $f_o = 75.2$  kHz,  $\zeta = 0.004$  and  $\alpha = -4.0E-6$ . When increasing the frequency, the curve

moves from point A to B, C, D. When decreasing the frequency, the curve moves from point D to E, F, A. Different peak frequencies are observed when scanning *up* ( $f_u$ ) or when scanning *down* ( $f_d$ ) [59]. Also shown in Figure 111 for comparison is 1/4 amplitude:  $\alpha = -0.25E-6$ .

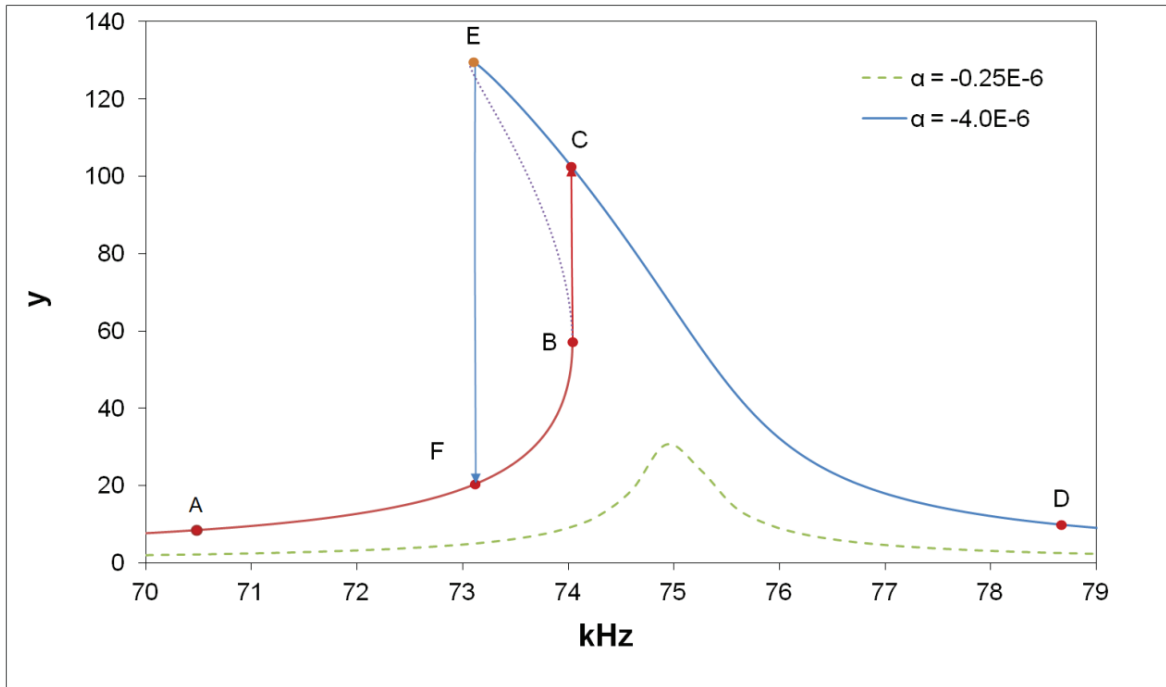


**Figure 111.** Plot of non-linear response of a mechanical system modeled by the Duffing equation for  $f_o = 75.2$  kHz,  $\zeta = 0.004$  and  $\alpha = -4.0E-6$ . Also shown for comparison is 1/4 amplitude  $\alpha = -0.25E-6$  as a dashed line. Letters as indicated in text

The experiments from Section 9.5 were repeated at a higher voltage of 7 Volts and the frequency scanned in both directions (upward and downwards) and the attenuations measured. The amplitudes were then obtained by best fitting the measured attenuation to a Bessel function. Figure 112 shows both backward and forward scanning. Also displayed is a forward scan at 3.5 V (1/4 amplitude). Comparing Figure 112 to Figure 111, the Figure displays the expected behavior outlined above.

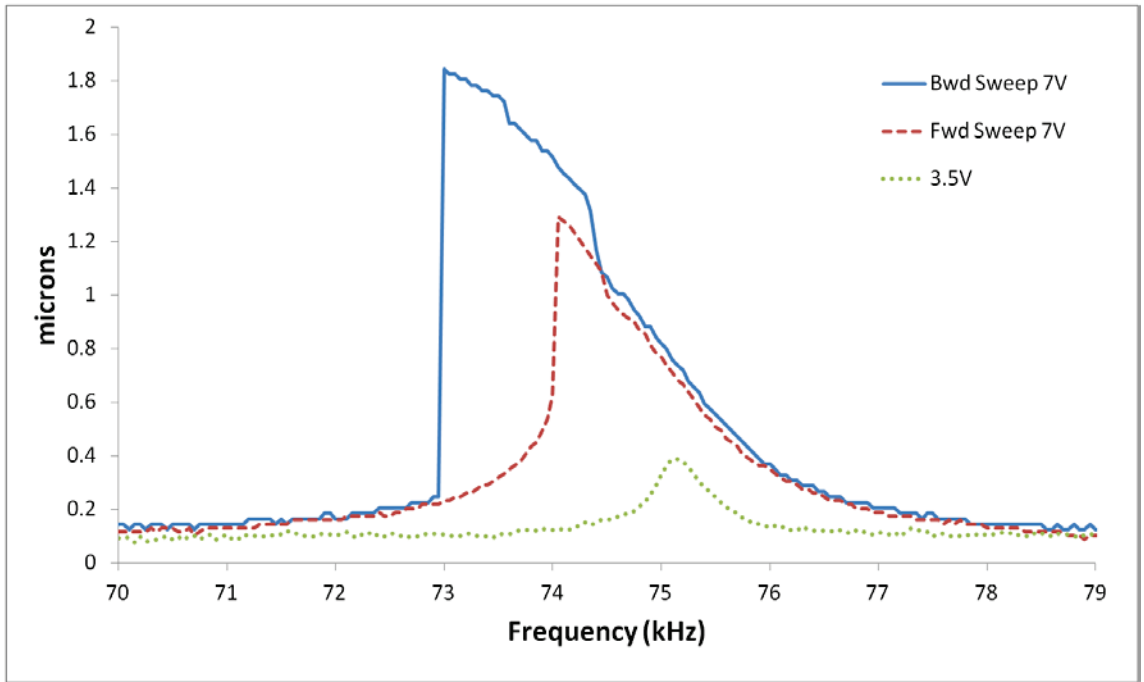


Figure 112. Experimental Duffing response of Device A at 7 and 3.5 Volts. Compare with Figure 14

Brennan [59] provides a formula for the Jump down frequency  $f_d$  (moving from points E to F on Figure 111):

$$\omega = \omega_0 * \frac{1}{2^{1/2}} \left[ 1 + \left( 1 + \frac{3\alpha}{4\zeta^2} \right)^{1/2} \right]^{1/2} \quad (9.13)$$

Figure 113 shows the experimentally measured jump down frequencies  $f_d$  for Device A operated from 3.5 to 7 Volts. Superimposed on the figure is the predicted frequency curve from Equation 13 using  $f_0 = 75.2$  kHz,  $\zeta = 0.004$ , and a voltage dependent  $\alpha$ . To convert from applied voltage to non-linear coefficient  $\alpha$ , from Equation 9.12:  $\alpha$  is proportional to  $x_0^2$ , and  $x_0$  is proportional to  $V^2$ , thus  $\alpha$  is proportional to  $V^4$ .  $\alpha$  was set to  $-4.0E-6$  at 7 Volts and varied with voltage to the fourth power:

$$\alpha(\text{volts}) = -4 * 10^{-6} \left( \frac{\text{volts}}{7V} \right)^4 \quad (9.14)$$

The experimental measurements of Figure 113 agree with the theoretical predictions from [59].

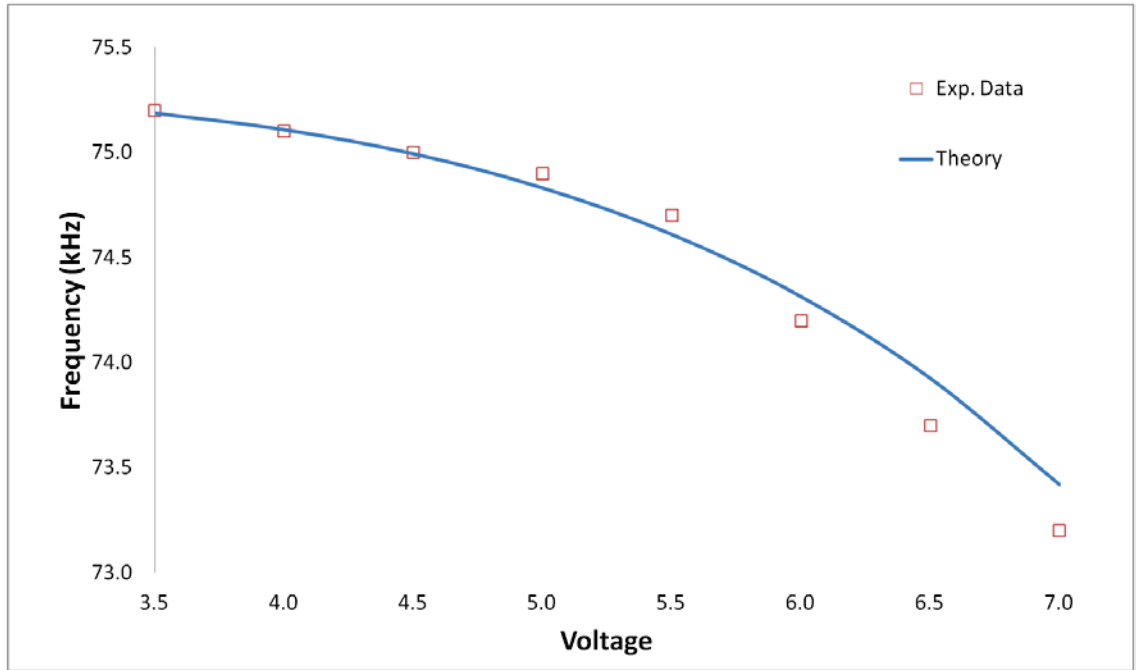


Figure 113. Experimental values of jump down frequency for Device A compared to theory

## 8.6 Summary of Fourier Analysis of Blurred Images

This chapter presented a simple and inexpensive FFT technique for determining the in-plane mechanical resonances and high frequency dynamics of XY pads and general MEMS structures exhibiting period features, using only commonly available camera equipment. A theoretical expression for the blurred induced attenuation of Fourier components using Bessel curves was presented and verified experimentally. Using this method, in-plane resonance frequencies in the 60 to 130 kHz range were detected and at 75 kHz & 3.5 V the amplitude was measured to a subpixel accuracy of between  $\pm 0.027 \mu\text{m}$  using a single image and  $\pm 0.011 \mu\text{m}$  using an average of 10 images. The method was

able to detect in-plane resonance amplitudes an order of magnitude smaller than could be visually observed. Reduction in voltage helped to minimize the non-linear behavior of the MEMS devices.

The presented technique combined blurred image analysis with Fourier analysis of images of repeated spatial patterns. In this study only pre-existing periodic features on the devices were used for the analysis; the method requires no modification to the structures. Any pre-existing periodic feature can be used, but the technique works best when the fundamental wavelength  $\lambda_1$  is short as the Bessel function describing the harmonics' attenuation is non-linear in  $\lambda$ , even a small reduction in  $\lambda_1$  would greatly improve the sensitivity.

## Chapter 9.0 Open and Closed Loop Results

### 9.1 Testing

Testing has shown that reasonable forces and displacements can be generated from devices in order to carry and manipulate various polyMUMPs and SOI plates.

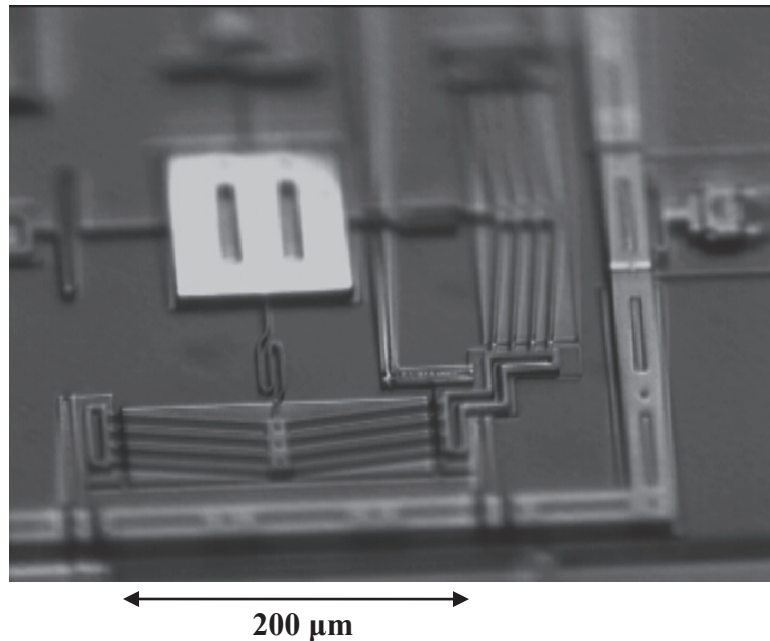


**Figure 114.** Corner of polyMUMPs lift and slide array showing XY pad and portion of the grid

The lift and slide array has also successfully been used to move an SOI platform with two degrees of freedom (X and Y). Rotational motion has not yet been achieved. Figure 115 demonstrates the SOI platform moving to different positions over a 2 x 2 portion of a larger 3 x 3 array. This motion is captured in Figure 116 showing a blurred composite image of the SOI platform moving along the array, and Figure 117 demonstrating four sequential frames showing horizontal motion.

This chapter describes in detail the results of testing both the open loop and closed loop control systems.

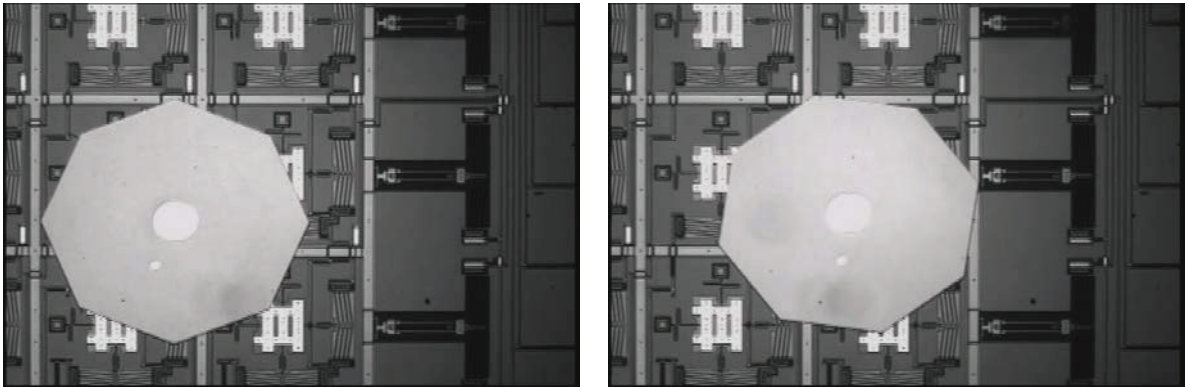


Figure 115. Two frames demonstrating motion of an SOI platform

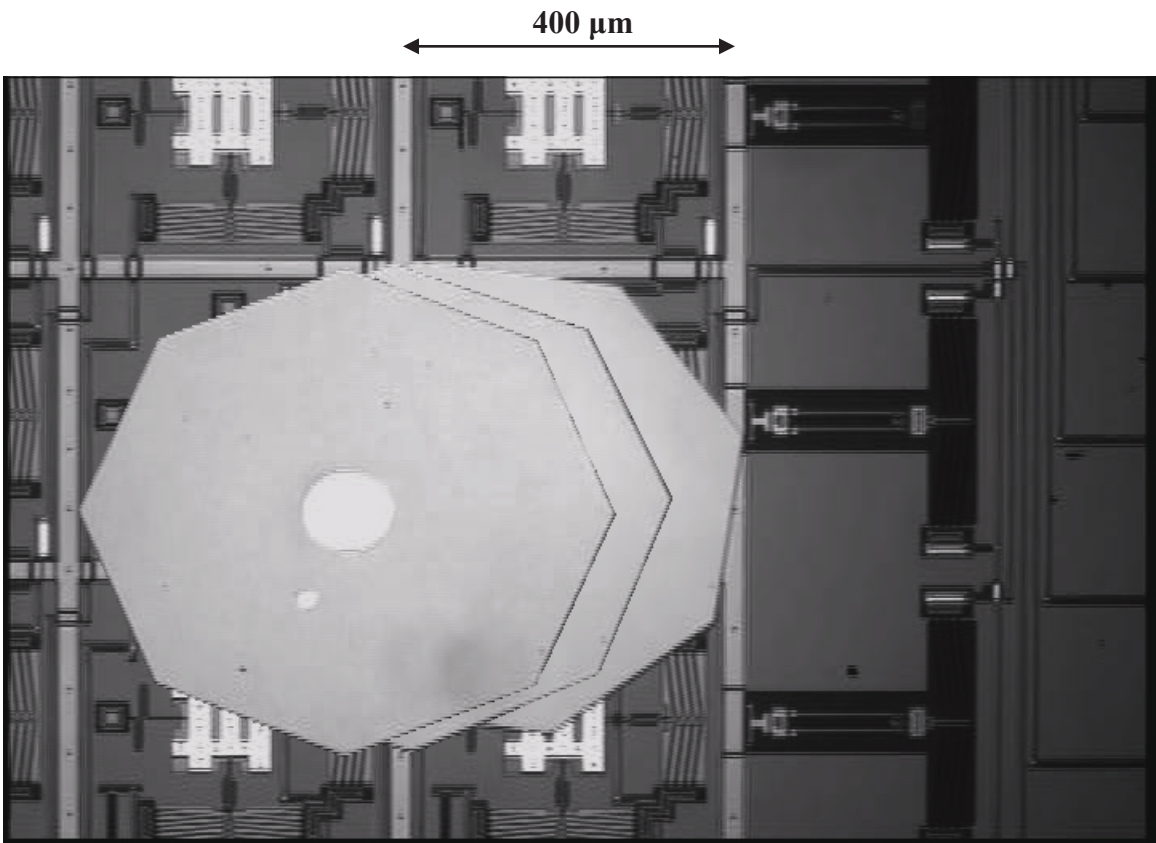


Figure 116. Composite image showing motion of SOI platform along the array



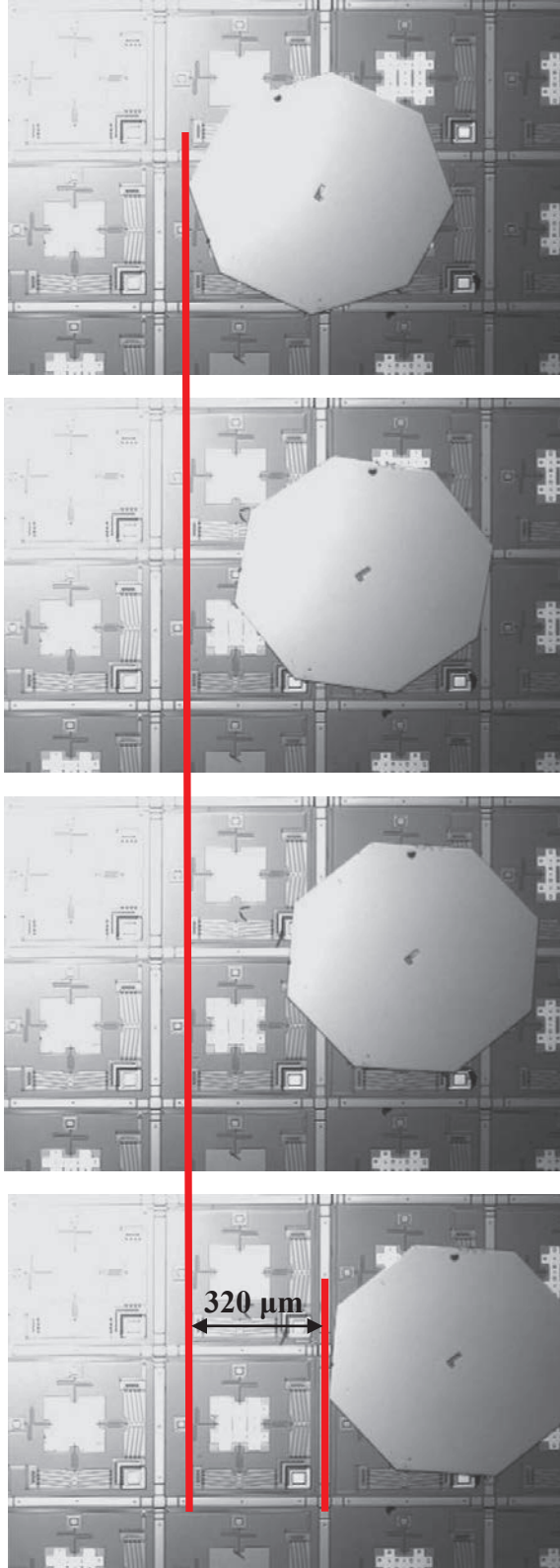


Figure 117. Motion of platform shown in four frames.

## 9.2 XY Pad Displacement

The motion of the plate is created from a displacement of the XY pads. The displacement of the XY pads is a function of the voltage supplied to the XY pad chevrons, and the spring stiffness. Since the chevron is connected to the XY pad through an axially stiff paperclip spring, anchored to the substrate on the opposite side of the pad with an axially soft S-spring and cross coupled with a paperclip and S-spring, both which are relatively soft transversely, a majority of the chevrons motion is directly transferred to the XY pad. While the determination of the static displacement of the XY pad given a DC input signal is relatively simple, of greater concern was the motion as a function of an AC input signal. As previously described in the last Chapter, the thermal time constant  $\tau$  results in a reduction in chevron displacement with increased frequency (Hickey [57]). Also note that the mass of the plate over the XY pad will also further reduce the displacement of the pad, though the exact effect cannot be measured directly.

The exact motion of the uncovered XY pad was determined experimentally by analyzing motion captured on video. Video was captured using a high speed Point Grey<sup>TM</sup> camera model GRAS-03K2M-C: a 1.4MP colour 1394b Firewire CCD Camera with a maximum resolution of 640x480 pixels. The camera was mounted on a Wentworth Probestation model MP0901 with a magnification of 25x. A video strip of dimensions 640x50 pixels was used to improve performance, resulting in a frame rate of 341 frames per second. In this configuration the camera provided a field of view of  $\sim 288 \times 23 \mu\text{m}$  and a resolution of  $0.45 \mu\text{m}/\text{pixel}$ . Video processing was done with National Instruments Vision Assistant 2009 using an edge detection routine to measure the relative displacement of the XY pad.

A square wave was supplied to the chevron through the Open Loop Labview program previously described. The square wave ranged from 0 V to the required voltage at the specified frequency. Figure 118 shows the displacement of the XY pad at various voltages from 7 V - 12 V at 4Hz. The graph is normalized to the average “off” position

and allows the relative displacement of the pad to be calculated from an average of each peak with the chevron in the “on” position.

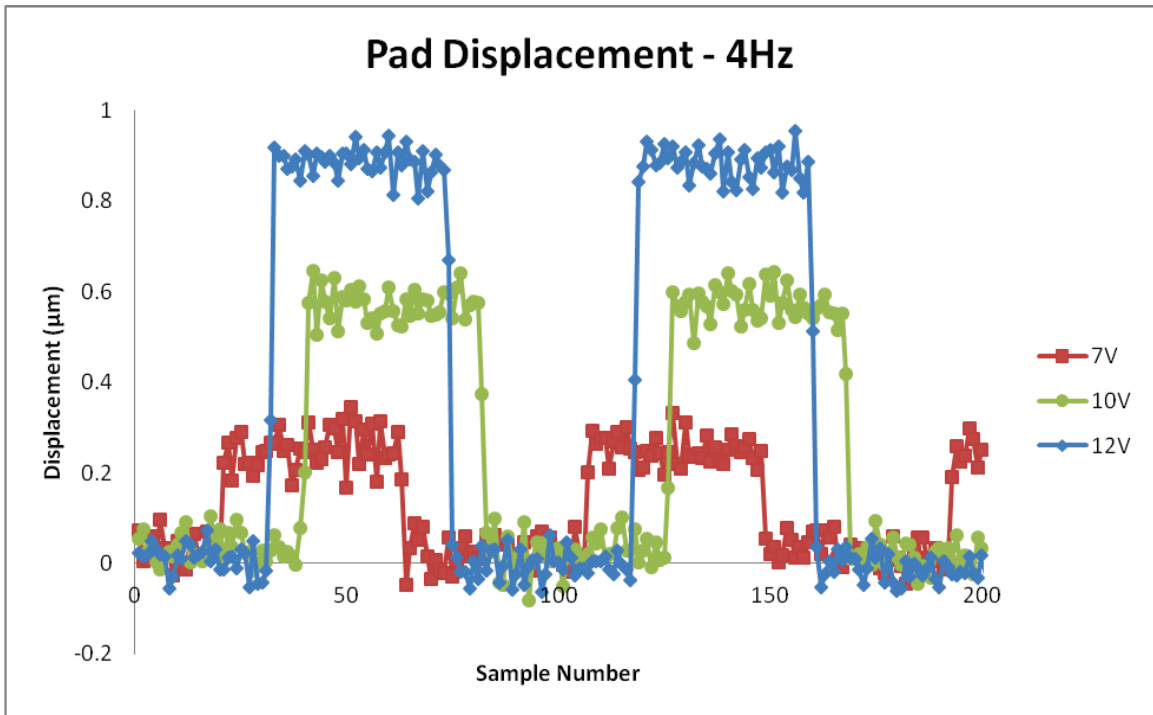


Figure 118. XY pad displacement; 7 V, 10 V and 12 V at 4 Hz

Figure 119 to Figure 123 show the XY pad displacement over a range of frequencies. It is clear that once the frequency exceeds 50 Hz the sampling rate (341 frames/sec) is insufficient to collect accurate data. At 100 Hz there are less than four points per cycle and the maximum displacement of the XY pad may not be correctly captured. At 50 Hz and below there are clearly at least three points along the maximum pad displacement ensuring the full displacement is correctly captured.

Figure 124 graphs the average pad displacement at each sampled voltage over a frequency range of 4 Hz to 100 Hz. There is a slight downward trend (even ignoring the data from the 100Hz sampled data) that is consistent with the expected trend for an AC input to a chevron. The average displacement was 0.28 μm at 7 V, 0.55 μm at 10 V and 0.89 μm at 12 V.

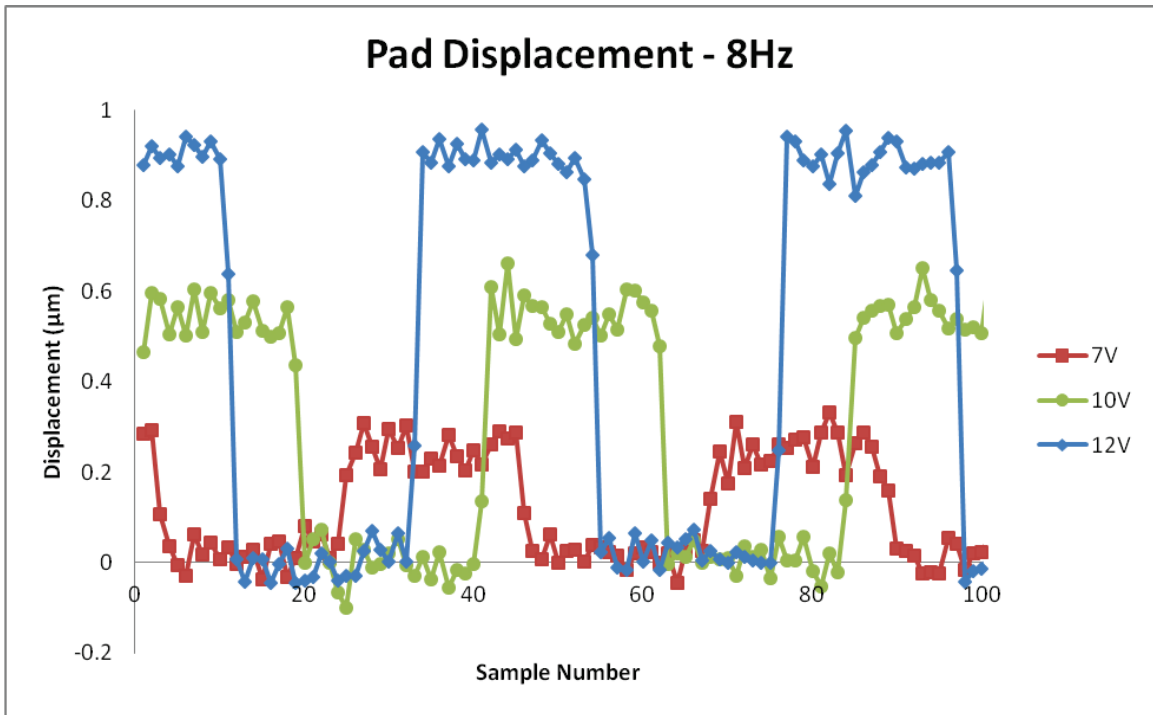


Figure 119. XY pad displacement; 7 V, 10 V and 12 V at 8 Hz

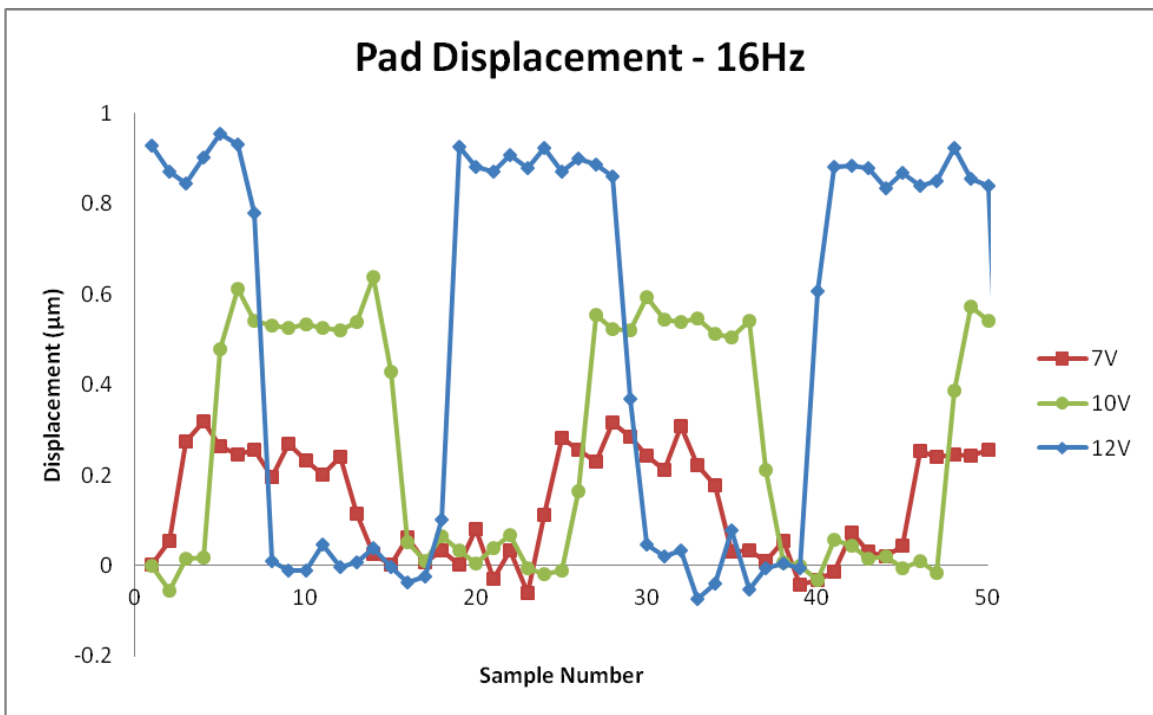


Figure 120. XY pad displacement; 7 V, 10 V and 12 V at 16 Hz

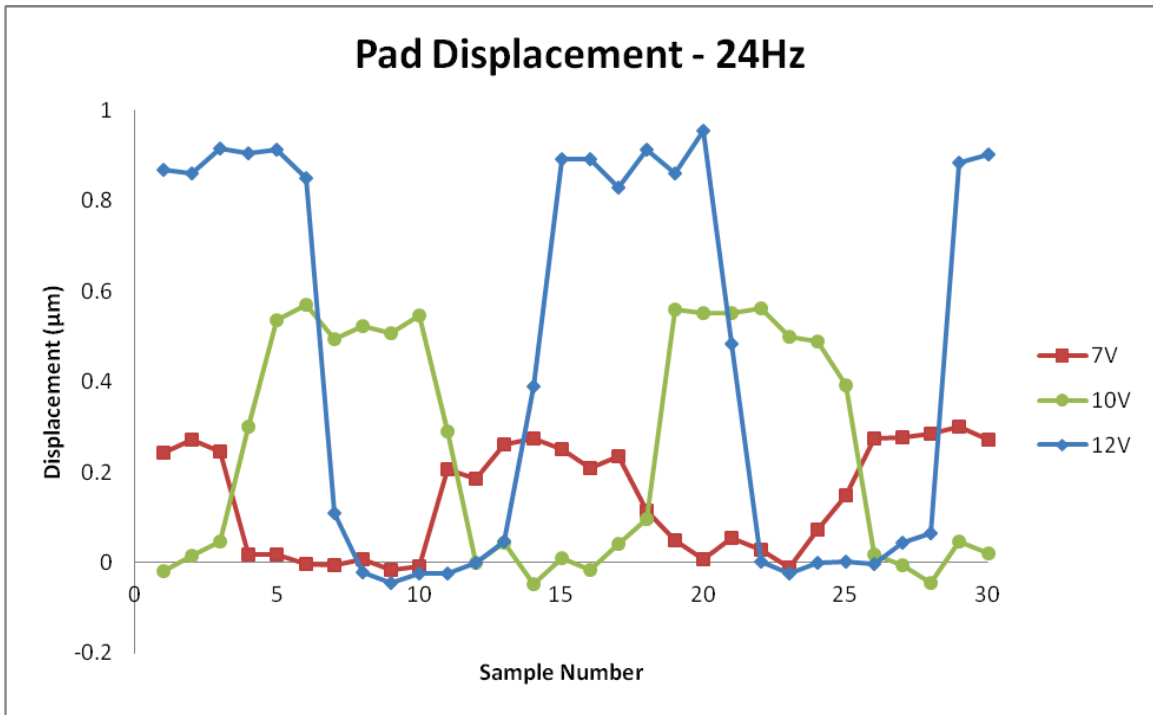


Figure 121. XY pad displacement; 7 V, 10 V and 12 V at 24 Hz

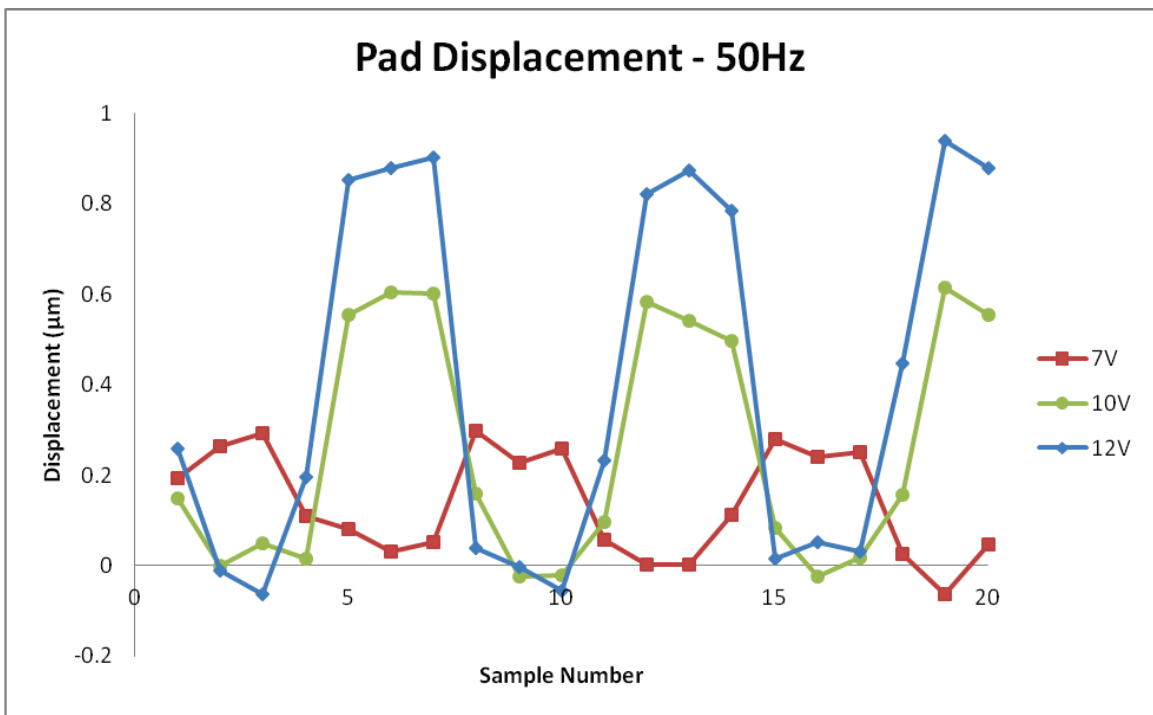


Figure 122. XY pad displacement; 7 V, 10 V and 12 V at 50 Hz

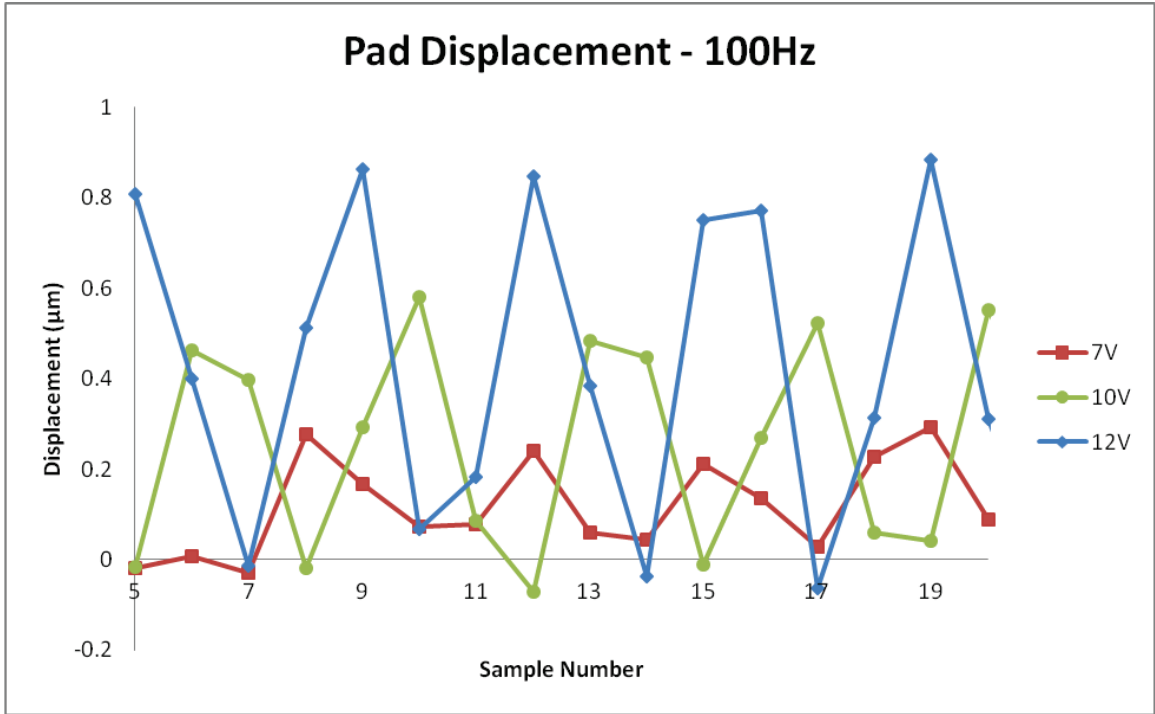


Figure 123. XY pad displacement; 7 V, 10 V and 12 V at 100 Hz

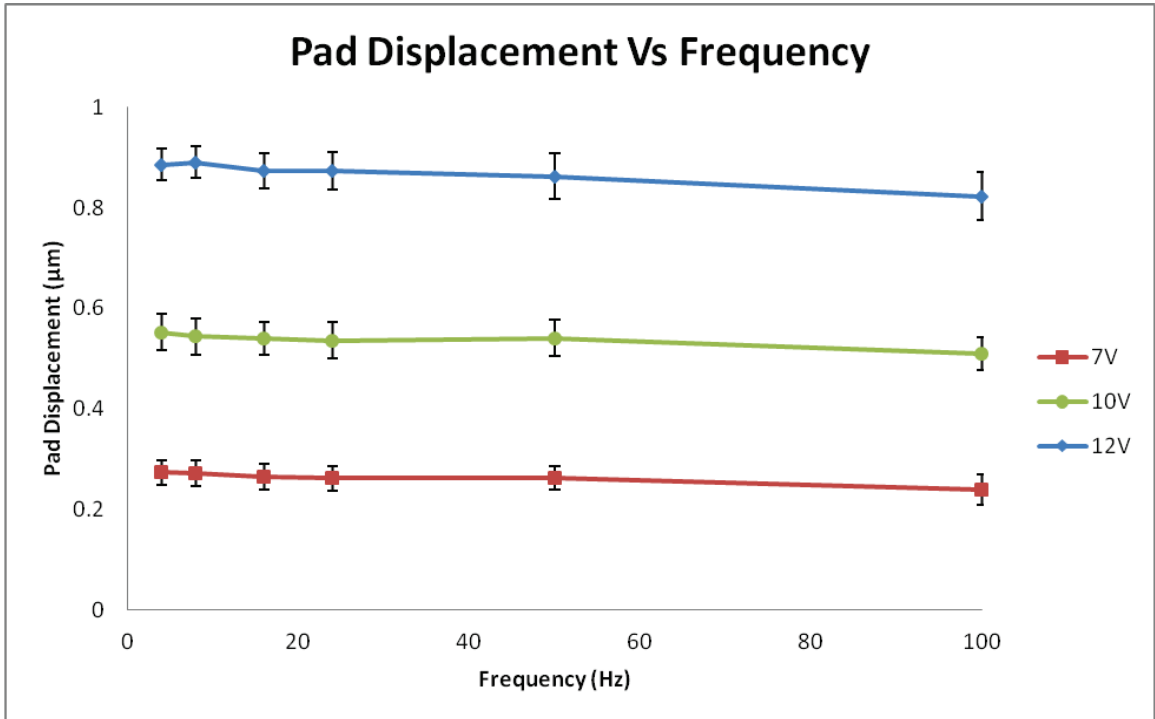


Figure 124. average XY pad displacement; 7 V, 10 V and 12 V at 4-100 Hz

### 9.3 Open Loop

The open loop control system developed using Labview (fully outlined in Chapter 5) allows for simple control of the plate. Figure 125 a series of horizontal and vertical paths. For each path, the control system was set to move the plate 100 steps in a given direction.

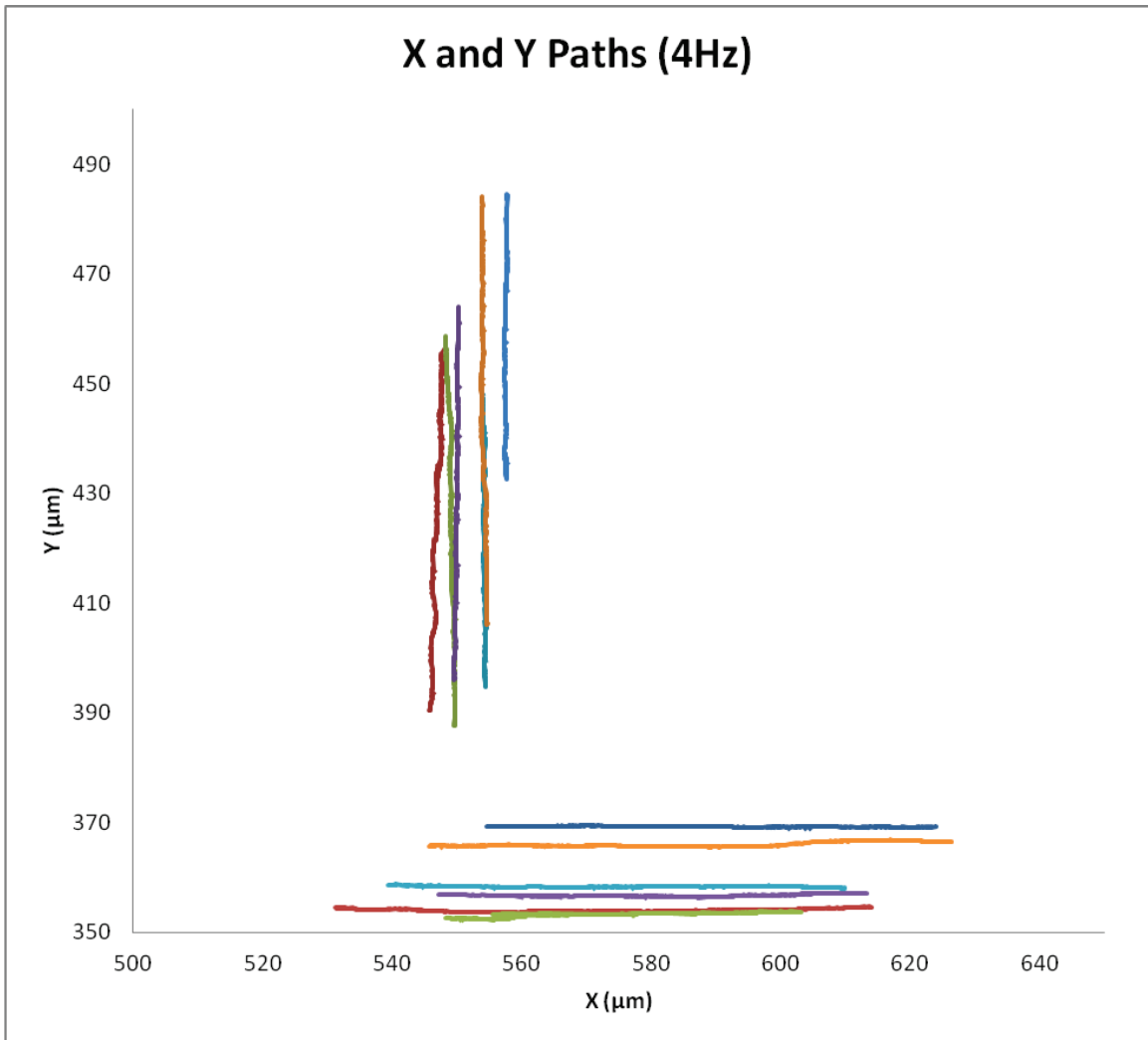


Figure 125. Plate travelling in a series of horizontal and vertical linear paths. XY Pads set at 12 V

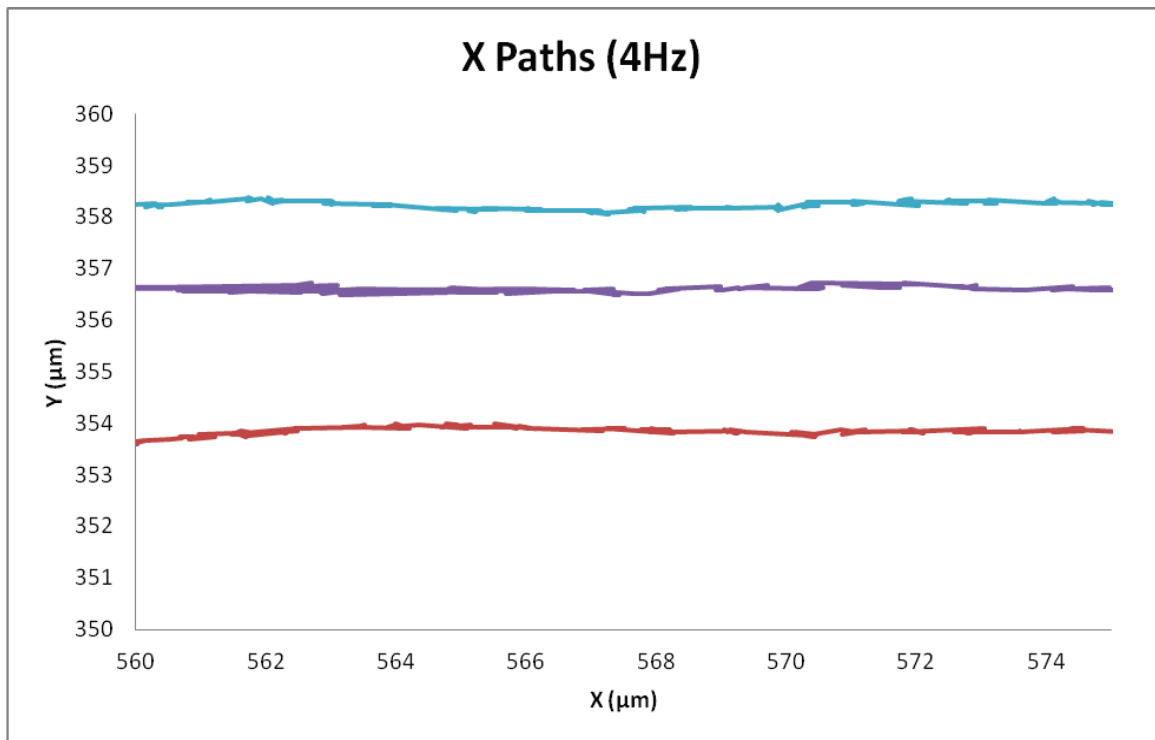
Table 17 shows the displacement and perpendicular disturbance (covered in later section) for the linear paths shown in Figure 125. The displacement and perpendicular

disturbance in each axis are well within the standard deviation of each other. XY Pads were set at 12 V for all runs.

	X ( $\mu\text{m}$ )	X Perpendicular disturbance ( $\mu\text{m}$ )	Y ( $\mu\text{m}$ )	Y Perpendicular disturbance ( $\mu\text{m}$ )
	82.8	2.1	65.9	1.2
	55.0	1.4	71.0	1.5
	66.2	0.9	68.1	0.8
	70.6	0.7	54.4	0.8
	80.6	1.0	78.0	1.3
	69.5	0.6	52.0	0.4
Average	70.8	1.1	64.9	1.0
Std Dev	10.1	0.6	10.0	0.4

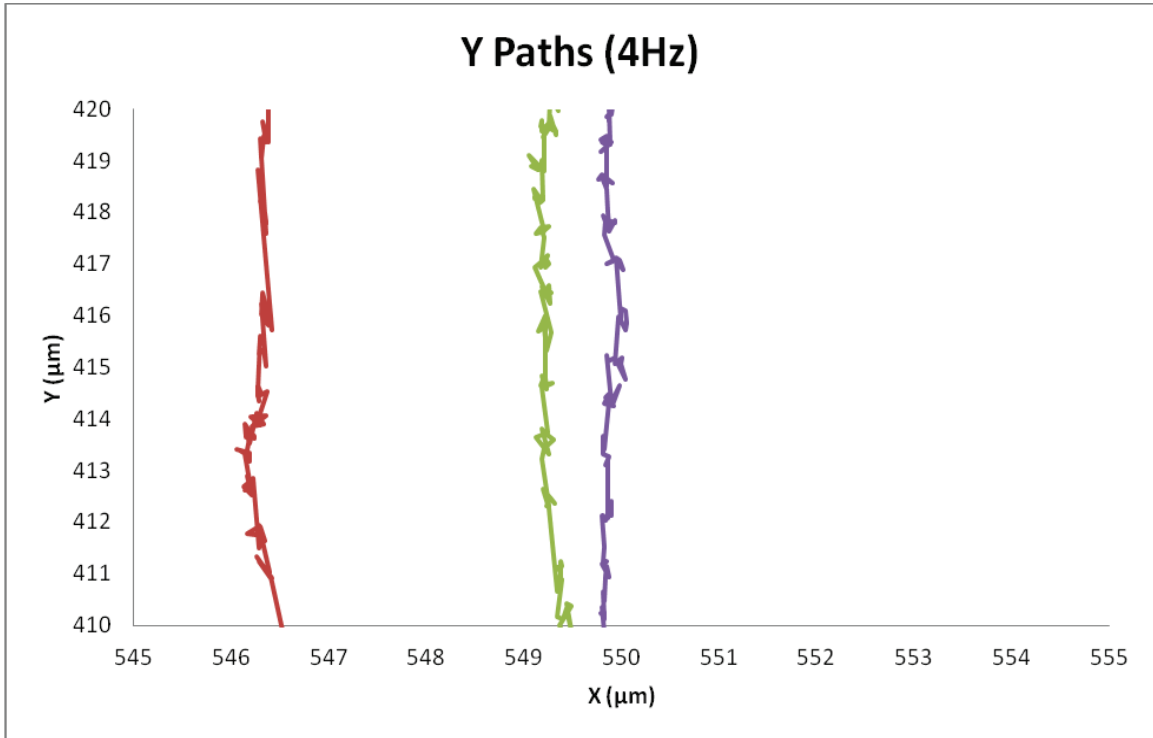
**Table 17. Displacement and perpendicular disturbance from sample of open loop linear paths (Figure 125)**

Figure 126 and Figure 127 demonstrate how the plates move along the surface with zoomed in views of Figure 125. The motion is somewhat jagged as the plates move forward and then slightly backwards.



**Figure 126. Zoomed in view of the horizontal paths of three lines from Figure 125**





**Figure 127. Zoomed in view of the vertical paths of three lines from Figure 125**

This was repeated for a range of voltages and frequencies, and the data was then compiled to show the related speed of the plate (Figure 128). There is a clear linear trend for the speed; increasing with voltage and frequency. Note that at 100 Hz, with a 12 V input to the XY pad chevron, a speed of 56.8 μm/s was obtained.

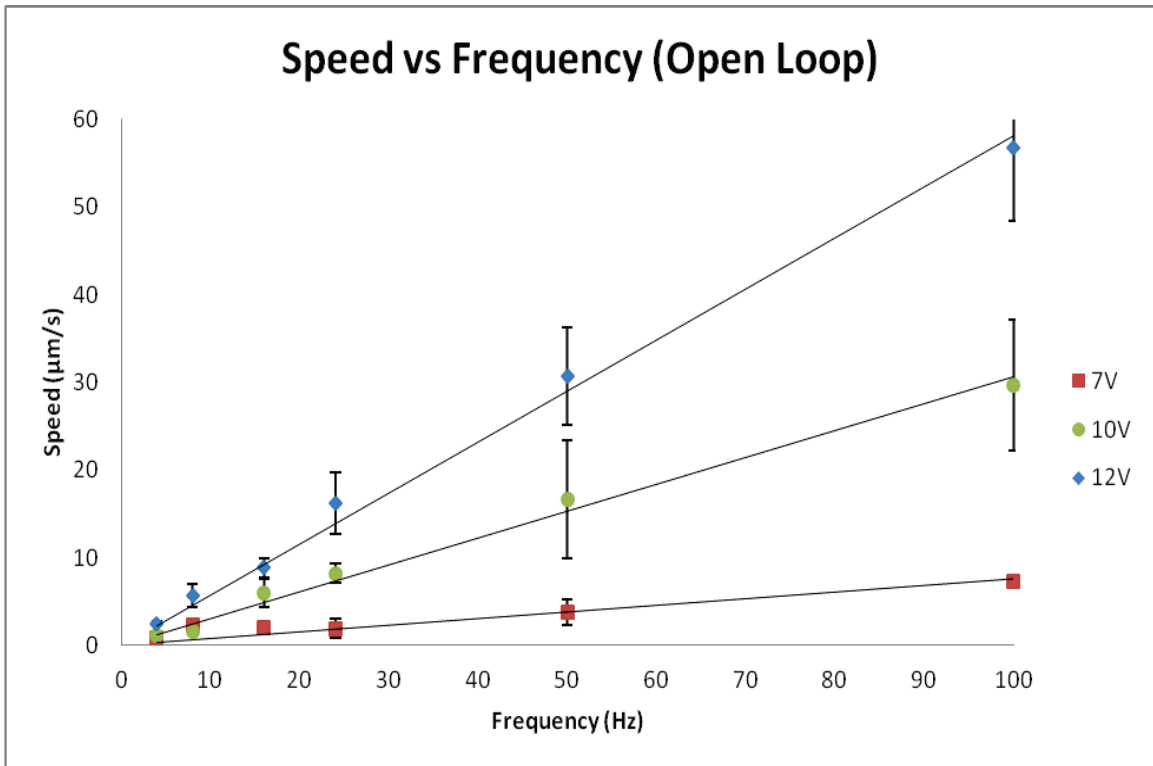


**Figure 128.** Speed of the plate; 7 V, 10 V and 12 V over a frequency range of 4-100 Hz

As there are a number of frictional variations and slight height differences over the platform, there is often a fair amount of off-center drag and resulting perpendicular motion. This is defined as perpendicular disturbance. It was well noted that there was a significant perpendicular disturbance associated with motion over the lift and slide platform. Figure 129 shows the perpendicular disturbance speed. As with linear plate speed, the perpendicular disturbance increases with increasing voltage and frequency. From Figure 130 it can be seen that the perpendicular disturbance is a relatively constant percentage of the plate speed at any given voltage. However, it should be noted that as the voltage increases, the perpendicular disturbance relative to the linear displacement decreases. The perpendicular disturbance averages almost 20% when driving the XY pads at 7 V, and averages about 10% when driving the pads at 12 V. Figure 131 demonstrates the perpendicular disturbance of a plate in relation to the horizontal motion travelled.

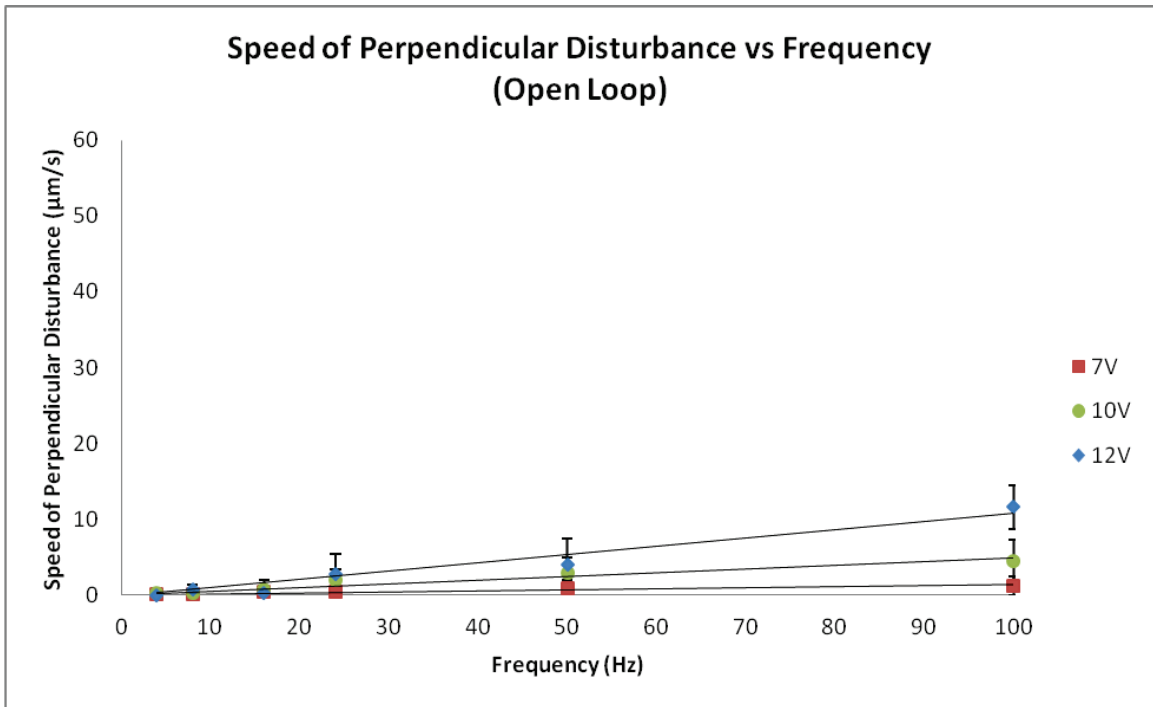


Figure 129. Speed of plate in direction perpendicular to intended path (perpendicular disturbance)

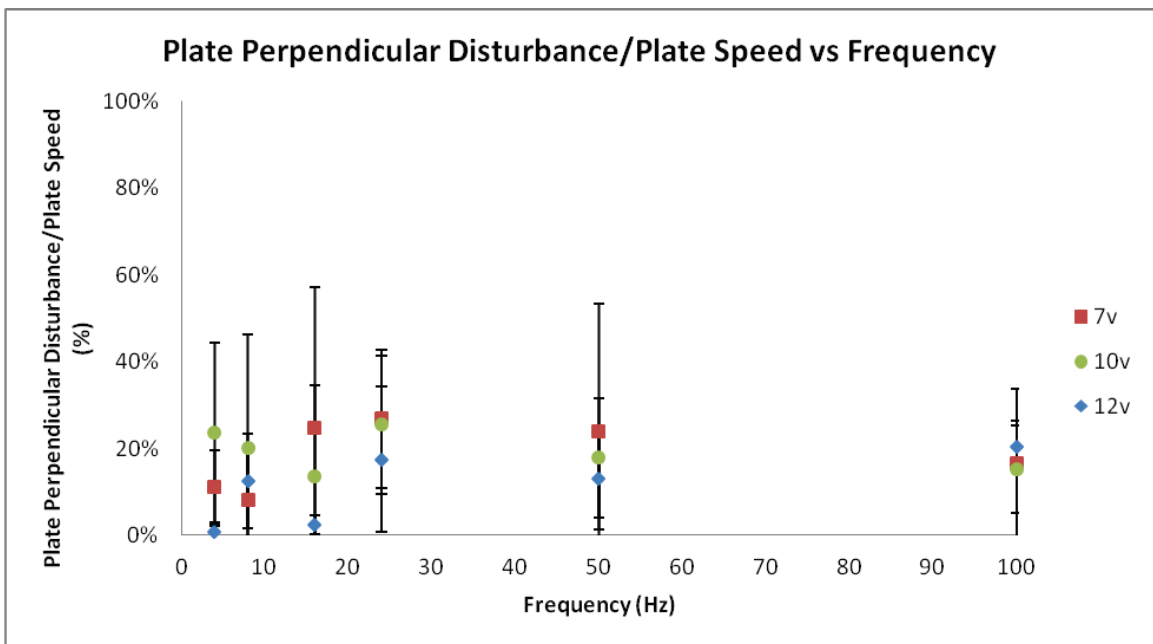
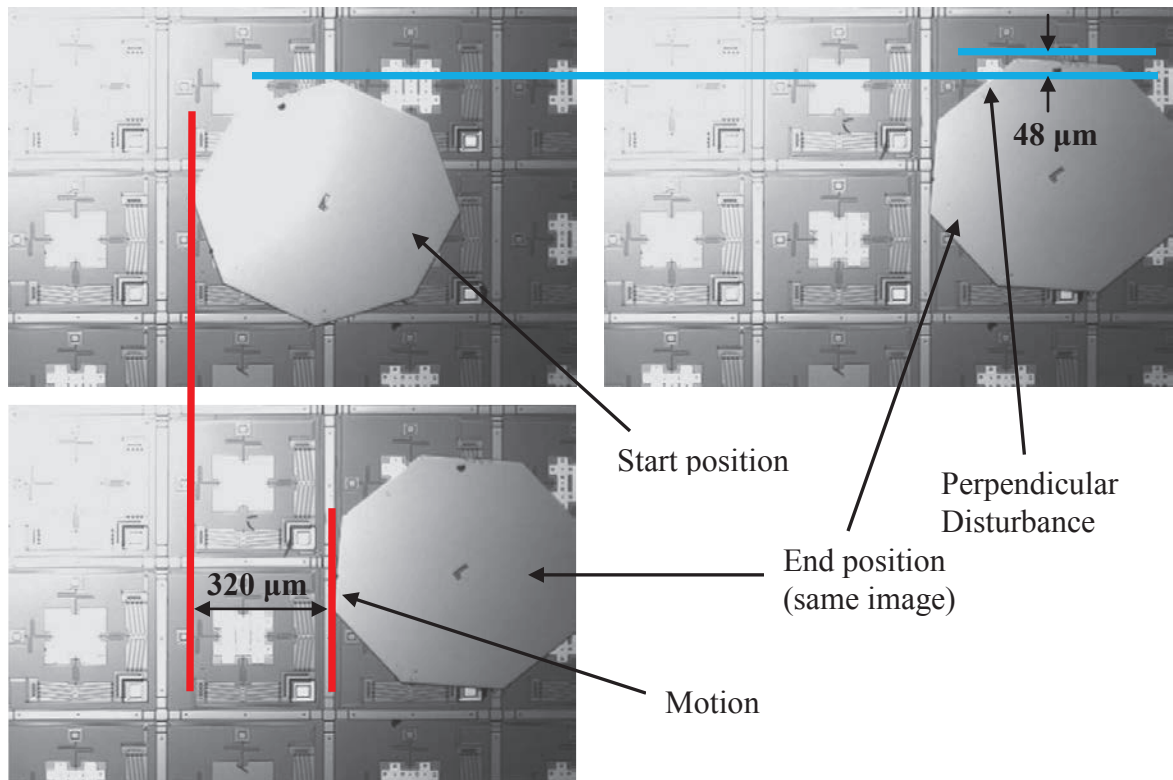


Figure 130. Plate perpendicular disturbance relative to the plate speed



**Figure 131. Frames showing the start and finish position of a platform using open loop control. The platform has a perpendicular disturbance of 48 μm while travelling 320 μm (15%)**

Figure 132 shows the average plate displacement for each single cycle (step) taken by the open loop control system. The plate displacement is relatively linear and constant for each voltage. The displacement is approximately 0.08 μm per step at 7 V, 0.32 μm per step at 10 V, 0.6 μm per step at 12 V.

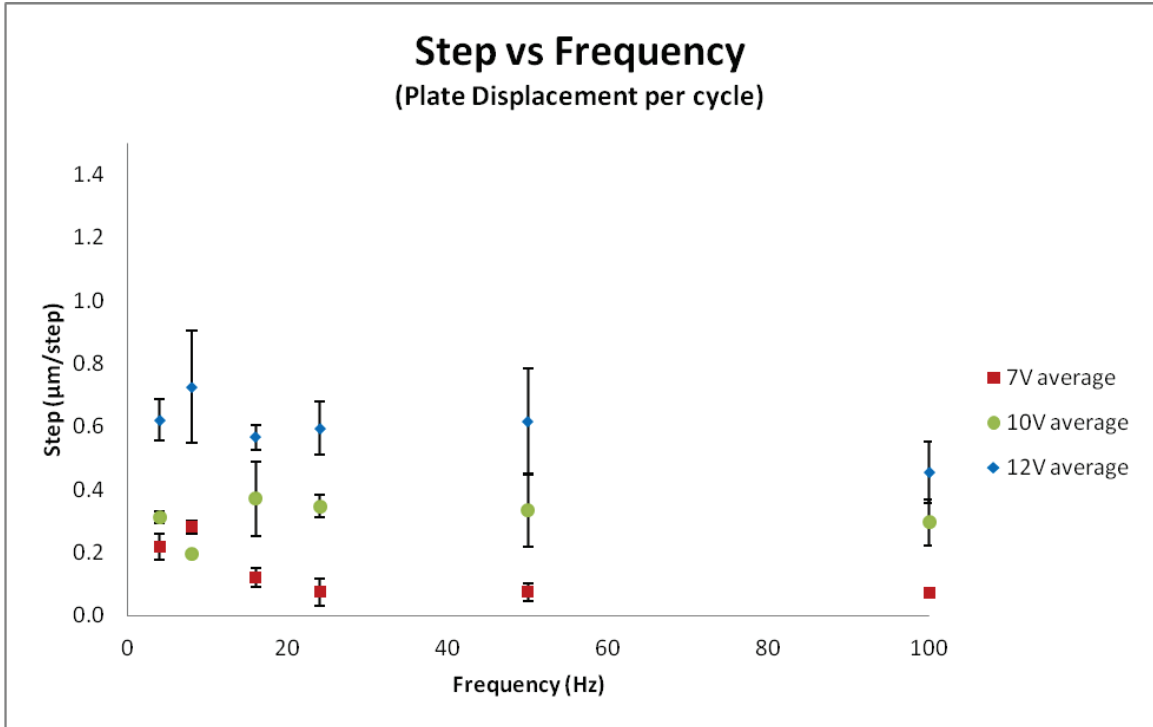


Figure 132. Displacement of each step vs frequency

Figure 133 shows the equivalent perpendicular disturbance per step. Perpendicular disturbance ranges up to approximately 0.1 µm, increasing as voltage increases, however, since the linear displacement steps increase significantly more as voltage increases, it is clear the the affect is more noticeable at lower voltages as was noted in Figure 130.

Finally, a new parameter can be defined; traction. Traction is the actual plate displacement relative to the XY pad displacement (Figure 134). There is a tendency to have better traction at lower frequencies. As the frequency increases, the traction settles between 30-60%.

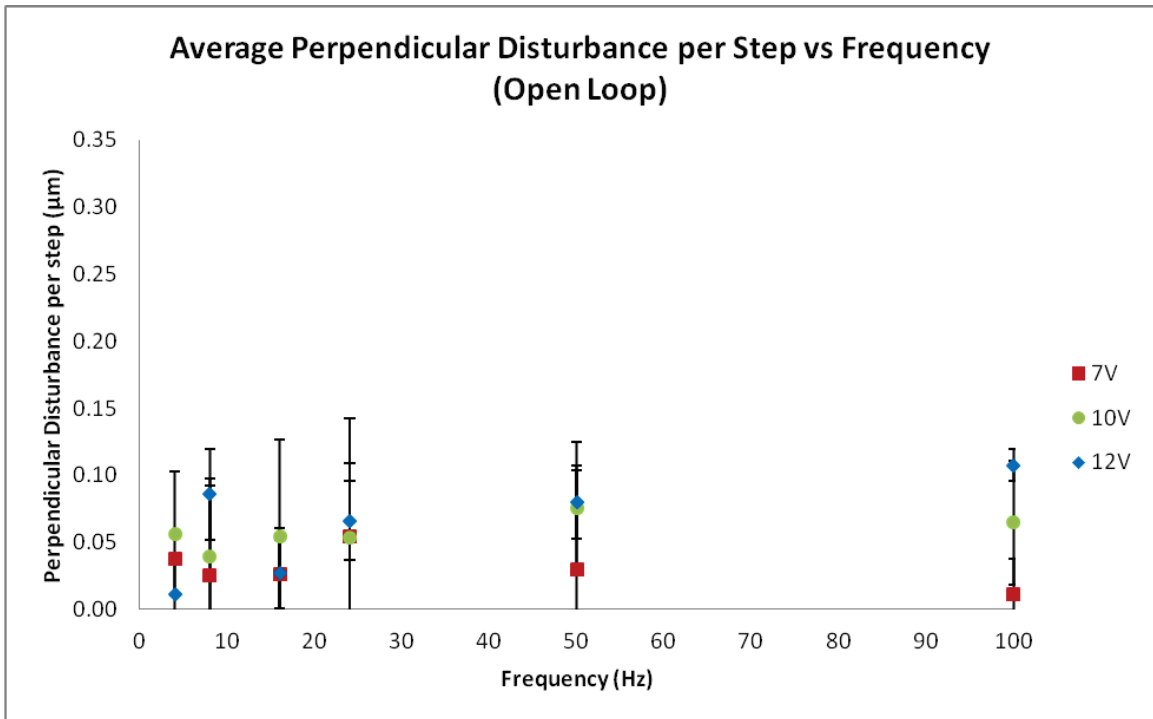


Figure 133. Average perpendicular disturbance per step vs frequency

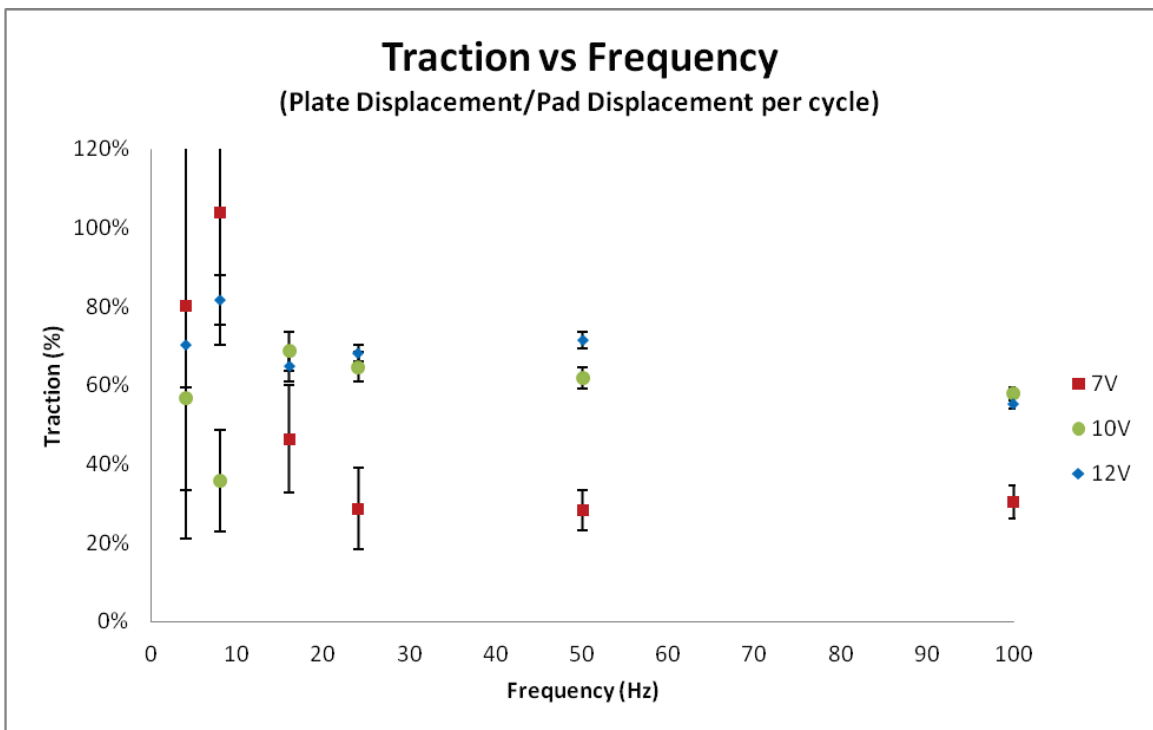


Figure 134. Plate displacement vs pad displacement (traction)

## 9.4 Closed Loop

A number of factors were retested with closed loop control to show consistency with open loop control. Testing was repeated at 7 V and 12 V over a frequency range of 4 Hz to 100 Hz.

Figure 135 shows very similar results to that of the open loop control for the speed of the plate over the given frequency range. Though the computer is processing each image to determine positional information between each step, the processing speed is sufficient not to cause any appreciable lag over the functional frequency range. The average maximum speed reached for 100 Hz and 12 V control was approximately 46  $\mu\text{m/s}$ .

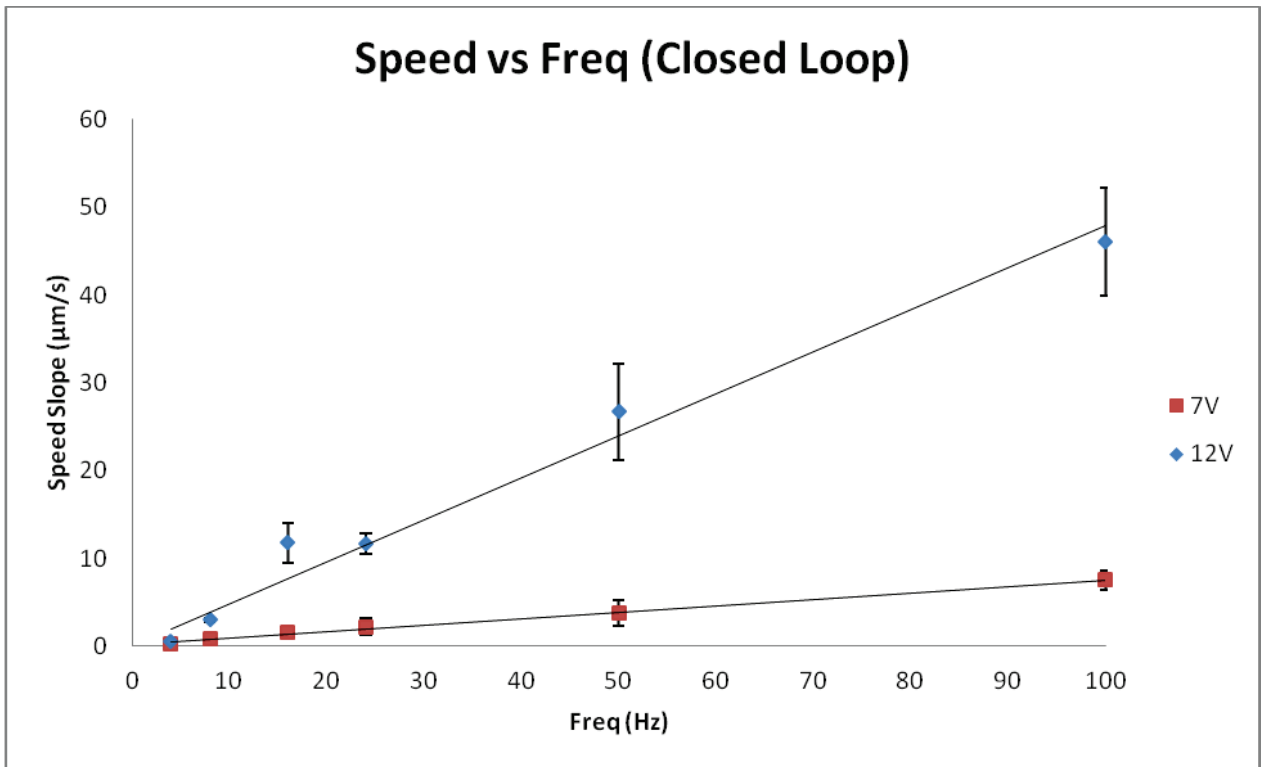


Figure 135. Speed of plate at various voltages and frequencies

The next factor for study was the perpendicular disturbance associated with closed loop control. While there is still a significant natural perpendicular disturbance, the closed loop system compensates for the perpendicular disturbance on a step by step basis. A comparison of Figure 129 and Figure 136 shows that the average perpendicular

disturbance of plates with the close loop control system is significantly less. This holds true when the plate is at the edge of “accuracy” setting. In the closed loop control system, accuracy can be set. The control system will attempt to keep (or move) the plate at the axis position, plus or minus the degree of accuracy. This concept will be further explained later in this Section.

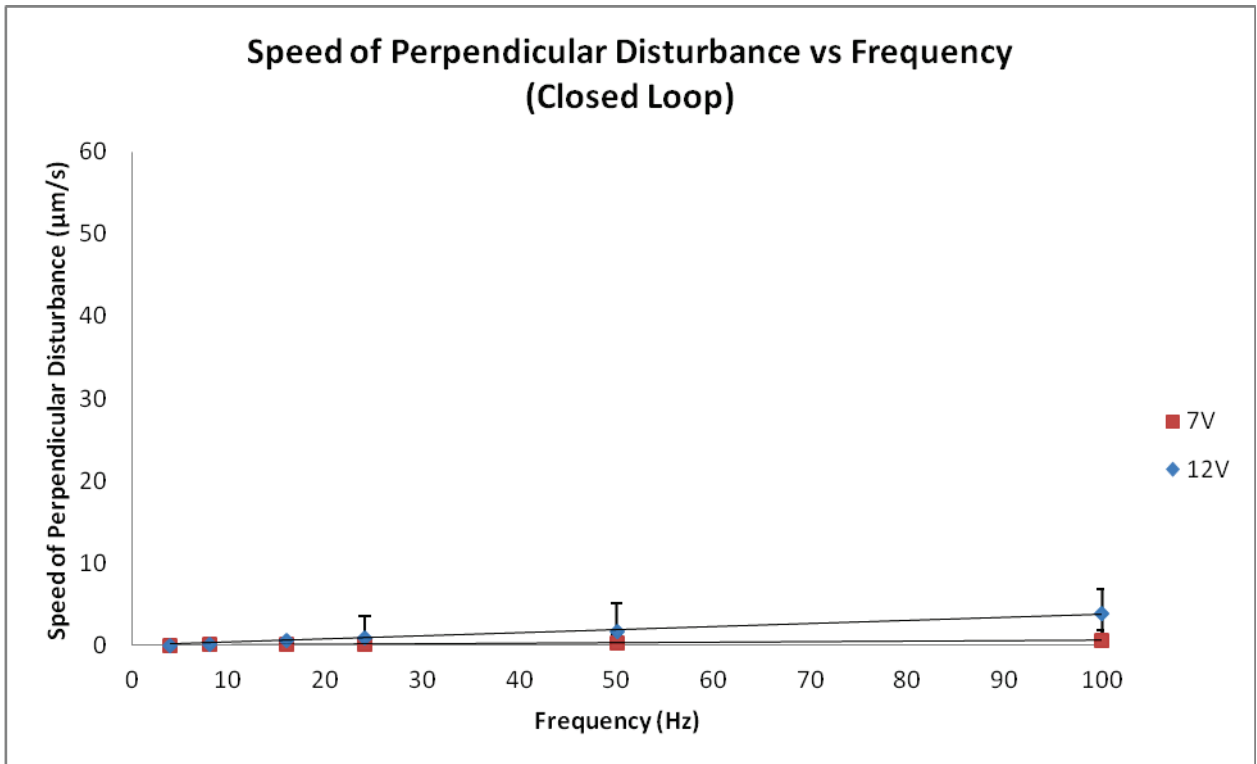


Figure 136. Speed of plate perpendicular disturbance

Figure 137 shows the plate perpendicular disturbance in relation to the plate speed for the closed loop control system. Perpendicular disturbance with the closed loop system is less than 10% of the plate speed, which is a significant improvement over the open loop control system that averaged between 15% to 45%.

Figure 138 shows the average perpendicular disturbance per step. The actual perpendicular disturbance per step is very similar that of the open loop system (Figure 133). However, once at the edge of the accuracy window, everytime the plate moves out



of the window the pad is moved to push the plate back into the window and maintain the accuracy requirement. The net result is very little overall perpendicular disturbance.

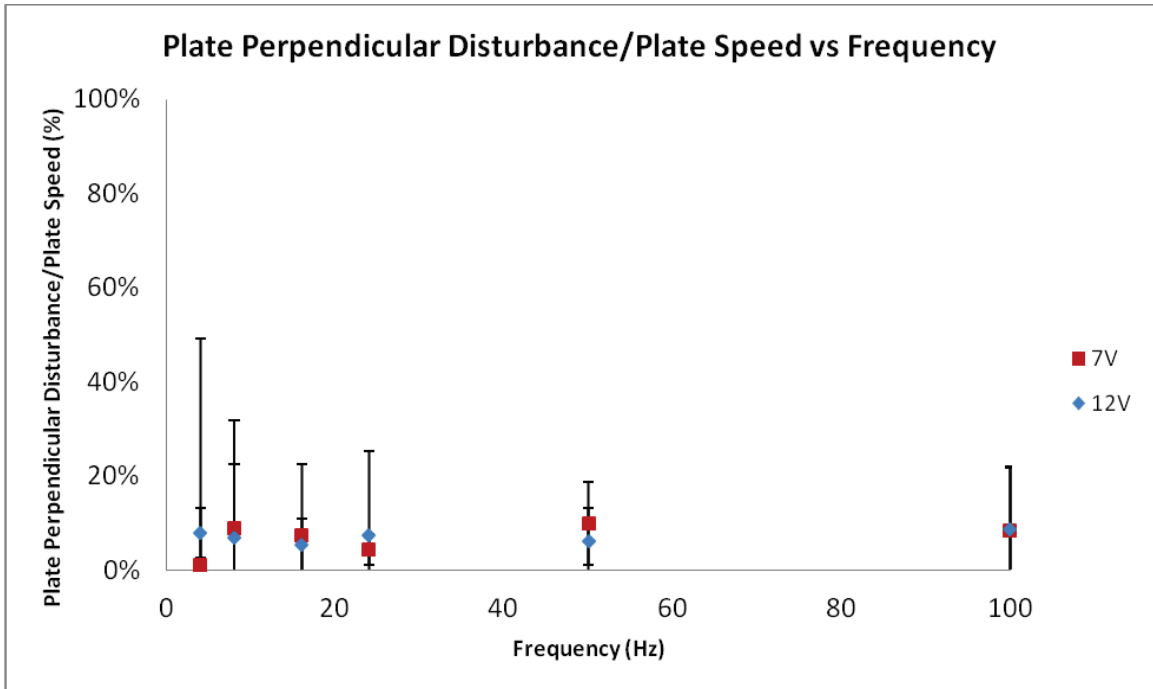


Figure 137. Plate perpendicular disturbance relative to the plate speed

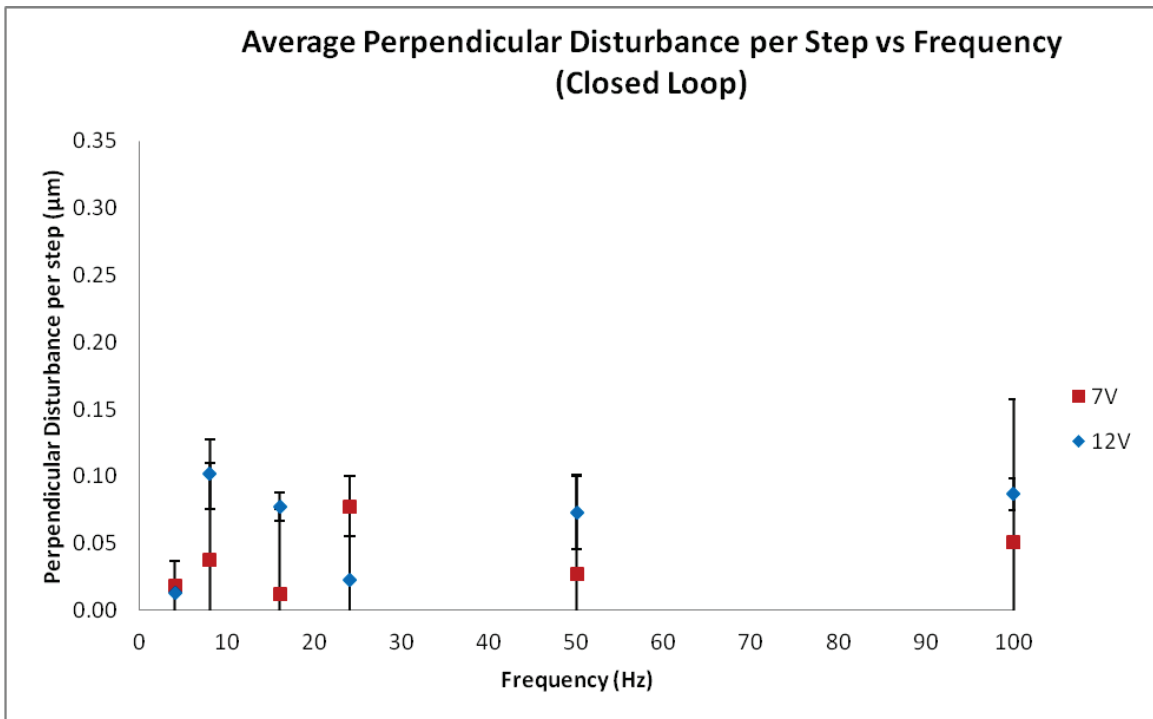
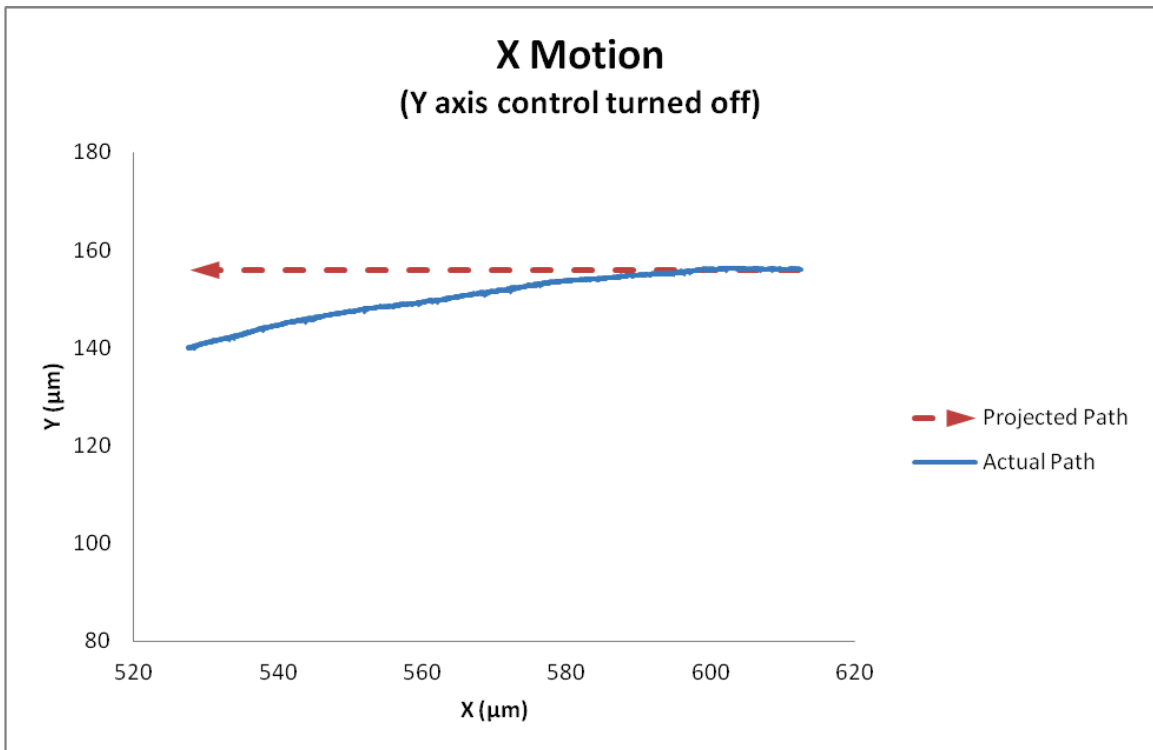


Figure 138. Average plate perpendicular disturbance for each closed loop cycle (step)

Figure 139 and Figure 142 show the results of turning off the axis control on either the X or Y axis. Once the axis control is turned off, the plate will drift off the path with no attempt to make any corrections. The axis control is turned off by simply making the axis delta (difference between the current location and the desired location along the given axis) zero regardless of the current location.



**Figure 139. The effect of perpendicular disturbance on long range X motion with the closed loop Y axis control turned off. XY Pads set at 7V**

Figure 139 shows motion with the XY Pads set at 7 V, while Figure 142 shows motion with them set at 12 V. Figure 140 and Figure 143 show the close up views of the paths with axis control turned off in the Y and X directions respectively. Steps are clearly greater at the higher voltage setting, likewise is the resultant perpendicular disturbance. Figure 140 shows how the net platform perpendicular disturbance of a badly drifting platform can be kept within 2 µm (set accuracy) of the projected path using the axis control.

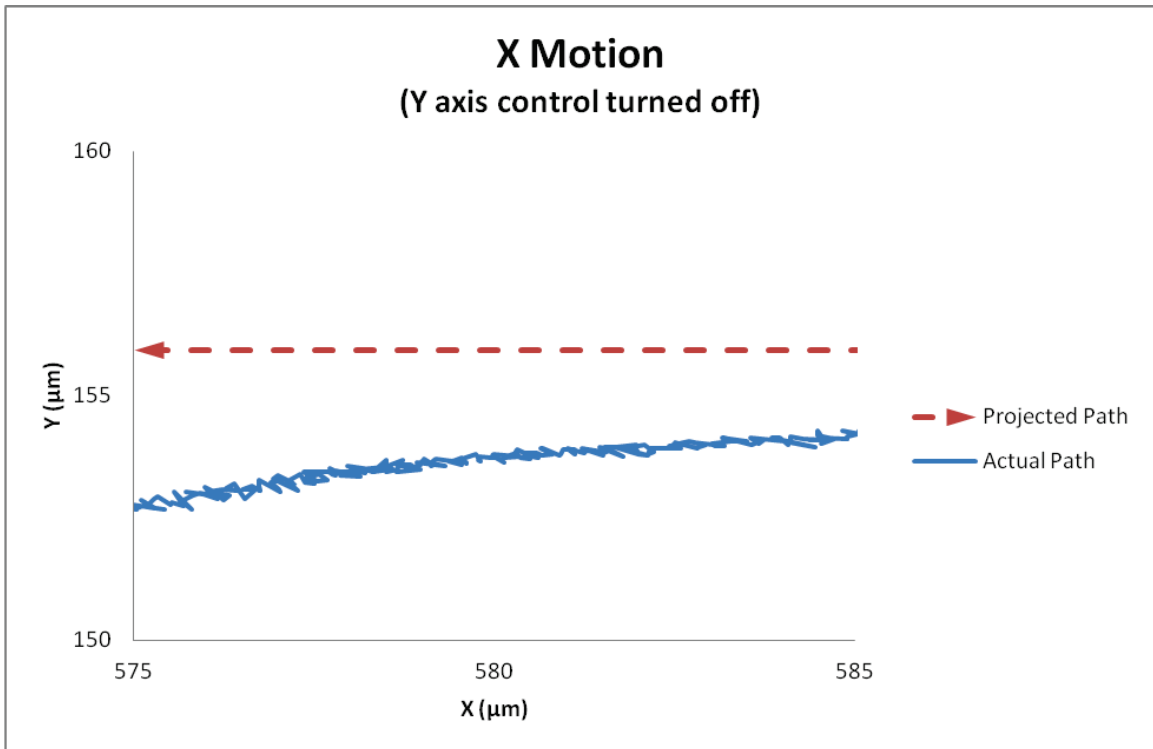
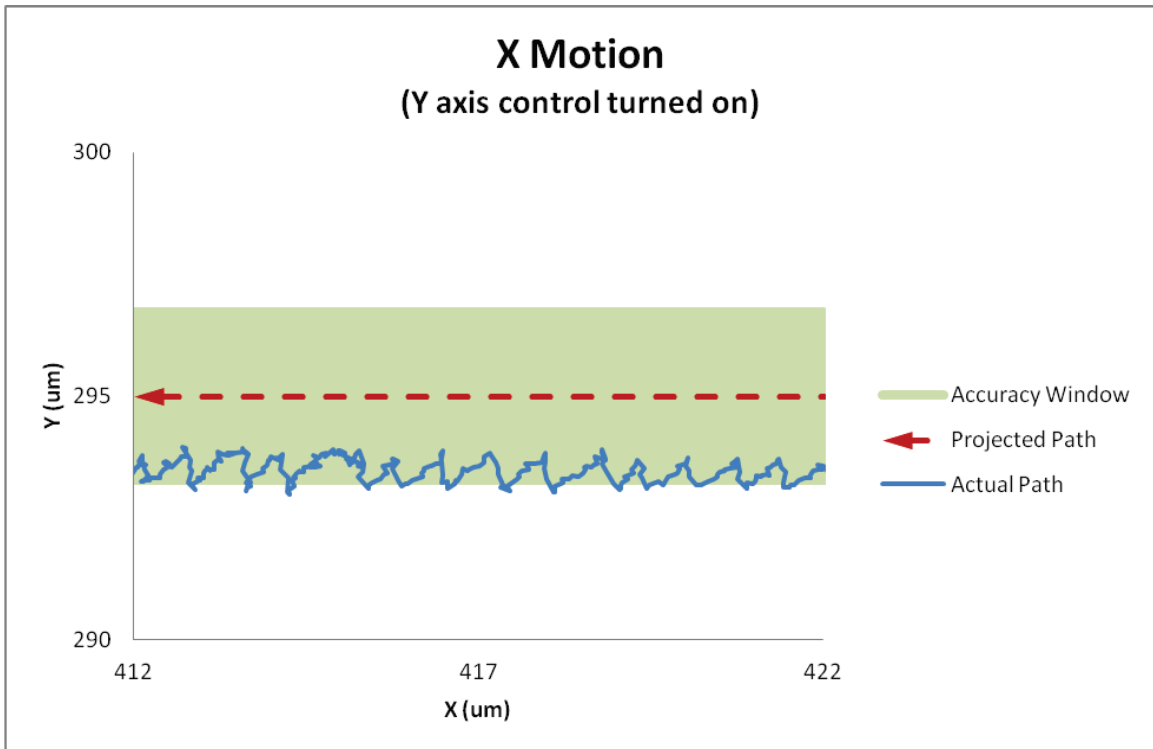
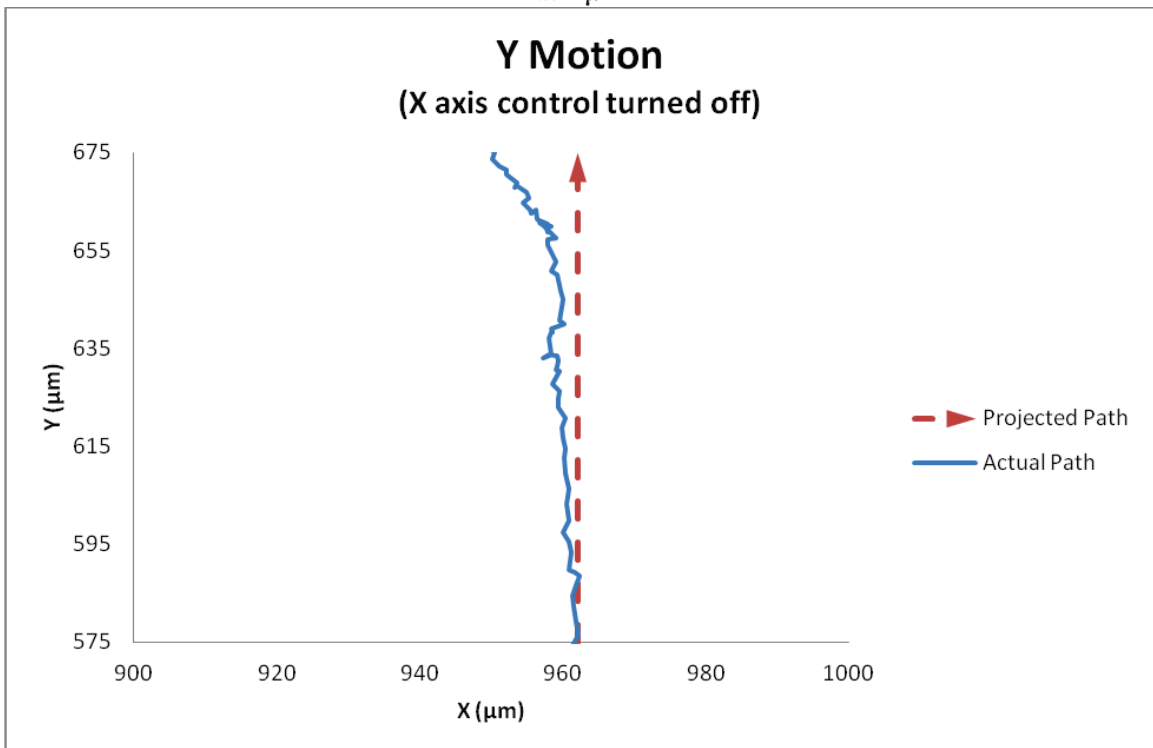


Figure 140. Closeup view of the effect of perpendicular disturbance on long range X motion with the closed loop Y axis control turned off. XY Pads set at 7V



**Figure 141. Closeup view of the net platform perpendicular disturbance on long range X motion being controlled with the closed loop Y axis control turned on. XY Pads set at 7 V, with accuracy set at 2  $\mu\text{m}$**



**Figure 142. The effect of perpendicular disturbance on long range Y motion with the closed loop X axis control turned off. XY Pads set at 1.2V**

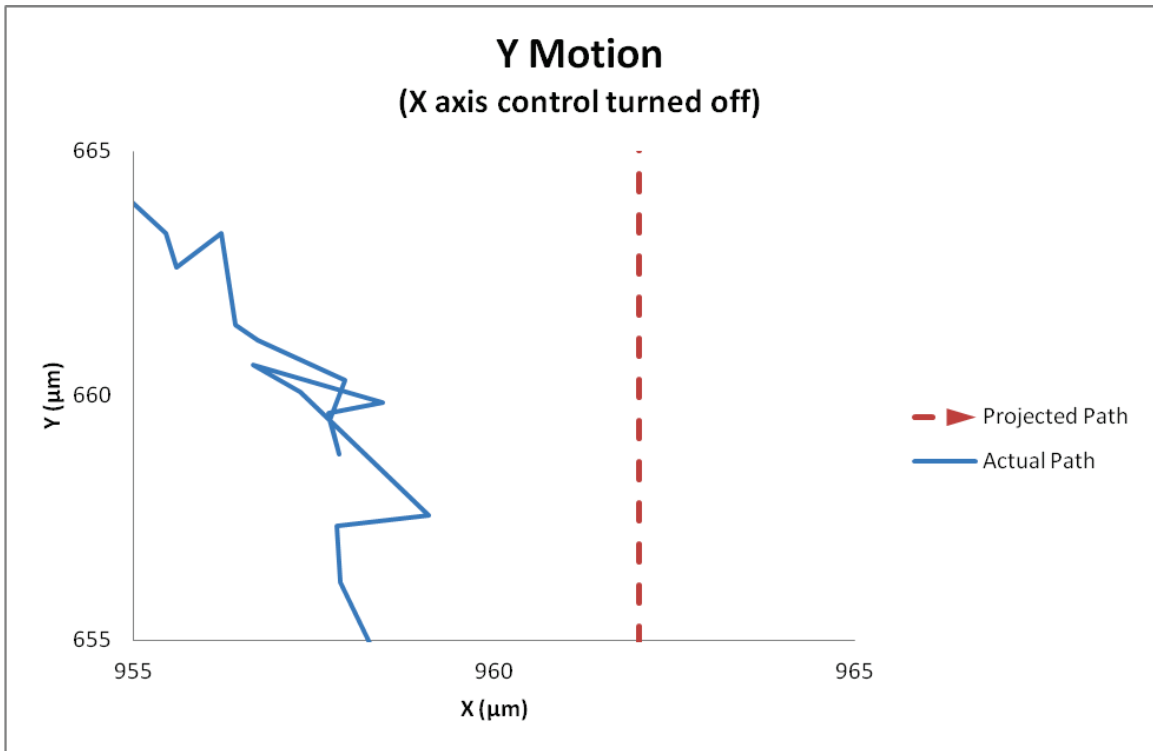


**Figure 143.** Closeup view of the effect of perpendicular disturbance on long range Y motion with the closed loop X axis control turned off. XY Pads set at 12 V

The concept of accuracy, already mentioned earlier in the Section, can be shown clearly when considering the closed loop point to point motion of the plate.

In essence, the plate can be driven in one of eight directions by the XY pad during any given step; up, down, left, right, up-left, up-right, down-left, down-right. The control system compares the current location on each axis to the desired end point (or waypoint), and moves the plate one step in the best direction until the plate is within the set accuracy from the desired end point. This results in a “dogleg” path for point to point motion. Figure 144 demonstrates a simple dogleg path when moving the plate between two arbitrary points. The red dashed line represents the direct path between two points; the initial location of the plate and an arbitrary end location. The thickness of the grey line indicates a 5 μm accuracy window that follows each axis from the desired end point. The thick green line represents a 45° path followed by a straight line to the end point. The plate will follow a 45° path until either the X or Y axis falls into the accuracy window.

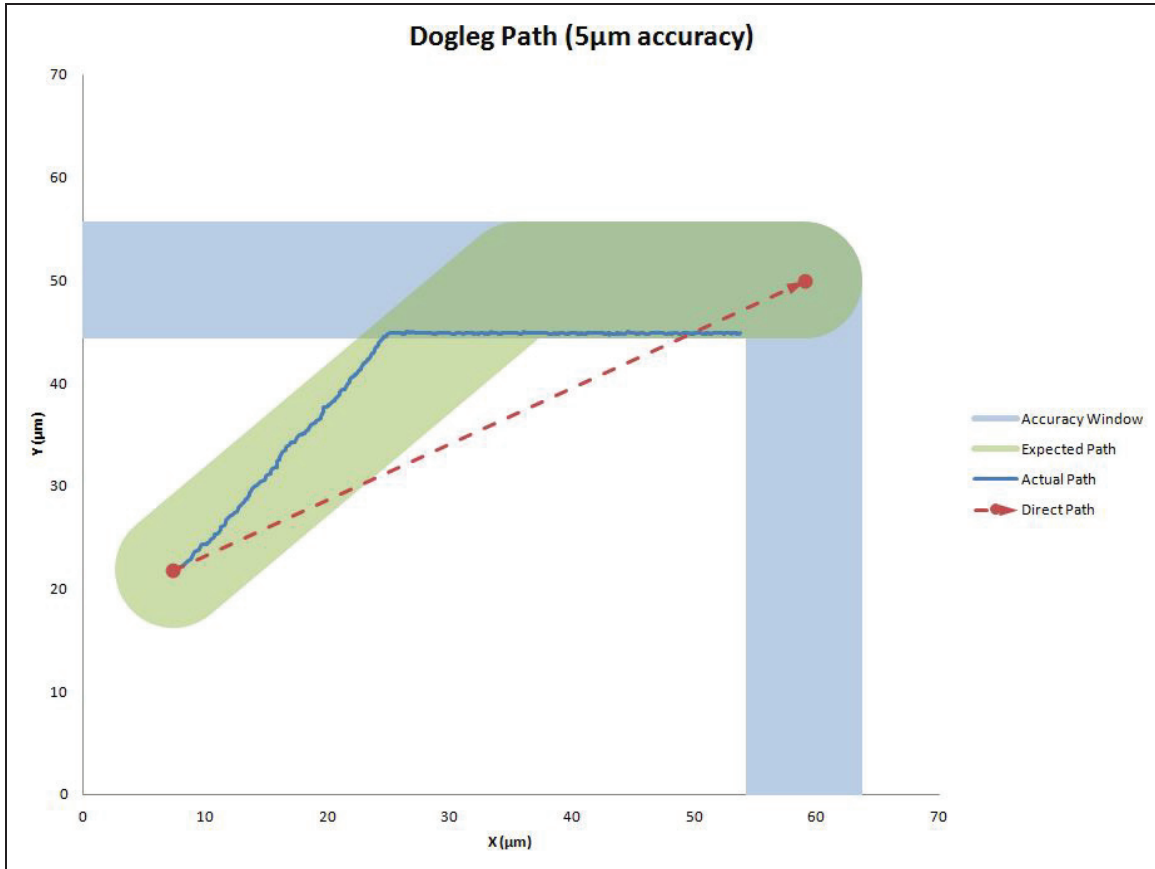


**Figure 144. The standard "dogleg" path used for point to point motion (smooth motion)**

The path show in Figure 144 represents a smooth path that was achieved experimentally. This is not always the case. Figure 145 that shows a similar dogleg path (2 µm accuracy with the plate reaching the vertical accuracy window first) where the plate was vibrating in a manner that gave a very rough path. Regardless of the smoothness of the motion, the path was still traced using the standard dogleg path functional rules.

In both cases (Figure 144 and Figure 145) note how the true end point of the plate is located at a point that is off by the given accuracy in each axis. This results in a final position that is:

$$d_p = \sqrt{2 * accuracy^2} \quad (10.1)$$

This is of note since the final position will not be within the set accuracy, but at a point located  $d_p$  away from the desired end point.

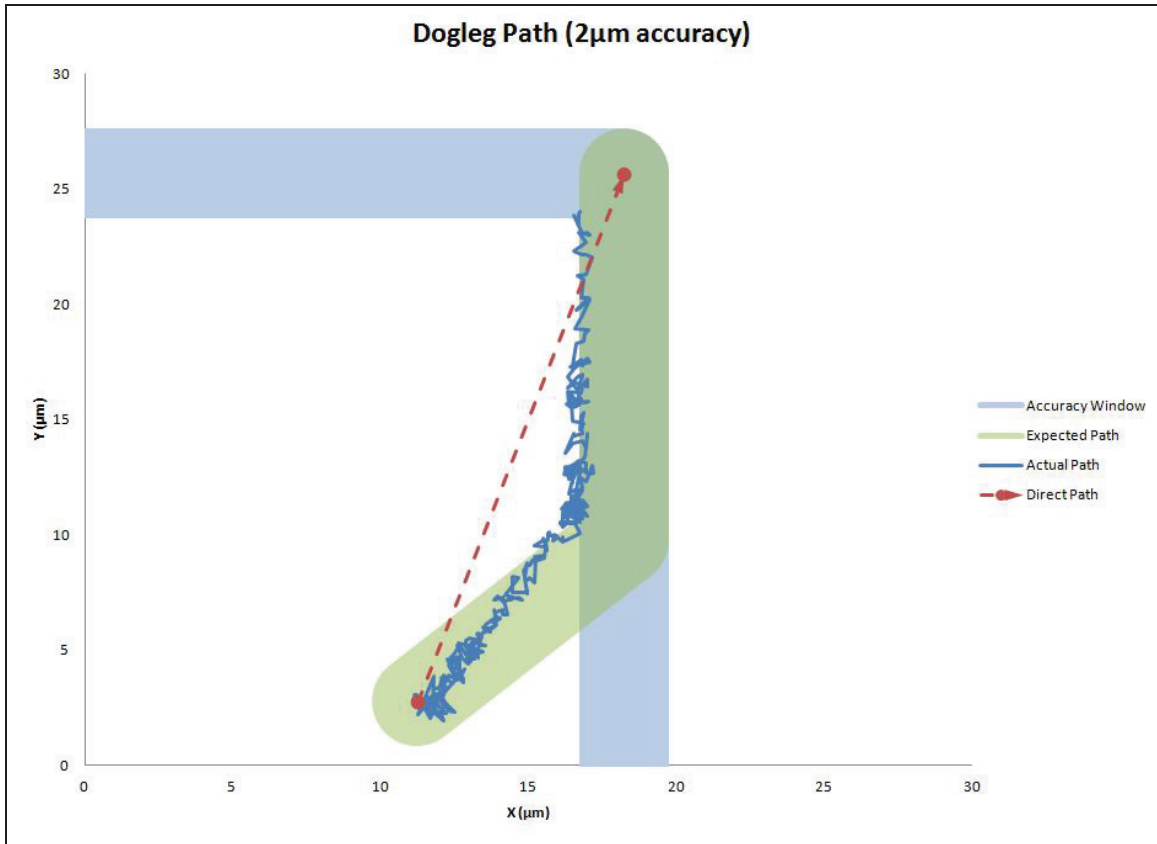


Figure 145. Standard "dogleg" path for point to point motion (rough motion)

Table 18 summarizes the control parameters measured.

Parameter	Unit	Open Loop		Closed Loop	
Max Speed	µm/s	56.8		46.3	
Average Perpendicular Disturbance	%	20		10	
Traction	%	50		50	
Accuracy (7V / 12V)	µm	0.1	0.5	0.1	0.5

Table 18. Control parameters

The parameters were measured at 100Hz and 12V, with an average taken from the results of at least 10 test runs. Accuracy refers to the smallest measure of displacement per step and is shown for 7V and 12V.

### 9.5 Rotation

Rotational motion of the platform is performed through adjacent XY pads moving in opposite directions for each step. While complete rotation was achieved for the micro-scale platforms, (see Figure 146), controlled motion was inconsistent. Rotational motion requires the platform to rest on XY pads of equivalent height. Height variations in the XY pads from the manufacturing process inevitably resulted in the platform lying on a single pad instead of multiple pads. While this did not affect straight line motion, there was often insufficient contact between adjacent pads to create a torque and rotational motion. The average rotation achieved was  $0.8^\circ$  per step at 12V, though position over the XY pads will greatly influence the results.

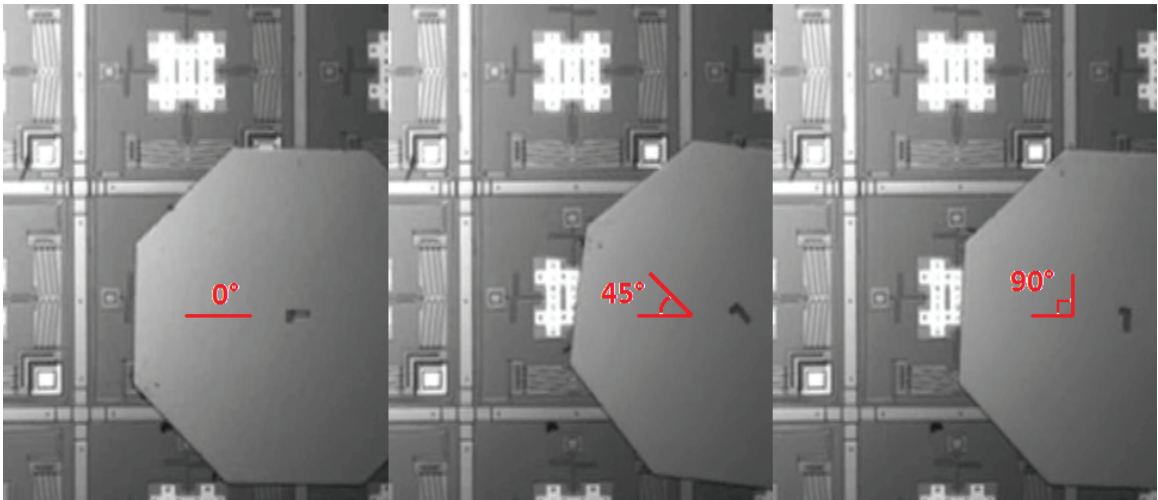


Figure 146.  $90^\circ$  rotation of a platform



## **9.6 Following a Path**

Using the closed loop system, plates can be moved following pre-programmed paths. Several paths were tested and compared with the equivalent paths followed by the macro Lift and Slide prototype. The paths of interest were the circular path (Figure 147 and Figure 148), the box path (Figure 149 and Figure 150) and the cross path (Figure 151 and Figure 152). The paths generated by the MEMS Lift and Slide platform follow the paths generated by the macro Lift and Slide prototype very closely. Note in Figure 150 and Figure 152 there are several “random” points well off the plate path that are artifacts of difficulties experienced by the tracking system due to limited tracking features on the specific plate used. This problem was only found when using a hole cut through plate as a tracking feature.

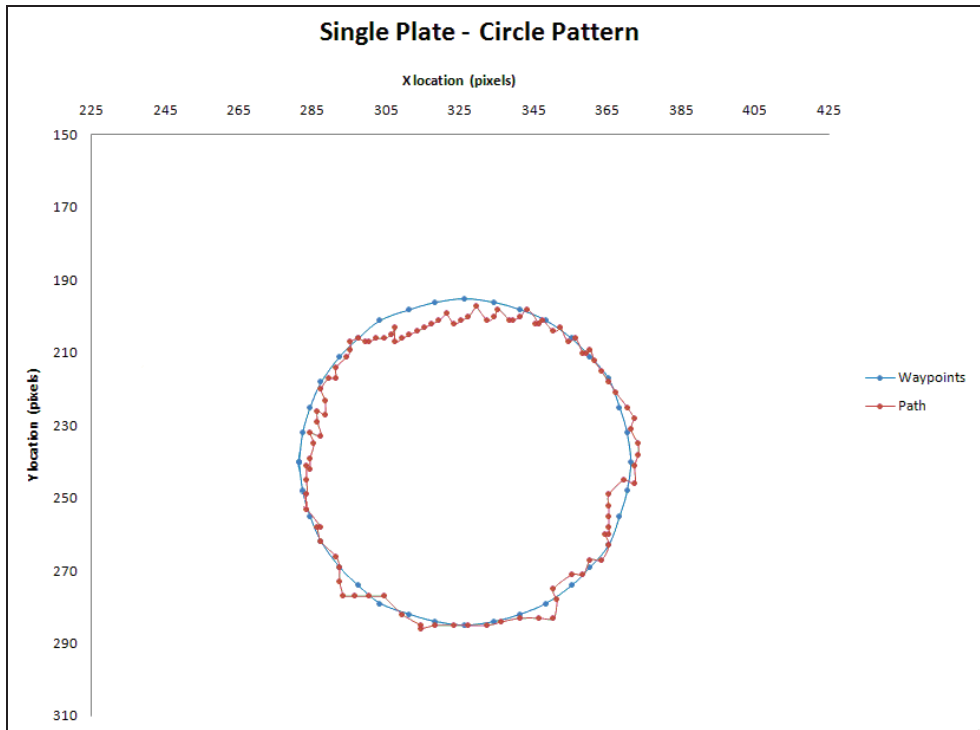


Figure 147. Circular pattern of a single plate on the macro Lift and Slide prototype

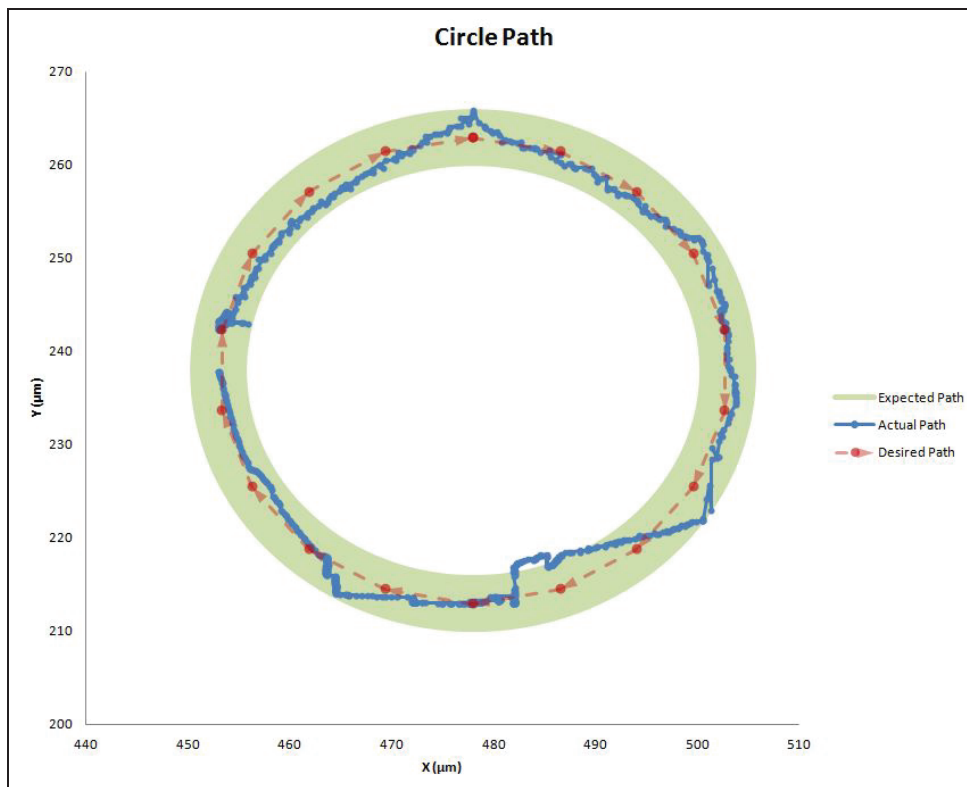


Figure 148. Circular path of a single plate on the MEMS Lift and Slide platform with a radius of 25 μm. Note: not all waypoints are displayed along the desired path for ease of viewing

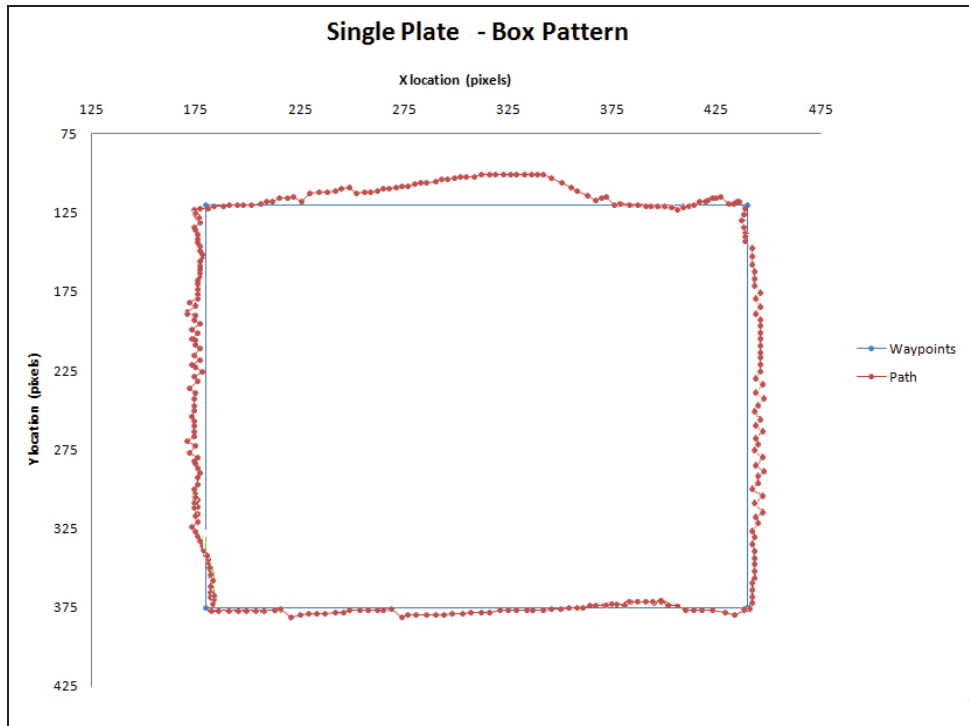


Figure 149. Box pattern of a single plate on the macro Lift and Slide prototype

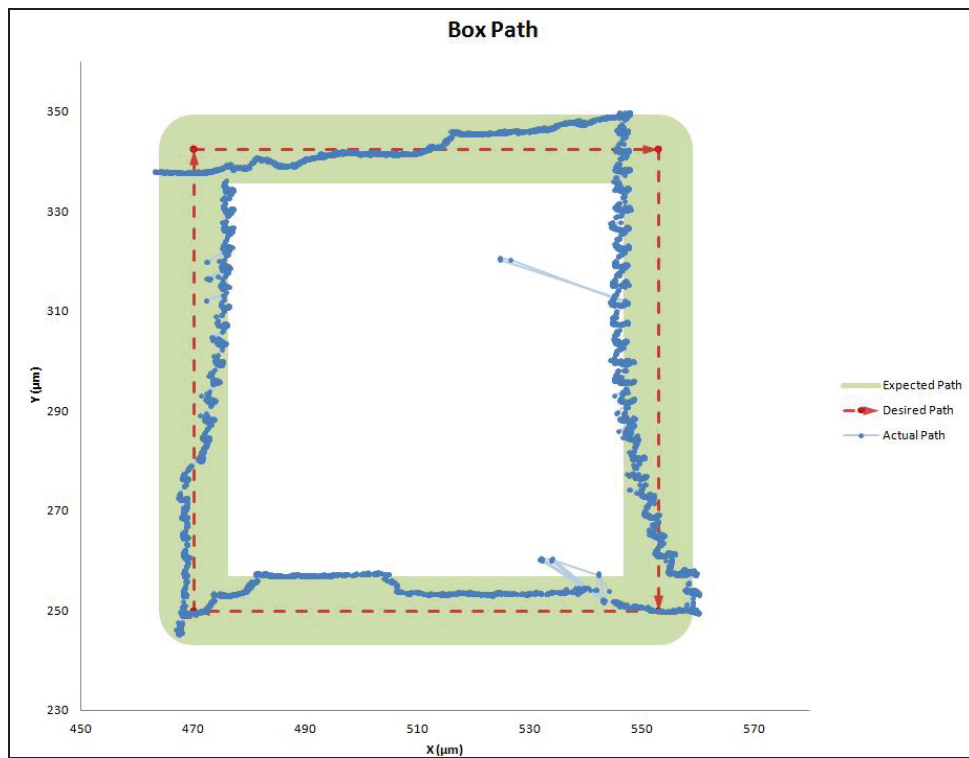


Figure 150. Box pattern of a single plate on the MEMS Lift and Slide platform. The waypoints are located at the four corners. Several “random” points well off the plate path can be seen as artifacts of difficulties experienced by the tracking system due to limited tracking features on the specific plate used

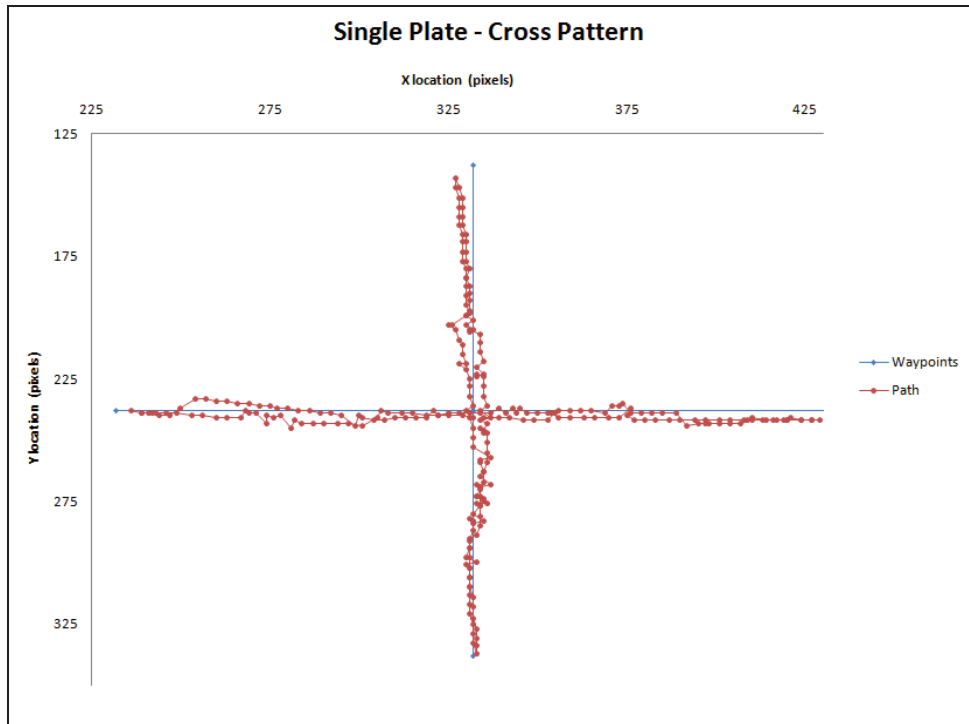


Figure 151. Cross pattern of a single plate on the macro Lift and Slide prototype

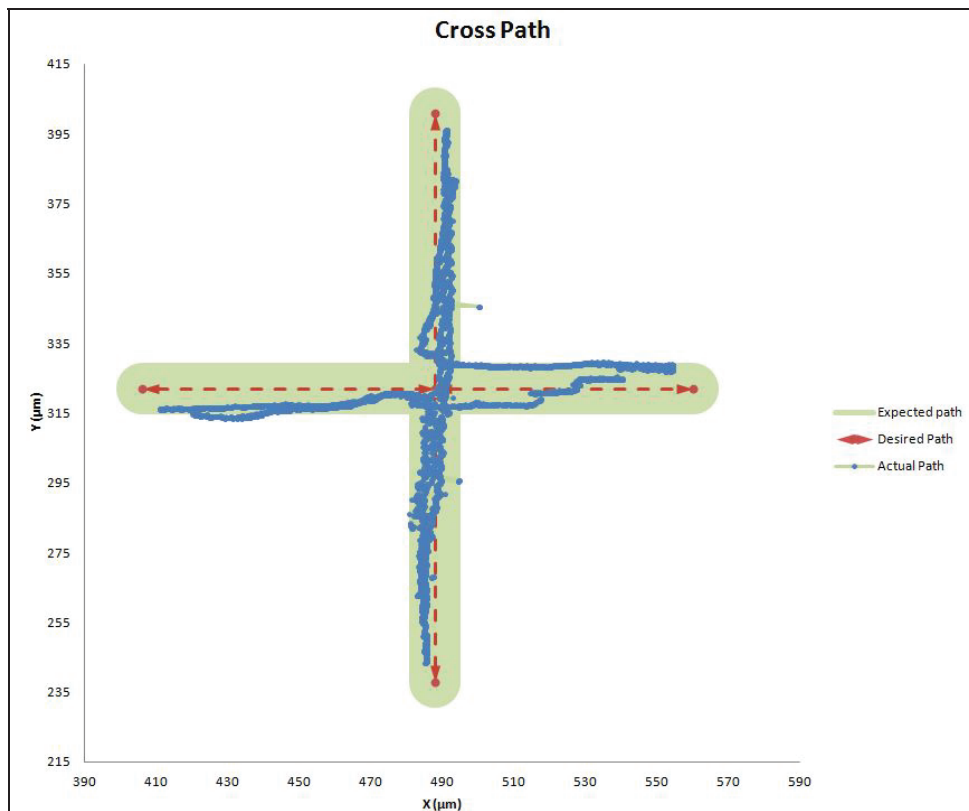
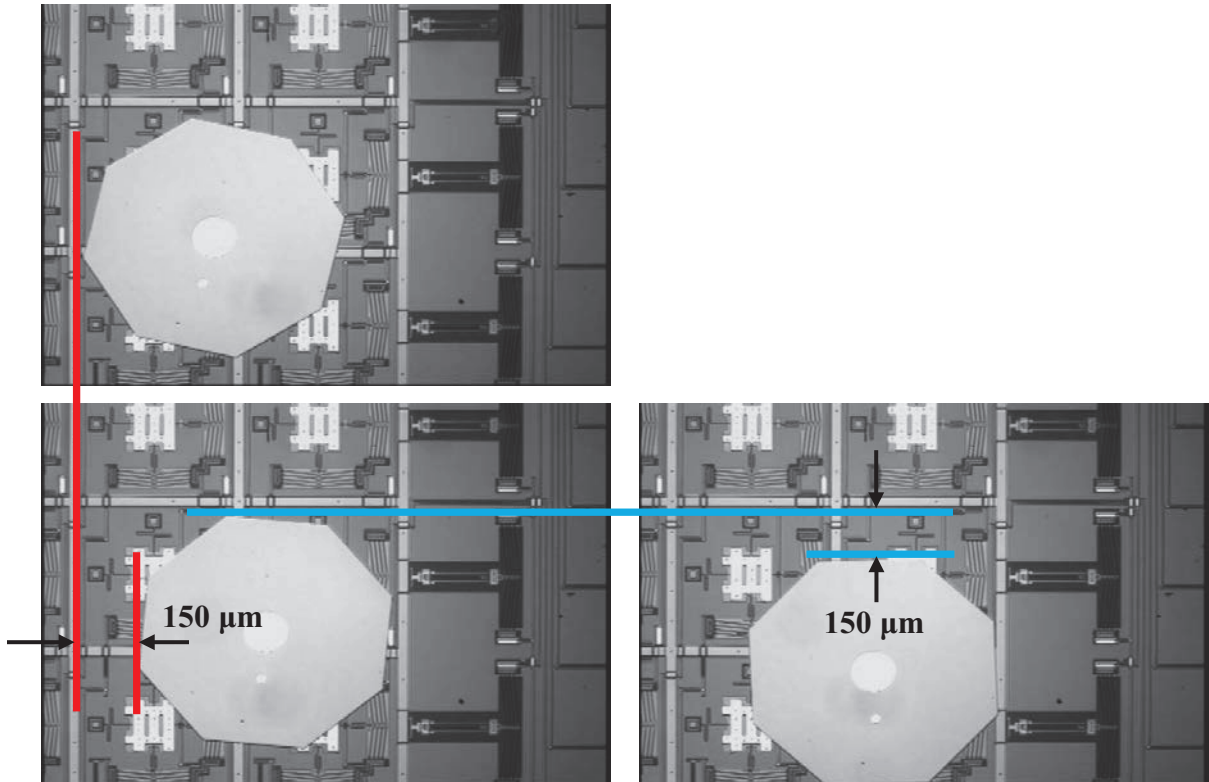


Figure 152. Cross pattern of a single plate on the MEMS Lift and Slide platform. Five waypoints were used, four outer points and a center point used as a turning point

Figure 153 shows the platform moving using closed loop control. The three frames show a platform moving on two sides of a box pattern, first 150  $\mu\text{m}$  in the horizontal direction and then 150  $\mu\text{m}$  in the vertical direction.



**Figure 153. Three frames showing closed loop motion; first horizontal then vertical following part of a box pattern**

The ultimate goal of the lift and slide conveyor is to be able to carry micro-objects on the platform. This is demonstrated in Figure 154. In this sequence of frames, a salt crystal is used as a test object. The salt crystal has an approximate mass of 78  $\mu\text{g}$  and is successfully seen moving approximately 400  $\mu\text{m}$  horizontally over a 4x4 array. The frames cover a timeframe of 13.5 seconds, with an average plate speed of 29.6  $\mu\text{m/s}$ . The XY pads are set at 12 V and run at 50 Hz.

To ensure the mass of the salt crystal does not adversely impact the dynamic response of the system, a quick calculation can be done. From the model, the natural frequency of the XY pad show in Figure 154 in both the X and Y axes is approximately 87.2 KHz. The ratio of mass between the XY pad with the salt crystal and the XY pad without the

crystal is  $\frac{78.242 \mu\text{g}}{0.242 \mu\text{g}} = 323.3 : 1$ . Since the natural frequency is proportional to  $\sqrt{\frac{1}{m}}$ , the expected natural frequency in both X and Y planes would be  $\frac{87.2 \text{ KHz}}{\sqrt{323.3}} = 4.85 \text{ KHz}$ . This is confirmed with the model yielding a result of 4.84 KHz for X and Y planes and 3.71 KHz for rotation. Since the operational range for the Lift and Slide conveyor is several hundred Hz, there is no issue for this mass.

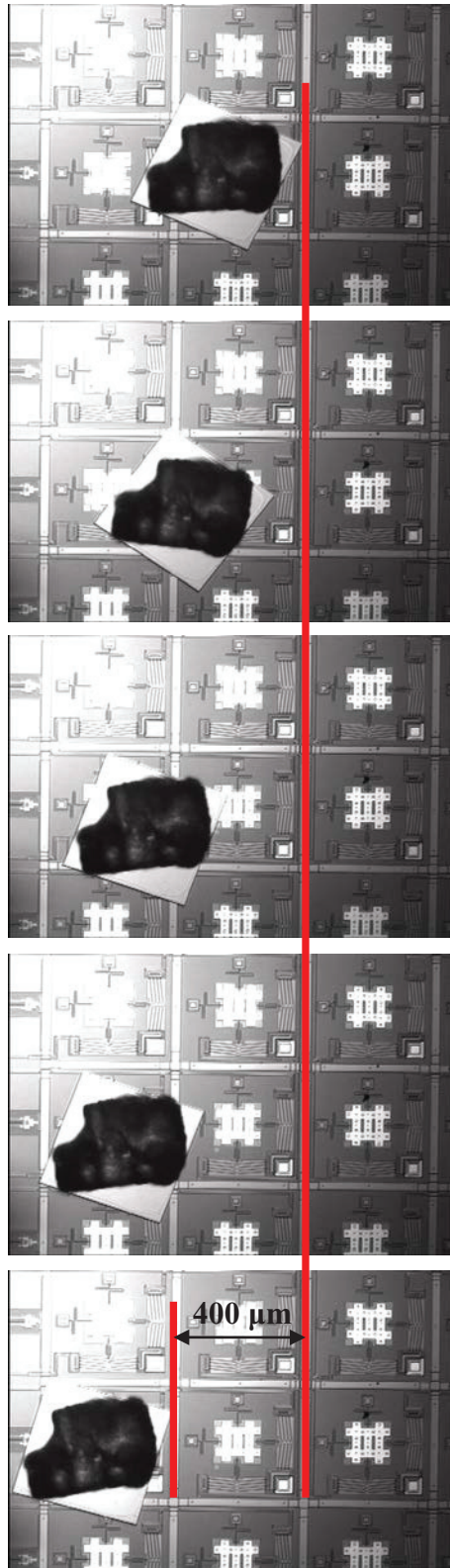


Figure 154. Motion of a salt crystal travelling approximately 400  $\mu\text{m}$  in 13.5 seconds over a 4x4 array. The pads are operating at 50 Hz, 12 V. The crystal has an approximate mass of 78  $\mu\text{g}$

## Chapter 10.0 Conclusion

### 10.1 Overview

The purpose of this thesis was to present a novel method of generating long range untethered motion for objects with multiple degrees of freedom and compare the design between a macromodel and a MEMS equivalent.

Previous MEMS designs have focused on either small displacement tethered control of objects or limited displacement untethered control. Until now there haven't been any MEMS devices presented that have an infinite work envelope with more than a single degree of freedom. The ability to manipulate micro objects has a number of wide reaching applications, including movement of micro-stages, assembly of micro components and biomaterial (cell) control for analysis.

The presented macromodel successfully proved the concept of the lift and slide conveyor and was used as a test bed for designing the Labview open loop and closed loop control systems. The macro model was used as a basis for the development of the MEMS equivalent design. The downside to the macromodel was the artificially high stiffness that was put into the components that should have been more closely matched to the dimensions available for polyMUMPs structures. This might have helped to identify several design issues earlier in the process. Nonetheless, the macromodel proved to be a valuable design tool and the resulting control was closely matched between the MEMS and macromodel designs. Since the macromodel became the "ideal" construction, it enabled the control system to be quickly designed and modified without control issues being confused with lift and slide design and fabrication issues.

The Labview control system was divided into open loop and closed loop control. Open loop control allowed direct access to the XY pad control, simply cycling the pads in a set direction at the push of a button. The closed loop control system added several features accompanied by a vision processing element that allowed for plates to follow pre-



programmed paths. The most important feature of the closed loop control was the ability to have plates follow a path and maintain a set accuracy along an axis, controlling the inherent perpendicular disturbance that resulted from an imbalance of friction due to component height variations.

A model was presented to characterize the dynamic response of the XY pads. The model was compared to FEM analysis of the pads and then compared to experimental results found through Fourier analysis of blurred images. The in-plane natural frequencies of the XY pads were determined by analysis of edge blurring of periodic structures using a standard video camera. The method was able to detect in-plane resonance amplitudes an order of magnitude smaller than could be visually observed.

Work up to now has proven the concept of the lift and slide conveyor through the use of a macromodel and a Labview control system. MEMS chips to date have been used to test variations of lifters and XY pads, and have resulted in a number of successful designs. The lift and slide conveyor design proposed has the potential to meet the needs of many applications where long range untethered control with multiple degrees of freedom is required.

New work presented by the author includes a novel micro-conveyor design that allows long range motion of micro-objects with multiple degrees of freedom, a Labview based vision-based control routine and a model for resonance frequency prediction and design optimization.

## **10.2 Future Work**

The Lift and Slide platform design has shown an exceptional ability to manipulate micro plates over a large work envelope, but testing has revealed a number of issues that need to be addressed in future versions of the design.

The design relies on an assembly process to position a plate over the array. Manipulating the plate is a time consuming process that, with absolute care, can result in damage to the array or some of its subcomponents. This process was made more difficult by the fact that plates from polyMUMPs chips did not work very well due to their flexibility. The more rigid 10 $\mu$ m thick SOI plates proved to be a better choice, they transferring micro-objects from one MEMS chip to another was a difficult and laborious process that frequently resulted in lost plates, of which there was a limited supply. The ultimate goal is to be able to use the Lift and Slide array without plates, where the micro object being manipulated can sit directly over the array. Further work needs to be done to improve the design to this end.

The vertical lifter (VTA) proved to be reliable, but since this is one of the key components future work is needed to optimize and stiffen the lifting mechanism. Future lifting devices need to have the ability to generate a high lifting force with a large range of motion. The grid needs to remain level and be lifted with balanced height control and force on all edges to be truly effective.

Residual stress was an extreme problem on early chips and was not identified until late in the design process once specialized equipment became available to map the surface profile. The residual stress in the long grids resulted in arching of the grids making them naturally the highest structure of the array and therefore rendering the array non-functional. The solution to residual stress for polyMUMPs proved to be making the height differential between the grid and the XY pads significant enough that the residual stress effect was minimal, though it was clearly never fully solved. Several solutions to this problem should be investigated. Firstly, if polyMUMPs is to remain the desired production method, then the grid should be separated into small sections that would be less prone to curl induced height issues. Alternately, other MEMS processes should be investigated that would possibly improve the height differential issues and may be better suited for the design and construction of VTAs.

Wiring always posed a problem and became a compromise between space and current carrying capacity. PolyMUMPs does not offer a method of running low resistance wires under a poly1 or poly2 structure. Poly0 jumpers that are used contribute to a high resistance that is cumulative. This can become a significant problem for larger arrays. The use of a breach ground for the ground plate connections worked well, but cannot be used for every connection, only a single connection such as the ground. The width of the wires also became a problem as the size of the array increased, rapidly requiring more wires than could be fit within the confines of the chip. Future work should investigate more efficient methods of routing signals and power through the array.

One of the greatest issues, and the one that warrants attention in future designs, involves the issue of friction and contact variability over various regions. The Lift and Slide conveyor relies on friction to move the plate. Inconsistent contact over multiple pads results in variations of frictional force and the resulting motion. The rigidity of the lifting grid also greatly affected the resulting motion, where flexing of the grid caused an imbalance of plate contact producing a plate disturbance. Future work in the design must be done to ensure balanced contact, which would allow for rotational control that was not truly achieved on the presented designs.

## References

- [1] M. de Boer, D. Luck, W. Ashurst, R. Maboudian, A. Corwin, J. Walraven and J. Redmond 2004 High-performance surface-micromachined inchworm actuator *J. Microelectromech. Syst.* 13 63–74
- [2] E. Sarajlic, E. Berenschot, N. Tas, H. Fujita, G. Krijnen and M. Elwenspoek 2005 High performance bidirectional electrostatic inchworm motor fabricated by trench isolation technology 13th Int. Conf. on Solid-State Sensors, Actuators and Microsystems (Seoul, Korea, June 2005) pp 53–6
- [3] N. Tas, J. Wissink, L. Sander, T. Lammerink and M. Elwenspoek 1997 The shuffle motor: a high force, high precision linear electrostatic stepper motor *Proc. 2000 IEEE/RSJ Int. Conf. on Solid-State Sensors and Actuators (Chicago, June 1997)* vol 2 pp 777–80
- [4] B. Shay, Development and Testing of Linear and Planar Frictional Micro Conveyors. MASC Thesis. Halifax, Nova Scotia, Dalhousie University, 2008
- [5] D. Meller, J. Reiter, M. Terry, K. Böhringer and M. Campbell, A Docking System for Microsatellites Based on MEMS Actuator Arrays, 2001 by the American Institute of Aeronautics and Astronautics, Inc.
- [6] J. Suh, S. Glander, R. Darling, C. Storment and G. Kovacs, Organic thermal and electrostatic ciliary microactuator array for American Institute of Aeronautics and Astronautics object manipulation, *Sensors and Actuators, A: Physical*, vol. A58, 1997, pp. 51–60
- [7] T. Ebefors, J. Mattsson, E. Kølvesten and G. Stemme, A robust micro conveyor realized by arrayed polyimide joint actuators, in *Proc. IEEE 12th Workshop on Micro Electro Mechanical Systems (MEMS)*, Orlando, FL, Jan. 1999, pp. 576–581
- [8] M. Edo, Y. Watanabe, O. Morita, H. Nakazawa, E. Yonezawa, Two-dimensional micro conveyer with integrated electrostatic actuators, *Proc 12th IEEE MEMS'99*, 1999, pp 43–8
- [9] R. Yeh, S. Hollar and K. Pister, Single mask, large force, and large displacement electrostatic linear inchworm motors, *J. Microelectromech. Syst.*, 2002, **11** 330
- [10] B. Donald, C. Levey, C. McGray, I. Paprotny and D. Rus, An untethered, electrostatic, globally controllable MEMS micro-robot, *J. Microelectromech. Syst.*, Feb. 2006, vol. 15, no. 1, pp. 1–15
- [11] C. Wu and W. Hsu, Design and fabrication of an electrothermal microactuator for multi-level conveying, *Microsyst. Technol.*, 2006, **12** 293–8

- [12] B. Shay, T. Hubbard and M. Kujath, Planar frictional micro-conveyors with two degrees of freedom, *J. Micromech. Microeng.*, 2008, **18** 065009
- [13] P. Kladitis, V. Bright, K. Harsh and Y. Lee, Prototype microrobots for micropositioning in a manufacturing process and micro unmanned vehicles, in *Proc. 12th IEEE Int. Conf. MEMS*, 1999, pp. 570–575
- [14] S. Baglio, S. Castorina, L. Fortuna and N. Savalli, Technologies and architectures for autonomous “MEMS” microrobots, in *Proc. IEEE Int. Symp. Circuits Syst.*, 2002, pp. 584–587
- [15] Y. Guozheng, L. Qihong, D. Guoqing and Y. Detian, The prototype of a piezoelectric medical microrobot, in *Proc. Int. Symp. Micromechatron. Human Sci.*, 2002, pp. 73–78
- [16] L. Sun, Y. Zhang, P. Sun and Z. Gong, Study on robots with PZT actuator for small pipe, in *Proc. Int. Symp. Micromechatron. Human Sci.*, 2001, pp. 149–154
- [17] K. Song, V. Kartik, J. Wickert and M. Sitti, An ultrasonic standing-wave actuated nano-positioning walking robot: PZT-metal composite beam modeling, *J. Vib. Control*, Dec. 2006, vol. 12, no. 12, pp. 1293–1309
- [18] K. Son, V. Kartik, J. Wickert, and M. Sitti, A piezoelectric unimorph actuator based precision positioning miniature walking robot, in *Proc. IEEE/ASME Int. Conf. Adv. Intell. Mechatronics*, 2005, pp. 176–182
- [19] R. Sahai, S. Avadhanula, R. Groff, E. Steltz, R. Wood and R. Fearing, Towards a 3g crawling robot through the integration of microrobot technologies, in *Proc. IEEE Int. Conf. Robot. Autom.*, 2006, pp. 296–302
- [20] T. Shigematsu, M. Kurosawa, XY surface acoustic wave motor with nanometer resolution, *Proc. 21st Sensors Symp.* 2004, pp 237–40
- [21] Chang Liu, T. Tsao, Yu-Chong Tai, Wenheng Liu, P. Will, Chih-Ming Ho, A micromachined permalloy magnetic actuator array for micro robotics assembly systems, *Proc. Transducers’95*, 1995, vol 1, pp 328–31
- [22] H. Nakazawa, Y. Watanabe and O. Morita, The two-dimensional micro conveyer: principles and fabrication process of the actuator, *Proc. Transducers ’97*, Chicago, 16–19 June 1997 pp 33–6
- [23] M. Tomie, A. Takiguchi, T. Honda and J. Yamasaki, Turning performance of fish-type microrobot driven by external magnetic field, *IEEE Trans. Magn.*, Oct. 2005, vol. 41, no. 10, pp. 4015–4018

- [24] A. Torii, T. Koyanagi and A. Ueda, Structure of microrobots using electromagnetic actuators, in Proc. Int. Symp. Micromechatron. Human Sci., 1999, pp. 235–241
- [25] C. Pawashe, S. Floyd and M. Sitti, Multiple magnetic microrobot control using electrostatic anchoring, Appl. Phys. Lett., Apr. 2009, vol. 94, no. 16, p. 164 108
- [26] K. Vollmers, D. Frutiger, B. Kratochvil and B. Nelson, Wireless resonant magnetic microactuator for untethered mobile microrobots, Appl. Phys. Lett., Apr. 2008, vol. 92, no. 14, p. 144 103
- [27] C. Livermore, course materials for 6.777J / 2.372J Design and Fabrication of Microelectromechanical Devices, Spring 2007. MIT penCourseWare(<http://ocw.mit.edu/>), Massachusetts Institute of Technology
- [28] MEMSCAP ‘*PolyMUMPs Design Handbook Revision 11.0*’, retrieved 30 Aug 2011 from <http://www.memscap.com/mumps/documents/PolyMUMPs.DR.v11.pdf>
- [29] M. van Spengen, R. Puers, I. De Wolf, A Physical Model to Predict Stiction in MEMS, J. Micromech. Microeng., 12, 2002, IOP Publishing Ltd, 702-713
- [30] H. Olsson, K. Astrom, C. Canudas de Wit, M. Gafvert, P. Lischinsky, Friction Models and Friction Compensation, 1997
- [31] A. Hariri, J. Zu, R. Ben Mrad, Modeling of Wet Stiction in Microelectromechanical Systems (MEMS), Journal of Microelectromechanical Systems, October 2007, Vol. 16, No. 5, 1276-1285
- [32] A. Hariri, J. Zu, R. Ben Mrad, Modeling of Dry Stiction in Micro Electro-Mechanical Systems (MEMS), J. Micromech. Microeng., 16, 2006, IOP Publishing Ltd, 1195-1206
- [33] N. Tas, T. Sonnenberg, H. Jansen, R. Legtenberg, M. Elwenspoek, Stiction in Surface Micromachining, J. Micromech. Microeng., 6, 1996, IOP Publishing Ltd, 385-397
- [34] N. Tambe, B. Bhushan, Friction Model for the Velocity Dependence of Nanoscale Friction, Nanotechnology, 16, 2005, IOP Publishing Ltd, 2309-2324
- [35] A. Lumbantobing, K. Komvopoulos, Static Friction in Polysilicon Surface Micromachines, Journal of Microelectromechanical Systems, August 2005, Vol. 14, No. 4, 651-663
- [36] N. Tas, C. Gui, M. Elwenspoek, Static Friction in Elastic Adhesive MEMS Contacts, Models and Experiment, MESA Research Institute, 2000

- [37] F. Bowden, D. Tabor, *The Friction and Lubrication of Solids*, Oxford Clarendon Press, 1950
- [38] S. Timpe, K. Komvopoulos, *The Effect of Adhesion on the Static Friction Properties of Sidewall Contact Interfaces of Microelectromechanical Devices*, *Journal of Microelectromechanical Systems*, December 2006, Vol. 15, No. 6, 1612-1621
- [39] Y. Lai, J. McDonald, M. Kujath and T. Hubbard, *Force, Deflection and Power Measurements of Toggled Micromachined Actuators*, *Journal of Micromechanics and MicroEngineering*, Vol 14, 2004, pp. 49-56, doi: 10.1088/0960-1317/04/010049
- [40] H. Fettig, *Design, Simulation and Testing of Micromachined Flexible Joint*, PhD Thesis, Dalhousie University, May 2001
- [41] W. Sharpe, Y. Bin, R. Vaidyanathan, R. Edwards, *Measurement of Young's modulus, Poisson's Ratio, and Tensile Strength of Polysilicon*, In proceedings of MEMS 97-IEEE Tenth Workshop on MicroElectroMechanical System, Nagoya, Japan, Jan. 1997. San Diego, CA: IEEE 424-429
- [42] N. Ellerington, B. Bscheiden, T. Hubbard, M. Kujath, *Fourier analysis of blurred images for the measurement of the in-plane dynamics of MEMS*, *Journal of Micromechanics and MicroEngineering*, Vol 22, No. 3, February 2012, 035019 doi:10.1088/0960-1317/22/3/035019
- [43] A. Bosseboeuf and S. Petitgrand, *Characterization of the Static and Dynamic Behaviour of M(O)EMS by Optical Techniques: Status and Trends*, *Journal of Micromechanics and MicroEngineering*, Vol 13, No. 4, June 2003. S23-S33 PII: S0960-1317(03)59973-9
- [44] S. Wang, B. Guan, G. Wang, Q. Li, *Measurement of Sinusoidal Vibration from Motion Blurred Images*, *Pattern Recognition Letters*, Vol 28, Iss 9, 2007, pp. 1029-1040, doi: 10.1016/j.patrec.2006.12.019
- [45] H. Le, M. Gouiffes, F. Parrain, A. Bosseboeuf, B. Zavidovique, *Image Blur Analysis for the Subpixel-Level Measurement of In-Plane Vibration Parameters of MEMS Resonators*, *Applications of Digital Image Processing XXX*, Proc. of SPIE Vol. 6696, 66962D, 2007, doi: 10.1117/12.733533
- [46] S. Krylov, Y. Gerson, T. Nachmias, U. Keren, *Excitation of Large-Amplitude Parametric Resonance by the Mechanical Stiffness Modulation of a Microstructure*, *Journal of Micromechanics and MicroEngineering*, Vol 20, 2010, 015041 (12pp), doi:10.1088/0960-1317/20/1/015041
- [47] D. Burns and H. Helbig, *A System for Automatic Electrical and Optical Characterization of Microelectromechanical Devices*, *JMEMS*, Vol 8, Iss 4 1999, pp. 473-482, doi: 10.1109/84.809063

- [48] B. Bscheiden, T. Hubbard, M. Kujath, Measurement of MEMS Thermal Actuator Time Constant Using Image Blur, *Journal of Micromechanics and MicroEngineering*, Vol 21, No. 4, Feb. 2011, 045001 (12pp) doi:10.1088/0960-1317/21/4/045001
- [49] J. Gilles, S. Megherbi, G. Raynaud, F. Parrain, H. Mathias, X. Leroux, A. Bosseboeuf, Scanning Electron Microscopy for Vacuum Quality Factor Measurement of Small-Size MEMS Resonators, *Sensors and Actuators A* 145–146, 2008, pp.187–193, doi:10.1016/j.sna.2007.11.026
- [50] H. Sehr, I. Tomlin, B. Huang, S. Beeby, A. Evans, A. Brunnschweiler, G. Ensell, C. Schabmueller, T. Niblock, Time Constant and Lateral Resonances of Thermal Vertical Bimorph Actuators, *Journal of Micromechanics and MicroEngineering*. Vol 12, No. 4, June 2012, pp. 410–413 PII: S0960-1317(02)31153-7
- [51] M. Ben-Ezra and S. Nayar, Motion-Based Motion Deblurring, *IEEE Transactions on Pattern Analysis and Machine Intelligence*, Vol. 26, No. 6, pp. 689-698, June 2004, doi: 10.1109/TPAMI.2004.1
- [52] S. Schuan and K. Diepold, Comparison of Motion De-blur Algorithms and Real World Deployment, *Acta Astronautica* 64 (2009) pp. 1050–1065, doi:10.1016/j.actaastro.2009.01.012
- [53] Y. Yitzhaky and N. Kopeika, Identification of Blur Parameters from Motion Blurred Images, *Graphical Models and Image Processing*, Vol. 59, No. 5, Sept. 1997, pp. 310–320, IP970435 doi:10.1006/gmip.1997.0435
- [54] M. Tanaka, K. Yoneji, and M. Okutomi, Motion Blur Parameter Identification from a Linearly Blurred Image, *International Conference on Consumer Electronics, ICCE 2007 Digest of Technical Papers*, Jan. 2007, doi: 10.1109/ICCE.2007.341570
- [55] C. Yamahata, E. Sarajlic, G. Krijnen, M. Gijs, Subnanometer Translation of Microelectromechanical Systems Measured by Discrete Fourier Analysis of CCD Images, *Journal of Microelectromechanical Systems*, Vol. 19, No. 5, Oct. 2010, pp. 1273-1275, doi:10.1109/JMEMS.2010.2067445
- [56] R. Hickey, M. Kujath and T. Hubbard, Heat Transfer Analysis and Optimization of Two-Beam Micro-Machined Thermal Actuators, *J. Vacuum Sci. Tech. A* 20, 2002, pp. 971–974, doi: 10.1116/1.1468654
- [57] R. Hickey, D. Sameoto, T. Hubbard, M. Kujath, Time and Frequency Response of Two-Arm Micromachined Thermal Actuators, *Journal of Micromechanics and MicroEngineering*, Vol 13, No. 1, Jan. 2003, pp. 40-46 40, doi: 10.1088/0960-1317/13/1/306

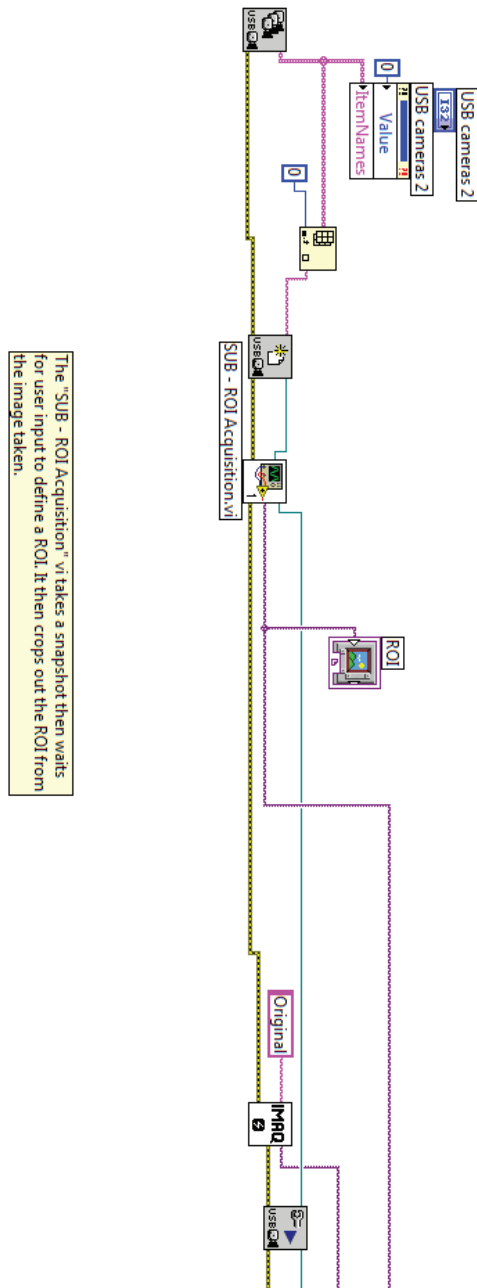


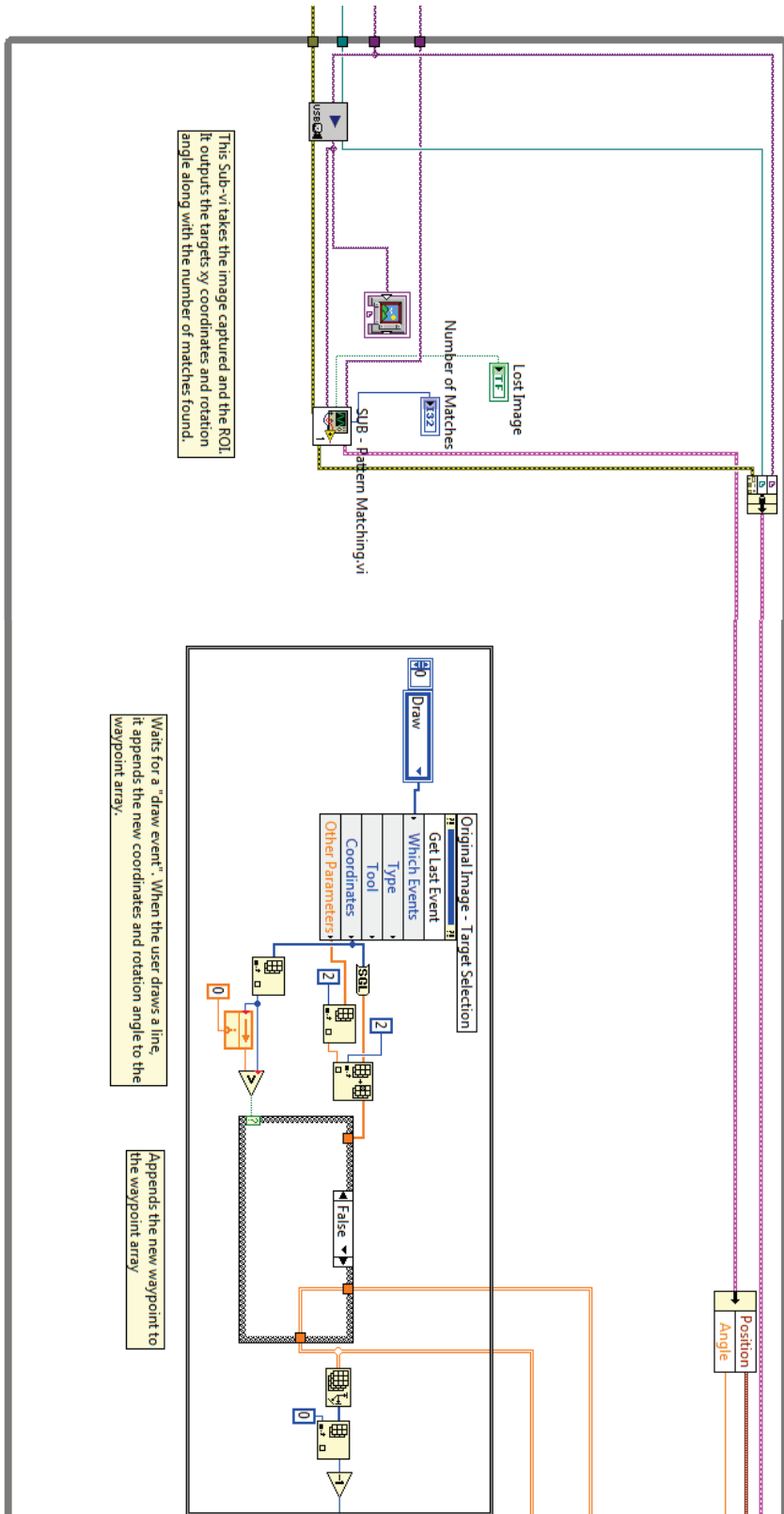
- [58] R. Reichenbach, M. Zalalutdinov, K. Aubin, R. Rand, B. Houston, J. Parpia, and H. Craighead Third-Order Intermodulation in a Micromechanical Thermal Mixer, *Journal of Microelectromechanical Systems*, Vol. 14, No. 6, , pp. 1244-1252, Dec. 2005, doi:10.1109/JMEMS.2005.859080
- [59] M.Brennan, I. Kovacic, A. Carrella, T. Waters, On the Jump-Up and Jump-Down Frequencies of the Duffing Oscillator, *Journal of Sound and Vibration*, Vol 318, Issue 4-5, Dec. 2008, pp. 1250–1261, doi:10.1016/j.jsv.2008.04.032
- [60] B. Armstrong-Helouvry, P. Dupont, C. Canudas de Wit, A Survey of Models, Analysis Tools and Compensation Methods for the Control of Machines With Friction, *Automatica*, 1994, 30(7):1083-1138
- [61] D. Haessig, B. Friedland, On the Modeling and Simulation of Friction, *J Dyn Syst Meas Control Trans ASME*, September 1991, 113(3):354-362
- [62] D. Karnopp, Computer Simulation of Slip-Stick Friction in Mechanical Dynamic Systems, *Journal of Dynamic Systems, Measurement, and Control*, 1985, 107(1):100-103
- [63] J. Jonker, R. Waiboer. R. Aarts, Modelling of Joint Friction in Robotic Manipulators with Gear Transmissions, 2007 Springer, J.C. Garc'ia Orden et al. (eds), *Multibody Dynamics. Computational Methods and Applications*, 221–243
- [64] J. Greenwood, J. Williamson, Contact of Nominally Flat Surfaces, 1966, *Proc. R. Soc, A* 295-300
- [65] F. Bowden, L. Leben, The Nature of Sliding and Analysis of Friction, 1939, *Proc. R. Soc, A* 169, 371-379
- [66] T. Yu, R. Ranganathan, N. Johnson, N. Yadav, R. Gale, T. Dallas, In Situ Characterization of Induced Stiction in a MEMS, *Journal of Microelectromechanical Systems*, April 2007, Vol. 16, No. 2, 355-364
- [67] W. Wang, Y. Wang, H. Bao, B. Xiong, M. Bao, Friction and Wear Properties in MEMS, *Sensors and Actuators*, 97-98, 2002, 486-491
- [68] B. Bhushan, J. Israelachvill, U. Landman, Nanotribology: Friction, Wear and Lubrication at the Atomic Scale, *Nature*, 13 April 1995, Vol 374, 607-616

# Appendix A – LabView Control System

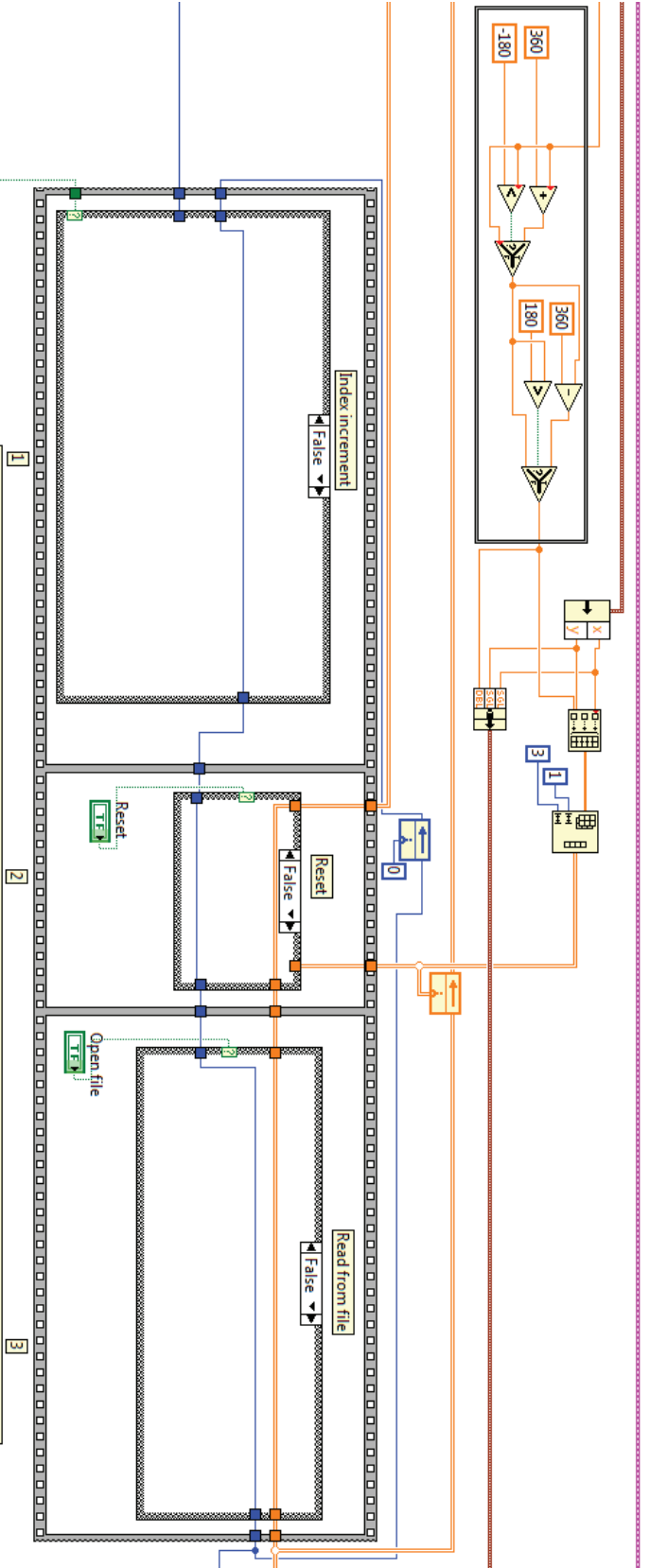
## A.1 Main VI

Note: the main VI (Figure 155) is reproduced over the next five pages for clarity.



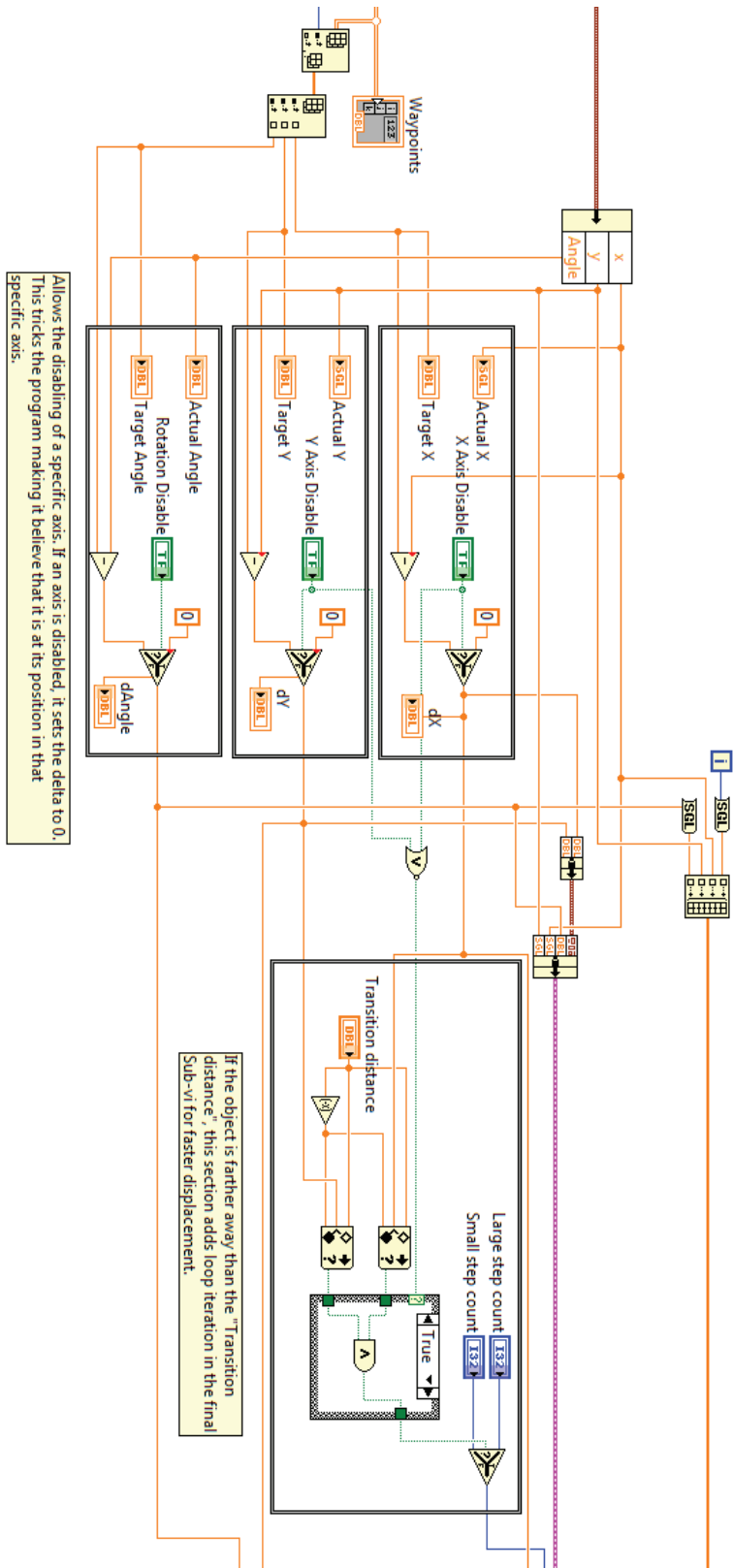


Ensures the angle is always in between  
-180 and 180 degrees



This entire stacked sequence defines index of the waypoint array to target the location for the object to move.

1. When the object reaches a waypoint, this frame increases the waypoint index by 1, then check to ensure it is a valid point. If it is, it simply passes the index value to the next frame. If the new index is not valid, it either subtracts one from the index to return the previous location and the object should stop moving. If looping is turned on, it will return the index to a value of 0 (the first waypoint of the array).
2. If the reset button is pressed, it reinitializes the waypoint array and changes the index to 0. If not, it simply passes its values through to the next frame.
3. This frame reads a waypoint array from a file if the button is pressed. It will prompt you to choose the file it should read. This replaces the existing waypoint array with the file's array. It also changes the index to 0. If the "Open file button is not pressed, it passes its values through.



Allows the disabling of a specific axis. If an axis is disabled, it sets the delta to 0. This tricks the program making it believe that it is at its position in that specific axis.

If the object is farther away than the "Transition distance", this section adds loop iteration in the final Sub-vi for faster displacement.

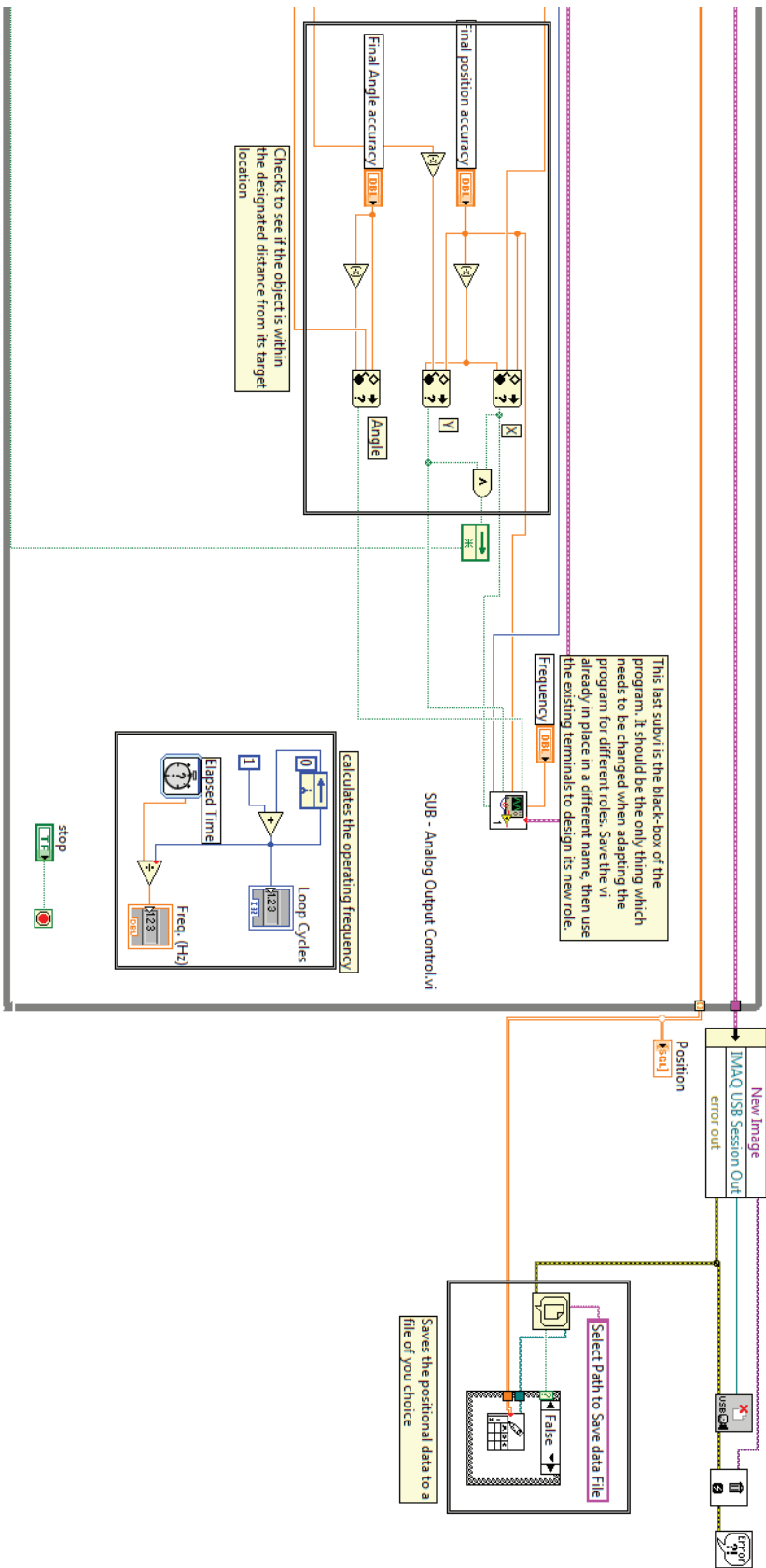


Figure 155. Main Labview control system VI

## A.2 Sub VIs

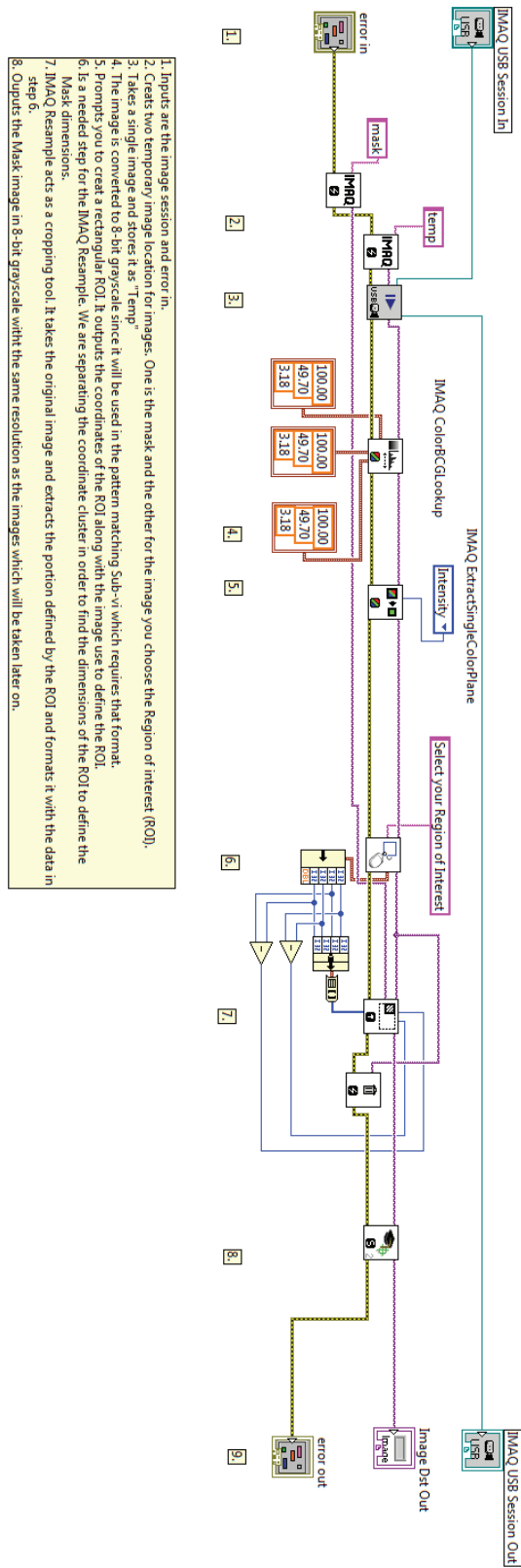


Figure 156. Region of Interest Capture Sub VI

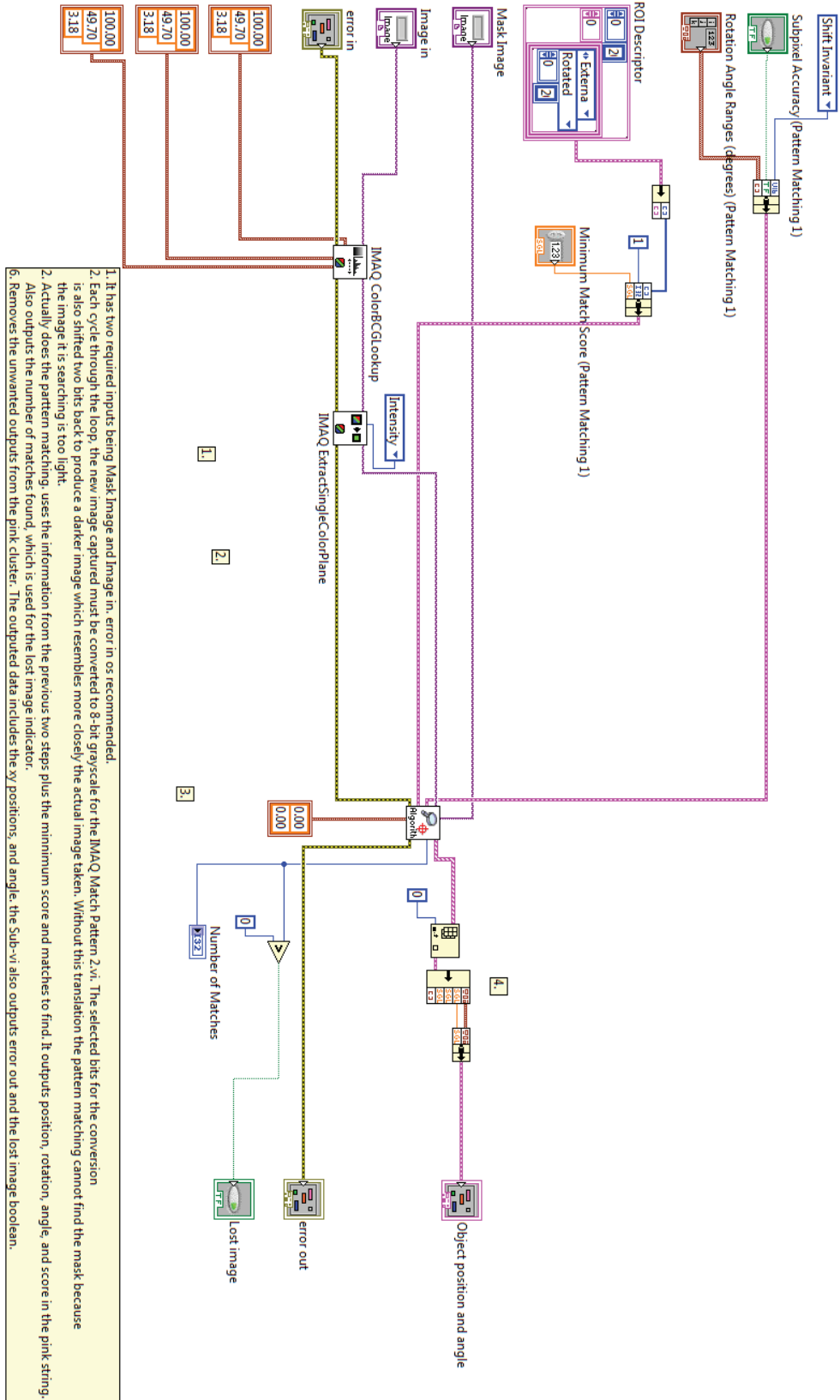
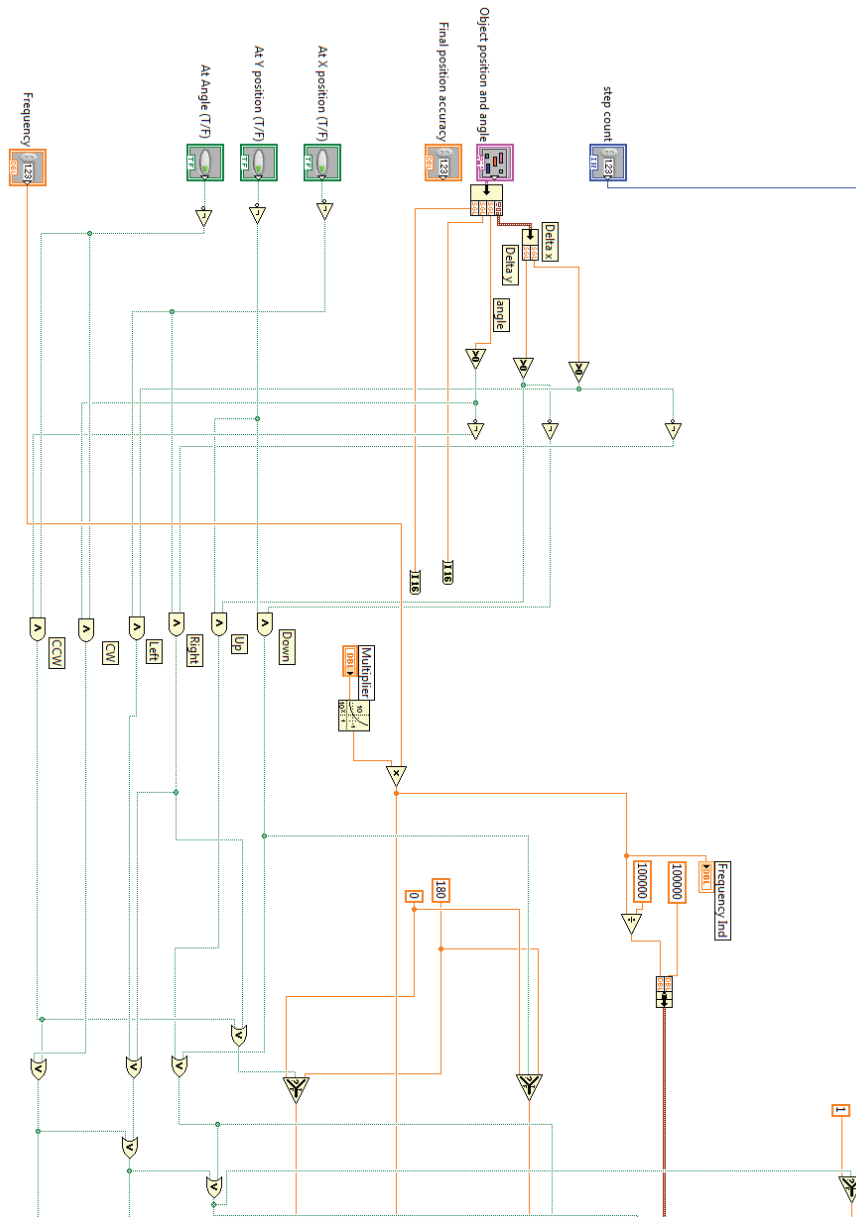


Figure 157. Pattern Recognition Sub VI



Note: the DAQ Output Sub VI (Figure 158) is reproduced over the next two pages for clarity.



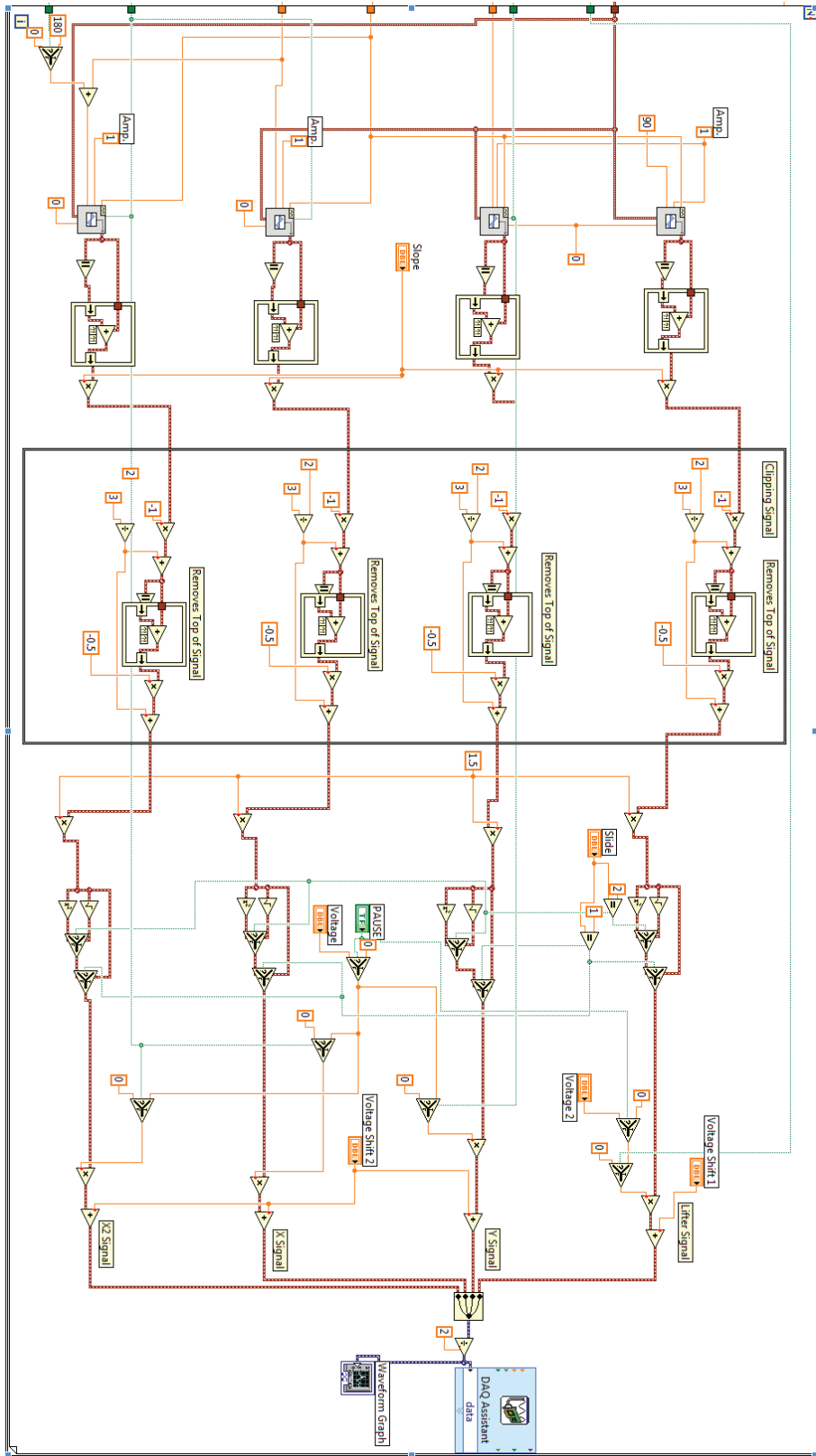


Figure 158. DAQ Output Sub VI

## **Appendix B – Macro Friction, Micro Friction and Stiction**

### **B.1 Introduction**

The purpose of this Appendix is to take a closer look at friction and stiction, a phenomenon closely linked to friction, at both the macro and micro scales. The main concentration of the Appendix will be micro friction and stiction relating to MEMS structures. Macro friction will be discussed initially to give a base understanding.

There are many different areas of friction that could be investigated, but again staying with the focus of MEMS structures the primary area of interest will be dry, static structures (where dry structures means surfaces that are not immersed in liquid nor lubricated, and static means two surfaces with no relative motion). Having said this, there will be times when the Appendix will touch on other areas, but only superficially and only to give a better understanding of the topic at hand. For this reason, major topics such as lubrication and its affect on friction, and dynamic friction will only be looked at briefly.

The Appendix will begin with a discussion of macro friction and outline several models that can be used. Once a basic understanding of friction has been put forth, the Appendix will move on to stiction and micro friction. The aim of this Appendix to give a general understanding of what elements contribute to friction and stiction and present some of the models that exist.

#### **B.1.1 What is the Difference Between Friction and Stiction?**

Before beginning into macro friction, the difference between friction and stiction should be outlined. The terms are used frequently in literature, often incorrectly. Friction has been defined as a resistance to relative motion of in contact surfaces. This can be broken down into two basic types; static and dynamic. Static friction is the initial level of resistance to motion, before the two surfaces have a relative motion. Dynamic friction is

resistance to motion while the two surfaces have a relative motion. Many publications, such as van Spengen *et al* [29] refer to stiction as a short term for static friction. It is, however, now widely accepted that the correct definition of stiction is actually an adhesion between two surfaces, as seen in papers by Olsson *et al* [30] and Hariri *et al* [31,32]. It will be shown in later sections that this adhesion not only is a force that resists relative motion in addition to friction, but also can be cause an increase in actual friction forces by increasing the normal force between surfaces.

At the macro scale stiction by itself is largely ignored as a separate entity, with its effect being included within a coefficient used for calculating friction. This is fine for the macro scale where adhesion really is not an issue, but at the micro scale, such as in MEMS devices, stiction can be catastrophic. MEMS devices such as SDAs (scratch drive actuators), RF switches and gears can fail completely due to adhesion of in-contact surfaces (Hariri *et al* [31]).

### **B.1.2 Contributions**

A number of papers were reviewed during the writing of this Appendix. This is by no means a complete list of available literature, but is representative of the research that has been done. This section presents the main areas of interest of each author.

A number of authors concentrated primarily on macro friction models. The work of Olsson *et al* [30] involved the development of a complete classical friction model, with a review of various macro computational models. Each model presented built on previous models, but was limited to computational theory. Their focus was a control system model used to compensate for friction. They presented macro computational models from authors such as Armstrong-Helouvry *et al* [60], Haessig *et al* [61] and Karnopp *et al* [62]. These authors were less concerned with the actual mechanisms of friction, and concentrated on the resulting measurable effects. Jonker *et al* [63] recaps classical macro friction models and then analyzes sliding friction between surfaces at a slow speed

regime. As with Olsson *et al* [30], they concentrate more on computational models that simulate measured results than the physical causes of friction.

Greenwood *et al* [64] are some of the first authors to investigate micro friction and separate it from macro friction. They took a close look at the interaction of asperities between surfaces and created a model that could be used for statistical analysis on the surface geometry based on roughness and hardness of the surface. Bowden *et al* [37,65] continued the investigation of surface interactions and developed a stick-slip model that helped to analyze the differences between static and kinetic friction.

Hariri *et al* [31,32] present several papers that concentrate on the adhesive effects of stiction. They describe the forces that contribute to both wet and dry stiction and introduce a computational model. Their model is successfully compared to experimental results. Tambe *et al* [34] combine the effects of micro friction with the adhesive effects of stiction into a single model. They cite the same major stiction mechanisms as Hariri *et al* [32] in a dry environment.

Many authors are focused on micro machined surfaces. van Spengen *et al* [29] create a model that can be used to describe a MEMS surface and predict the sensitivity to stiction based on atmospheric conditions. Tas *et al* [33,36] describe the mechanisms of stiction and propose methods to counteract the adhesive effects. Other authors such as Timpe *et al* [38], Yu *et al* [66], Wang *et al* [67] and Lumbantobing *et al* [35] describe experimental setups that can be used to measure both stiction and friction with MEMS structures.

Bhushan *et al* [68] take a closer look at the mechanisms of friction at the atomic scale. They report on friction simulations and concentrate on nano-indentation, wear and lubrication between contact points.

## B.2 Macro Friction

As previously mentioned, in order to understand micro-friction we must first study macro-friction. However, it should be pointed out that while many people consider macro friction and micro friction as the study of friction of large objects and small objects respectively, this isn't entirely true. A closer look at macro friction reveals that the elements that contribute to friction are the same regardless of size, however, when looking at friction models of larger scale surfaces in contact many of the factors have such a small impact that they can be neglected. When considering micro-scale friction these factors now become more critical and therefore require analysis.

When investigating macro friction, the reaction forces are found to be the result of a number of different mechanisms. This includes, but is not limited to, contact geometry, topography (or roughness), material properties of the surface interfaces, displacement, relative velocity, contamination and lubrication, as outlined by Olsson *et al* [30]. Roughness is commonly seen as the major contributor to friction, affecting many other friction factors, and will be discussed in much detail in later sections.

### B.2.1 Classical Models

A number of classical models are used to define friction. The ideal model is a simplistic relay model, where a step function is used (see Figure 159). With a first order approximation, friction force is proportional to the normal load. A friction force is not defined for a zero velocity. The force always opposes the motion such that:

$$F = F_c \text{sgn}(v) \tag{A.1}$$

and

$$F_C = \mu F_N \tag{A.2}$$

Where:  $F_c$  = Coulomb Friction (based on Amonton's Law described by Wang *et al* [67],

$$F_f = \mu L \tag{A.3}$$

$v$  is the velocity

$\mu$  is the coefficient of friction

$F_N$  is the normal force

$F_f$  is the friction force

$L$  is the applied load

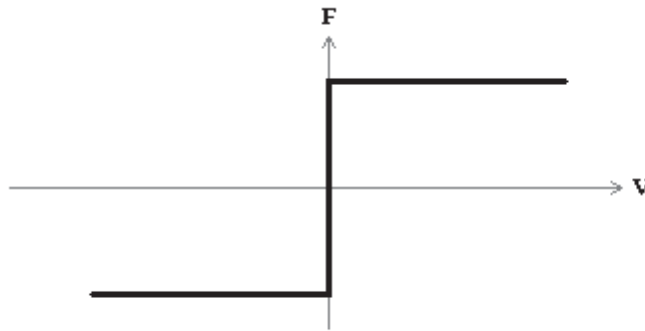


**Figure 159. Simple relay model (Coulomb Friction). Adapted from Olsson *et al* [30]**

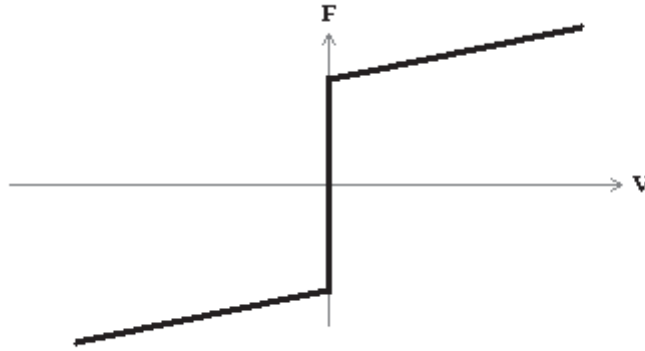
With the traditional friction theories (equation A.3), the friction force is related to the normal load through a coefficient of friction (a proportionality constant) and is independent of the apparent area of contact. In a later section we will see that this doesn't hold at the microscale.

Figure 160 takes the simple relay model and adds the friction due to the viscosity of lubricants. The increase in friction is proportional to the velocity.

$$F = F_v v \tag{A.4}$$

Where:  $F_v$  = Friction due to viscosity

$v$  = Velocity



**Figure 160. Combination of Coulomb and viscous friction. Adapted from Olsson *et al* [30]**

Experimentally there is a non-linear dependence on velocity. Olsson *et al* [30] state that a better fit to experimental data would be:

$$F = F_v |v|^{\delta v} \text{sgn}(v) \quad (\text{A.5})$$

Where  $\delta v$  is a value that depends on the geometry of the application and can only be found through experimentation, but is typically in the range of 0.5 to 1 as reported by Jonker *et al* [62]. Thus Figure 160 may curve slightly downward at large velocities.

The next step in the model would be to include the static friction, which is typically higher than the kinetic (Coulomb) friction. This force resists relative motion by counteracting external forces below a threshold value (see Figure 161). Note that without lubrication the sloped portion of the figure would be flat, which is often considered the most common macro model in use.



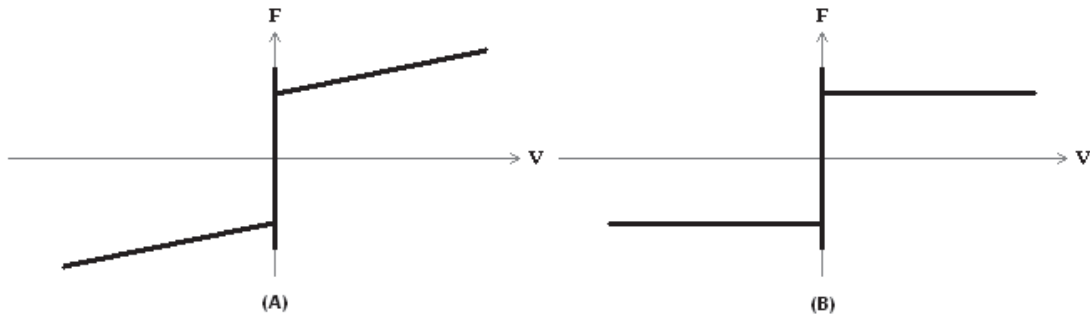


**Figure 161. Model combining Coulomb and viscous friction with static friction (A) in comparison to equivalent model without lubrication (B). Adapted from Olsson *et al* [30]**

Friction at rest (zero velocity) is modeled as a function of an external force,  $F_e$  and not the velocity. This applies until the external force exceeds the static force. At this moment the velocity becomes non-zero and the Coulomb friction applies instead of static friction.

$$F = \begin{cases} F_e & \text{if } v=0 \text{ and } |F_e| < F_s \\ F_s \operatorname{sgn}(F_e) & \text{if } v=0 \text{ and } |F_e| = F_s \end{cases} \quad (\text{A.6})$$

Where:  $F_s = \mu_s F_N$

$\mu_s$  = proportionality constant

$\mu_s > \mu_k$  (where  $\mu_k$  is the Coulomb (kinetic) proportionality constant)

Further inspection of the previous model reveals a discontinuity as the velocity becomes a non-zero value. This discontinuity is commonly accepted in simplistic classical macro models. However, as reported by Jonker *et al* [63], Richard Stribeck (1902) discovered that friction forces do not actually decrease discontinuously at the moment where  $F_e > F_s$ , velocity dependence is continuous. For a more complete model, a new arbitrary function  $F(v)$  is introduced to remove the discontinuity (see Figure 162):

$$F = \begin{cases} F(v) & \text{if } v \neq 0 \\ F_e & \text{if } v=0 \text{ and } |F_e| < F_s \\ F_s \operatorname{sgn}(F_e) & \text{if } v=0 \text{ and } |F_e| = F_s \end{cases} \quad (\text{A.7})$$

The complete form of the equation takes into account the Coulomb friction, static friction, the continuity between static and Coulomb friction and friction as a result of lubrication. The equation becomes:

$$F(v) = F_c + (F_s - F_c)e^{-|v/v_s|^{\delta}} + F_v v \quad (\text{A.8})$$

Where  $v_s$  is called the Stribeck Velocity and is a material dependant characteristic velocity where friction has switched completely to Coulomb friction.

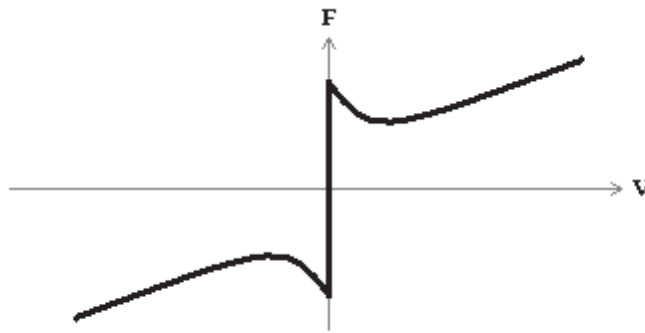


**Figure 162. Stribeck curve to remove discontinuity. Adapted from Olsson *et al* [30]**

Olsson *et al* [30] report that the friction force is actually lower for decreasing velocities than for increasing velocities until the Stribeck velocity is reached (Figure 163). For further accuracy, they state that a hysteresis loop can be defined that becomes wider as velocity variations become faster. Olsson *et al* [30] don't offer any explanation for the hysteresis loop, nor do they include a model.

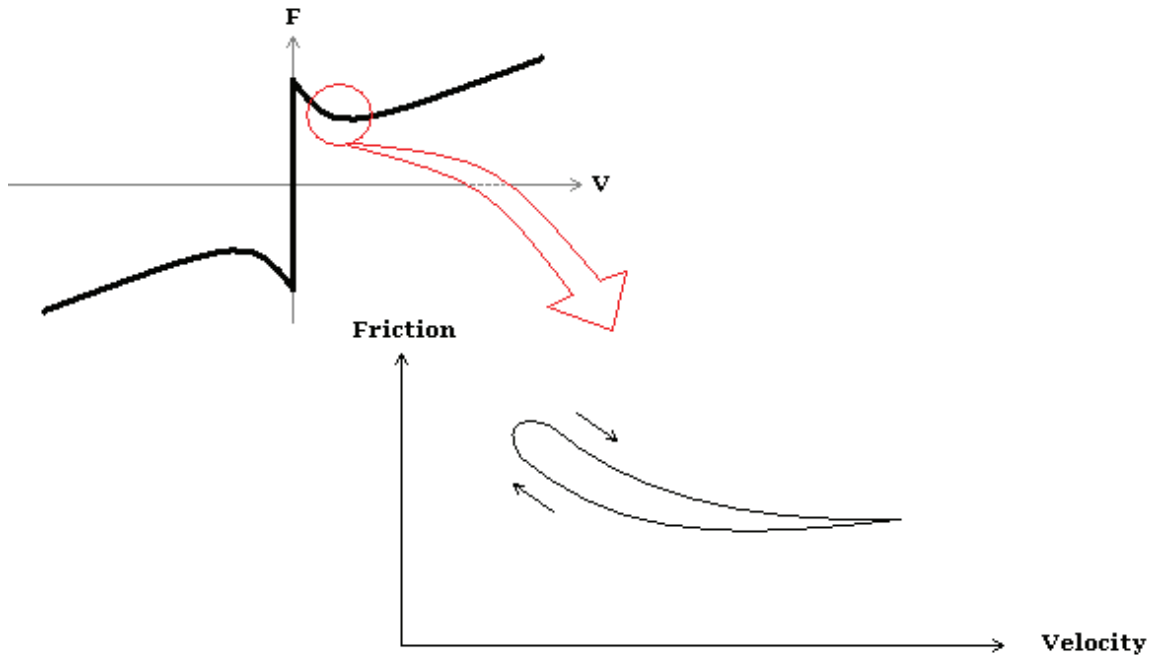


**Figure 163.** Friction hysteresis loop from increasing and decreasing velocity in the vicinity of the continuity between static and Coulomb friction. Adapted from Olsson *et al* [30]

### B.3 Stiction

As previously defined, stiction is a phenomena that causes adhesion between two surfaces. It is a relatively minor force at the macro scale, and is usually ignored. However, at the micro scale it can play a significant role (for reasons that will be discussed shortly) and is often responsible for the failure of MEMS devices. Devices designed to function correctly at the macro scale can unexpectedly fail at the micro scale. Having said that, as with friction, when properly understood it can be used to the advantage of a device. For example, stiction can be used for self assembly of 3-D microstructures (van Spengen *et al* [29]), or to aid in transferring displacement forces from actuators such as with platforms resting on moving pads, or with linear impact drives. A solid knowledge of the underlying physics involved is required to make stiction forces controllable and predictable.

There are two types of stiction; fabrication stiction and in-use stiction. Fabrication stiction is major failure mode as a result of the use of wet etchants. The evaporation of the wet etchant between two surfaces can draw the surfaces together causing them to permanently adhere. Since this is a function of the manufacturing process, it will not be addressed in this Appendix. However, an understanding of in-use stiction will allow the reader to grasp the concept of fabrication stiction, since ultimately the failure is related.

van Spengen *et al* [29] and Tas *et al* [33] suggest that there are four major adhesion mechanisms that result in stiction; capillary forces, van der Waals forces, hydrogen bridging and electrostatic forces. In the next sections, each of these will be analyzed.

Despite knowledge of the adhesion mechanisms, stiction effects are actually not very predictable quantitatively. They are highly dependent on both the surfaces and the environment. Minor changes to either can have enormous effect on stiction. It can also be extremely complicated to get a true picture of surface geometry. Most models rely on either surface sampling or Gaussian predictions to approximate surface roughness distributions. Surface sampling creates an extreme amount of data requiring large amount of computational power to analyze with the trade off being surface distribution predictions that are not very accurate. Models using both methods will be presented in later sections.

In order to understand why stiction is a major factor at the micro scale, one must have a basic understanding of scaling laws. Stiction is a direct result of the dominance of surface forces over body forces (Hariri *et al* [32]). Surface forces become more pronounced over the body forces due to large surface over volume ratio (van Spengen *et al* [29]). As devices are scaled down, the volume of the device scales down with third power of dimension ( $L^3$ ), while surface area only scales down as square ( $L^2$ ) (Hariri *et al* [32]). Therefore as the size of the device decreases, the ratio of the surface area to the volume increases with a factor of the scaling ratio. The consequence of this is that body forces such as weight and inertial forces that are proportional to volume lose their significance against surface forces (Hariri *et al* [32]).

The surfaces themselves must first be defined to account for the surface roughness. Where in the macro scale surfaces have an apparent area of contact, for example length  $x$  width of a rectangular surface, when looking at the micro scale it becomes clear that two rough surfaces in contact only have a certain number of contact points. When investigating stiction, Hariri *et al* show that it is advantageous to map the contact between two rough surfaces as a smooth rigid surface and a single equivalent rough surface (Figure 164). The use of a single equivalent surface aids in stiction analysis and is used in most models including those developed by Hariri *et al* [31,32], van Spengen *et al* [29] and Tas *et al* [33].

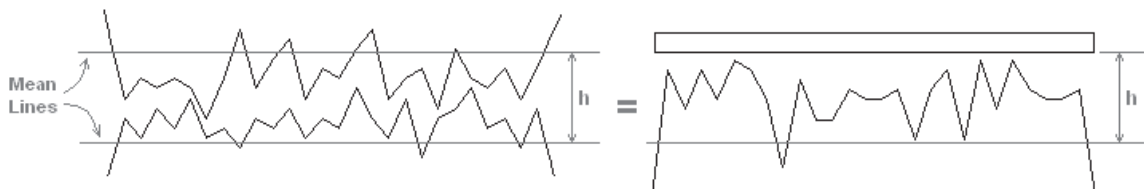


**Figure 164. Two surfaces in contact only have a finite number of contact points. An equivalent rough surface can be defined against a perfectly flat surface to aid in analysis. Adapted from Hariri *et al* [32]**

One thing not yet mentioned is plastic and elastic deformation. The real contact area will actual depend on the amount and type of deformation experienced by the surface contact points, known as asperities. This will be discussed later.

### **B.3.1 Capillary Forces**

A thin liquid layer can act as an adhesive between two surfaces. This is strongest of the factors that cause stiction. It is a factor that is highly dependent on the environmental conditions, specifically relative humidity and atmospheric pressure. Hariri *et al* [31] show that it can be a result of either immersion or capillary condensation. With immersion of contacting surfaces, liquid fills all gaps between rough surfaces. With capillary condensation, liquid from a vapour phase can condense between sufficiently

close asperities producing stiction. Wang *et al* [67] suggest that capillary forces can be eliminated by changing the atmospheric conditions, texturing surfaces, supercritical drying, chemical treatment and the use of hydrophobic surfaces and materials.

Consider a droplet between two smooth surfaces (Figure 165). If the droplet contact angle  $\theta_c$  between the liquid and the solid is less than  $90^\circ$ , the pressure inside the liquid “droplet” will be lower than outside and a net attraction force between the plates exists.

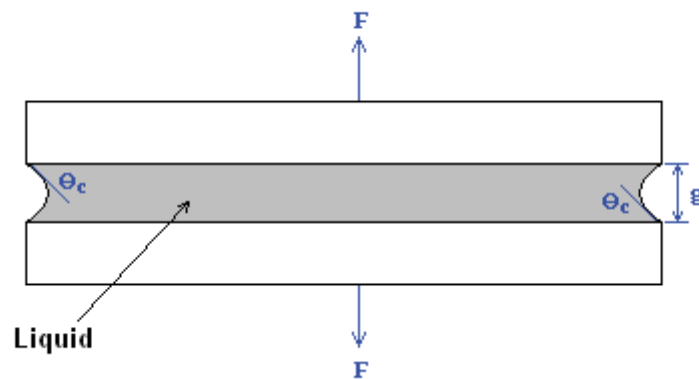


Figure 165. Droplet between two smooth surfaces. Adapted from Tas *et al* [33]

Where:  $g$  = liquid layer thickness

The pressure difference  $\Delta P_{la}$  at liquid-air interface is:

$$\Delta P_{la} = \frac{\gamma_{la}}{r} \quad (\text{A.9})$$

Where:  $\gamma_{la}$  = surface tension (force per unit length, or energy per unit area)

$r$  = radius of curvature of meniscus

$r = -g/2 \cos\theta_c$  (simple geometry)

In equilibrium, the external force  $F$  separating the surfaces must be applied to counterbalance the capillary pressure forces:

$$F = -\Delta P_{la} A = \frac{2A\gamma_{la} \cos\theta_c}{g} \quad (\text{A.10})$$

Where  $A$  is the wetted area.

A negative Laplace pressure (difference in pressure between the inside and outside of a droplet due to surface tension) indicates a positive force ( $F$ ). Pressure inside the liquid is lower than outside and the surfaces are pushed together by pressure forces.

Surface interaction energy is the energy required to separate the sticking surfaces. van Spengen *et al* [29] propose that surface energy stored at the interface that is bridged by liquid drop is therefore a quantitative measure of amount of stiction.

In order to calculate the surface interaction energy, consider a simple droplet on a surface (Figure 166) where  $\theta_c$  is the contact angle:

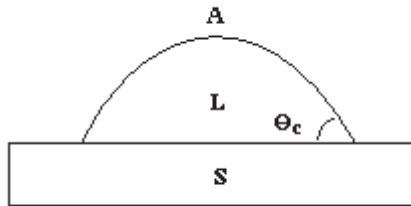


Figure 166. Droplet on a surface. Adapted from Tas *et al* [33]

The surface tension of the solid-air interface can be calculated as:

$$\gamma_{sa} = \gamma_{sl} + \gamma_{la} \cos\theta_c \quad 0 < \theta_c < \pi \quad (\text{A.11})$$

Where:  $\gamma_{sa}$  = surface tension of solid-air interface

$\gamma_{sl}$  = surface tension of solid-liquid interface

The contact angle is the same on a curved or irregular shaped surface, such as inside the capillary space between two surfaces. If  $\gamma_{sa} < \gamma_{la} + \gamma_{sl}$  then the contact angle is greater than zero ( $\theta_c > 0$ ) and the liquid will be non-spreading (Figure 167). If  $\gamma_{sa} > \gamma_{la} + \gamma_{sl}$  then it will be energetically favourable for the liquid to spread. In this case the contact angle will be flat ( $\theta_c = 0$ ) (Figure 168).

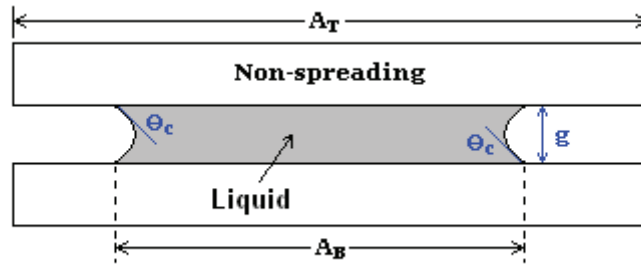


Figure 167. Non-spreading liquid droplet between two surfaces. Adapted from Tas *et al* [33]

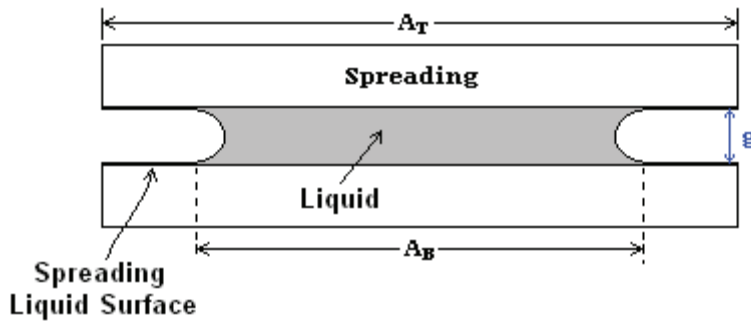


Figure 168. Spreading liquid droplet between two surfaces. Adapted from Tas *et al* [33]

The liquid area is confined to the bridged area ( $A_B$ ), which is smaller or equal to the total facing area ( $A_T$ ). The surface interaction energy for a spreading droplet is:

$$\begin{aligned}
 E_S &= 2 [ A_T ( \gamma_{sl} + \gamma_{la} ) - A_B \gamma_{la} ] \\
 &= 2 [ A_T ( \gamma_{sl} + \gamma_{la} ) - A_B \gamma_{la} \cos \theta_c ] \quad \text{(spreading)} \quad \text{(A.12)}
 \end{aligned}$$



For a non spreading droplet, the energy of the liquid-air meniscus area is neglected. This is since there is a small gap and meniscus area is small compared to bridged area.

$$\begin{aligned} E_S &= [ A_T \gamma_{sa} - A_B ( \gamma_{sa} - \gamma_{sl} ) ] \\ &= 2 [ A_T \gamma_{sa} - A_B \gamma_{la} \cos \theta_c ] \end{aligned} \quad \text{(non-spreading)} \quad \text{(A.13)}$$

Since the total area  $A_T$  and the surface tension are constant, the total surface energy can be written as a general form:

$$\begin{aligned} E_S &= C - 2A_B \gamma_{la} \cos \theta_c \\ \text{(A.14)} \end{aligned}$$

Where:  $\gamma_{la} \cos \theta_c$  is the adhesion tension

C is a constant

The surface interaction energy is changed by variations in the temperature and relative humidity of the environment. van Spengen *et al* [29] state that the surface tension of most liquids decreases as temperature increases:

$$\gamma_{1(\text{water})} \approx (75.6 - 0.167T) \times 10^{-3} \text{ J/m}^2 \quad \text{(A.15)}$$

Capillary condensation results in a large increase in the real contact area of surfaces by means of liquid bridging. Liquids that “wet” (low surface tension) or have a small contact angle on surfaces will spontaneously condense into cracks, pores and into small gaps surrounding the points of contact between the contacting surfaces (Figure 169) (Tas *et al* [33]). At equilibrium, the meniscus curvature of the bridging droplet is equal to the Kelvin radius:

$$r_K = \frac{\gamma_{la} V}{RT \ln(p/p_s)} \quad \text{(A.16)}$$

Where:  $V$  = molar volume

$p$  = vapour pressure

$p_s$  = saturated vapour pressure

$R$  = Gas constant

$T$  = absolute temperature

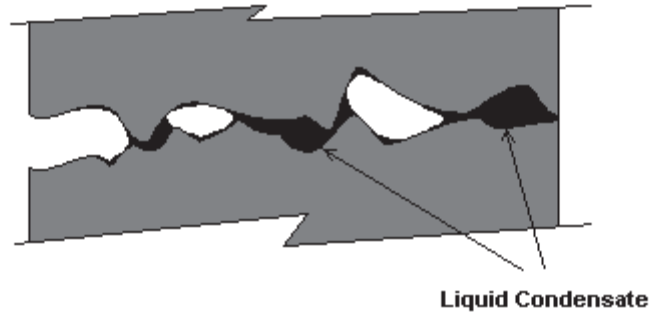


**Figure 169. Liquid condensate creates bridges between close asperities. Adapted from Tas *et al* [33]**

At room temperature:  $\frac{\gamma_{la}V}{RT} = 0.54$  nm for water

$p/p_s$  is the relative humidity. The Kelvin radius for various relative humidity is:

50%: $\ln(p/p_s) = -0.69$	$r_k = -0.8$ nm
75%: $\ln(p/p_s) = -0.29$	$r_k = -1.86$ nm
100%: $\ln(p/p_s) = 0$	$r_k = \infty$

It can be seen that for 100% relative humidity, the water film can grow over the complete surface. The amount of condensed liquid in thermodynamic equilibrium is determined by both the Kelvin radius and the contact angle (Tas *et al* [33]).

The characteristic distance of capillary condensation ( $d_{cap}$ ) (Figure 170) is given by:

$$d_{cap} \approx \frac{2\gamma_{la}V \cos \theta}{RT \ln(p/p_s)} \quad (\text{A.17})$$

Depending on  $d_{\text{cap}}$ , more or less surface will be covered with water, varying the level of stiction force. As with the Kelvin radius,  $d_{\text{cap}}$  depends on the relative humidity and the temperature.

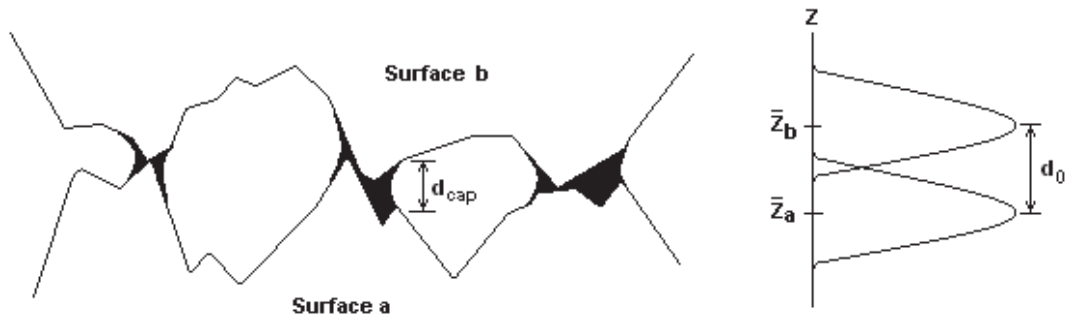


Figure 170. Characteristic distance of capillary condensation. Adapted from van Spengen *et al* [29]

The temperature dependence is primarily at a low relative humidity (<50%). As the relative humidity increases over 80%, the temperature has little bearing on the stiction force (Figure 171). Stiction force is higher at low temperatures and decreases as temperature rises. Working in a semi-vacuum can greatly reduce the effect of capillary stiction.

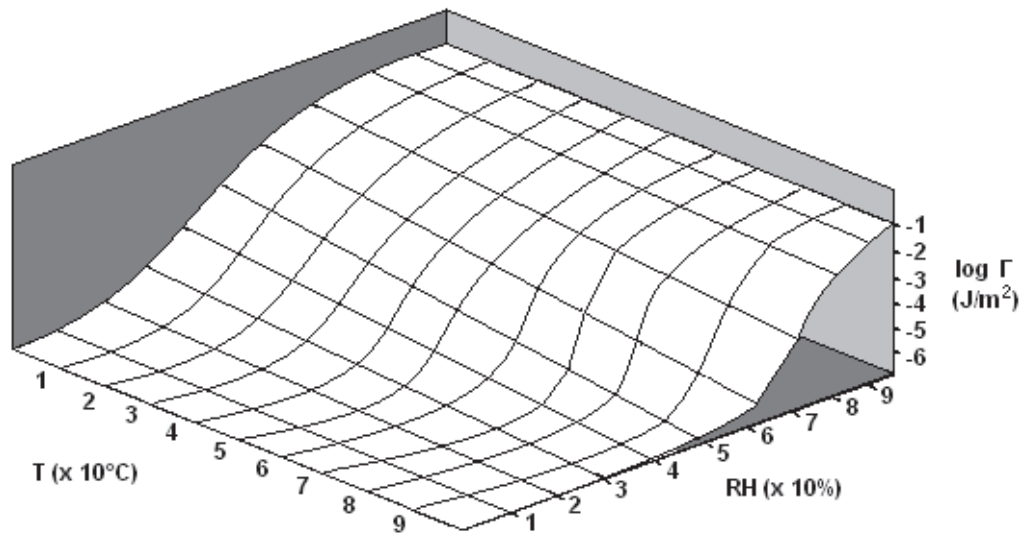


Figure 171. Capillary stiction as a function of temperature and relative humidity. Adapted from van Spengen *et al* [29]

### B.3.2 van der Waals Forces

van der Waals dispersion forces occur between two bodies and is caused by mutual electric interaction of induced dipoles. Research of Tas *et al* [33] shows that these forces dominate over orientation forces (polar molecule dipole-dipole forces) and induction forces (interaction of a polar molecule dipole moment and the induced dipole moment of a non-polar molecule), except for strongly polar molecules. Once again, interaction energy can be assessed between surfaces. Given two flat surfaces, with a separation distance ( $d$ )  $< 20\text{nm}$ , then:

$$E_{vdW} = -\frac{A}{12\pi d^2} \quad (\text{A.18})$$

Where:  $A$  = Hamaker constant =  $0.4 - 4 \times 10^{-19}$  J (most solids/liquids)

$d$  = distance between surfaces

When in contact, the Universal Cutoff Distance  $d_0 = 0.165$  nm. The Universal Cutoff Distance is commonly accepted as the minimum distance between surfaces. When distances are smaller than the Universal Cutoff Distance, a repulsive force acts to separate the surfaces (van Spengen *et al* [29]). This repulsive force is due to electron shell deformation.

When present, *capillary forces account for the largest of the adhesion forces*. By providing a hydrophobic surface, capillary adhesion can be eliminated. However, van der Waals forces will always remain (Figure 172) and van Spengen *et al* [29] have shown that there is surface roughness dependence. *van der Waals forces are most important when surfaces are dry and depend on the material dispersion only*. van Spengen *et al* [29] have also shown that these forces are insensitive to temperature variations.

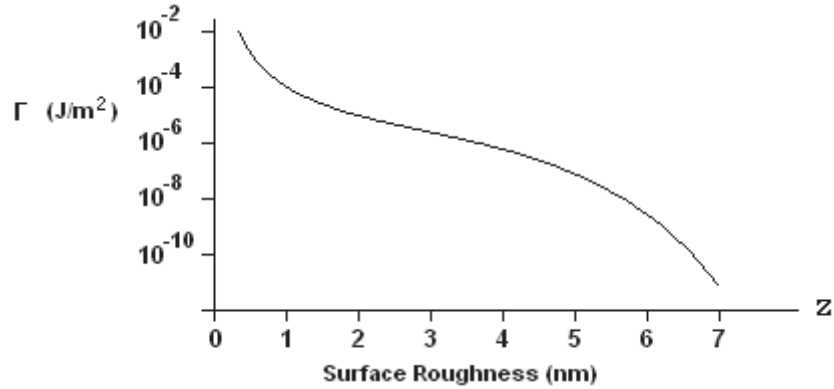


Figure 172. Typical van der Waals surface interaction energy vs roughness. Adapted from van Spengen *et al* [29]

### B.3.3 Electrostatic Forces

Stiction behaviour is influenced by parasitic electrical charges caused by either differences in contact potential, “tribocharging” of rubbing surfaces and ion trapping in oxide layers (van Spengen *et al* [29]). Electrostatic charges of opposed surfaces can cause attractive forces across the surface interface. At small separations the electrostatic pressure between flat surfaces is generally lower than the van der Waals pressure. Coulomb interaction between charged surfaces can be calculated as:

$$F_{El} = \frac{\epsilon V^2}{2z^2} \quad (\text{A.19})$$

Where:  $\epsilon$  = dielectric permittivity of material in the gap

$V$  = voltage differences between the surfaces

$z$  = distance between surfaces

Contact potentials hardly ever exceed 0.5 V and therefore have little effect.

Tribocharging is the voltage difference caused by rubbing surfaces together. This can generate high voltages that can create significant electrostatic forces. However, if

movement of structures ceases, then the charge tends to flow back slowly and therefore doesn't result in permanent stiction. Time for the surface potential to return to equilibrium is dependent on the contact resistance as a result of oxide surfaces and contamination. van Spengen *et al* [29] have shown that high resistivity coatings can be used to limit back flow of the charge to increase the stiction effect, if desired.

Charge accumulation in a dielectric layer, due to ion trapping, can also result in high electrostatic forces over a long period of time (van Spengen *et al* [29]).

### **B.3.4 Hydrogen Bridging (H-Bond) Forces**

Surfaces covered with OH bonds can lead to "H-bonds" that increases the surface interaction energy (van Spengen *et al* [29]). When water layers are brought together, hydrogen bonds can form between oxygen and hydrogen atoms. However, these surfaces are hydrophilic and as such likely to have capillary condensation. The capillary forces would then dwarf the H-bond forces unless relative humidity is low.

*Hydrogen bridging is a short range force (<0.27 nm), and is sensitive to surface roughness* (van Spengen *et al* [29]). Rough surfaces have a real contact area significantly lower than the apparent contact area.

### **B.3.5 Relative Contribution of Stiction Forces**

The four factors that result in stiction all have various significance (Figure 173). All reviewed papers concerned with stiction, Hariri *et al* [31,32], van Spengen *et al* [29] and Tas *et al* [33], are in agreement with the relative contribution of the forces. Capillary forces are usually the major dominant force, and often the only force that need be considered. However, in low pressure environments, or when relative humidity is significantly low, then van der Waals forces would be the next significant force. Electrostatic forces usually disappear with contact, and so are unlikely to be of any

concern, though a high contact resistance could lead to forces in the order of magnitude of the capillary forces, leading to them being a significant stiction force contributor. Normally electrostatic forces are much lower than the van der Waals forces and unlikely to be considered. Hydrogen bridging implies hydrophilic surfaces that would be prone to capillary bridges, making hydrogen bridging forces negligible. Even in a completely dry environment (zero relative humidity) the van der Waals forces would dwarf the hydrogen bridging forces. Electrostatic forces are marginally larger than the hydrogen bridging forces.

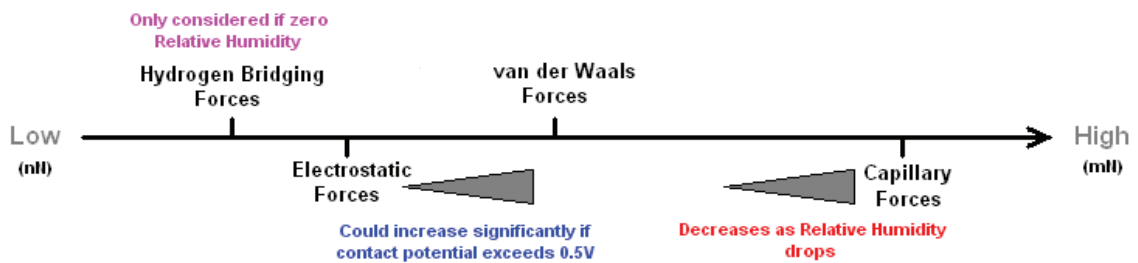


Figure 173. Relative contribution of various stiction forces

Relative motion of surfaces has a significant effect on stiction forces. Tambe *et al* [34] have shown that the number of capillary bridges formed increases with rest time (or residence time of an asperity tip during sliding). The meniscus bridges will not form if the spacing is greater than a critical distance that can be calculated. As the velocity increases, the time for stable meniscus formation reduces resulting in a decrease in the number of bridges. The maximum height of the bridges also decreases logarithmically. The contribution of viscous shearing of the water film, at the contacting and near-contacting asperities where menisci are formed, to the adhesive stiction force is very small and can usually be neglected, according to Tambe *et al* [34]. The research of Tambe *et al* [34] shows that there is a critical sliding velocity that is too high for stable menisci to form, causing the adhesive force to drop off. At this point the adhesive force contribution to the overall friction force diminishes and friction is now dominated only by deformation-related friction force and stick-slip. These two forces will be covered in the next section.

## B.4 Micro Friction

In traditional macroscale friction theories, as seen in a previous section, the friction force is related to the normal load through a proportionality constant, the coefficient of friction. This force is considered independent of the apparent area of contact. However, as noted by Lumbantobing *et al* [35] this doesn't hold at the microscale.

Most static friction models are based on simple surface topography representation. Tas *et al* [36] have shown that MEMS surfaces can have a wide range of surface roughness, from atomically smooth, as with chemical-mechanical polished silicon, to rough surfaces of deposited polysilicon. It was noted in the previous section that ***greater roughness generally results in reduced adhesion forces***. This contrasts micro friction forces that have increased forces when roughness increases.

Bowden and Tabor [37] indentified two basic micro friction mechanisms. These included the ploughing of asperities of a harder material through a softer material and the shearing of junctions formed in the region of contact of two surfaces. In MEMS, materials are usually of similar hardness and asperities are mostly blunt, although contaminations between surfaces can lead to friction variations (Olsson *et al* [30]). Tambe *et al* [34] further defined an additional mechanism for micro friction, stick-slip, that represents the primary mechanism of static friction of an interface.

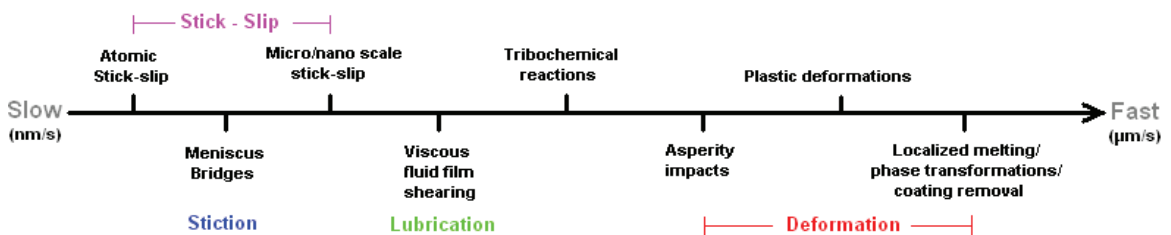


Figure 174. Dominant friction mechanisms with increasing velocity. Adapted from Tas *et al* [36]



Figure 174 outlines a more complete list of the dominant friction mechanisms as a function of velocity, as adapted from Tas *et al* [36]. For hydrophilic interfaces, meniscus (capillary) forces dominate at low velocities and hence the contributions of atomic stick-slip can be neglected.

Timpe *et al* [38] have shown that at the MEMS scale, adhesion forces also represent an additional normal force that can significantly raise the frictional forces when the external load is on the same order of magnitude as the adhesion forces. As the loads increase, such as in macro loads, the relevance of the adhesion forces to the friction forces becomes negligible. Stiction forces also tend to disappear as relative motion between surfaces increases.

#### B.4.1 Deformation

As previously mentioned, deformation is the compression of surface asperities. When considering a low sliding velocity, there is less energy for deformation. As such, this friction mechanism is not considered for static surfaces.

$$F_{def} = \frac{\text{Work done (frictional energy dissipated)}}{\text{Sliding distance over which energy is expended}}$$

$$= (\text{force to deform one asperity}) \times (\text{number of asperities deformed})$$

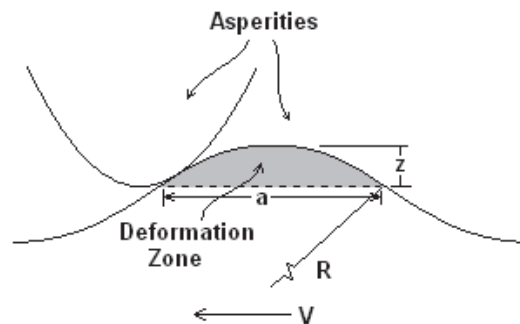


Figure 175. Deformation zone of asperity. Adapted from Tambe *et al* [34]

The deformation of the asperity depends on the relative hardness of the contacting surfaces, the normal load and the sliding velocity. The energy required for deformation comes from the kinetic energy from the asperity impact. Asperity wear will be initiated when the velocity is sufficiently high. Below the critical velocity, no frictional losses occur due to deformation.

If the normal load is insufficient to cause deformation then the friction force due to deformation will only become dominant at higher sliding velocities. There is a clear distinction between the adhesive force regime and the deformation-related friction force regime.

At very high sliding velocities, the energy dissipation creates high flash temperatures. Once high enough temperatures are reached, localized melting will set in and the friction force will drop. At this point, sliding mechanism becomes viscous shearing of melted contact zone.

#### B.4.2 Stick-Slip

Stick-slip is a buildup of friction force to certain value, the static friction force, which is then followed by a slip at the interface once this static force is overcome (Figure 176) (Bowden *et al* [65]).

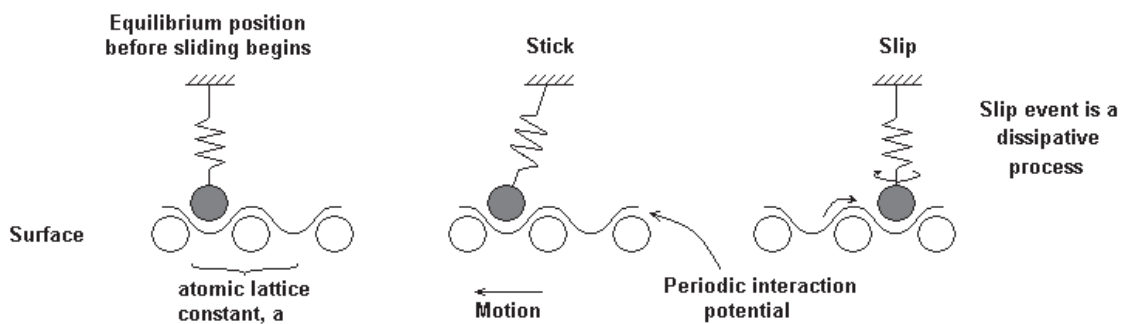


Figure 176. Stick-slip motion. Adapted from Tambe *et al* [34]

The stick-slip mechanism falls into two levels, the atomic level and the nano/micro level. At the atomic level, the atomic lattice of one surface interfaces with the atomic lattice of the contacting surface. The interface is the manner in which the atoms of one surface rest between the depressions between two atoms of the opposing surface. At the nano/micro level, asperities of the two contacting surfaces are interfaced in a similar fashion. Clearly, the roughness of the two surfaces dictates the quantity of asperity interfaces. Slippage is then a function of the surface hardness.

The depth of the interfaces is dependent on the normal force, which is balanced by the surface plastic and elastic deformation. The adhesive stiction forces are an attractive force that contributes to the normal force, thereby increasing the depth of the interfaces.

At rest, stick-slip is the primary mechanism of friction resisting the applied tangential force. Once this applied force exceeds the threshold friction, slippage begins. The resulting kinetic energy then contributes to the deformation and ploughing of asperities. For this reason, the kinetic friction is lower than the static friction.

#### **B.4.3 Friction and Stiction Comparison**

Figure 177 shows a comparison of friction and stiction forces and their relative strengths. As can be seen, the actual magnitude of individual contributing mechanisms is dependent on the conditions. *Generally, the micro/nano scale stick-slip mechanism of the static surfaces will have the highest values, unless there is higher humidity or pressure. In the static state, or at low velocities, the capillary forces not only contribute greatly, but also create an additional normal force that adds to the friction effect of the stick-slip mechanism. As velocity increases from the static state, capillary forces drop off and kinetic energy reduces the stick-slip mechanism, leaving the deformation as the dominant friction force.*

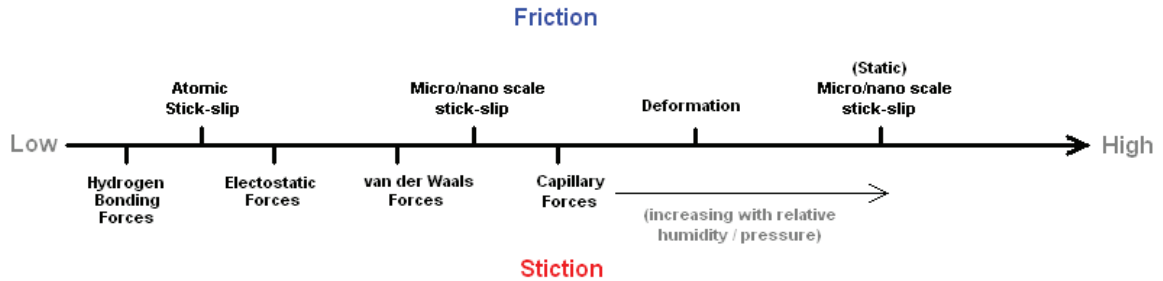


Figure 177. A comparison of friction and stiction forces.

## B.5 Summary

This Appendix has presented a number of different models to define macro friction, stiction and micro friction. The main contributing factors for both friction and stiction were described. The four contributing factors of stiction are capillary forces, van der Waals forces, hydrogen bonds and electrostatic forces. With the presence of water, capillary forces are clearly the dominant stiction forces. In dry conditions, van der Waals becomes the dominant force. Roughness of the surface makes a large contribution to friction, but also results in a reduction of real contact area. The net result is a reduction in the stiction force. A clear description of stiction as an adhesive force, and its contribution to micro friction was given. Since stiction is an adhesive force, it provides an additional normal force that contributes to the micro friction forces. Stiction as a force always exists, but as a surface force, it is neglected at the macro scale where body forces dominate. Micro friction is a result of both deformation and the stick-slip mechanisms. Once applied forces exceed the initial stick-slip threshold, kinetic energy allows for deformation of asperities making that the dominant mechanism of friction.

Most of the models described are highly complex to use and computationally expensive. Most require detailed surface analysis to gather topography information. Though table values can be used for some approximations, for a true assessment, accurately measured samples of the surface are required. For many MEMS structures, this is not practical since it would require the component to be broken apart to access the mated surfaces. In this case approximations would be the best alternative.

## **Appendix C – Assignment of Copyright**

### **Assignment of copyright form - IOP Publishing Limited**

#### **1. IOP Publishing Limited (“IOP”) agrees to publish:**

**Manuscript Title:** Fourier analysis of blurred images for the measurement of the in-plane dynamics of MEMS. (**“the Article”**) **written by Names of all Authors:** Neil Ellerington, Ben Bschaden, Ted Hubbard, Marek Kujath . (**“the Named Authors”**) **in the following journal:** Journal of Micromechanics and MicroEngineering. (**“the Journal”**)

#### **2. Transfer of Copyright Agreement**

2.1 On acceptance for publication the undersigned author(s) (“Author”) of the Article assigns exclusively to IOP worldwide copyright in the Article for the full term and for all media and formats in all material published as part of the Article, which expression includes but is not limited to the text, abstract, tables, figures, graphs, video abstracts and other multimedia content but excludes any other item referred to as supplementary material.

2.2 If any of the Named Authors are Government employees, on acceptance for publication the Author shall grant IOP a royalty free exclusive licence for the full term of copyright for all media and formats to do in relation to the Article all acts restricted by copyright worldwide.

2.3 On acceptance for publication the Author shall grant IOP a royalty free non-exclusive licence for the full term of copyright for all media and formats to do in relation to any supplementary material deemed to be part of the Article all acts restricted by copyright worldwide.

#### **3. Author Rights**

3.1 IOP grants the Named Authors the rights specified in 3.2 and 3.3. All such rights must be exercised for non- commercial purposes, if possible should display citation

information and IOP's copyright notice, and for electronic use best efforts must be made to include a link to the on-line abstract in the Journal. Exercise of the rights in 3.3 additionally must not use the final published IOP format but the Named Author's own format (which may include amendments made following peer review).

3.2 The rights are:

3.2.1 To make copies of the Article (all or part) for teaching purposes;

3.2.2 To include the Article (all or part) in a research thesis or dissertation;

3.2.3 To make oral presentation of the Article (all or part) and to include a summary and/or highlights of it in papers distributed at such presentations or in conference proceedings; and

3.2.4 All proprietary rights other than copyright.

3.3 The additional rights are to:

3.3.1 Use the Article (all or part) without modification in personal compilations or publications of a Named Author's own works (provided not created by third party publisher);

3.3.2 Include the Article (all or part) on a Named Author's own personal web site;

3.3.3 Include the Article (all or part) on web sites of the Institution (including its repository) where a Named Author worked when research for the Article was carried out; and

3.3.4 No sooner than 12 months after publication to include the Article (all or part) on third party web sites including e- print servers, but not on other publisher's web sites.

#### **4. Signature**

In signing this Agreement the Author represents and warrants that the Article is the original work of the Named Authors, it has not been published previously in any form (other than as permitted under clause 3.2.2 which fact has been notified to IOP Publishing Ltd in writing), all Named Authors have participated sufficiently in the conception and writing of the Article, have received the final version of the Article, agree to its submission and take responsibility for it, and submission has been approved as necessary by the authorities at the establishment where the research was carried out.

The Author warrants that he/she signs this Agreement as authorised agent for all Named Authors and has the full power to enter into this Agreement and to make the grants it contains, that the Article has not been and will not be submitted to another publisher prior to withdrawal or rejection, it does not infringe any third party rights, it contains nothing libellous or unlawful, all factual statements are to the best of the Author's knowledge true or based on valid research conducted according to accepted norms, and all required permissions have been obtained in writing.

All Named Authors assert their moral rights.

**Author's signature . . . . . Date . . . . .**

**Signature on behalf of Institution . . . . . Date . . . . .**

**Note that if the Article was prepared as part of a Named Author's duties for their institution this Agreement must be signed by their institution as Author. Further, if there are several Named Authors it should be signed by one author in a representative capacity. If all Named Authors are employees of the US Government and the Article was prepared as part of their duties the Article is not eligible for copyright and one of the Named Authors should sign below to confirm this fact. If at least one of the Named Authors is not a US Government employee the above should be signed.**

**I . . . . . (print name . . . . .  
. . . . . ) confirm that all Named Authors are employees of the US  
Government and the Article was prepared as part of their duties and consequently  
the Article is not eligible for copyright.**

Please return ALL of this form as soon as possible to IOP Publishing Ltd, Temple  
Circus, Temple Way, BRISTOL BS1 6BE, UK.